1089

ornl

ORNL/Sub/86-47985/2&V1

OAK RIDGE
NATIONAL
LABORATORY

MARTIN MARIETTA

Free-Piston Stirling Engine Diaphragm-Coupled Heat-Actuated Heat Pump Component Technology Program

Volume I
Phase IIA and IIB Final Report:
Technical Discussion

OPERATED BY
MARTIN MARIETTA ENERGY SYSTEMS, INC.
FOR THE UNITED STATES
DEPARTMENT OF ENERGY

ornl

ORNL/Sub/86-47985/2&V1

FILE COPY
DO NOT
REMOVE

OAK RIDGE
NATIONAL
LABORATORY

MARTIN MARIETTA

Free-Piston Stirling Engine Diaphragm-Coupled Heat-Actuated Heat Pump Component Technology Program

Volume I
Phase IIA and IIB Final Report:
Technical Discussion

OPERATED BY
MARTIN MARIETTA ENERGY SYSTEMS, INC.
FOR THE UNITED STATES
DEPARTMENT OF ENERGY

Printed in the United States of America. Available from
National Technical Information Service
U.S. Department of Commerce
5285 Port Royal Road, Springfield, Virginia 22161
NTIS price codes—Printed Copy: A13 Microfiche A01

This report was prepared as an account of work sponsored by an agency of the United States Government. Neither the United States Government nor any agency thereof, nor any of their employees, makes any warranty, express or implied, or assumes any legal liability or responsibility for the accuracy, completeness, or usefulness of any information, apparatus, product, or process disclosed, or represents that its use would not infringe privately owned rights. Reference herein to any specific commercial product, process, or service by trade name, trademark, manufacturer, or otherwise, does not necessarily constitute or imply its endorsement, recommendation, or favoring by the United States Government or any agency thereof. The views and opinions of authors expressed herein do not necessarily state or reflect those of the United States Government or any agency thereof.

MTI 88TR9

FREE-PISTON STIRLING ENGINE DIAPHRAGM-COUPLED HEAT-ACTUATED HEAT PUMP COMPONENT TECHNOLOGY PROGRAM

Volume I

PHASE IIA and IIB FINAL REPORT:
TECHNICAL DISCUSSION

R. A. Ackermann

25 January 1988

Report Prepared by

MECHANICAL TECHNOLOGY INCORPORATED
968 Albany-Shaker Road
Latham, New York 12110

under

Subcontract 86X-47985V

for the

ENERGY DIVISION
OAK RIDGE NATIONAL LABORATORY
Oak Ridge, Tennessee 37831
operated by
MARTIN MARIETTA ENERGY SYSTEMS, INCORPORATED
for the
U.S. DEPARTMENT OF ENERGY
under contract DE-AC05-84OR21400

ACKNOWLEDGMENTS

MTI wishes to acknowledge the support provided to this program by the technicians, engineers, and managers at both Lennox Industries and John Deere & Co. Their background and knowledge of heating, ventilating and air-conditioning equipment, and manufacturability were key elements in the success of this work.

ABSTRACT

This report presents the results of an effort to develop and demonstrate the technical feasibility of a residential size Stirling-engine-driven diaphragm-coupled compressor for a heat pump application. The heat pump module consists of a 3-kW free-piston Stirling engine (FPSE), an efficient hydraulic transmission, and a nominal 3-ton capacity refrigerant (R-22) reciprocating compressor. During earlier Phase I activity, the lower end (hydraulic transmission and compressor) was designed, fabricated, mated to an existing Mechanical Technology Incorporated (MTI) FPSE, and tested. After several years of development, this heat pump module achieved a capacity of 2.5 refrigeration tons at 95°F ambient conditions. While this was below the module's rated 3.0-ton capacity, it demonstrated the potential of the FPSE heat pump (FPSE/HP) and identified a lack of engine power as the main reason for the low capacity. During a companion engine development program sponsored by the Gas Research Institute, the engine was improved by developing a new displacer drive that increased the FPSE's power capability. During Phase II, the new engine, the Mark I, was mated to the lower end (transmission/compressor) and tested. The testing of the Mark I FPSE/HP module was very successful, with the system achieving its 3.0-ton capacity goal and all other proof-of-concepts targets.

In addition to the MTI testing, the Mark I FPSE/HP module was also sent to Lennox Industries for their evaluation and an independent assessment during Phase II. The testing at Lennox substantiated the MTI results and provided a comprehensive performance mapping of the system that can now be used to perform both system and economic studies. Phase II efforts were also directed at the design of a second generation lower end that would meet a manufacturing cost goal of $250 for a production base of 50,000 units per year.

Included herein is a disucssion of the Phase II activity, including the results of the Mark I FPSE/HP module testing, a component design effort of several key lower end components that was performed to optimize the design, and the Lennox evaluation. The results of a value engineering study and cost evaluation performed by the John Deere & Co. on the lower end are also discussed. Through this value engineering effort, the lower end manufacturing

cost target of $250 was shown to be feasible, further substantiating the commercial potential of the FPSE/HP.

TABLE OF CONTENTS

NUMBER		PAGE
	ACKNOWLEDGMENTS	iii
	ABSTRACT	v
	LIST OF FIGURES	ix
	LIST OF TABLES	xv
	EXECUTIVE SUMMARY	xvii
1.0	INTRODUCTION	1-1
2.0	PHASE IIA TECHNICAL DISCUSSION	2-1
	2.1 Mark I Heat Pump Compressor/Hydraulic Transmission Assembly	2-1
	2.2 Mark I Serial No. 1 Heat Pump Module Test Results	2-3
	2.2.1 Mark I Heat Pump Module Comparative Results	2-15
	2.2.2 Modulation Test at the 47°F Ambient Temperature Conditions	2-19
	2.3 Modifications to Existing Compressor/Transmission	2-21
	2.3.1 Bore-to-Stroke Ratio Analysis	2-21
	2.3.2 Bore-to-Stroke Performance Results	2-43
	2.3.3 Main Oil Seal Design	2-43
	2.4 Advanced Diaphragm Design and Analysis	2-60
	2.4.1 Contoured Diaphragms	2-67
	2.4.2 Convoluted Diaphragms	2-80
	2.4.3 Articulated Diaphragms	2-92
	2.4.4 Results of the Diaphragm Analysis	2-94
	2.5 Hydraulic Simulator Modifications Review	2-101
	2.5.1 Hydraulic Simulator Power Requirements	2-105
	2.5.2 Hydraulic Simulator Modifications	2-107
	2.5.3 Weighted Assessment of Three Options	2-120

TABLE OF CONTENTS (Continued)

NUMBER		PAGE
3.0	PHASE IIB TECHNICAL DISCUSSION	3-1
3.1	Results of Mark I Heat Pump Module Testing at Lennox	3-1
3.1.1	Summary of Test Results	3-1
3.1.2	Test Plan	3-2
3.1.3	Description of Lennox Test Facility	3-5
3.1.4	Test Results	3-8
3.1.5	Conclusions of Lennox Testing	3-27
3.2	Advanced Compressor Design	3-27
3.2.1	Mark II Design Procedure	3-37
3.2.2	Alternative Design Options	3-43
3.2.3	Future VA/VE Activities	3-64
APPENDIX A:	DESCRIPTION OF AN FPSE HEAT PUMP	A-1
APPENDIX B:	COOKE-YARBOROUGH ARTICULATED DIAPHRAGM ANALYSIS	B-1

LIST OF FIGURES

NUMBER		PAGE
1-1	Phase II Program Schedule	1-3
1-2	Mark I Heat Pump Module	1-4
2-1	Breadboard FPSE/HP Module with Direct-Drive Transmission	2-2
2-2	Mark I Heat Pump Module Data (September 1986)	2-5
2-3	Engine Heat Recovery	2-13
2-4	Mark I Heat Pump Performance Test (Capacity Modulation Test - 47°F Conditions and Steady-State Tests at Different Strokes)	2-20
2-5	Refrigerant Pressure Volume Diagram	2-23
2-6	Direct-Drive Hydraulic Transmission and Compressor Assembly	2-25
2-7	Breadboard Compressor Piston Cylinder Configuration	2-26
2-8	Suction/Discharge Valve Plate Assembly	2-27
2-9	Heating and Cooling Capacity and Load for a Typical 3-Bedroom House in the Mid-Atlantic Region	2-32
2-10	Curve Fit for Measured Hydraulic Transmission Power Loss on Breadboard Heat Pump Module	2-38
2-11	Transmission Power Loss versus Compressor Piston Stroke for EM No. 4 Heat Pump Module with 10-cs Mineral Oil	2-39
2-12	Hydraulic Transmission Power Loss for Mark I Heat Pump Module with 10-cs Silicone Oil (Engine Build 22 - September 1986)	2-40
2-13	Hydraulic Transmission Power Loss Test Drive-Drive Transmission-Hydraulic Simulator with 10-cs Silicone Oil	2-41
2-14	Compressor Performance as a Function of Bore Diameter Assuming Constant $P_{discharge}/P_{suction}$ at Each Condition	2-46
2-15	Compressor Volumetric Efficiency as a Function of Bore Diameter Assuming Constant $P_{discharge}/P_{suction}$ at Each Condition	2-49
2-16	Mark I Hydraulic Transmission Efficiency as a Function of Compressor Piston Stroke	2-50
2-17	Mark I Hydraulic Transmission Showing Chevron Seal Pack Location	2-51
2-18	Oil Management System Schematic	2-52

LIST OF FIGURES (Continued)

NUMBER		PAGE
2-19	Chevron Seal Design	2-54
2-20	Original Chevron Seal Pack Design	2-55
2-21	Simplified Seal Pack	2-56
2-22	Present and Proposed Modified Chevron Seal Designs	2-61
2-23	Rod T-Seal Design	2-62
2-24	Diaphragm Alternatives	2-64
2-25	Welded Metal Bellows	2-65
2-26	Contoured Diaphragm: Standard Bendix Shape	2-68
2-27	Improved Contoured Diaphragm: Revised Shape	2-69
2-28	Contoured Diaphragm: Straight Region and Convolution Added Shapes	2-70
2-29	Comparison of PLATEA and NONLIN Code Results for Standard Bendix Diaphragm: ΔP versus Displaced Volume	2-71
2-30	Comparison of PLATEA and NONLIN Code Results for Standard Bendix Diaphragm: Maximum Bending Stress versus Displaced Volume	2-72
2-31	Comparison of NONLIN Code Results for Bendix Standard and Revised Diaphragms: Maximum Bending Stress versus Displaced Volume	2-74
2-32	Comparison of NONLIN Code Results for Bendix Standard and Revised Diaphragms: ΔP versus Displaced Volume	2-75
2-33	Comparison of NONLIN Code Results for Bendix Standard and Flat Diaphragms: Maximum Bending Stress versus Displaced Volume	2-76
2-34	Comparison of NONLIN Code Results for Bendix Standard and Flat Diaphragms: ΔP versus Displaced Volume	2-77
2-35	Comparison of NONLIN Code Results for Bendix Revised Steel and Titanium Diaphragms: Maximum Bending Stress versus Displaced Volume	2-78
2-36	Comparison of NONLIN Code Results for Bendix Revised Steel and Titanium Diaphragms: ΔP versus Displaced Volume	2-79
2-37	Convoluted Diaphragm Geometries	2-81

LIST OF FIGURES (Continued)

NUMBER		PAGE
2-38	NONLIN Code Results for Zurn Shape Diaphragm (8, 12, 16 mil): Maximum Bending Stress versus Displaced Volume	2-82
2-39	NONLIN Code Results for Zurn Shape Diaphragm (8, 12, 16 mil): ΔP versus Displaced Volume	2-83
2-40	NONLIN Code Results for 3-Ripple Diaphragm (0.05-in. Amplitude, 8 mil): Maximum Bending Stress versus Displaced Volume	2-84
2-41	NONLIN Code Results for 3-Ripple Diaphragm (0.05-in. Amplitude, 8 mil): ΔP versus Displaced Volume	2-85
2-42	NONLIN Code Results for 3-Ripple Diaphragm (0.05-in. Amplitude, 12 and 16 mil): Maximum Bending Stress versus Displaced Volume	2-86
2-43	NONLIN Code Results for 3-Ripple Diaphragm (0.05-in. Amplitude, 12 and 16 mil): ΔP versus Displaced Volume	2-87
2-44	NONLIN Code Results for 3-Ripple Diaphragm (0.10-in. Amplitude, 8, 12, 16 mil): Maximum Bending Stress versus Displaced Volume	2-88
2-45	NONLIN Code Results for 3-Ripple Diaphragm (0.10-in. Amplitude, 8, 12, 16 mil): ΔP versus Displaced Volume	2-89
2-46	NONLIN Code Results for 3-Ripple Diaphragm (0.15-in. Amplitude, 8, 12, 16 mil): Maximum Bending Stress versus Displaced Volume	2-90
2-47	NONLIN Code Results for 3-Ripple Diaphragm (0.15-in. Amplitude, 8, 12, 16 mil): ΔP versus Displaced Volume	2-91
2-48	Articulated Diaphragm	2-93
2-49	NONLIN Code Results for Case 1A Articulated Diaphragm: Maximum Combined Stress versus Displaced Volume	2-96
2-50	NONLIN Code Results for Case 1A Articulated Diaphragm: ΔP versus Displaced Volume	2-97
2-51	NONLIN Code Results for Articulated Diaphragm (40 and 60 mil): Maximum Combined Stress versus Displaced Volume	2-98
2-52	NONLIN Code Results for Articulated Diaphragm (40 and 60 mil): ΔP versus Displaced Volume	2-99

LIST OF FIGURES (Continued)

NUMBER		PAGE
2-53	Hydraulic Simulator Test Rig	2-102
2-54	Schematic for Hydraulic Simulator with Direct-Drive Compressor	2-104
2-55	Required Motor Input Power to Overcome Losses in Hydraulic Simulator and Transmission as a Function of Compressor Piston Stroke	2-106
2-56	Laminated Stator and Plunger	2-108
2-57	Hydraulic Simulator Layout	2-110
2-58	Cross-Section Schematic of Moving-Magnet, Moving-Back-Iron Linear Motor	2-114
2-59	MTI FPSE Engineering Model Linear Motor Displacer Drive System Hardware	2-116
2-60	Two-Motor Electrical Circuit	2-121
3-1	Mark I System Package Installed in Lennox Test Facility	3-6
3-2	Lennox Calorimeter Test Loop	3-7
3-3	Verification Test Data COP	3-9
3-4	Mark I Performance Thermal Capacity	3-11
3-5	Mark I Heat Pump Module Measured COP	3-12
3-6	Mark I Heat Pump Module Data Comparison	3-13
3-7	Schematic of Refrigeration Cycle	3-20
3-8	Motor Input Power versus Cooler Inlet Temperature	3-24
3-9	Performance versus Coolant Temperature	3-25
3-10	Mark I Hydraulic Transmission	3-26
3-11	High Stroke Engine Parameters: All Condenser Temperatures	3-28
3-12	Heat Pump Module Heating Performance	3-30
3-13	Heat Pump Module Cooling Performance	3-31
3-14	Compressor Heating Performance	3-32
3-15	Compressor Cooling Performance	3-33
3-16	Lower End COP	3-37
3-17	Mark I Lower End Design	3-38
3-18	Vibration Absorbers	3-40
3-19	Mark II Compressor Design	3-42

LIST OF FIGURES (Continued)

NUMBER		PAGE
3-20	FPSE (Contacting Seals) Coupled to Refrigerant Compressor via Hydraulic Transmission (Chevron Seals)	3-44
3-21	Preliminary Mark II Hydraulic Transmission/Compressor Design	3-46
3-22	Schematic Representation of Linear Magnetic Coupling	3-47
3-23	Force Diagram for Coupling	3-48
3-24	FPSE Coupled to Refrigerant Compressor via Hydraulic Transmission and Magnetic Coupling	3-49
3-25	FPSE Coupled to Refrigerant Compressor via Magnetic Coupling	3-54
3-26	FPSE/HP Lower End Cost Reductions	3-56
3-27	Mark II Torque Bar Vibration Absorber and Compressor Assembly	3-57
3-28	Mark IIVE Compressor Design	3-59
3-29	Mark IIB Compressor Design	3-62

LIST OF TABLES

NUMBER		PAGE
2-1	Test Conditions for R-22 Refrigerant	2-6
2-2	Typical Measured Data and Computations for Heating/Cooling Rating Points: Refrigerant Condition	2-7
2-3	Typical Measured Data and Computations for Heating/Cooling Rating Points: Refrigerant Energy Quantities	2-8
2-4	Typical Measured Data and Computations for Heating/Cooling Rating Points: Mark I Input Energy	2-9
2-5	Typical Measured Data and Computations for Heating/Cooling Rating Points: Mark I Engine Rejected Heat	2-10
2-6	Typical Measured Data and Computations for Heating/Cooling Rating Points: Mark I Heat Pump Module Performance	2-11
2-7	Mark I versus EM Engine Heat Pump Performance Comparison: Raised Coolant Temperature	2-16
2-8	Mark I versus EM Engine Heat Pump Performance Comparison: High Cooling Capacity	2-17
2-9	Mark I versus EM Engine Heat Pump Performance Comparison: High Heating Capacity	2-18
2-10	Compressor Residual Clearance Volume	2-31
2-11	Calculated Effect of Bore Diameter on Compressor Performance at 95°F Ambient Conditions	2-44
2-12	Calculated Effect of Bore Diameter on Compressor Performance at 17°F Ambient Conditions	2-45
2-13	Calculated Effect of Bore Diameter on Compressor Volumetric Efficiency at 95°F Ambient Conditions	2-46
2-14	Calculated Effect of Bore Diameter on Compressor Volumetric Efficiency at 17°F Ambient Conditions	2-47
2-15	Oil Leakage Test Results for the HAHP Direct-Acting Externally Balanced Compressor	2-57
2-16	Chevron Seal Frictional Force	2-58
2-17	Articulated Diaphragm	2-95

LIST OF TABLES (Continued)

NUMBER		PAGE
2-18	Summary of Results	2-100
2-19	Hydraulic Simulator Test Data (No Refrigerant Pumping; 8 January 1985; Scan No. 33)	2-112
2-20	Comparison of Calculated Losses of Single- and Double-Motor Installations	2-118
2-21	Weighted Assessment of Hydraulic Simulator Modifications	2-122
3-1	Planned Test Matrix	3-4
3-2	Conditions for Compressor Mapping	3-14
3-3	Completed Performance Mapping Data Points	3-16
3-4	Variation in Measured Refrigerant Flow	3-18
3-5	Variation in Measured Engine PV Power	3-19
3-6	Effect of Cooler Temperature on Performance	3-23
3-7	Linear Regression Curve Fit for Engine Performance Parameters	3-29
3-8	Mark II Design: Operating Points and Heat Pump Performance Parameters	3-35
3-9	Summary of Major Subassembly Costs	3-39
3-10	Loss Calculations for Existing Direct Acting Transmission	3-51
3-11	Loss Calculations for In-Line Transmission	3-52
3-12	Loss Calculations for Horizontal Transmission	3-53
3-13	Mark II Compressor Cost Summary	3-58
3-14	Mark IIVE Improved Compressor Cost Summary	3-61
3-15	Mark IIB Compressor Cost Summary	3-63

EXECUTIVE SUMMARY

At the start of the Heat--Actuated Heat Pump (HAHP) component development program in 1981, the performance goals established for the free piston Stirling engine (FPSE) compressor were:

- Demonstrate stable heating and cooling performance
- Achieve 3.0 refrigeration tons cooling capacity at the 95°F ambient conditions
- Demonstrate the FPSE heat pump (FPSE/HP) compressor load matching capability and load modulation range
- Demonstrate a lower end coefficient of performance (COP) at the 95°F conditions of 3.6 or higher
- Demonstrate good laboratory reliability and data repeatability.

During the first phase of the program, a breadboard lower end (transmission and compressor) was designed, fabricated, mated to an existing Mechanical Technology Incorporated (MTI) FPSE, and tested to demonstrate its potential for commercialization as an FPSE/HP. The engine/transmission/compressor assembly (FPSE/HP module) operated successfully and demonstrated many of the intended goals. However, it did not achieve the capacity goal of 3.0 refrigeration tons.

In order to achieve the capacity goal, Phase II was initiated. The objective of this phase was to evaluate several key components in the lower end to determine what redesigns were necessary to improve performance. In parallel, a program sponsored by the Gas Research Institute (GRI) was investigating the FPSE for improvements. Through these two efforts, the shortfall in capacity was identified as a mismatch between the engine and lower end power characteristics and that an improved displacer drive for the engine was required. A new displacer drive was designed, and a new engine, the Mark I FPSE, incorporating the redesigned displacer drive was tested with the breadboard lower end during Phase II.

With the Mark I FPSE, all of the performance goals for the FPSE/HP module were achieved. The achievement of these goals was further verified in an off-site test program conducted at the Lennox Corporation's engineering facilities.

Conducted over a 60-day period, this testing verified the performance of the Mark I FPSE/HP module and demonstrated the assembly's repeatability and reliability by running for this period with no degradation in performance and trouble free.

A second major effort conducted in Phase II was the value engineering of the lower end with John Deere & Co. The objective of this work was to evaluate the manufacturing cost of the Mark I lower end and assess if a manufacturing cost target of $250 could be achieved through a value-engineering effort.

The specific results of the Phase II effort can be summarized as follows:

- Further improvement in the performance of the lower end can be achieved by a more precise optimization of the compressor bore/stroke ratio. The maximum hydraulic transmission efficiency measured with the breadboard system was 87%. By a more precise optimization of the bore/stroke ratio to reduce viscous losses in the hydraulic transmission, the efficiency could be increased to 92%.

- Alternative diaphragm configurations, i.e., Cooke-Yarborough's articulated diaphragms, convoluted diaphragms, and titanium-contoured diaphragms, could all lead to increased volumetric deflections over the existing steel-contoured diaphragms and, therefore, greater refrigerant heating and cooling capacity. However, centering of the diaphragm and stability problems occur when the diaphragm thickness is reduced too much to achieve the larger deflections.

- An initial manufacturing cost of $2,550 was estimated for the Mark I lower end. However, by redesigning the unit to eliminate the oil management system, simplify the vibration absorber, and use a single-acting instead of a double-acting compressor, the cost could be reduced to $418. This significant cost reduction enhances the potential for commercializing the HAHP, as well as emphasizes the need to extend the value engineering analyses to the engine.

Considering the success made during Phase II in advancing the technology of the FPSE/HP module, it is apparent that the goal of commercializing an FPSE/HP can be achieved.

SECTION 1.0

INTRODUCTION

1.0 INTRODUCTION

Previous efforts under Phases I through IC of the HAHP program were concerned with proof-of-concept of the FPSE/HP module, improvement of transmission/compressor performance, and performance testing of the heat pump module with the existing EM engine. These efforts, together with the complementary FPSE programs conducted at MTI, have resulted in major improvements in component performance and system operation.

The original engine/compressor/transmission design, as defined in the Phase I/IA report, was intended to provide 3.0 RT[1] capacity at the 95°F ambient conditions with a 19-mm compressor stroke and 40,000-psi diaphragm stress, as well as effective operation over the entire range of heating and cooling conditions. In test, the first assembly attained a compressor stroke of 16 mm, but no measurable capacity was produced in the breadboard system because of excessive losses in the compressor/transmission.

In Phases IB and IC, changes were made to provide more power from the engine (increased size of hydraulic piston), increase transmission efficiency (external counterweight, low viscosity fluid, reduced leakage, and seal modification), and improve compressor efficiency (reduced clearance volume, reduced leakage, and reduced oil circulation). This resulted in 2.5 RT capacity in cooling (95°F) at a compressor stroke of 16.4 mm. The diaphragm stress was a safe 35,000 psi at these conditions, but the displacer was at maximum stroke, thus limiting the capacity. At the 17°F ambient heating condition, a compressor stroke of 18.5 mm was attained before the displacer limit was reached, but the diaphragm stress was 50,000 psi. Since this stress level was 43% greater than the 35,000 psi recommended by the manufacturer for long life, operation at this condition was unacceptable.

From the above, it was clear that a number of modifications had to be made if the heat pump module was to achieve 3.0 RT and perform effectively over the required range of conditions with long life.

[1]RT represents refrigeration tons of cooling (1 ton = 12,000 Btu/hr).

This report describes the work performed during Phase II of the program, which consisted of two sequential subphases as shown in Figure 1-1. The work performed was designed to further advance the development of an FPSE/HP module by performing parametric analyses on several key components and performing a value engineering evaluation of the Mark I lower end (hydraulic transmission and compressor). One objective of this work was to design a second generation lower end that would meet a manufacturing cost goal and provide improved performance over the breadboard lower end used in the Mark I FPSE/HP module. MTI was supported in this effort by John Deere & Co., who provided a value engineering team from their facility in Waterloo, Iowa. A second objective was to provide an independent evaluation of the FPSE/HP by an HVAC manufacturer. To accomplish this objective, a Mark I unit (see Figure 1-2) was shipped to Lennox Industries engineering facility in Carrollton, Texas, for test and evaluation. The specific tasks performed in each subphase are outlined below.

During Phase IIA, a second breadboard hydraulic transmission and compressor was assembled for performance testing with either a second Mark I FPSE or modified hydraulic simulator, whichever was appropriate to demonstrate full capacity performance and performance repeatability with the first breadboard compressor. The first breadboard compressor was limited to 2.5 RT capacity at the 95°F ambient conditions because of the insufficient power produced by the first generation heat pump engine, the engineering model (EM) FPSE, when coupled to the breadboard lower end.

Phase IIA efforts also involved evaluation of modifications made to the breadboard lower end to increase its efficiency. This effort included two subtasks:

- Evaluation of the refrigerant compressor piston rod seal performance and recommendations for improving the lower end performance.

- A compressor bore stroke sensitivity analysis to determine the effect of stroke on the lower end performance.

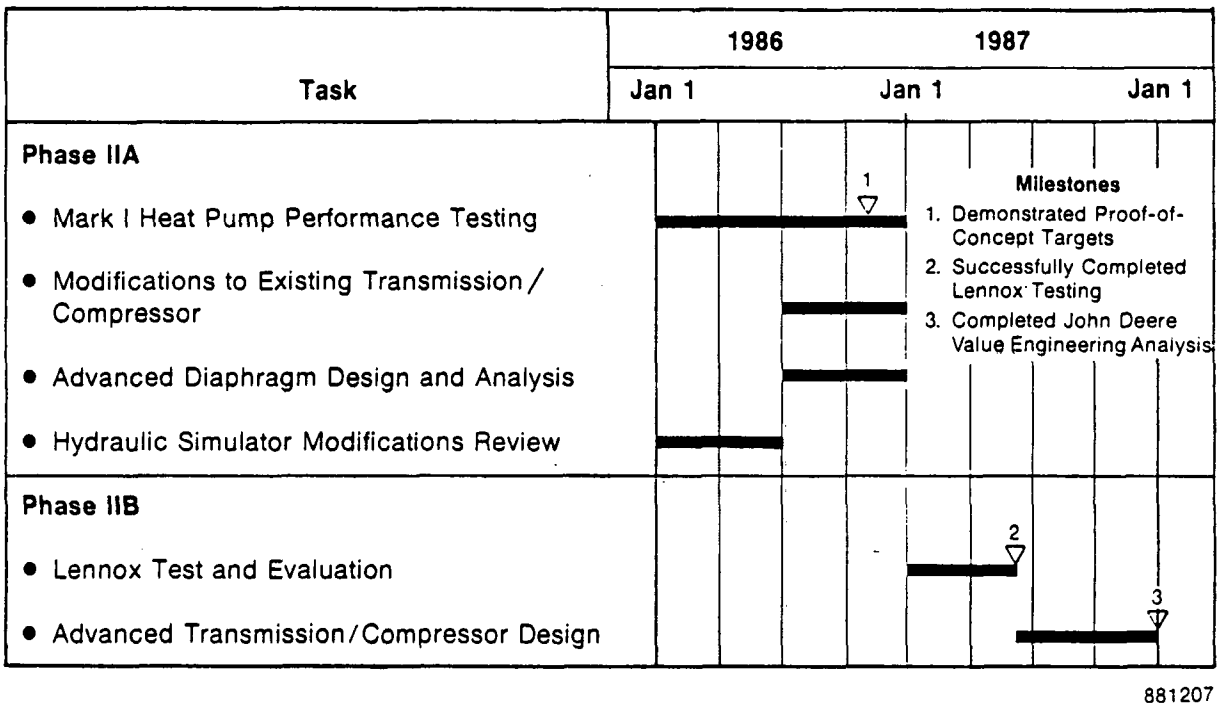

Fig. 1-1 Phase II Program Schedule

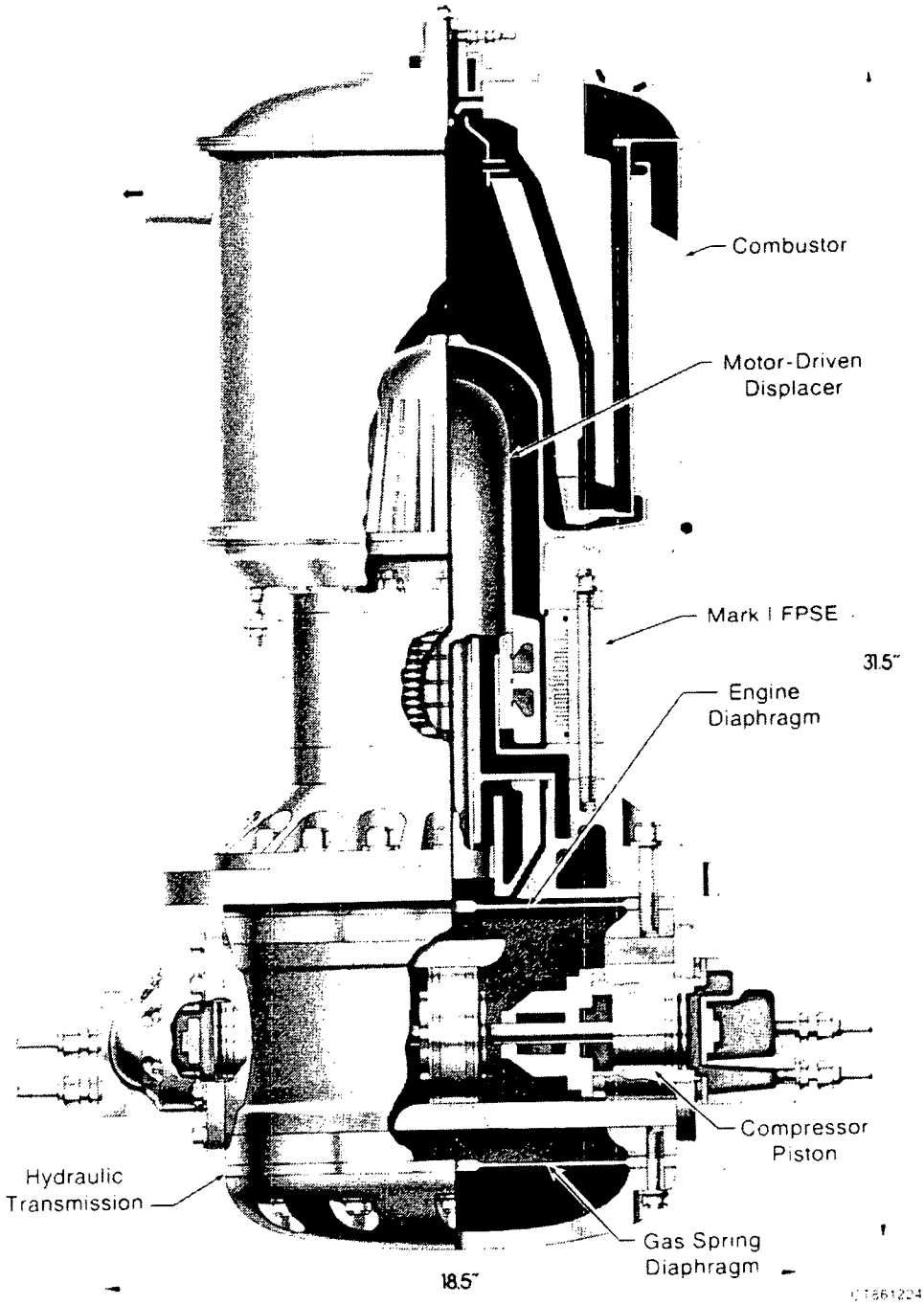

Fig. 1-2 Mark I Heat Pump Module

In addition to the above activities, the alternative diaphragm designs were evaluated to reduce size and increase the displaced volume over the present contoured designs. Alternative design modifications were also investigated to increase the power capability of the hydraulic simulator and its usefulness for full capacity compressor testing.

Phase IIB efforts involved an independent performance evaluation of the Mark I FPSE/HP module at Lennox Industries. A value engineering analysis on the Mark I lower end (transmission/compressor) was also performed, and a second generation, low cost, improved performance lower end to mate with an FPSE was designed. This work was performed in cooperation with John Deere.

The following sections of this report describe the Phase IIA and Phase IIB activities in detail. This includes a discussion of the analyses performed to evaluate the alternative approaches investigated to achieve the program performance goals. In addition, the successful achievement of these performance goals and the developments responsible for this success are discussed. A comprehensive description of the Lennox testing, the results obtained at Lennox, and the results of the John Deere value engineering analyses for the lower end are also presented.

SECTION 2.0

PHASE IIA TECHNICAL DISCUSSION

2.0 PHASE IIA TECHNICAL DISCUSSION

At the end of Phase I, it was concluded that in order to demonstrate the commercial viability of the FPSE/HP module, a more powerful engine would be required and additional improvements would have to be made to the lower end (hydraulic transmission and compressor) to achieve the targeted 3.0 RT of cooling at the 95°F ambient temperature conditions. To achieve this objective, an upgraded FPSE (the Mark I) was designed under the GRI program, and Phase IIA of the HAHP Program was initiated to consider several areas with a high potential for leading to improvements to the lower end. The specific tasks contained in Phase IIA were:

- 1.0 Mark I Heat Pump Module Performance Testing
- 2.0 Modifications to Existing Transmission/Compressor
- 3.0 Advanced Diaphragm Design and Analysis
- 4.0 Hydraulic Simulator Modifications Review.

At the conclusion of this work, it was intended that the breadboard hydraulic transmission and compressor would be coupled to the Mark I engine and a comprehensive off-site test program conducted to map the performance of the Mark I heat pump module. Lennox Industries in Carrollton, Texas, has agreed to conduct the performance mapping using their refrigerant calorimeters. A description of the Mark I heat pump module that was tested by Lennox is given in Appendix A.

A discussion of the results obtained from the work in Phase IIA, along with some preliminary test data for the Mark I heat pump module, is presented in the following sections.

2.1 Mark I Heat Pump Compressor/Hydraulic Transmission Assembly

The breadboard lower end assembly is shown in Figure 2-1. The lower end consists of the hydraulic transmission, refrigerant compressor, and gas spring below the gas spring diaphragm.

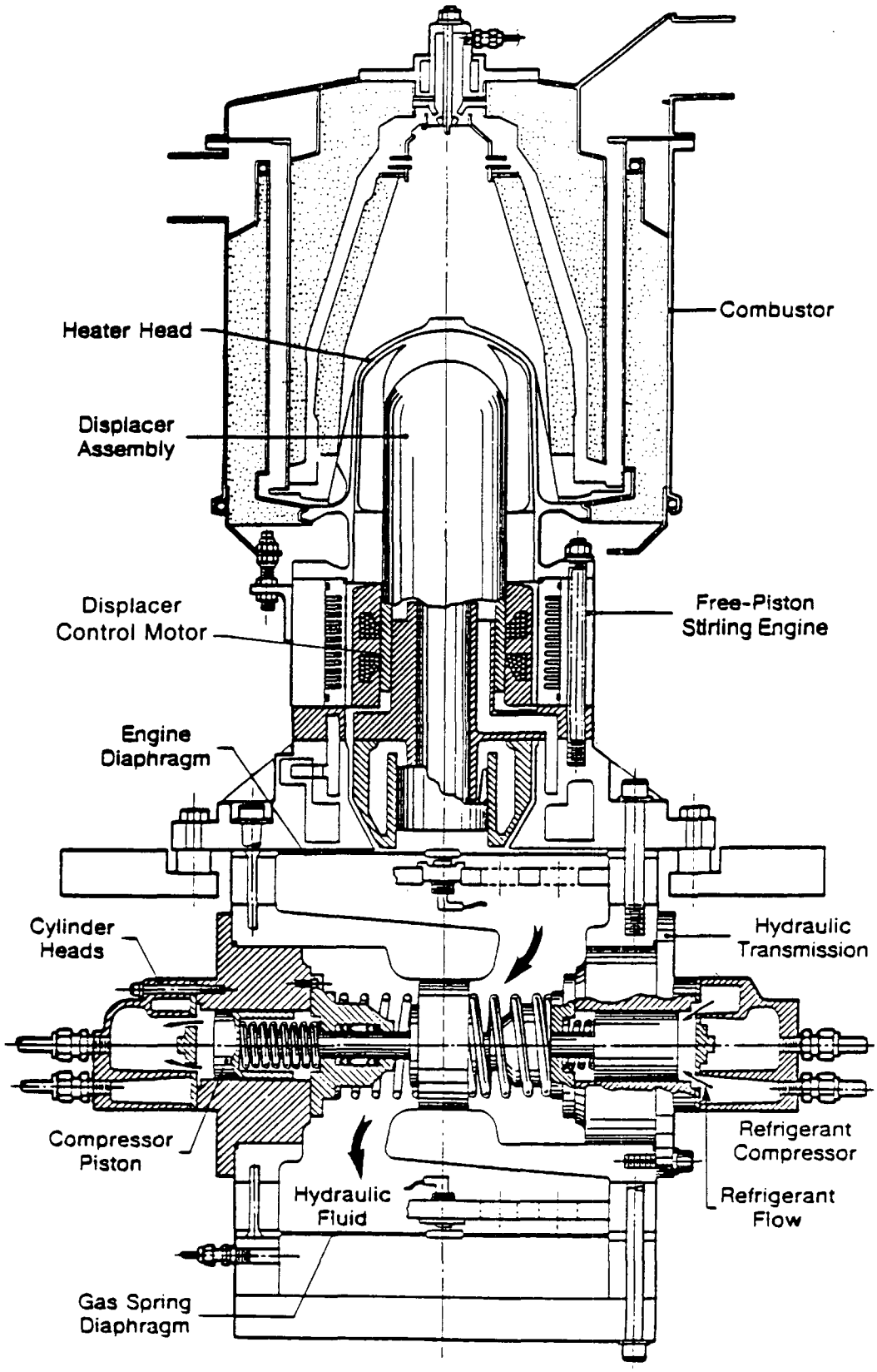

Fig. 2-1 Breadboard FPSE/HP Module with Direct-Drive Transmission

The objective of this task was to assemble a second lower end that incorporated all of the improvement modifications made to the first lower end during three years of development testing while maintaining a high degree of quality control on all critical parts. After the lower end was assembled, a second Mark I engine was also assembled to the same rigid quality standards. It was felt that adherence to rigid quality control would provide optimum performance for the Mark I FPSE/HP module and the best system for off-site testing at Lennox Industries.

Prior to this assembly, however, the first Mark I engine (Serial No. 1) was coupled to the breadboard lower end used previously with EM No. 4 engine and tested under Phase IC.[2] Some very encouraging results were obtained from these tests, namely:

- The Mark I engine achieved an efficiency of 25% based on the higher heating value (HHV) of the fuel
- The heat pump module achieved a capacity of 3.2 RT at the 95°F ambient conditions with a COP of 0.86
- The heat pump module achieved a projected heating capacity of 60,000 Btu/hr at the 47°F ambient conditions with a COP of 1.61.

The following section describes the Mark I Serial No. 1 engine configuration and the initial heat pump module test results achieved.

2.2 Mark I Serial No. 1 Heat Pump Module Test Results

The Mark I engine was assembled and run for the first time in February 1986. After resolution of a displacer bearing problem, the engine was coupled to the breadboard compressor, which had been run previously with the EM No. 4 engine, and developmental testing of the Mark I engine began. The purpose of this development was to raise the engine efficiency from the EM No. 4 engine base-

[2]Details on this effort are contained in MTI report 86FPSE32 (86TR46), "Diaphragm-Coupled Heat-Actuated Heat Pump Component Technology Program", Phase IC Final Report.

line value of 16.4 to 25% and increase the power output from the engine to achieve the target capacity of 3.0 RT at 95°F.

After several months of modification and testing, the 25% engine efficiency goal was achieved and preliminary heat pump module testing conducted. Tests were run at the 95, 47, and 17°F ambient temperature conditions. Mark I heat pump module tests were also conducted at elevated cooler inlet temperatures up to 104°F (40°C). A cooler temperature of 32°F (0°C) was required earlier to achieve the maximum capacity of 2.5 RT using the EM No. 4 engine. Therefore, the Mark I results, reported herein, represent a major improvement in performance.

Results of this testing are shown in Figure 2-2. These results were achieved with the Mark I build configuration consisting of:

- G6-D1 combustor
- Mark I Serial No. 1
- Breadboard Serial No. 1 hydraulic transmission and compressor.

The data were obtained using the MTI refrigerant desuperheater calorimeter test loop, and the capacities and COPs were computed as described below. This test loop enables evaporator and condenser pressures to be set for any representative ambient temperature. The specific conditions are given in Table 2-1, where the ambient temperature is the outdoor temperature, and the pressures and temperatures represent the appropriate refrigerant conditions at the compressor.

An example of the calculations performed to determine the heating and cooling performance are given in Tables 2-2 through 2-6. First, as shown in Tables 2-2 and 2-3, the state point enthalpies are calculated from the measured state point properties. Then, the heating and cooling capacity is determined from the enthalpies and measured refrigerant mass flow rate. For cooling, the capacity is:

$$Q \text{ (cooling capacity)} = \dot{m}\,(h_1 - h_3) \qquad (2\text{-}1)$$

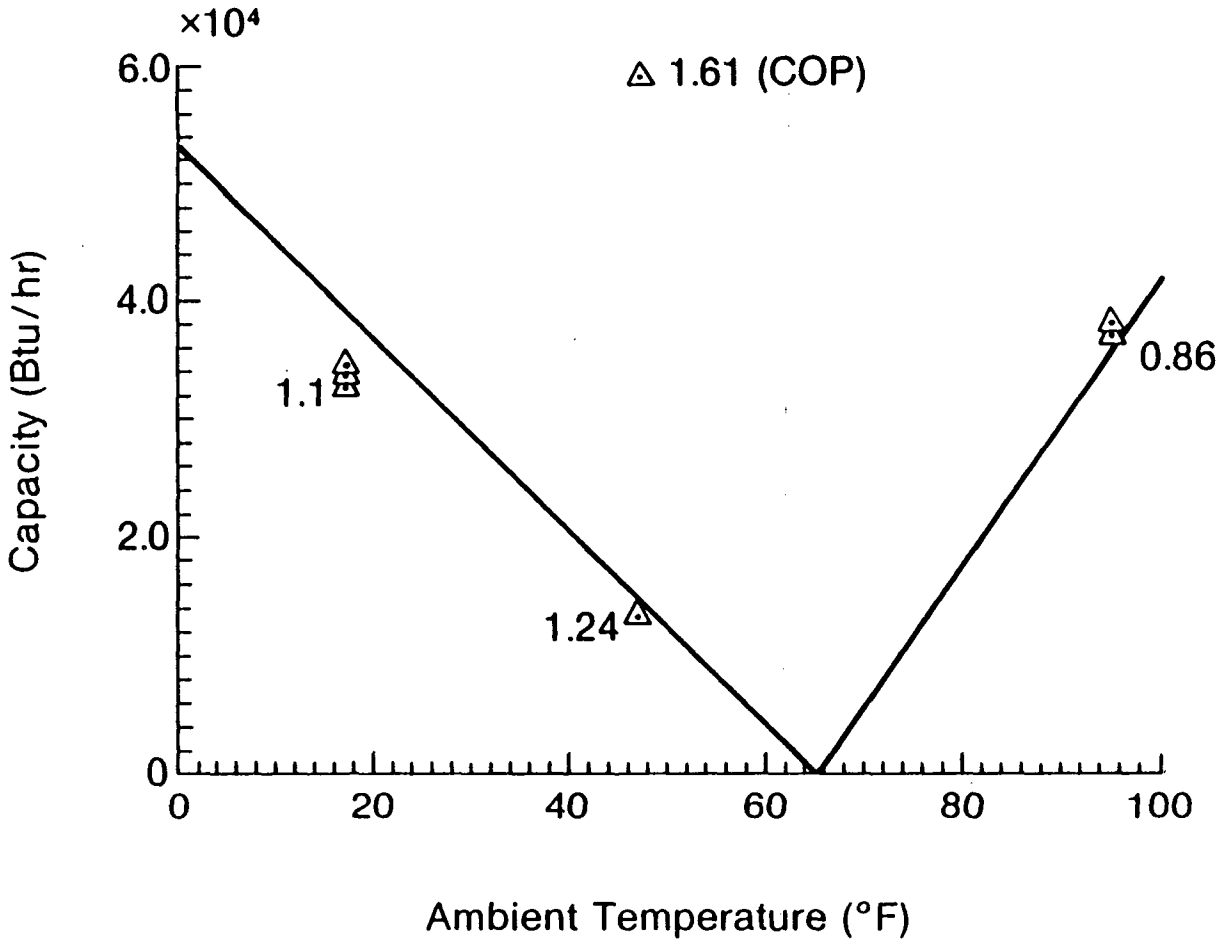

Fig. 2-2 Mark I Heat Pump Module Data (September 1986)

87163

Table 2-1

Test Conditions for R-22 Refrigerant

	Ambient Outdoor Temperature						
	Cooling, °F			Heating, °F			
	95	87	80	47	32	17	0
Discharge Pressure, psia	277.4	225.5	196.5	210.6	202.1	196.5	183.1
Saturation Temp, °F (Condenser)[1]	121	105	95	100	97	95	90
Suction Pressure, psia	90.7	94.7	98.7	76.2	57.7	42.9	29.8
Saturation Temp, °F (Evaporator)	45	47.5	50	35	20	5	-12
Suction Temp, °F	55	57.5	60	45	30	15	-2
Pressure Ratio	3.06	2.38	1.99	2.76	3.50	4.58	6.14

[1] As established at the compressor.
[2] Includes at least 10°F superheat.

Table 2-2

Typical Measured Data and Computations for Heating/Cooling Rating Points: Refrigerant Condition

Measured Performance Parameters	Ambient Outdoor Temperature 95°F	47°F
Suction Gas at Compressor Inlet		
Saturation Temperature, °F	45.0	32.0
Pressure, psia	90.7	72.96
Compressor Inlet Temperature, °F	63.6	52.5
Discharge Gas Leaving Compressor		
Saturation Temperature, °F	121.0	100.3
Pressure, psia	275.7	211.3
Superheat Temperature, °F	179.9	167.5
Liquid Refrigerant Temperature Entering Expansion Valve °F	106.0	85.0

Table 2-3

Typical Measured Data and Computations for Heating/Cooling Rating Points: Refrigerant Energy Quantities

Calculated Performance Parameter	Ambient Outdoor Temperature 95°F	47°F
Refrigerant Mass Flow,[1] lbm/hr	384.4	417.2
Enthalpy, Btu/lbm		
Evaporator, Inlet, h_3	41.17	34.63
Outlet, h_1	111.86	110.89
Condenser, Inlet, h_2	126.37	126.26
Outlet, SAT[2]	46.04	39.27
Heating/Cooling Capacity, Btu/hr	27,173.2	38,228.0

[1] Measured data.
[2] Saturated liquid.

Table 2-4

Typical Measured Data and Computations for Heating/Cooling Rating Points: Mark I Input Energy

Input Energy Parameter	Ambient Outdoor Temperature 95°F	47°F
Gas Fuel Flow,[1] scfm	33.0	35.4
Btu/hr @ 1032 Btu/scfm,[2] HHV	34,019	36,489
Auxiliary Power, W		
Combustion Blower[1]	100.0	100.0
Coolant Pump[2]	150.0	150.0
Displacer Motor[1]	248.5	209.0
Controls[1]	50.0	50.0

[1]Measured data.
[2]Engineering estimates.

Table 2-5

Typical Measured Data and Computations for Heating/Cooling Rating Points: Mark I Engine Rejected Heat

Calculated Performance Parameter	Ambient Outdoor Temperature 95°F	47°F
Engine Cooling Water		
Volume Flow Rate,[1] gpm	2.6	2.6
Temperature,[1] °F		
Inlet	97.5	90.7
Outlet	111.4	106.5
Engine Rejected Heat, Btu/hr	18,227.8	20,879.4
Heating/Cooling Capacity, Btu/hr	27,173.2	55,975.5[2]

[1]Measured (no combustor heat recovery).
[2]60% overall rejected heat recovery (85% of engine reject heat)

Table 2-6

Typical Measured Data and Computations for Heating/Cooling Rating Points: Mark I Heat Pump Module Performance

Calculated Performance Parameter	Ambient Outdoor Temperature 95°F	47°F
Heating/Cooling Capacity, Btu/hr	27,173.2	55,975.5[1]
COP, Fuel	0.80	1.53
COP, Electric and Fuel	0.76	1.46

[1]Based on heat recovery shown in Figure 2-3.

where:

$\dot{m}$ = measured refrigerant mass flow rate

h_1 = enthalpy of refrigerant in suction manifold prior to entering compressor

h_3 = enthalpy of liquid refrigerant prior to expansion.

For heating, the refrigerant heating capacity is:

$$Q \text{ (refrigerant heating capacity)} = \dot{m}\,(h_2 - h_3) \tag{2-2}$$

where:

h_2 = enthalpy of refrigerant leaving compressor discharge manifold and prior to entering condenser.

Second, as shown in Table 2-4, the input energy to the heat pump module is measured. The input energy consists of the fuel (natural gas) energy and the parasitic electrical power needed to drive the auxiliaries, displacer motor, and controls. Third, as shown in Table 2-5, the engine rejected heat is calculated from the measured temperature difference across the engine cooler and the coolant mass flow. For the heating mode, 85% of the engine rejected heat is added to the refrigerant capacity to give the total heating capacity, i.e.,

$$Q_T \text{ (heating capacity)} = \dot{m}\,(h_2 - h_3) + 0.85\,(Q_{rej}). \tag{2-3}$$

As shown in Figure 2-3, heat recovered from the engine does not include reject heat from the combustor and, therefore, represents 60% of the overall rejected heat from the heat pump module. The 85% is used to represent the heat recovery heat exchanger efficiency. The 60% recovered heat is arrived at from the ratio of the recovered heat to the total available recoverable heat, i.e.,

$$\% \text{ Recovered Heat} = \frac{\text{Recovered Heat}}{\text{Total Available Recoverable Heat}} \tag{2-4}$$

$$= \frac{0.85 \text{ Engine Reject Heat}}{\text{Firing Rate} - \text{Engine PV Power}} = \frac{0.85\ Q(rej)}{FR - PV}.$$

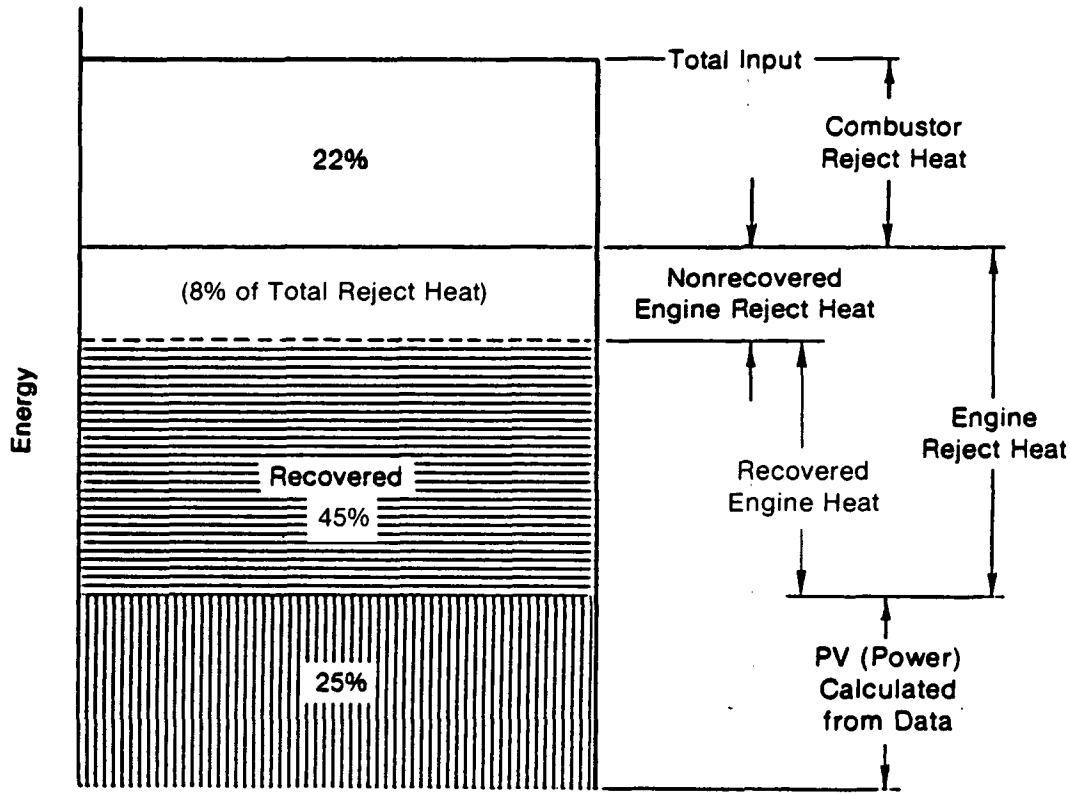

Fig. 2-3 Engine Heat Recovery

Then, by performing an energy balance over the engine, we have from Figure 2-3

$$\% \text{ Recovered Heat} = \frac{0.85\ [(1 - 0.22)\ FR - PV)]}{FR - PV}(100) \qquad (2\text{-}5)$$

$$= \frac{0.85\ [(1 - 0.22) - 0.25](100)}{1.0 - 0.25} = 60.01.$$

From the heating and cooling capacity, the heat pump performance (gross thermal COP) is calculated as follows:

$$\text{Gross thermal COP (fuel)} = \frac{\text{Heating/Cooling Capacity}}{FR} \qquad (2\text{-}6)$$

where:

FR = combustor firing rate (input fuel energy) based on HHV of fuel.

Also, a second performance parameter is defined to account for the electric parasitics:

$$\text{COP (EL + fuel)} = \frac{\text{Heating/Cooling Capacity}}{FR + EL} \qquad (2\text{-}7)$$

where:

EL = electric parasitic power in equivalent thermal units of Btu/hr.

Table 2-6 presents the gross thermal COPs for the 95 and 47°F ambient temperature conditions as calculated for these two sample points. Several other terms used to describe the performance of the Mark I heat pump module are the hydraulic transmission efficiency, the compressor COP, and lower end (hydraulic transmission and compressor) efficiency. These terms are defined as follows:

- Hydraulic Transmission Efficiency - ratio of PV power measured in the compressor divided by PV power measured in the engine

- Compressor COP - ratio of heating and cooling effect made available by the compressor divided by PV power measured in the engine

- Lower End Efficiency - ratio of compressor isentropic power divided by PV power measured in the engine.

2.2.1 Mark I Heat Pump Module Comparative Results

Comparative testing was conducted to measure the performance improvements of the Mark I heat pump module over the EMs. This involved testing the two modules with the same lower end (i.e., the same hydraulic transmission and refrigerant compressor). The following tests were performed:

1. Compare performance at a similar operating point for the two modules. However, the engine coolant temperature was raised for the Mark I testing to 104°F (40°C).

2. Compare the maximum refrigeration capacity at the 95°F ambient temperature conditions for the two modules.

3. Compare the heating performance at the 47°F ambient temperature conditions for the two modules.

The results of these comparative tests are given in Tables 2-7 through 2-9.

Table 2-7 compares the EM and Mark I performance at a similar cooling capacity of 2.3 RT. (In the Mark I tests, the engine coolant temperature was raised to 104°F (40°C).) These results show clearly the performance improvements that were achieved with the Mark I:

- The Mark I efficiency was improved by 43% from 16.4 to 23.5%. This improvement manifested itself in a much lower displacer stroke and motor input power, even with a much higher coolant temperature.

- COP increased from 0.60 to 0.80. This improvement is attributable to the improved Mark I engine efficiency, which resulted from:

Table 2-7

Mark I versus EM Engine Heat Pump Performance Comparison:[1]
Raised Coolant Temperature

Parameter	Breadboard EM No. 4 (7 Jan 86)	Mark I (23 Sept 86; Scan No. 73)
Displacer Stroke, mm	21.9	16.2
Piston Stroke, mm	16.2	16.6
Firing Rate, W, HHV	13,511.0	9,976.2
Engine PV Power, W	2,214.0	2,350.1
Displacer Motor Power, W	669.3	248.5
Average Coolant Temperature, °F	41.0	104.0
(°C)	(5.0)	(40.3)
Capacity, Btu/hr	-27,681.0	-27,166.0
Engine Efficiency, %	16.4	23.5
Lower End Efficiency, %	66.0	63.3
Compressor COP	3.67	3.53
Heat Pump Gross Thermal COP, Fuel, HHV	0.60	0.80
Heat Pump COP, EL[2] and Fuel, HHV	0.57	0.76

[1] Ambient outdoor temperature, 95°F; suction superheat, 15°F; liquid subcooling, 15°F.

[2] Includes displacer power and 300 W parasitics for blower, pump, and controls as shown in Table 2-4.

Table 2-8

Mark I versus EM Engine Heat Pump Performance Comparison: High Cooling Capacity[1]

Parameter	Breadboard EM No. 4 (7 Jan 86)	Mark I (18 Sept 86; Scan No. 45)
Displacer Stroke, mm	21.9	17.7
Piston Stroke, mm	16.2	18.2
Firing Rate, W, HHV	13,511.0	13,013.0
Engine PV Power, W	2,214.0	3,036.1
Displacer Motor Power, W	669.3	431.3
Capacity, Btu/hr	-27,681.0	-38,283.0
Engine Efficiency, %	16.4	23.3
Compressor COP	3.67	3.70
Heat Pump Gross Thermal COP, Fuel, HHV	0.60	0.86
Heat Pump COP, EL[2] and Fuel, HHV	0.57	0.84
Average Coolant Temperature, °F	41.0	45.9
(°C)	(5.0)	(7.7)

[1] Ambient outdoor temperature, 95°F; suction superheat, 15°F; liquid subcooling, 15°F.

[2] Includes displacer power and 300 W parasitics for blower, pump, and controls as shown in Table 2-4.

Table 2-9

Mark I versus EM Engine Heat Pump Performance Comparison:[1]
High Heating Capacity

Parameter	Breadboard EM No. 4 (7 Jan 86)	Mark I (16 Sept 86; Scan No. 20)
Displacer Stroke, mm	22.0	15.0
Piston Stroke, mm	17.2	17.5
Firing Rate, W, HHV	13,118.0	10,840.0
Engine PV Power, W	2,203.0	2,148.0
Displacer Motor Power, W	769.5	146.5
Capacity, Btu/hr	+62,342.0	+59,481.0
Compressor COP	4.92	4.89
Heat Pump Gross Thermal COP, Fuel, HHV	1.39	1.61
Heat Pump COP, EL[2] and Fuel, HHV	1.29	1.59
Average Coolant Temperature, °F	41.0	45.1
(°C)	(5.0)	(7.3)

[1]Ambient temperature, 47°F; suction superheat, 15°F; liquid subcooling, 15°F.

[2]Includes displacer power and 300 W parasitics for blower, pump, and controls as shown in Table 2-4.

- Reduced internal gas leakages because of better control of the seal clearances
- Improved heat transfer characteristics of the regenerator and heater head
- Reduced losses in the displacer gas springs due to reduced internal leakages and lower gas spring pressure amplitudes.

Table 2-8 compares the EM and Mark I performance at the maximum capacity achieved with each module. The significant improvements in this testing were the increase in capacity from 2.3 to 3.2 RT and the increase in COP from 0.60 to 0.86. It should also be noted that, at this point, the capacity is limited by the safe working stress in the diaphragm. The engine, as measured by the reduced displacer stroke, is capable of producing more power.

Table 2-9 compares the EM and Mark I in the heating mode. At the 47°F ambient temperature conditions, the COP of the Mark I module was increased from 1.39 to 1.61 under similar operating conditions, and the displacer motor power was decreased from 769.5 to 146.5 W.

This comparative testing has shown that the Mark I engine has improved the performance of the heat pump module and has enabled the compressor to achieve its targeted goal of 3.0 RT at 95°F. With this accomplishment, the system was ready for off-site testing at Lennox Industries. The objective of this testing was to perform parametric mapping of the Mark I heat pump module over a broad range of operating conditions. Phase IIB of this program was dedicated to performing this testing, and the results are presented in Section 3.0.

2.2.2 Modulation Test at the 47°F Ambient Temperature Conditions

As shown in Figure 2-4, the capacity at 47°F was modulated down to the load line to determine the modulation capability of the Mark I module by varying the displacer stroke through the displacer motor control. Modulating the displacer, as shown in Figure 2-1, changes the engine power and, therefore, the capacity of the compressor. From Figure 2-4, it can be seen that the COP of the module remains fairly constant at 1.5 to 1.6 down to a capacity of approximately 25,000 Btu/hr before it falls off. The reasons for the falloff

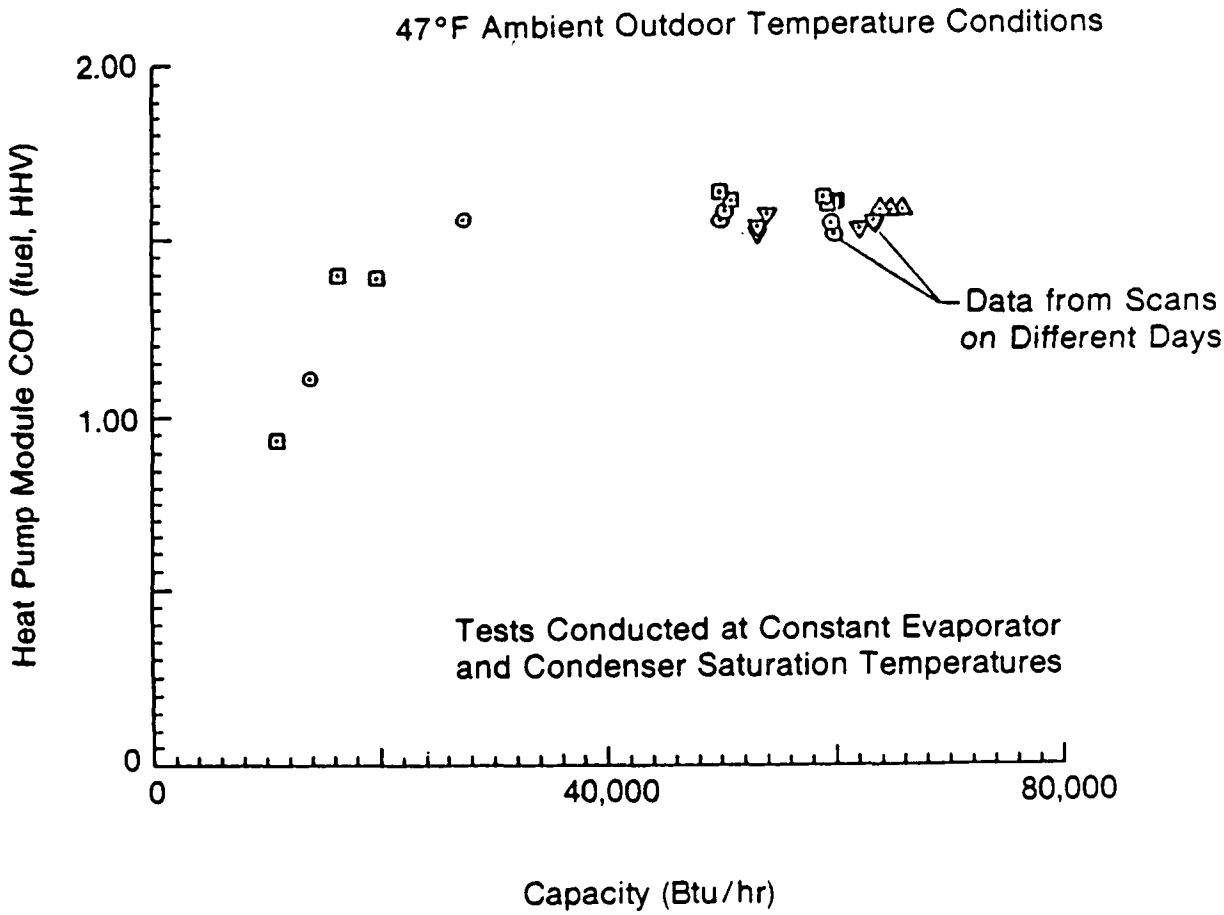

Fig. 2-4 Mark I Heat Pump Performance Test (Capacity Modulation Test - 47°F Conditions and Steady-State Tests at Different Strokes)

have not been investigated at this time. However, the flatness of the curve down to about 25,000 Btu/hr is a good indication of the modulation effectiveness of the module. This evidence suggests that a high COP can be achieved over a very wide range of modulation with some further development.

2.3 Modifications to Existing Compressor/Transmission

This task was organized to consider two areas of the transmission and compressor where improvements could be made to improve overall performance:

- Bore-to-stroke ratio of the compressor
- Design of the transmission main oil seal.

The bore-to-stroke ratio was evaluated by considering the trade-off between viscous losses in the hydraulic transmission and the compressor clearance volume. The main oil seal was evaluated by considering several alternative designs that could reduce seal friction.

2.3.1 Bore-to-Stroke Ratio Analysis

The bore-to-stroke ratio analysis was performed by comparing the compressor COP and volumetric efficiency performance characteristics as a function of the compressor bore diameter at the 95 and 17°F ambient temperature conditions. The compressor COP is defined as:

$$\text{COP (compressor)} = \frac{\text{Heating/Cooling Capacity}}{\text{PV (engine)}} \qquad (2\text{-}8)$$

In equation 2-8, the cooling capacity is defined as the heat absorbed by the refrigerant in the evaporator, and the heating capacity is defined as the heat rejected by the refrigerant in the condenser. The engine PV power is defined as the power developed in the FPSE and transferred to the engine diaphragm and hydraulic transmission. The engine PV power may also be expressed as:

$$\text{PV (engine)} = \text{PV (compressor)} + \text{Q (loss)} \qquad (2\text{-}9)$$

where:

PV (compressor) = PV power delivered to refrigerant in compressor

Q (loss) = all power losses in hydraulic transmission.

Thus, for a fixed capacity, the lower end (hydraulic transmission plus compressor) COP is mainly a function of the losses in the hydraulic transmission, i.e.,

$$\text{COP (lower end)} = \frac{\text{Heating/Cooling Capacity}}{\text{PV (compressor)} + \text{Q (loss)}} \tag{2-10}$$

The compressor volumetric efficiency[3] is defined from Figure 2-5:

$$\text{Volumetric Efficiency } (\eta_v) = \frac{(V_b - V_a)\,\nu_1}{(V_b - V_d)\,\nu_b} \tag{2-11}$$

where:

V = compressor volume at prescribed points

ν = specific volume of refrigerant at prescribed state points

1 = refrigerant suction conditions prior to pressure drop through suction valve

b = refrigerant suction conditions in compressor cylinders.

The compressor volumetric efficiency, η_v, may be defined as the mass of vapor actually pumped by the compressor divided by the mass of vapor which the compressor could pump if it handled a volume of vapor equal to its piston displacement and if no thermodynamic state change occurred during the intake stroke. Referring to Figure 2-5:

$$\eta_v = [1 + C - C\,(P_c/P_b)^{1/n}]\;\nu_1\nu_b \tag{2-12}$$

where C, the clearance factor, is defined as:

$$C = V_d/(V_b - V_d) = V_{cl}/V\ \text{(swept)} \tag{2-13}$$

---

[3]Threlkeld, James L. Thermal Environmental Engineering. Englewood Cliffs, N.J.: Prentice Hall, 1970.

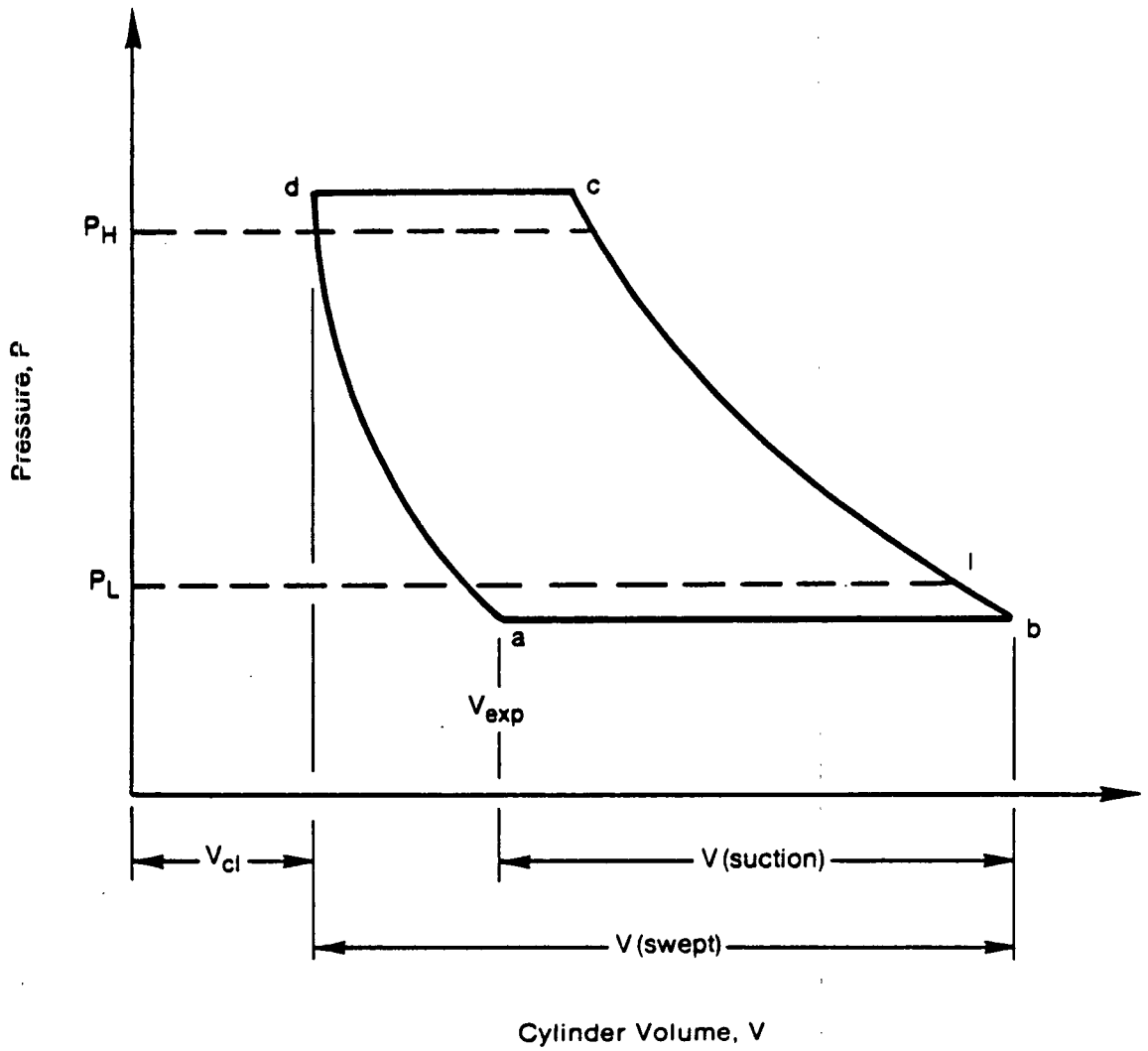

Fig. 2-5 Refrigerant Pressure Volume Diagram

and n is the polytropic constant.

To calculate the volumetric efficiency, the volume at point d on Figure 2-5 must be calculated from the residual clearance volume in the compressor and the piston stroke, i.e.,

$$Vd = V_{cl} = V_{clo} + [(V_{pp} - V_{swept})/2] \qquad (2\text{-}14)$$

where:

V_{clo} = Residual clearance volume in compression space. This is volume remaining with piston in top dead center position.

V_{pp} = Peak-to-peak displaced volume of compressor when compressor piston is displaced from top dead center stop to bottom dead center stop.

The residual clearance volume is found from the compression volume geometry described in Figure 2-6 and shown in Figures 2-7 and 2-8 for the piston cylinder and valve plate geometry. The residual clearance volume is found from the following.

With the piston in the top dead center position as shown in Figure 2-7, the residual clearance volume in the compression volume consists of spaces around and above the piston and includes:

- Clearance volume between the piston and compressor cylinder above the piston ring
- Discharge port openings in the valve plate
- Volume cutout of the suction valve
- Suction valve stop clearance.

The residual clearance volume calculation for the breadboard compressor, with a bore diameter of 2.17 in., is found from the following calculations.

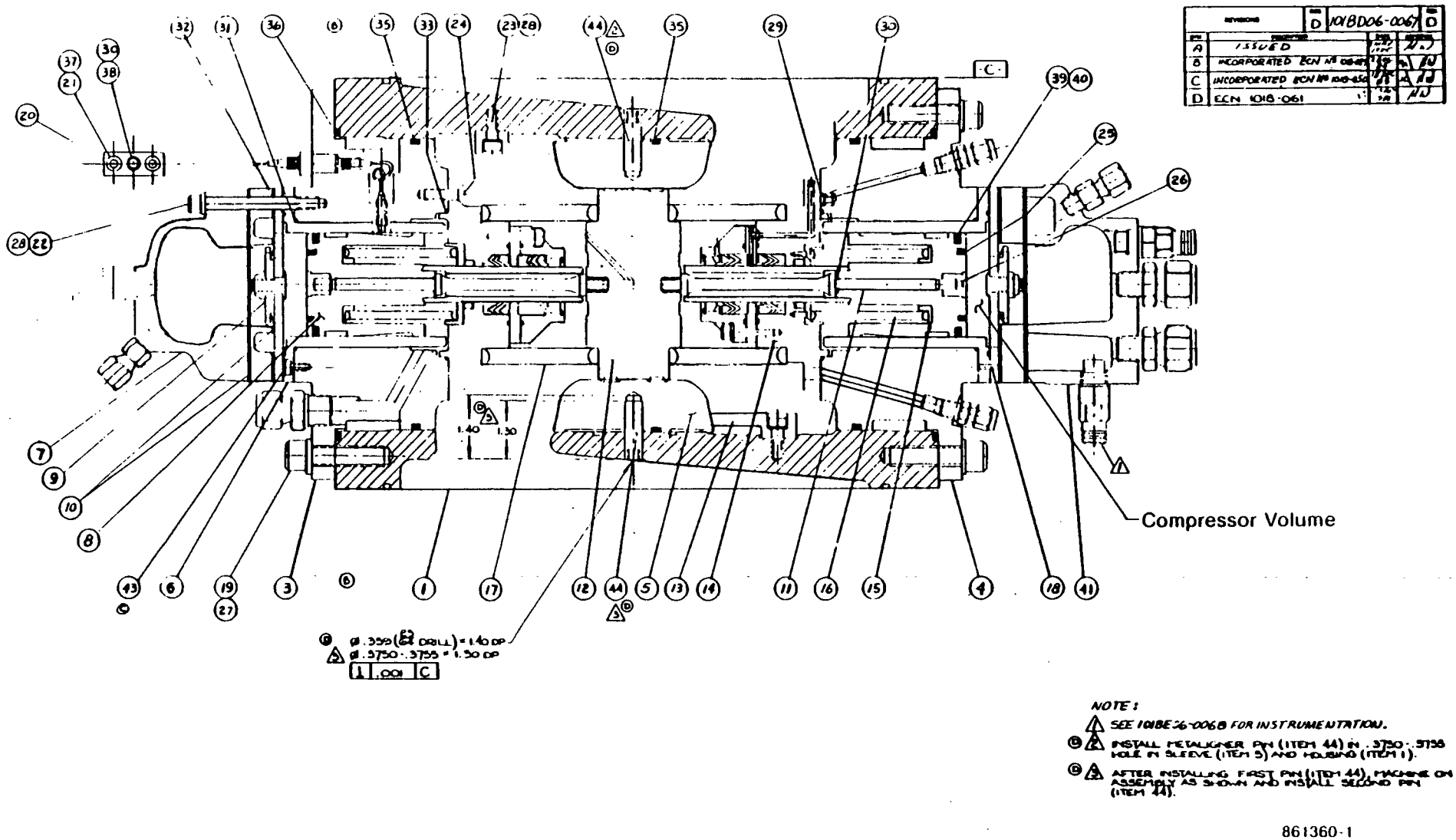

Fig. 2-6 Direct-Drive Hydraulic Transmission and Compressor Assembly

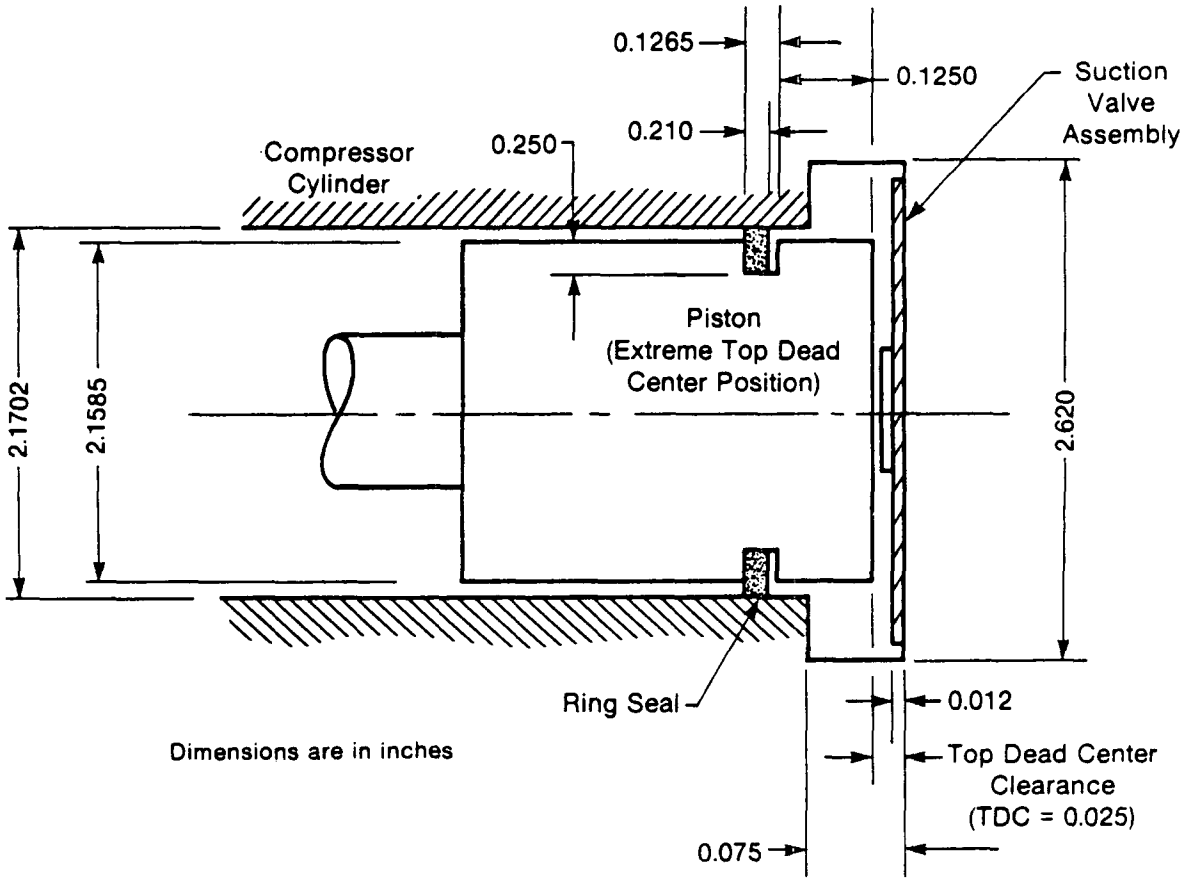

Fig. 2-7 Breadboard Compressor Piston Cylinder Configuration

88565

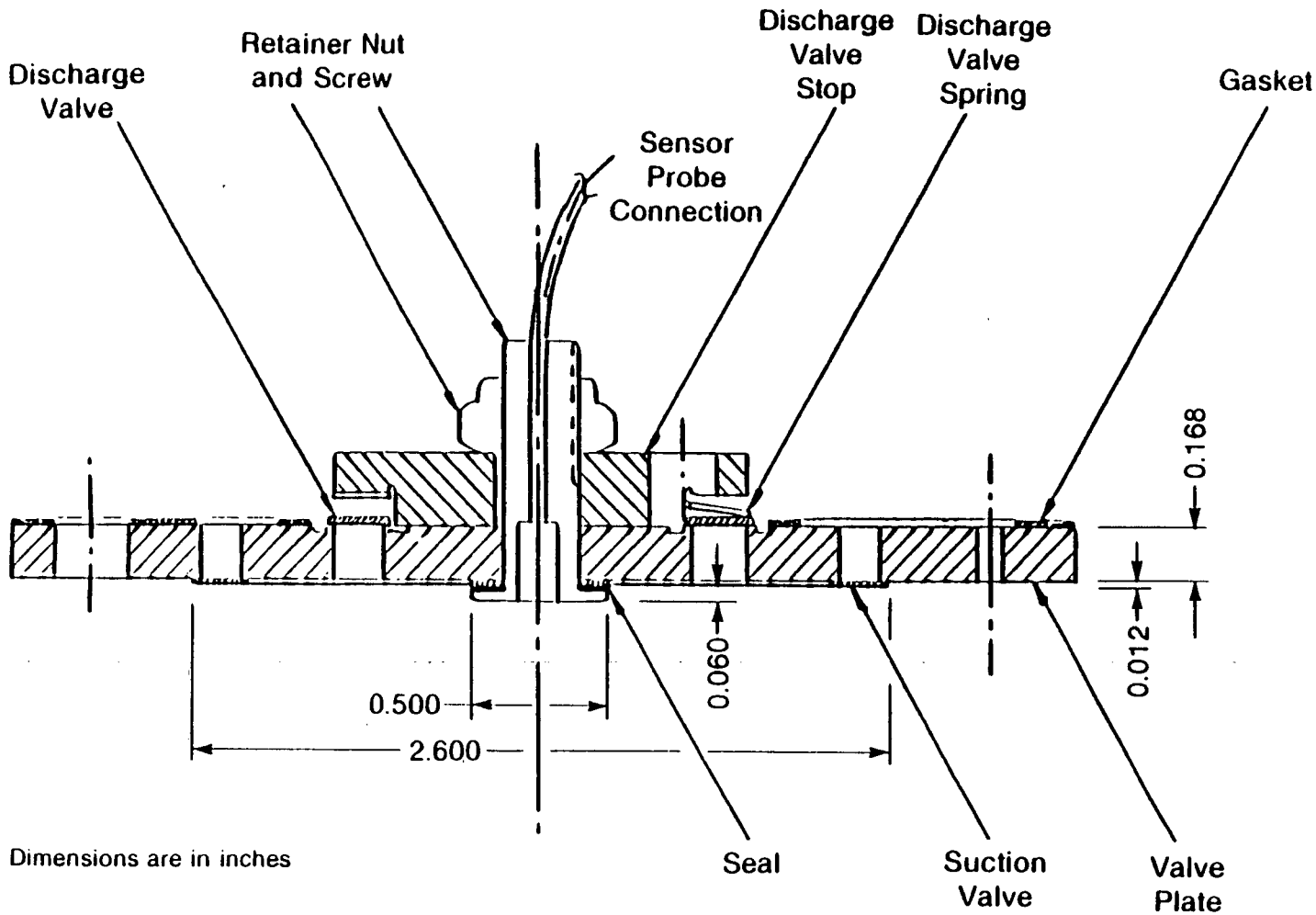

Fig. 2-8 Suction/Discharge Valve Plate Assembly

841839-1

1. The clearance volume between the piston, crankcase cylinder, and suction valve consists of three spaces: the annular clearance between the piston and cylinder, the clearance in the piston ring seal groove, and the piston face clearance between the piston and suction valve. Also, as shown in Figure 2-8, the piston face clearance must be reduced by the volume occupied by the suction valve bolt and bolt seal assembly. The calculation for the first of these spaces is:

$$VC1 = \pi/4\ (2.17022 - 2.1585^2)\ [0.125 + (0.1265 - 0.1210)] \qquad (2\text{-}15)$$
$$= 5.634 \times 10^{-3}\ \text{in.}^3$$

where:

VC_1 = piston cylinder clearance volume.

The clearance volume in the seal groove is:

$$VC_2 = \pi/4\ (2.1585^2 - 1.6585^2)\ (0.1265 - 0.1210) \qquad (2\text{-}16)$$
$$= 8.240 \times 10^{-3}\ \text{in.}^3$$

where:

VC_2 = seal groove clearance.

And, the clearance volume between the piston face and the suction valve (Figures 2-7 and 2-8) is the piston face clearance less the volume occupied by the sitted suction valve annulus and bolt assembly:

$$VC_3 = \pi/4\ (2.1702)^2\ (0.025 - 0.012) - \pi/4\ (0.50)^2(0.060) \qquad (2\text{-}17)$$
$$= 3.629 \times 10^{-2}\ \text{in.}^3$$

where:

VC_3 = TDC piston face clearance - seal/bolt assembly.

2. The discharge port opening in the valve plate consists of four kidney-shaped grooves. The valve plate is 0.168-in. thick and the discharge port clearance is:

$$VP_1 = 4.0\ [\pi/4\ (0.180)^2 + (58/360\ \pi\ (2.245)(2.555-2.245)/2.0]\ 0.168 \quad (2\text{-}18)$$
$$= 0.135\ \text{in.}^3$$

where:

VP_1 = discharge port clearance.

3. The suction valve consists of an annular ring suspended by two 200-mil thick radial arms from the center hub. The calculation for the cutout volume between the spokes is:

$$VS_1 = [\pi/4\ (2.560^2 - 0.50^2) - 2(0.20)(2.560 - 0.50/2.0)]0.012 \quad (2\text{-}19)$$
$$= 5.444 \times 10^{-2}\ \text{in.}^3$$

where:

VS_1 = suction valve center cutout volume.

4. The 0.075-in. step in the compressor cylinder is designed to provide clearance and a stop for the suction valve. This suction valve stop clearance is given by:

$$VSV_1 = \pi/4\ (2.620^2 - 2.1702^2)(0.075) \quad (2\text{-}20)$$
$$= 0.131\ \text{in.}^3$$

where:

VSV_1 = suction valve stop clearance.

The sum of these three terms is the total residual clearance volume of the compressor:

$$V_{clo} = VC_1 + VC_2 + VC_3 + VP_1 + VS_1 + VSV_1 \quad (2\text{-}21)$$
$$= 0.334 \text{ in.}^3$$

where:

V_{clo} = compressor residual clearance volume.

The residual clearance volumes for five bore diameters ranging from 1.50 to 3.00 in. are given in Table 2-10. In Table 2-10, the four individual clearance volumes are found by scaling the bore and suction valve geometries from the nominal breadboard geometry of a 2.17-in. diameter. Thus, as shown for a 3.00-in. bore diameter, the VC terms increase because of the larger bore diameter, the discharge port opening stays the same because the flow remains constant, and the larger bore leads to a larger suction valve that increases VS_1 and VSV_1.

2.3.1.1 Calculation of Compressor COP. An example of the compressor COP calculation is presented below for the breadboard compressor at the 95°F ambient temperature conditions:

- P_L (suction) = 90.7 psia
- P_H (discharge) = 277.4 psia
- T_L (suction) = 55°F (considering 10°F of superheating in evaporator)
- T (liquid) = 106°F (considering 15°F of liquid subcooling prior to expansion.)

From these conditions and the compressor geometry (peak-to-peak stroke = 1.000 in. (25.4 mm); piston frontal area = 3.659 in.^{2}; and residual clearance volume = 0.343 in.^{3}), the compressor COP (equation 2-8) is computed as follows.

1. The heating and cooling capacity is found from the residential load line shown in Figure 2-9. This load line is representative of a typical 3-bedroom home located in the mid-Atlantic region and requiring 3.0 RT of cooling at the 95°F ambient temperature.

Table 2-10

Compressor Residual Clearance Volume

	Bore Diameter, in.				
	1.50	1.75	2.17[1]	2.50	3.00
Piston Cylinder Clearance Volume					
VC_1	0.004	0.004	0.005	0.006	0.007
VC_2	0.007	0.008	0.008	0.011	0.013
VC_3	0.010	0.026	0.036	0.040	0.065
Discharge Opening Port, VP_1	0.135	0.135	0.135	0.135	0.135
Suction Valve Cutout Volume	0.023	0.046	0.054	0.056	0.093
Suction Valve Stop Clearance, VSV_1	0.089	0.102	0.131	0.141	0.168
Total Residual Clearance Volume, V_{clo}	0.268	0.321	0.334	0.389	0.482

[1] Breadboard dimensions.

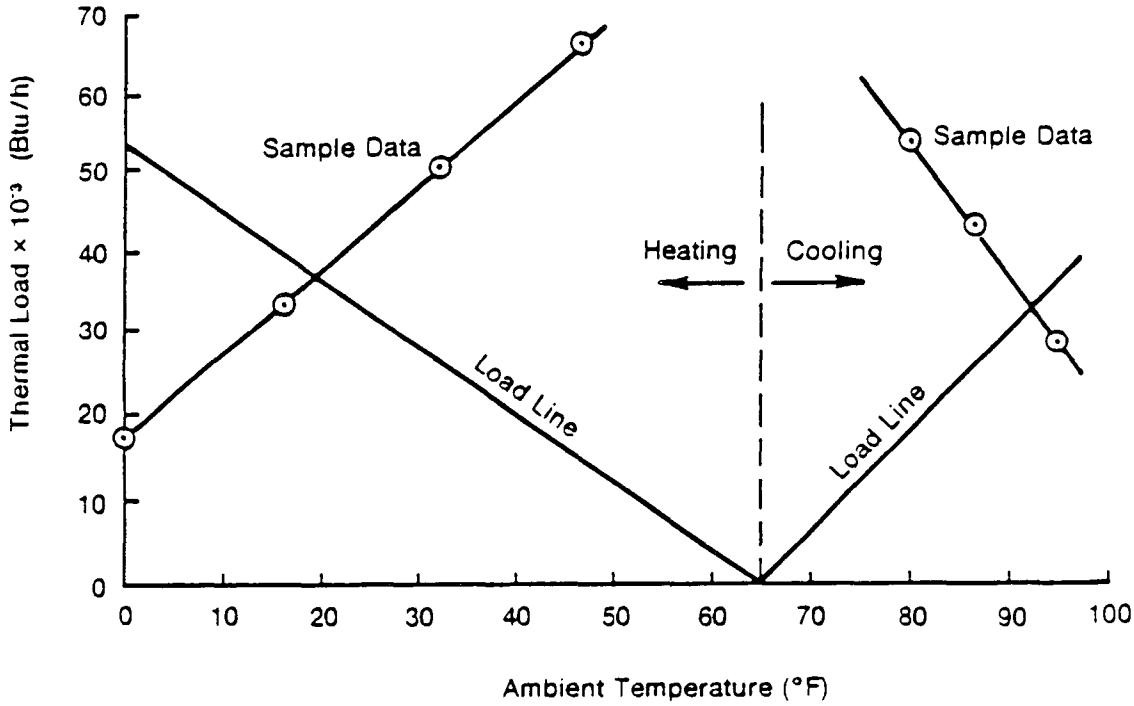

Fig. 2-9 Heating and Cooling Capacity and Load for a Typical 3-Bedroom House in the Mid-Atlantic Region

2. Based on the capacity requirement and the refrigerant evaporator and condenser state point conditions, the refrigerant flow rate is computed.

3. Knowing the refrigerant flow rate and the evaporator and condenser pressures, the compressor adiabatic power is computed assuming a polytropic process. By assuming a compressor isentropic efficiency based on engineering experience, the compressor PV power (PV (compressor)) may be computed.

4. From measured hydraulic transmission power loss data as a function of stroke, Q (loss) may be found by determining the compressor piston stroke. The stroke is found by the following computations:

   a. The suction volume is computed from the refrigerant flow rate and an assumed isenthalpic pressure drop across the suction valve

   b. The total clearance volume is computed from the suction volume and the residual volume

   c. The swept volume is computed from the suction volume and total clearance volume

   d. The piston stroke is computed from the swept volume. From the piston stroke, the hydraulic transmission power loss is found from the measured data.

An example of the calculations for the 95°F ambient temperature conditions follows.

Refrigerant Mass Flow Rate. From the state point conditions across the evaporator, the evaporator enthalpies are:

- h (liquid) = 40.85 Btu/lbm
- h (suction) = 110.39 Btu/lbm

and the refrigerant flow rate through the evaporator is:

$$\dot{m}_e = \frac{36{,}000 \text{ Btu/hr}}{(110.39 - 40.85) \text{ Btu/lbm}} = 518 \text{ lbm/hr.} \tag{2-22}$$

If we assume 11% losses (line and leakage in the compressor), then the compressor must pump 580 lbm/hr to achieve 3.0 RT:

$$\dot{m} = \frac{1}{(1 - 0.11)} \dot{m}_e = 580 \text{ lbm/hr.} \tag{2-23}$$

Compressor PV Power. For a polytropic process, the compressor PV power is given by:

$$\text{PV (compressor)} = \dot{m} \left(\frac{n}{n - 1}\right) P_b \nu_b \left[\left(\frac{P_c}{P_b}\right)^{\frac{n-1}{n}} - 1\right] \tag{2-24}$$

where:

n = 1.173, polytropic constant for refrigerant R-22

$P_b \nu_b$ = suction conditions of refrigerant in compressor cylinders (see Figure 2-5)

P_c = discharge pressures of refrigerant in cylinders.

Also, based on test data from the breadboard compressor, a 10-psi pressure drop occurs across the discharge valves, and a 5-psi pressure drop occurs across the suction valves at the 95°F ambient conditions that were used as normal conditions for these analyses. If

$$\frac{P_c}{P_b} = \frac{277.4 + 10.0}{90.7 - 5.0} = 3.354 \tag{2-25}$$

Then,

$$\text{PV (compressor)} = 580 \text{ lbm/hr } (1.173/.173) \ (85.7 \text{ psia}) \ (144 \text{ in.}^2/\text{ft}^2)$$

$$(0.662 \text{ ft}^3/\text{lbm}) \left[(3.354)^{0.173/1.173} - 1\right] \tag{2-26}$$

$$= 6.277 \times 10^6 \text{ lbf-ft/hr} = 2{,}366 \text{ W.}$$

From this, the compressor efficiency can be defined as:

$$\eta_c = \frac{\dot{m}_e \ (n/n - 1) \ P_L \ \nu_1 \ [(P_H/P_L)^{n - 1/1} - 1]}{PV \ (\text{compressor})} \tag{2-27}$$

where the state points P_H and P_L are defined in Figure 2-5 and refer to the refrigerant properties prior to entering and after exiting the compressor.

Calculations for Hydraulic Transmission Power Loss (Q loss). Calculations for Q (loss) proceed as follows. First, the suction volume is found from the mass flow rate:

$$\dot{m} = 2f \cdot 1/\nu_b \cdot V \ (\text{suction}) \tag{2-28}$$

where:

$2f$ = frequency of operation for a double-acting compressor or 2-cylinder opposed, single-acting compressor.

ν_b = specific volume of refrigerant in compression cylinders during suction stroke.

By assuming a 5-psi pressure drop across the suction valve, the suction volume is:

$$V \ (\text{suction}) = \frac{(580) \ \text{lbm/hr} \ (0.662 \ \text{ft}^3/\text{lbm})}{2 \ (60 \ \text{cycles/sec}) \ (3600 \ \text{sec/hr})} = 8.9 \times 10^{-4} \ \text{ft}^3 = 1.536 \ \text{in.}^3 \tag{2-29}$$

Second, the swept volume is computed from the total clearance volume, equation 2-14:

$$V_{cl} = V_{clo} + \left(\frac{V_{pp} - V \ (\text{swept})}{2.0}\right) \tag{2-30}$$

Also, from Figure 2-5, we have:

$$V \ (\text{swept}) = V \ (\text{suction}) + (V_{exp} - V_{cl}) \tag{2-31}$$

and from the polytropic expansion of the gas in Figure 2-5, we obtain:

$$V_{exp} = V_{cl} \, (P_c \, / \, P_b)^{\,1/n} \tag{2-32}$$

Substituting for V_{exp}, we have:

$$V \text{ (swept)} = V \text{ (suction)} + V_{cl} \, [(P_c \, / \, P_b)^{\,1/n} - 1] \tag{2-33}$$

Substituting for V_{cl} in equation 2-30, we obtain the following expression for the swept volume:

$$V \text{ (swept)} = \frac{\dfrac{V \text{ (suction)}}{[(P_c/P_b)^{1/n} - 1]} + V_{clo} + \dfrac{V_{pp}}{2.0}}{\dfrac{1.0}{[(P_c/P_b)^{1/n} - 1]} + 1/2} \tag{2-34}$$

For the breadboard compressor geometry given in Figure 2-6, the peak-to-peak swept cylinder volume is:

$$V_{pp} = 3.659 \text{ in.}^2 \; (1.00 \text{ in.}) = 3.659 \text{ in.}^3 \tag{2-35}$$

Substituting for V (suction) and V_{pp}, and recalling that:

$$(P_c/P_b) = \left(\frac{277.4 + 10.0}{90.7 - 5.0}\right) = 3.354 \tag{2-36}$$

then,

$$V \text{ (swept)} = \frac{\dfrac{(1.557 \text{ in.}^3)}{[(3.354)^{0.853} - 1]} + 0.334 \text{ in.}^3 + \dfrac{3.659}{2.0} \text{ in.}^3}{\dfrac{1.0}{[(3.354)^{0.853} - 1]} + 1/2} \tag{2-37}$$

$$= 2.872 \text{ in.}^3$$

From the piston frontal area, (A_p), the compressor piston stroke is:

$$\text{Stroke} = V \text{ (swept)}/A_p = 2.872 \text{ in.}^3/3.659 \text{ in.}^2 = 0.785 \text{ in.} \tag{2-38}$$

$$= 19.93 \text{ mm.}$$

From the piston stroke and the measured Q (loss) data for the hydraulic transmission presented in Figure 2-10, the hydraulic transmission loss is:

$$Q\ (\text{loss}) = 595\ W \tag{2-39}$$

The hydraulic transmission power loss is determined from and measured as part of the energy of the compressor piston in the energy balance involving the piston. The hydraulic transmission power loss, Q (loss), equals the difference between the PV power measured in the engine and the PV power measured in the compressor cylinders.

$$Q\ (\text{loss}) = PV\ (\text{engine}) - PV\ (\text{compressor}). \tag{2-40}$$

The curve fit for the hydraulic transmission loss given in Figure 2-10 was computed from the loss data measured from the EM No. 4 engine breadboard heat pump module, the more recent data obtained from the Mark I heat pump module, and some data obtained from compressor tests conducted on the hydraulic simulator. Figures 2-11, 2-12, and 2-13 present all of these data, and the curve presented in Figure 2-10 represents a curve fit for the data.

Compressor Performance. Compressor performance is defined by the compressor isentropic efficiency and the compressor COP. The compressor isentropic efficiency is found from:

$$\eta_{(\text{isentropic})} = \frac{\dot{m}_e\ (h_h - h_l)_{\text{ideal}}}{PV\ (\text{compressor})} \tag{2-41}$$

where:

m_e = refrigerant flow rate into compressor without leakage loss

h_l = enthalpy of refrigerant prior to entering compressor;
h_l (90.7 psia, 55°F) = 110.39 Btu/lbm

h_h = in this case, compressor process is assumed adiabatic and $(h_h - h_l)_{\text{ideal}}$ represents the adiabatic enthalpy rise of the refrigerant across the compressor;
h_h [P_h = 277.4 psia, T_h = T (isentropic)] = 124.13 Btu/lbm.

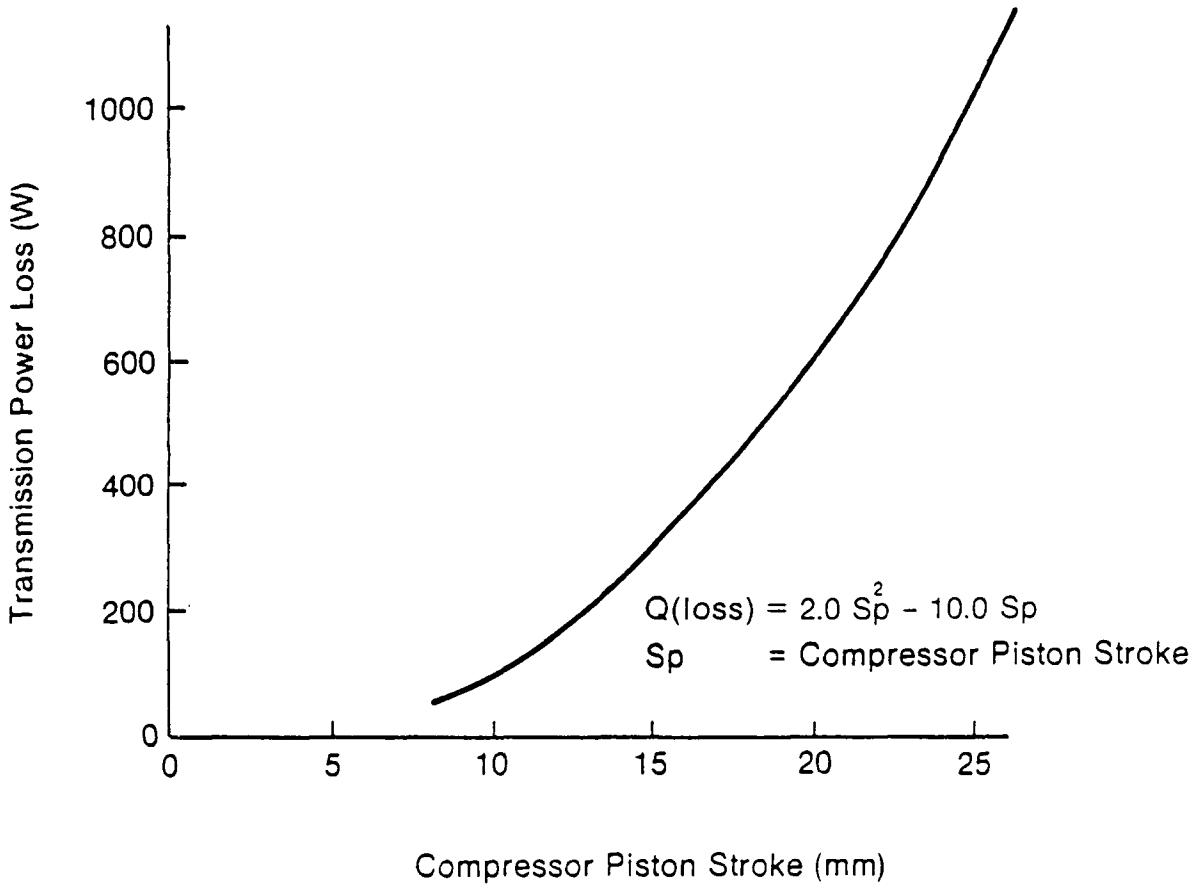

Fig. 2-10 Curve Fit for Measured Hydraulic Transmission Power Loss on Breadboard Heat Pump Module

87748

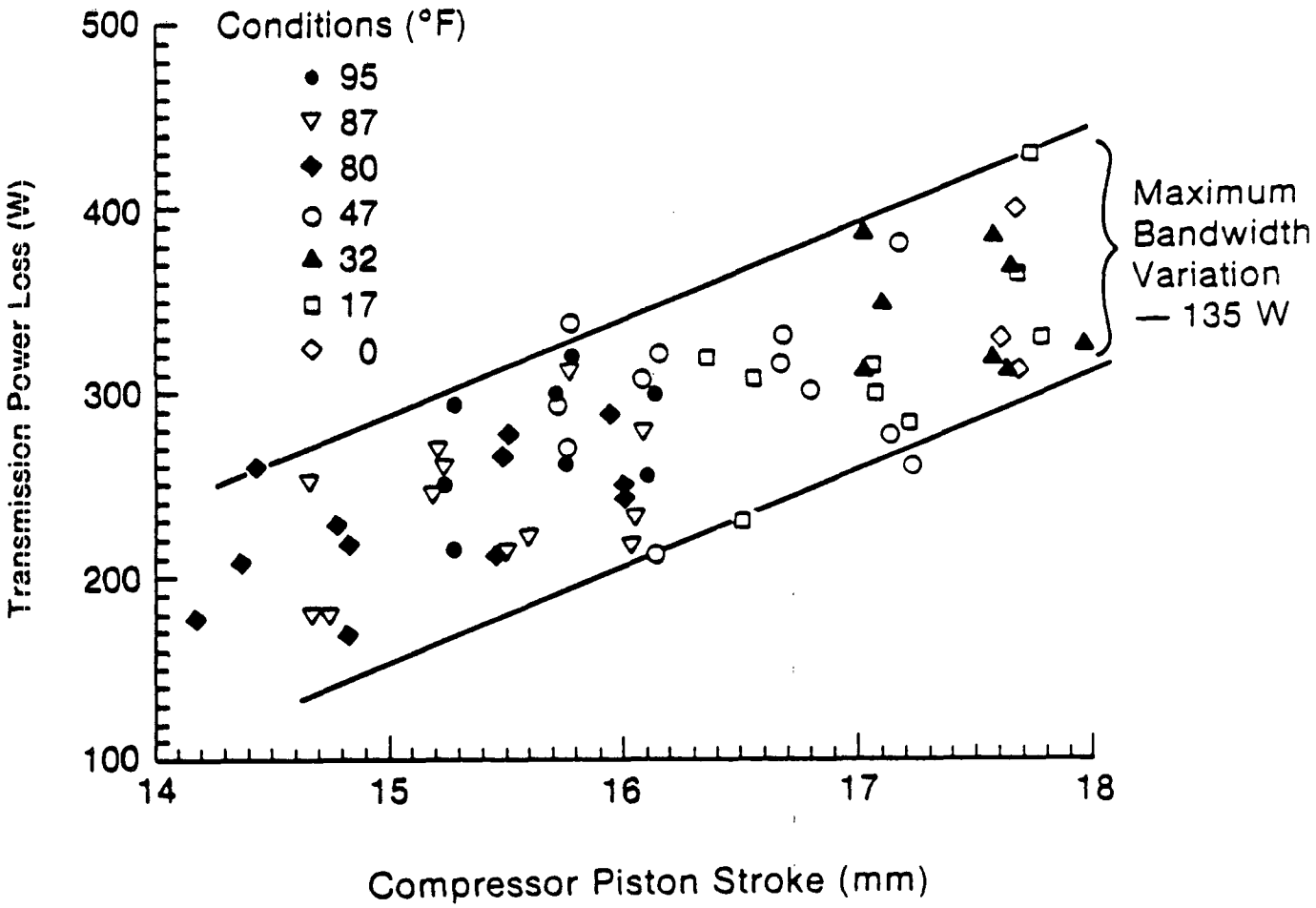

Fig. 2-11 Transmission Power Loss versus Compressor Piston Stroke for EM No. 4 Heat Pump Module with 10-cs Mineral Oil

86236 -3

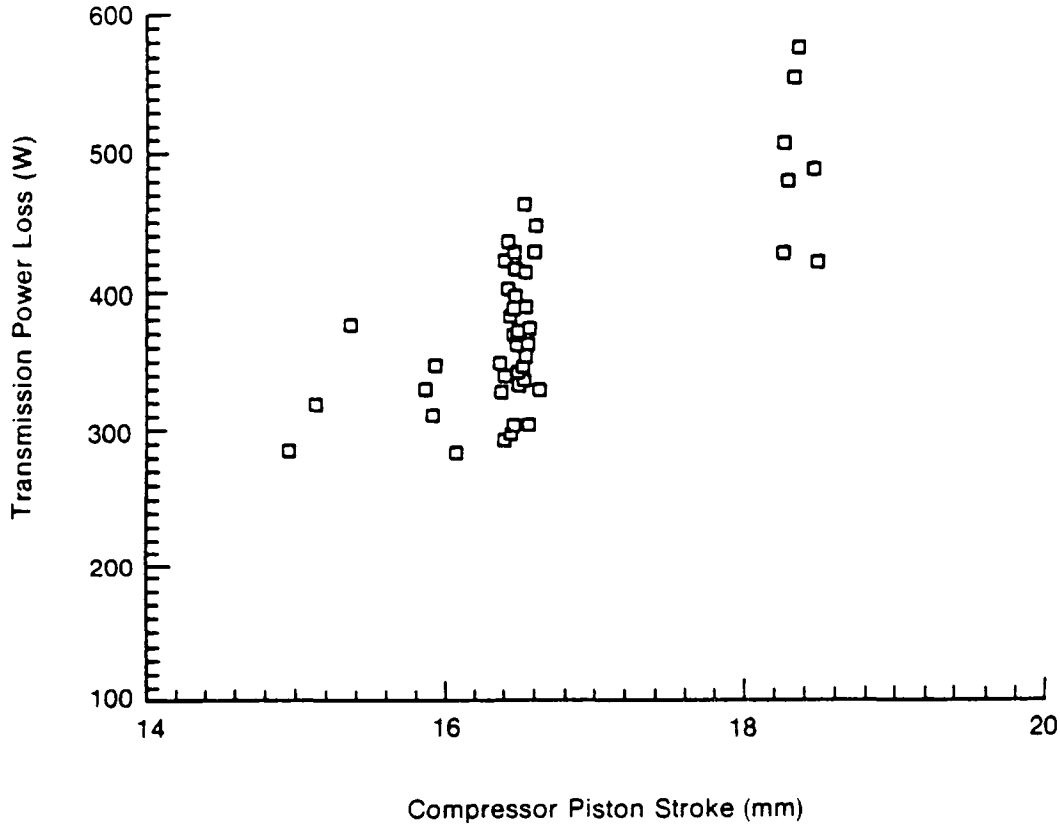

Fig. 2-12 Hydraulic Transmission Power Loss for Mark I Heat Pump Module with 10-cs Silicone Oil (Engine Build 22 - September 1986)

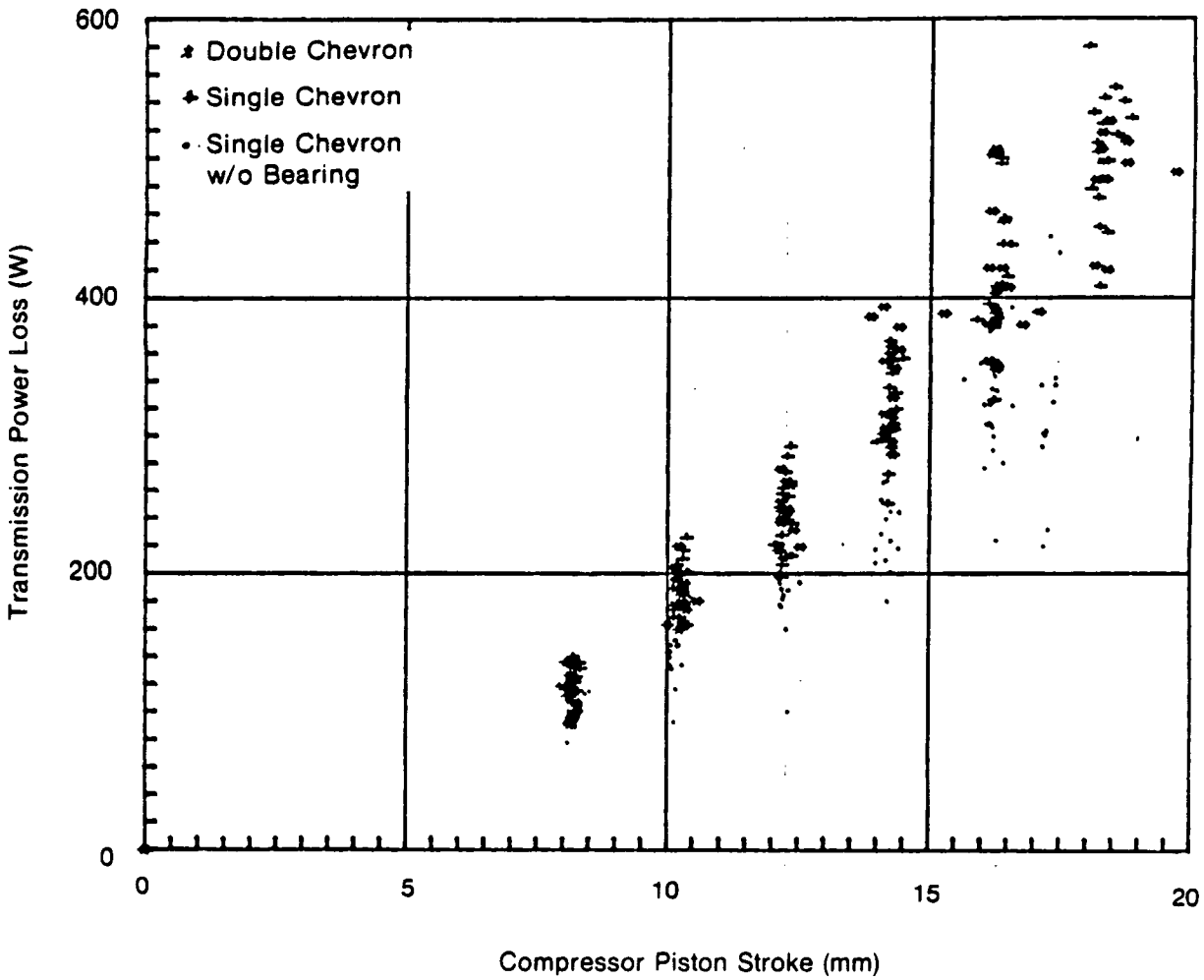

Fig. 2-13 Hydraulic Transmission Power Loss Test Drive-Drive Transmission-Hydraulic Simulator with 10-cs Silicone Oil

Thus, for the breadboard compressor. The actual compressor efficiency, (from the measured values at the selected 95°F conditions) is:

$$\eta_c = \frac{518 \text{ lbm/hr } (122.85 - 110.39) \text{ Btu/lbm}}{2{,}366 \text{ W } (3.41 \text{ Btu/W-hr})} = 80\%. \tag{2-42}$$

The compressor COP is found from equation 2-8:

$$\text{COP (compressor)} = \frac{36{,}000 \text{ Btu/hr}}{(2{,}366 \text{ W} + 595 \text{ W}) \ 3.41 \text{ Btu/W-hr}} = 3.57 \tag{2-43}$$

2.3.1.2 Compressor Volumetric Efficiency Calculation. Calculation of the volumetric efficiency proceeds from equation 2-11, where V_d is found from equation 2-14. V_b is computed from Figure 2-5 as:

$$V_b = V_d + V \text{ (swept)} = V_{cl} + V \text{ (swept)}, \tag{2-44}$$

and the pressure ratio and specific volumes at the 95°F ambient conditions are:

$$(P_c/P_b)^{1/n} = [(277.4 + 10.0)/(90.7 - 5.0)]^{1/1.173} = 2.81 \tag{2-45}$$

$$\nu_L \text{ (at 90.7 psia)} = 0.630 \text{ ft}^3/\text{lbm}$$
$$\nu_b \text{ (at 85.7 psia)} = 0.670 \text{ ft}^3/\text{lbm}$$

From the above:

$$C = \frac{V_{cl}}{V \text{ (swept)}} = \frac{V_{clo} + \dfrac{V_{pp} - V \text{ (swept)}}{2.0}}{V \text{ (swept)}} \tag{2-46}$$

$$= \frac{0.334 \text{ in.}^3 + [(3.659 \text{ in.}^3 - 2.872 \text{ in.}^3) \ / \ 2.0]}{2.872 \text{ in.}^3} = 0.255$$

and

$$\eta_v = [1 + 0.255 - 0.255 \ (2.81)] \ (0.630/0.670) = 50.6\% \tag{2-47}$$

2.3.2 Bore-To-Stroke Performance Results

The results of the bore-to-stroke analysis are given in Tables 2-11 and 2-12 for the compressor COP at the 95°F and 17°F ambient temperature conditions, and Tables 2-13 and 2-14 for the volumetric efficiency at the same two conditions. Figures 2-14 and 2-15 depict these results. From these two figures, it is clear that overall, the compressor COP is much more dependent on the bore diameter than the compressor volumetric efficiency.

To reduce the hydraulic transmission power loss in future designs, it would appear appropriate to consider a larger bore diameter than the 2.17-in. bore selected for the breadboard compressor. In addition, it is recommended that the components of the hydraulic transmission loss, especially at the cold ambient temperatures where large strokes are required to pump adequate amounts of the refrigerant, be defined and studied. The significance of the hydraulic transmission loss at cold ambient temperatures is demonstrated in Figure 2-16, where the measured transmission efficiency is plotted as a function of piston stroke at various ambient temperatures. Figure 2-16 shows that the low refrigerant flow rate and large strokes lead to a degradation in performance at ambient temperatures of 17°F and below.

2.3.3 Main Oil Seal Design

The hydraulic transmission of the HAHP, shown in Figure 2-17, is the critical link between the FPSE and the Freon compressor. The transmission fluid is maintained at engine mean pressure of 900 psia (60 bar) and is sealed from the helium working gas of the engine and lower gas spring by round metal diaphragms. The transmission fluid is sealed from the Freon system by a chevron seal pack, consisting of two pairs of chevron seals, which seals around the reciprocating Freon compressor piston shafts.

A consideration of this transmission is that the oil inventory must always be precisely maintained to avoid diaphragm offset and consequent fatigue failure. Any oil which leaks past the chevron seal packs must be reintroduced into the transmission cavity via an oil management system, shown in Figure 2-18.

Table 2-11

Calculated Effect of Bore Diameter on Compressor Performance at 95°F Ambient Conditions

	Bore Diameter, in.				
	1.50	1.75	2.17[1]	2.50	3.00
Piston Area, in.^{2}	1.77	2.41	3.66	4.91	7.07
Compressor Refrigerant Flow Rate, lbm/hr	580	580	580	580	580
V_{clo} (residual clearance), in.^{3}	0.268	0.321	0.334	0.389	0.482
V (suction), in.^{3}	1.536	1.536	1.536	1.536	1.536
V (swept), in.^{3}	2.798	2.848	2.872	2.913	3.001
Piston Stroke, mm	40.2	30.0	19.9	15.1	10.8
Refrigerant Capacity, Btr/hr	36,000	36,000	36,000	36,000	36,000
Compressor PV Power, W	2,366	2,366	2,366	2,366	2,366
Compressor Isentropic Power, W	1,922	1,922	1,922	1,922	1,922
Compressor Isentropic Efficiency, %	80	80	80	80	80
Transmission Loss, W	2,830	1,500	593	305	125
Hydraulic Transmission Efficiency, %	46	61	80	89	95
Compressor COP	2.03	2.73	3.57	3.95	4.24

[1] Breadboard dimensions.

Table 2-12

Calculated Effect of Bore Diameter on Compressor Performance at 17°F Ambient Conditions

	Bore Diameter, in.				
	1.50	1.75	2.17[1]	2.50	3.00
Piston Area, in.^{2}	1.77	2.41	3.66	4.91	7.07
Compressor Refrigerant Flow Rate, lbm/hr	330	330	330	330	330
V_{clo} (residual clearance), in.^{3}	0.268	0.321	0.334	0.389	0.482
V (suction), in.^{3}	1.923	1.923	1.923	1.923	1.923
V (swept), in.^{3}	3.329	3.395	3.422	3.479	3.594
Piston Stroke, mm	47.8	35.8	23.7	18.0	12.9
Refrigerant Capacity, Btu/hr	25,572	25,572	25,572	25,572	25,572
Compressor PV Power, W	1,904	1,904	1,904	1,904	1,904
Compressor Isentropic Power, W	1,468	1,468	1,468	1,468	1,468
Compressor Isentropic Efficiency, %	77	77	77	77	77
Transmission Loss, W	4,092	2,205	886	468	204
Hydraulic Transmission Efficiency, %	32	46	68	80	90
Compressor COP	1.25	1.83	2.69	3.16	3.56

[1] Breadboard dimensions.

Table 2-13

Calculated Effect of Bore Diameter on Compressor Volumetric Efficiency at 95°F Ambient Conditions

	Bore Diameter, in.				
	1.50	1.75	2.17[1]	2.50	3.00
V_{clo} (residual clearance), in.^{3}	0.268	0.321	0.334	0.389	0.482
V_{cl} (total clearance), in.^{3}	0.699	0.727	0.738	0.762	0.811
V (swept), in.^{3}	2.798	2.848	2.872	2.913	3.001
$(P_c/P_b)^{1/n}$	2.81	2.81	2.81	2.81	2.81
ν_b (actual sp volume), ft^3/lbm	0.662	0.662	0.662	0.662	0.662
ν_1 (ideal sp volume), ft^3/lbm	0.620	0.620	0.620	0.620	0.620
Clearance Factor, C	0.250	0.255	0.255	0.262	0.270
Volumetric Efficiency, %	51.0	50.4	50.63	49.2	47.9

[1] Breadboard dimensions.

Table 2-14

Calculated Effect of Bore Diameter on Compressor Volumetric Efficiency at 17°F Ambient Conditions

	Bore Diameter, in.				
	1.50	1.75	2.17[1]	2.50	3.00
V_{clo} (residual clearance), in.^{3}	0.268	0.321	0.343	0.389	0.482
V_{cl} (total clearance), in.^{3}	0.433	0.453	0.462	0.479	0.515
V (swept), in.^{3}	3.329	3.395	3.422	3.479	3.594
$(P_c/P_b)^{1/n}$	4.25	4.25	4.25	4.25	4.25
ν_b (Actual Sp Volume), ft^3/lbm	1.456	1.456	1.456	1.456	1.456
ν_1 (Ideal Sp Volume), ft^3/lbm	1.275	1.275	1.275	1.275	1.275
Clearance Factor, C	0.130	0.133	0.135	0.138	0.143
Volumetric Efficiency, %	50.6	49.7	49.2	48.3	46.9

[1] Breadboard dimensions.

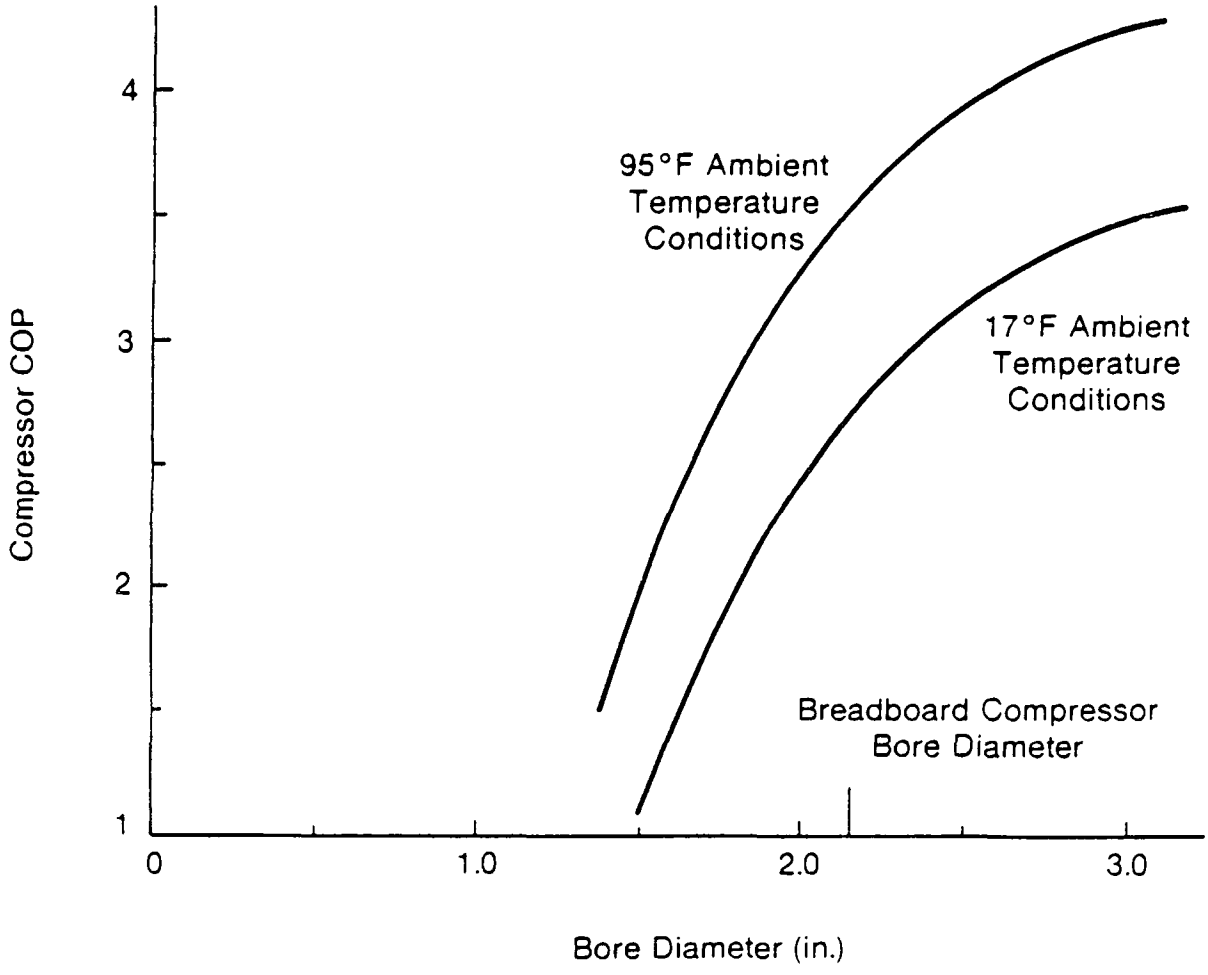

Fig. 2-14 Compressor Performance as a Function of Bore Diameter Assuming Constant $P_{discharge}/P_{suction}$ at Each Condition

87750

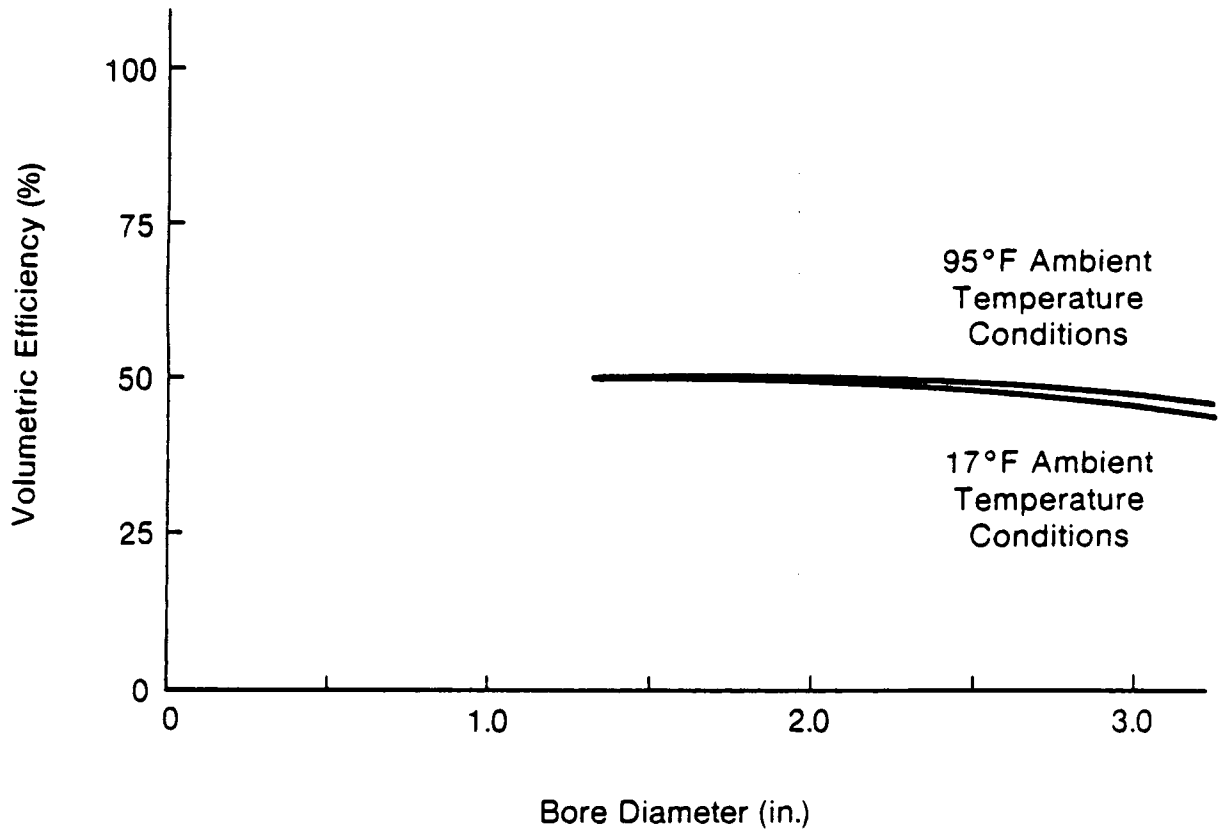

Fig. 2-15 Compressor Volumetric Efficiency as a Function of Bore Diameter Assuming Constant $P_{discharge}/P_{suction}$ at Each Condition

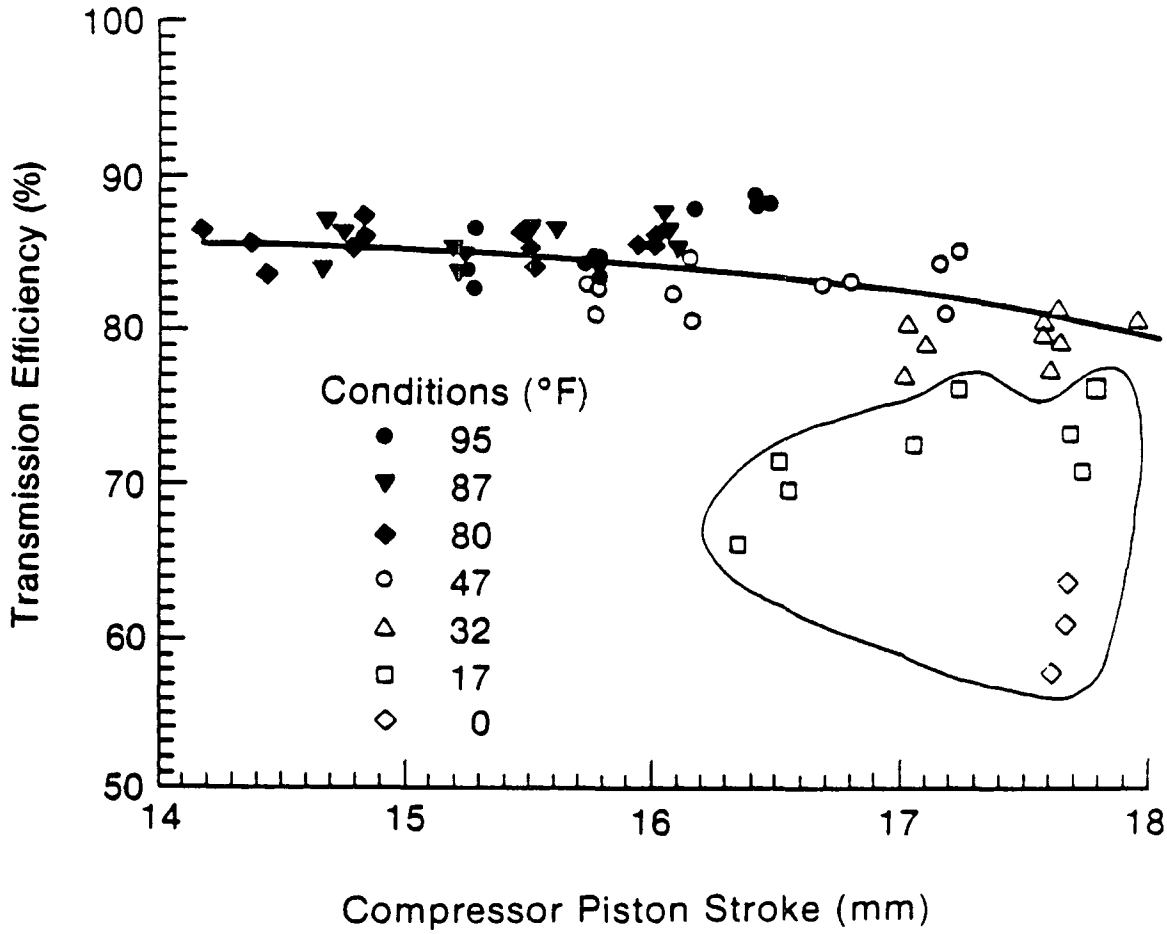

Fig. 2-16 Mark I Hydraulic Transmission Efficiency as a Function of Compressor Piston Stroke

86233 -1

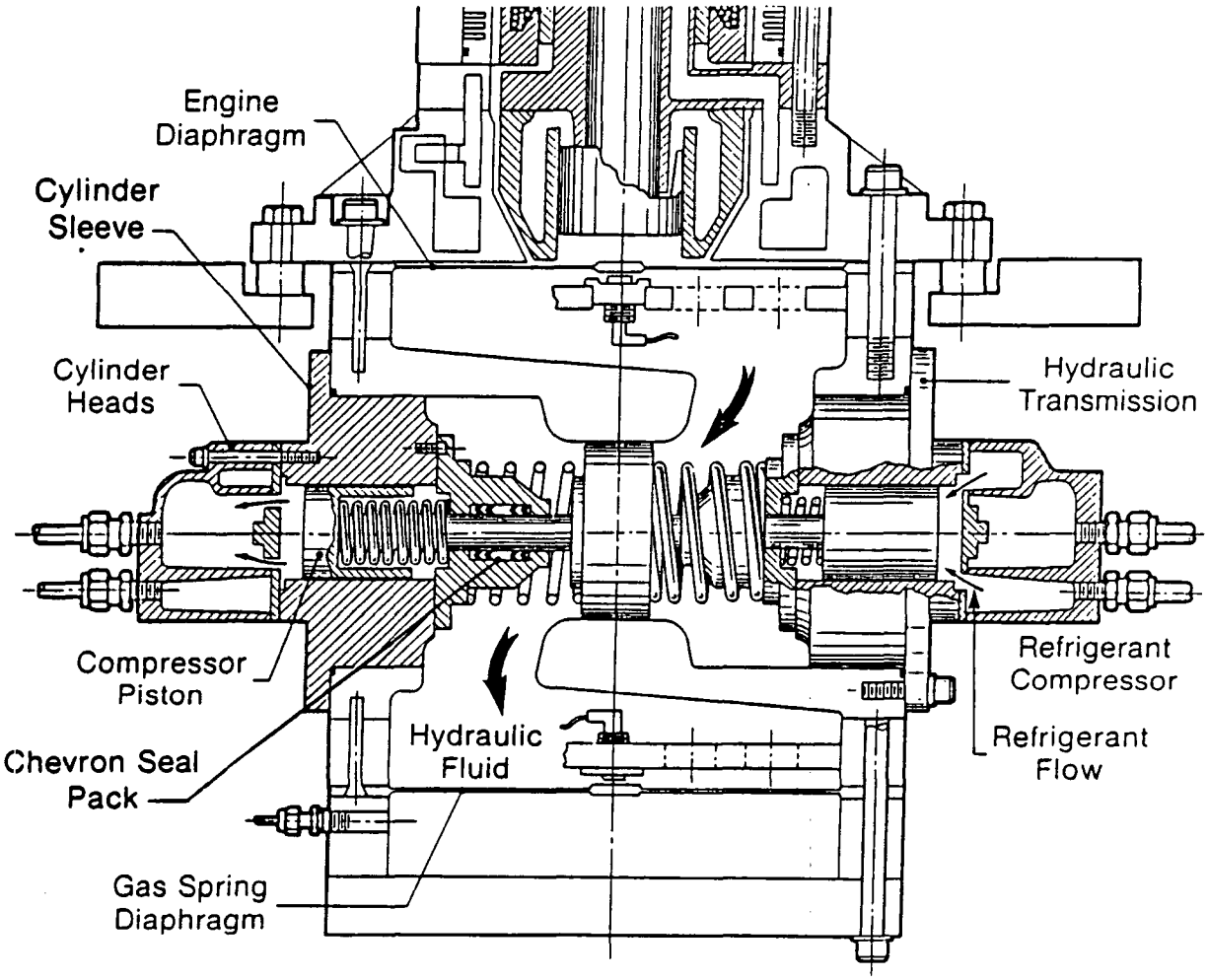

Fig. 2-17 Mark I Hydraulic Transmission Showing Chevron Seal Pack Location

87739 -1

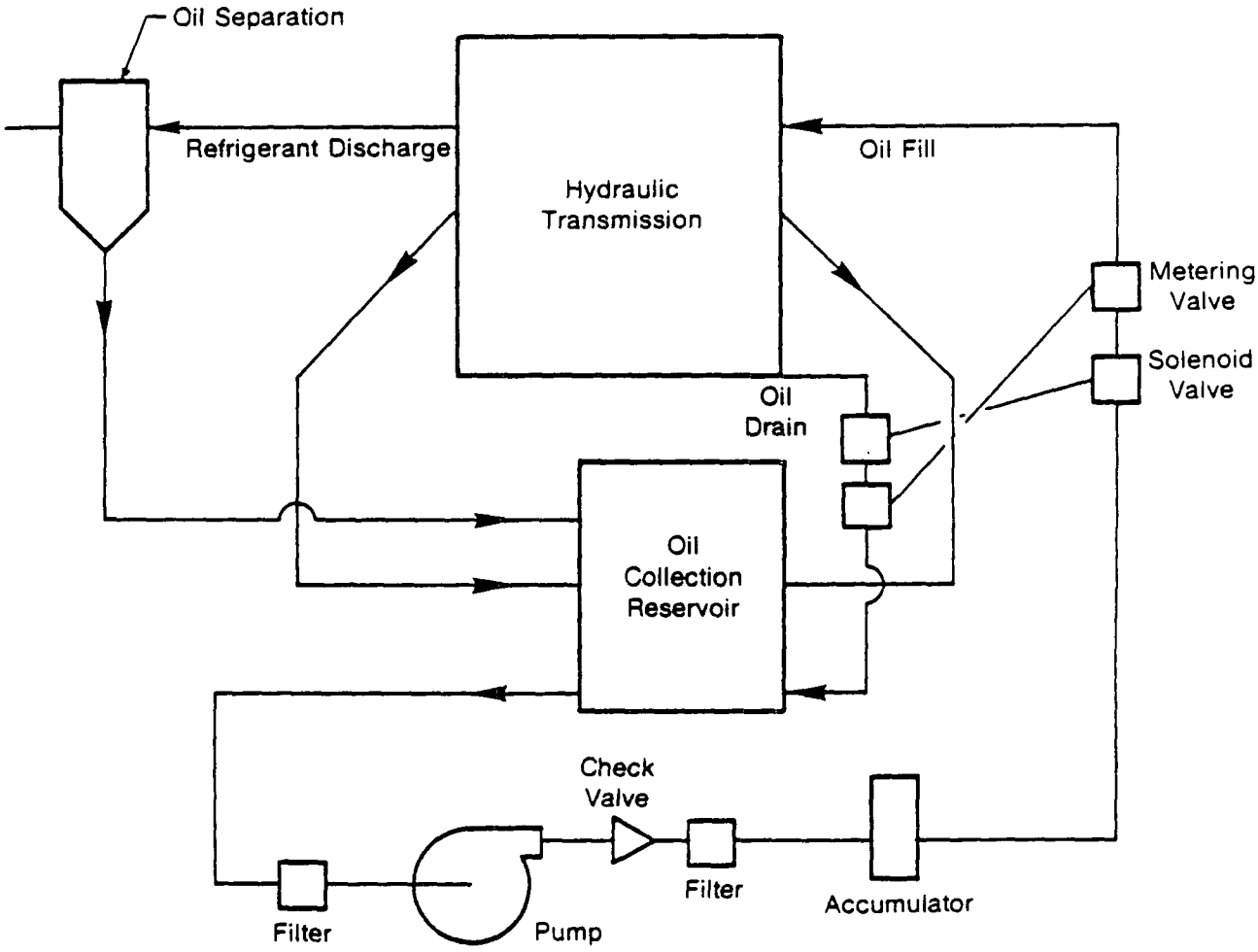

Fig. 2-18 Oil Management System Schematic

8774

The Freon compressor piston shafts can never be perfectly sealed. In addition, the seal employed on this shaft must not create excessive friction. Thus, chevron seals with 30° angled surfaces, as shown in Figure 2-19, were originally selected as "good seals" with low friction characteristics.

At this time, it is felt that the original seal pack design, shown in Figure 2-20, has been sufficiently tested and quantified to permit a redesign effort. This effort was directed toward both reducing current leak rates and frictional losses.

2.3.3.1 Seal Pack Use/Characterization. The original seal pack design made use of a vent tube between the seal pack clusters so that the ΔP across each cluster could be maintained (see Figure 2-20). This feature has not been used. In addition, the outer oil scrapper seal has not been used. To this extent, the original design can be cleaned up, reflecting the deletions of the vent ring, oil scrapper seal, vent hole O-ring seals, vent ring O-ring seal, and vent hole plugs. Figure 2-21 presents this version with only one chevron seal cluster.

Measured leakage values are given in Table 2-15. These values represent leakage from both seal packs while the machine is in operation. Static leakage values have not been as rigorously measured but are estimated to be much lower. Note also that the total leak rate consists of $\sim$10% that works its way into the Freon system and must be separated and reintroduced to the transmission case.

Chevron seal pack friction has been measured as a function of pressure, and the results are presented in Table 2-16. These values were obtained by pushing and pulling a lubricated piston assembly through its stroke with a hand crank mechanism and, thus, are not true dynamic measurements. However, using a drag force of 80 N, a piston stroke of 16.4 mm, and a frequency of 56.3 Hz, one estimates a frictional loss of 148 W.

$$\text{Frictional loss, (W)} = 2.0 f\ Fo \cdot Xp \qquad (2\text{-}48)$$

where:

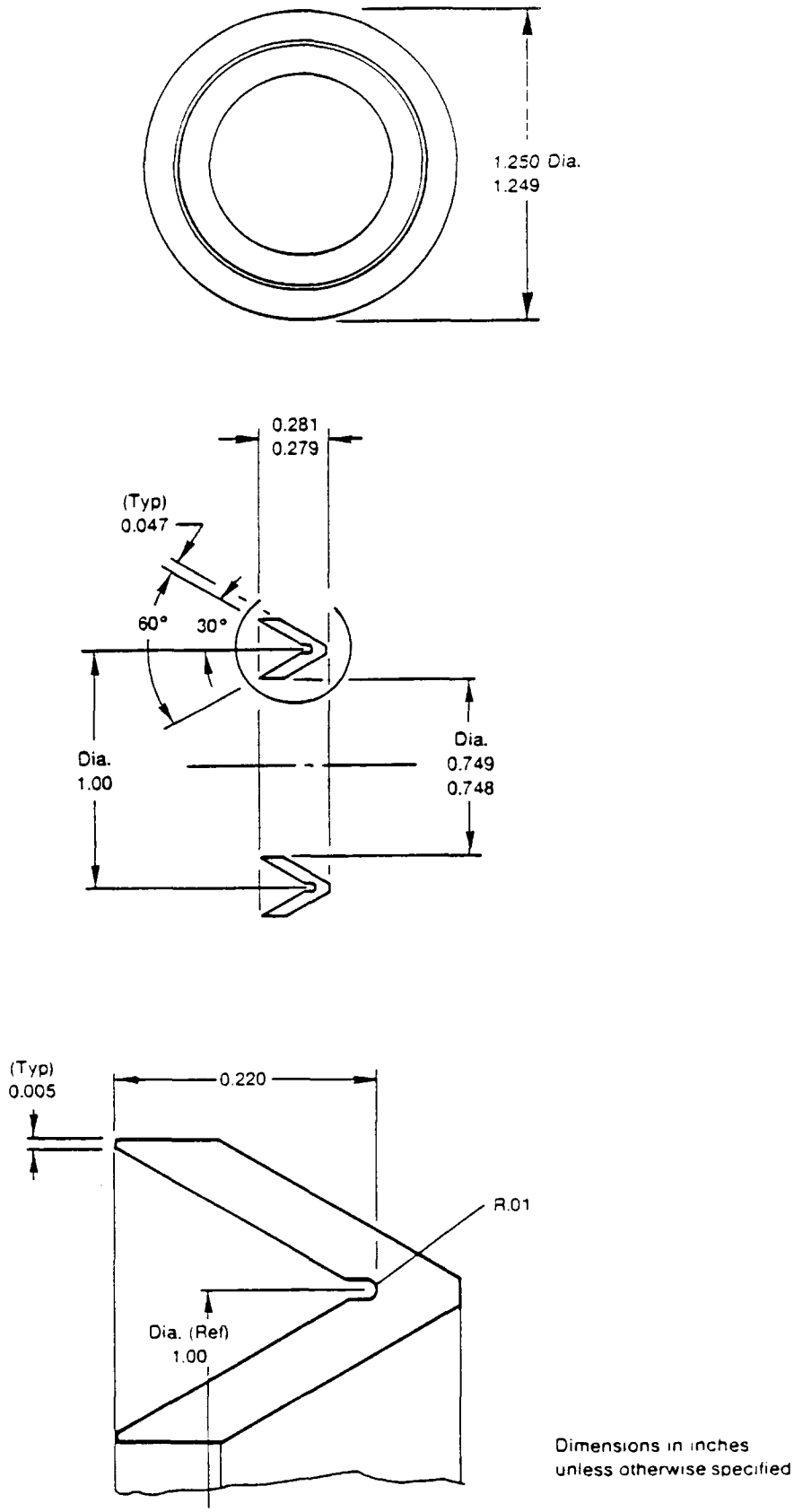

Fig. 2-19 Chevron Seal Design

87753

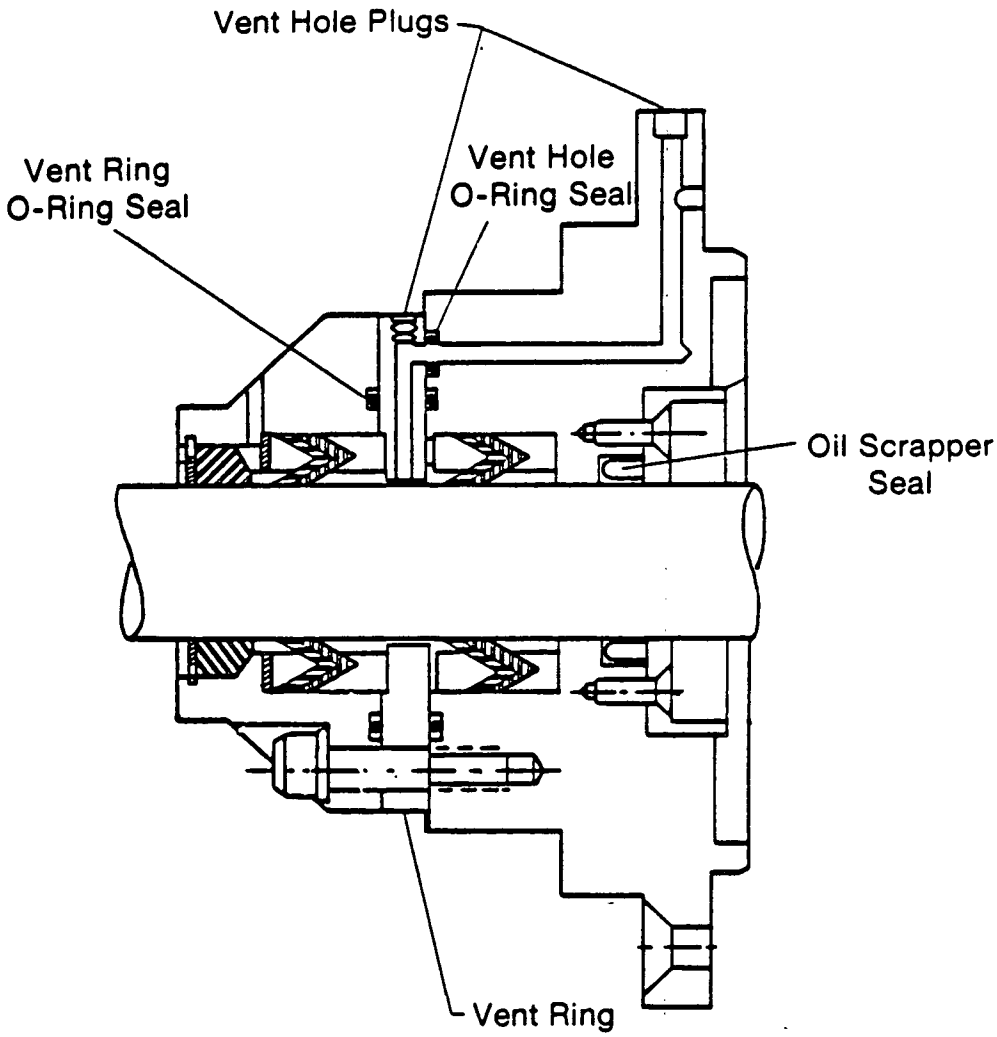

Fig. 2-20 Original Chevron Seal Pack Design

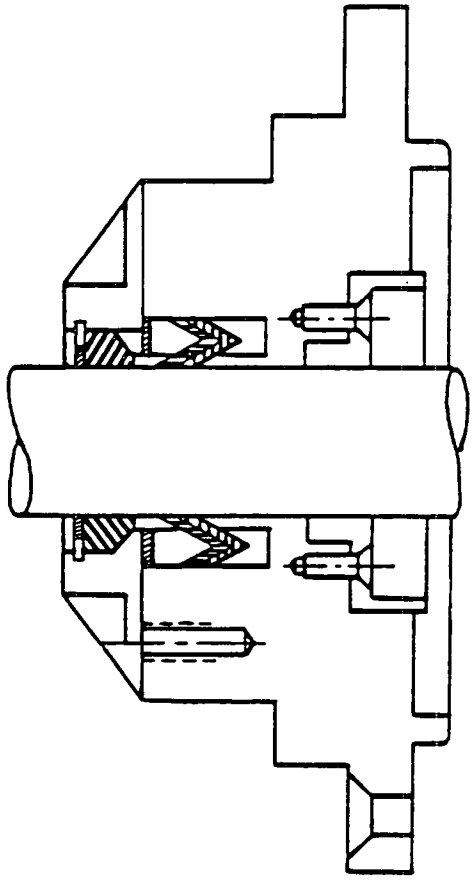

Fig. 2-21 Simplified Seal Pack

Table 2-15

Oil Leakage Test Results for the HAHP Direct-Acting Externally Balanced Compressor[1]

Oil Type	Oil Collection Can	Freon Loop	Total
10-cs silicone	155	17	172
2-cs silicone	84	18	102
33-cs mineral (refrigeration)	130	7	137
10-cs mineral (transformer)	105	9	114

[1]Oil Leakage Rates (ml/hour).

Table 2-16

Chevron Seal Frictional Force

Pressure, psia	Frictional Force Measurement[1], lbf
Ambient	10.7
150	12.5
300	12.5
450	14.3
600	16.4
750	17.8

[1] Data as measured from push/pull tests of 28 September 1984.

f = frequency (1/sec)

Fo = drag force (lbf)

Xp = piston amplitude (ft).

The transmission efficiency has been measured and is reported in Figure 2-16. At 95°F conditions, the data scan indicates lower end power loss (hydraulic transmission loss) of 268 W at a piston stroke of approximately 16 mm. The loss mechanisms which comprise this loss are:

- Center body seal/port losses
- Chevron seal frictional losses
- Bearing frictional losses
- Piston ring frictional losses
- Hydraulic losses
- Load side gas spring losses.

However, the chevron seal frictional loss appears to dominate these mechanisms.

Redesign of the existing seal packs should stress simplification with reduced frictional losses. Reduced seal friction may permit greater oil leakage. The pumping power required to reintroduce this oil into the transmission is currently ~0.6 W. Therefore, if leak rates were to increase by a factor of 10 to 20, pumping power would not increase greatly. Certainly, the complexity of the oil management circuit would remain unchanged.

2.3.3.2 Redesign Options. The redesign options for the main oil seal design include the following.

1. The most obvious redesign is the seal pack simplification discussed in Section 2.3.3.1 and shown in Figure 2-21). Elimination of the inner seal pack cluster should not increase leakage, nor will it reduce frictional drag. The overall shortening of the pack should somewhat improve hydraulic fluid flow path losses.

2. There are several changes which could be initiated that would reduce frictional drag

   a. Reduce the chevron seal ID. A layout of this option was made in which the present 3/4-in. ID was reduced to 7/16 in. This change should reduce friction as well as reduce leakage. Assuming that the frictional force is proportional to diameter, frictional losses may be reduced by 70 W.

   b. Increase the chevron seal/rod contact angle from 30° to 45°. As shown in Figure 2-22, this would reduce the normal force from 309 to 89 lbf, perhaps reducing the frictional losses by ~100 W.

3. The chevron seal could be changed in favor of a modified chevron seal with less rod contact area or a rod T-seal as shown in Figure 2-23. This latter seal would have less contact area than the present chevron seals.

2.3.3.3 Recommendations. It is important to note that the current leak rates of 100 ml/hr (~6 in.^{3}/hr), while not excessive, do represent fairly large values compared to the diaphragm deflection of 4 in.^{3} The entire oil and Freon systems must be designed in such a way as to permit this oil to drain back to the oil pump reservoir. Careful, adequate oil inventory control must be achieved on the system level.

It is MTI's opinion that the present chevron seals are working reasonably well. Therefore, the design should be altered as little as possible with a minimum of hardware changes. It is recommended that consideration be given to redesign options No. 1 and 2b.

2.4 Advanced Diaphragm Design and Analysis

This task was performed to evaluate alternative diaphragm concepts to the existing contoured diaphragm. The contoured diaphragms currently in use have been fabricated to MTI specifications by the Bendix Corporation, which uses similar diaphragms in its line of shaft couplings for power transmissions. The need for a new diaphragm is discussed in the following paragraphs.

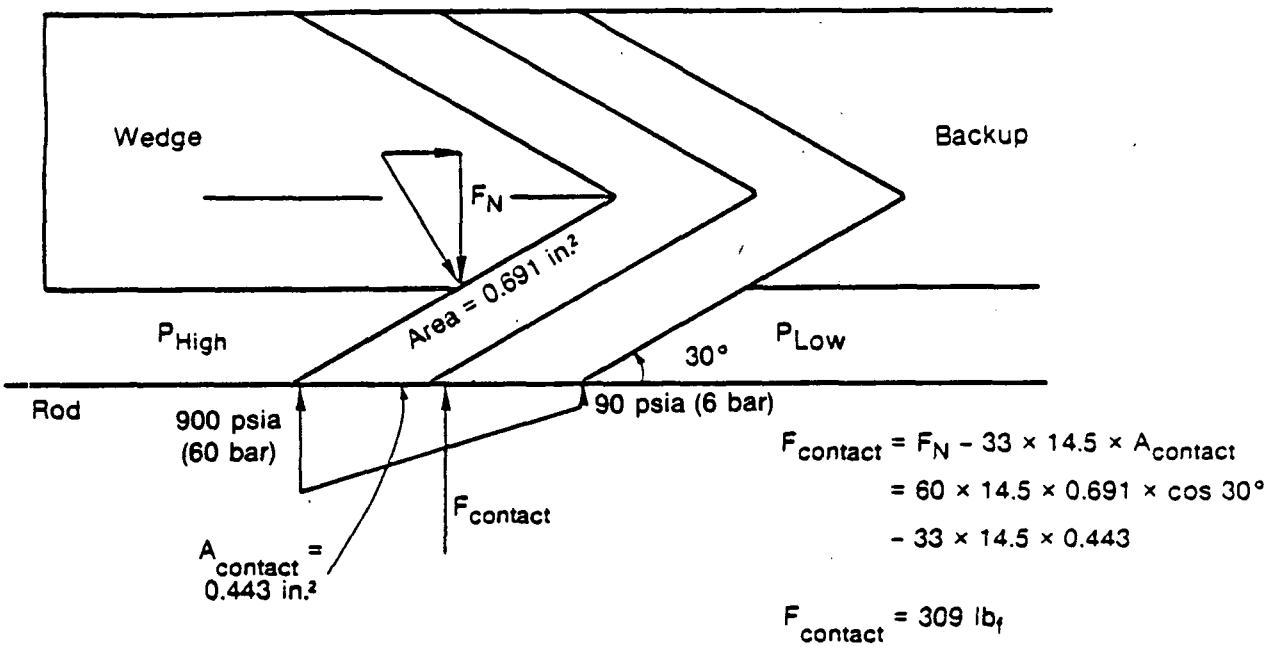

Present Design

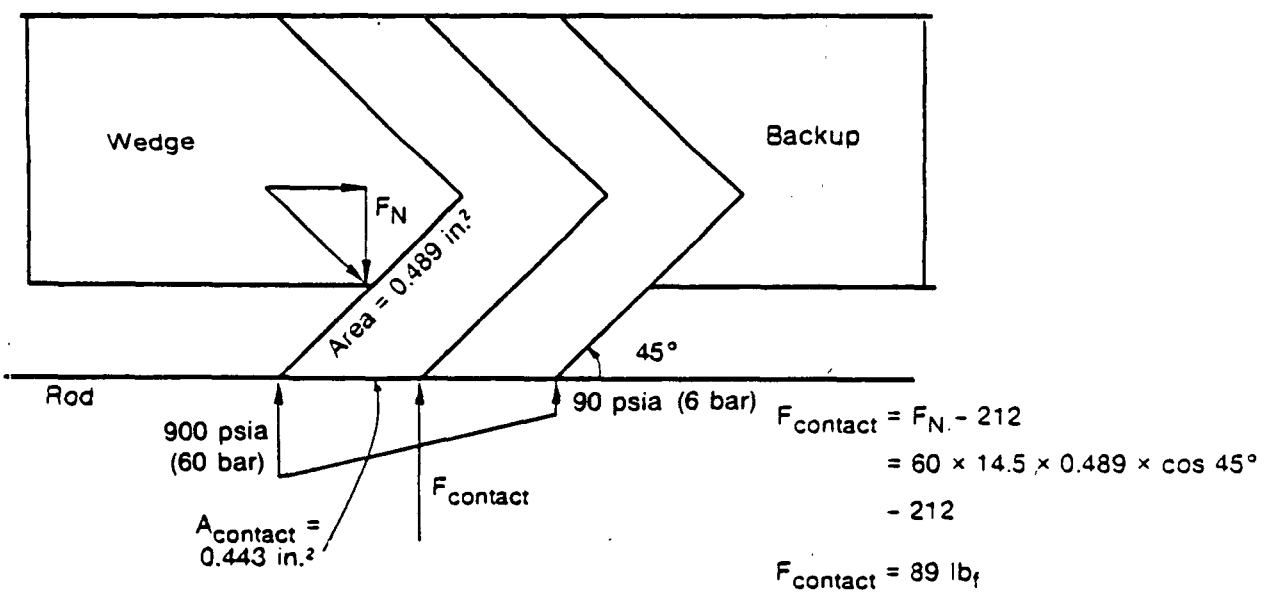

Proposed

Fig. 2-22 Present and Proposed Modified Chevron Seal Designs

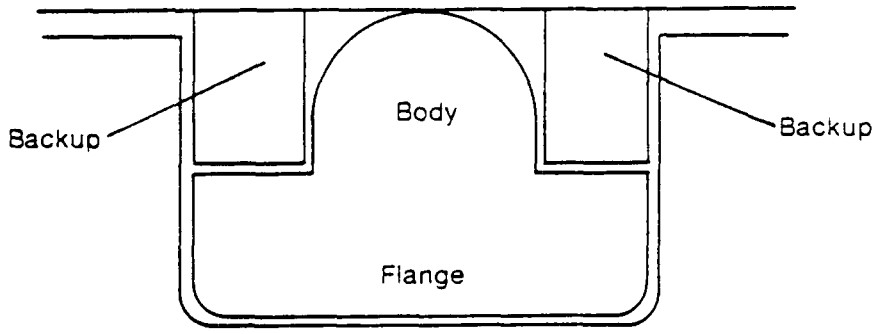

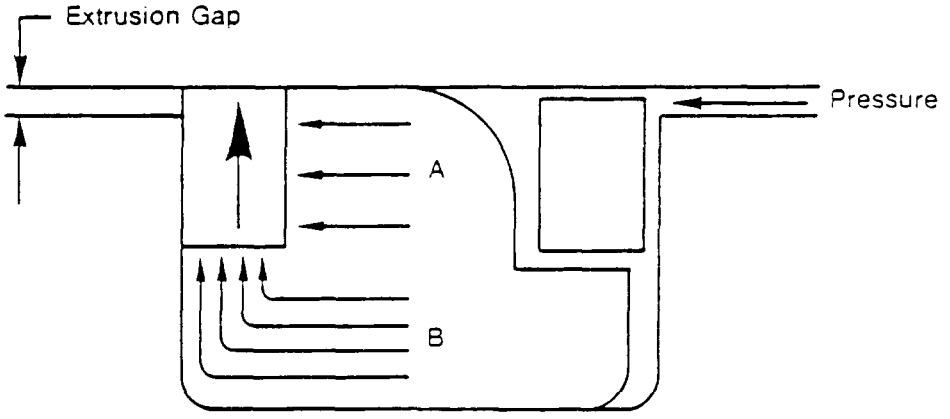

Fig. 2-23 Rod T-Seal Design

In its current configuration, the Mark I heat pump module is limited to only 18.1-mm piston stroke if diaphragm bending stress is not to exceed 40 ksi (corresponding diaphragm volume amplitude is 4.3 in.^{3}). At this stroke, the achieved compressor output of 34,500 Btu/hr at 17°F conditions is below the level required of 38,000. Although other changes to the compressor might be made to improve output while not exceeding 4.3-in.^{3} volume amplitude, the objective of this task is to evaluate alternative diaphragm designs that offer significantly greater volume deflections. If excess volume amplitude can be obtained with other designs, the working diameter would be reduced below the current 10.0 in. so compressor size and weight can be minimized (volume deflection capability varies approximately with the cube of diameter).

Four different diaphragm concepts are proposed.

- Improved models of the Bendix contoured diaphragm made of titanium or higher strength steel.
- Convoluted diaphragm similar to that used in Zurn's[4] flexible shaft couplings. This design uses fairly thin material (0.010 in.), resulting in low centering stiffness.
- Articulated diaphragm in which both the outer and inner edges are simply supported based on the Cooke-Yarborough design.
- Welded metal bellows with a relatively small diameter operating at long stroke. Operation of this design in oil should be investigated.

These alternatives are shown in Figures 2-24 and 2-25. No analytical results are presented at this time concerning the welded metal bellows. Vendor catalog information has been obtained and is shown in Figure 2-25. Further information is needed, however, concerning high-speed operation with one side of the bellows immersed in oil. The focus of work performed for this study has been to compare only the first three concepts listed above.

The criteria for final diaphragm selection included:

[4]Zurn Industries, Inc., 1801 Pittsburgh Avenue, Erie, PA 16512.

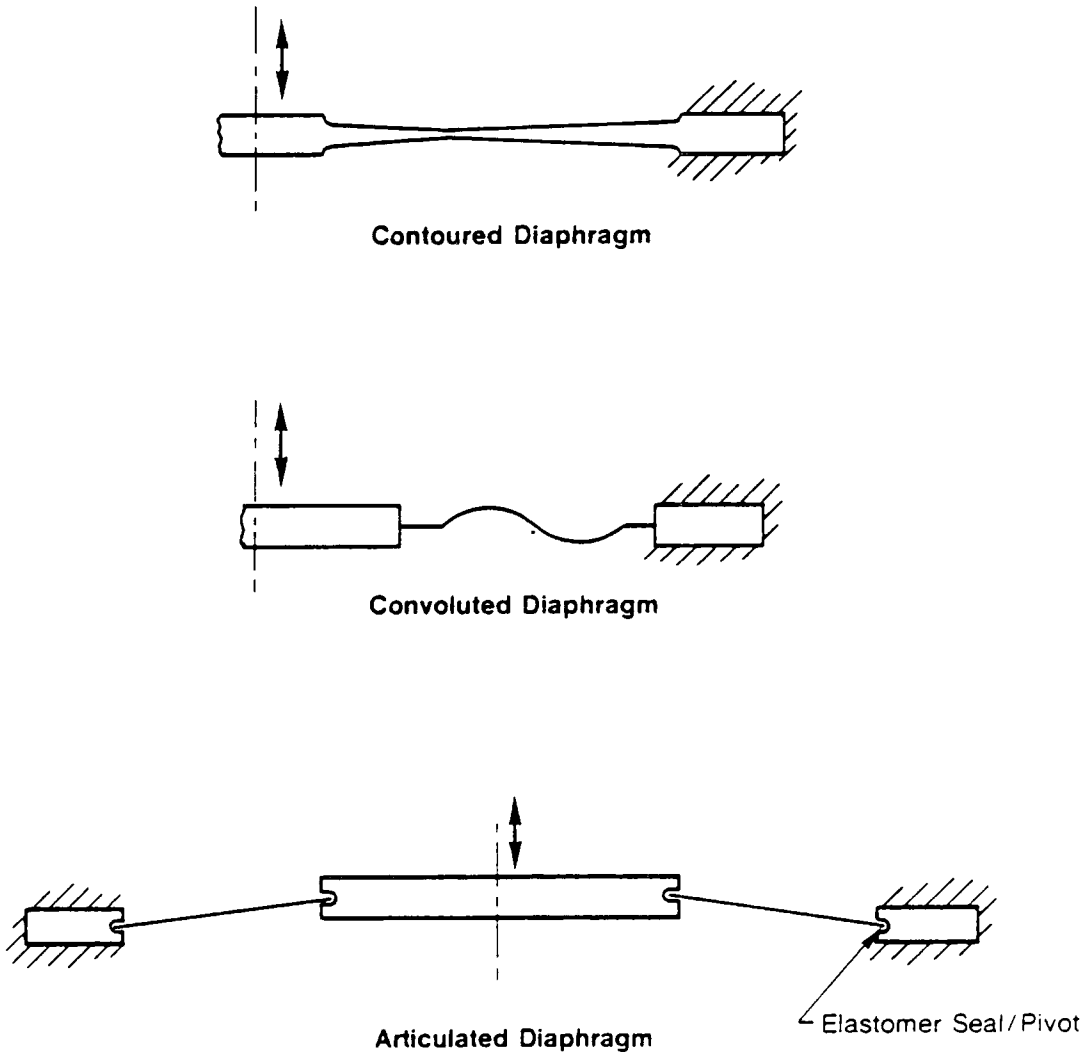

Fig. 2-24 Diaphragm Alternatives

87746

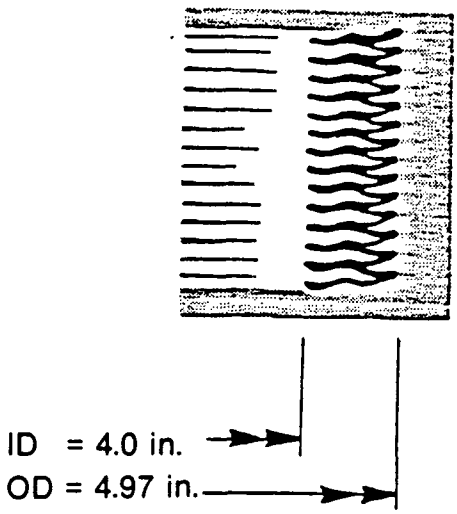

Metal Bellows Corporation

Code 90 Bellows:

13 Convolutions
Effective Area = 15.8 in.^{2}
Stroke Per Capsule = 0.80 in.
Displaced Volume = 12.64 in.^{3}

Not Suitable for 60-Hz Operation in Oil at 0.8-in. Stroke

Small Diameter, Long Stroke of Bellows May Be Needed for Optimum Packaging of Single-Acting Compressor

Fig. 2-25 Welded Metal Bellows

88564

- High-volume displacement: >5.4 in.^{3} at maximum stress $\leq$40 ksi (existing diaphragm reaches 40 ksi at 4.3 in.^{3})
- Working diameter $\leq$10 in.
- High centering stiffness, capable of operating with 1- to 2-psi pressure imbalance
- Low cost production quantities.

The analytical approach used in this study was to:

- Use Battelle NONLIN code to model contoured, convoluted, and articulated designs. Investigate various geometries for each type
- Determine volume displacement at 40 ksi maximum stress for 10-in. OD
- Determine centering stiffness of diaphragms, ΔP versus volume deflection.

The Battelle NONLIN code, used intermittently at MTI since 1980, was the primary tool used in the analysis. The NONLIN code was specifically developed to analyze large deflections and the resulting stress in diaphragms and bellows. A series of axisymmetric conical and toroidal shells are defined in the input data to represent the geometry of interest, and the nonlinear differential equations are integrated numerically. The code is quite general, and good correlation between predicted and measured deflections and stresses was found by Battelle in their evaluation of the code. The various diaphragm configurations analyzed with the NONLIN code included:

- Bendix shape:
  - Compare MTI PLATEA and Battelle NONLIN code results
  - Compare existing and improved shapes
  - Compare titanium and steel in improved shape

- Zurn convoluted diaphragm, 10-in. OD:
  - Results for 8-, 12-, and 16-mil thick

- 3-ripple diaphragm, convolution amplitudes of 0.05, 0.10, and 0.15 in.:
  - Results for 8-, 12-, and 16-mil thick

- Articulated diaphragm, test case from Cooke-Yarborough, then 10-in. OD:
  - Results for 40- and 60-mil thick.

One of the selection criteria for alternative diaphragms in this application was the need for high centering stiffness. This criterion was included because a passive oil management system is planned for eventual use on the Mark I. Such a system would probably not achieve perfect equalization of mean pressures above and below a diaphragm and, therefore, it is desirable to select a diaphragm that does not deflect beyond about one-third of full amplitude when 2 psig is applied. An auxiliary centering spring could be used with certain configurations if needed. This will be analyzed more fully when the passive oil management system is better defined.

For comparison of diaphragms, the various geometries and material thicknesses for each type were analyzed only at 10-in. working diameter, which is the size of the current Bendix diaphragms. The diaphragms were compared by determining the volume displacement corresponding to maximum stress equal to 40 ksi under uniform pressure loading. A diaphragm was judged superior to the existing type if the volume displacement was 5.4 in.^{3} or greater and the ΔP required to reach 40 ksi was at least 5 psig. Nonlinear deflection characteristics were not important in this application. The results obtained for the contoured, convoluted, and articulated diaphragms are discussed in detail in the following sections.

2.4.1 Contoured Diaphragms

Four configurations of contoured diaphragms, illustrated in Figures 2-26 though 2-28, were analyzed in this study. First, the nominal Bendix shape, in use for the past five years, was analyzed with the NONLIN code and the results compared to those from MTI's PLATEA code. Figures 2-29 and 2-30 illustrate this comparison and show that MTI's previous analysis was probably somewhat conservative. The NONLIN code predicted about 10% lower maximum bending stress at 4.0 in.^{3} volume displacement than did the MTI code.

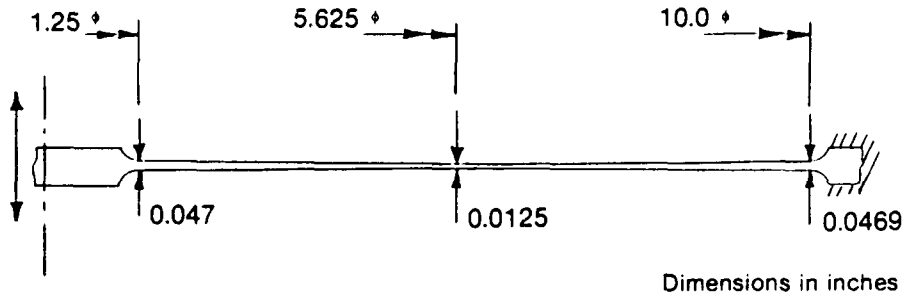

Bendix Diaphragm Materials:

4340, Vacuum Melted	Endurance Limit = 70 ksi
Ti 6A1 - 4V	Endurance Limit = 62 ksi
Vasco-max, Maraging Steel	Endurance Limit = 103 ksi

Fig. 2-26 Contoured Diaphragm: Standard Bendix Shape

88562

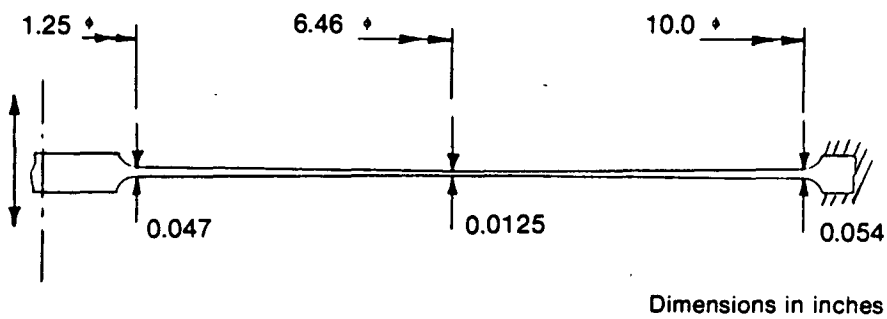

Thickness at rim increased 0.007 in., and minimum thickness region moved radially out by 0.42 in.
Maximum bending stress decreased 12%.

Fig. 2-27 Improved Contoured Diaphragm: Revised Shape

88801

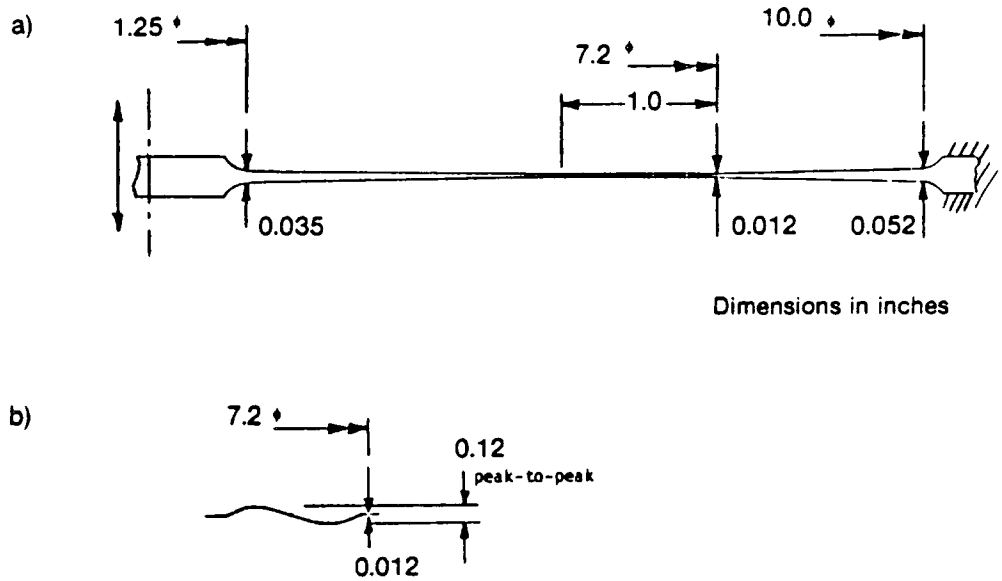

Revised Shapes:

a) 1-in. Flat Diaphragm. Revised contour results in 19% reduction in bending stress.

b) Convolution Added. Very high bending stress occurs at peak of outermost convolution.

Fig. 2-28 Contoured Diaphragm: Straight Region and Convolution Added Shapes

88561

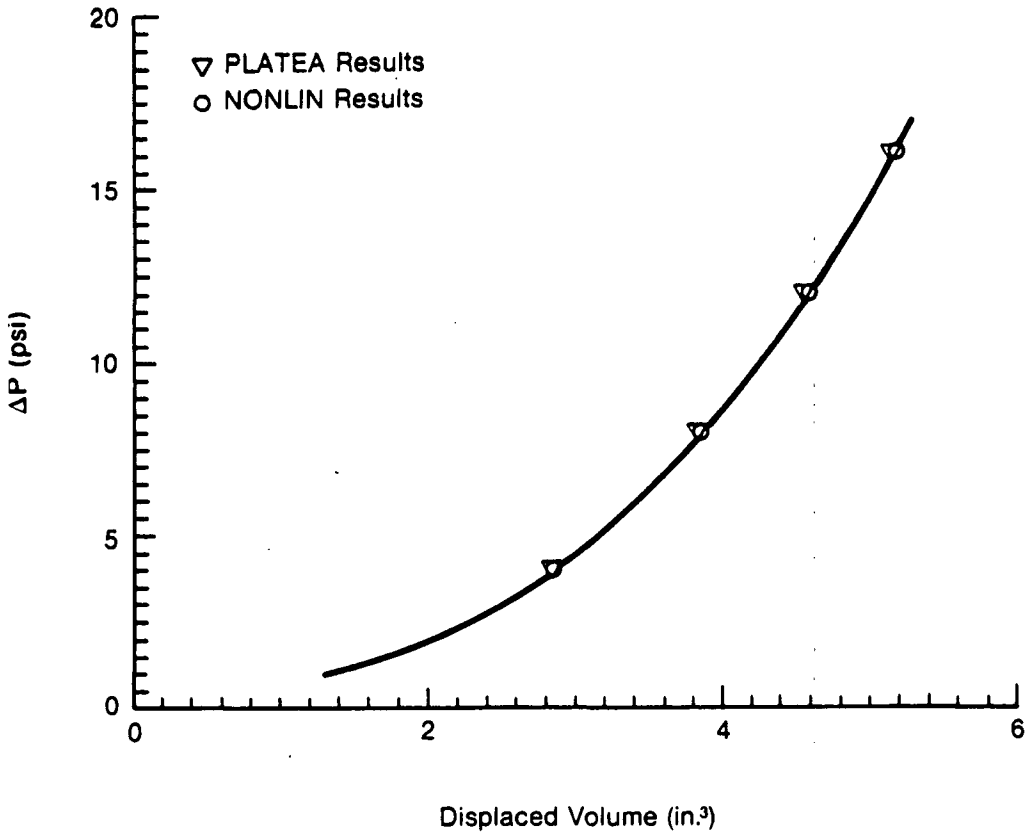

Fig. 2-29 Comparison of PLATEA and NONLIN Code Results for Standard Bendix Diaphragm: ΔP versus Displaced Volume

87832

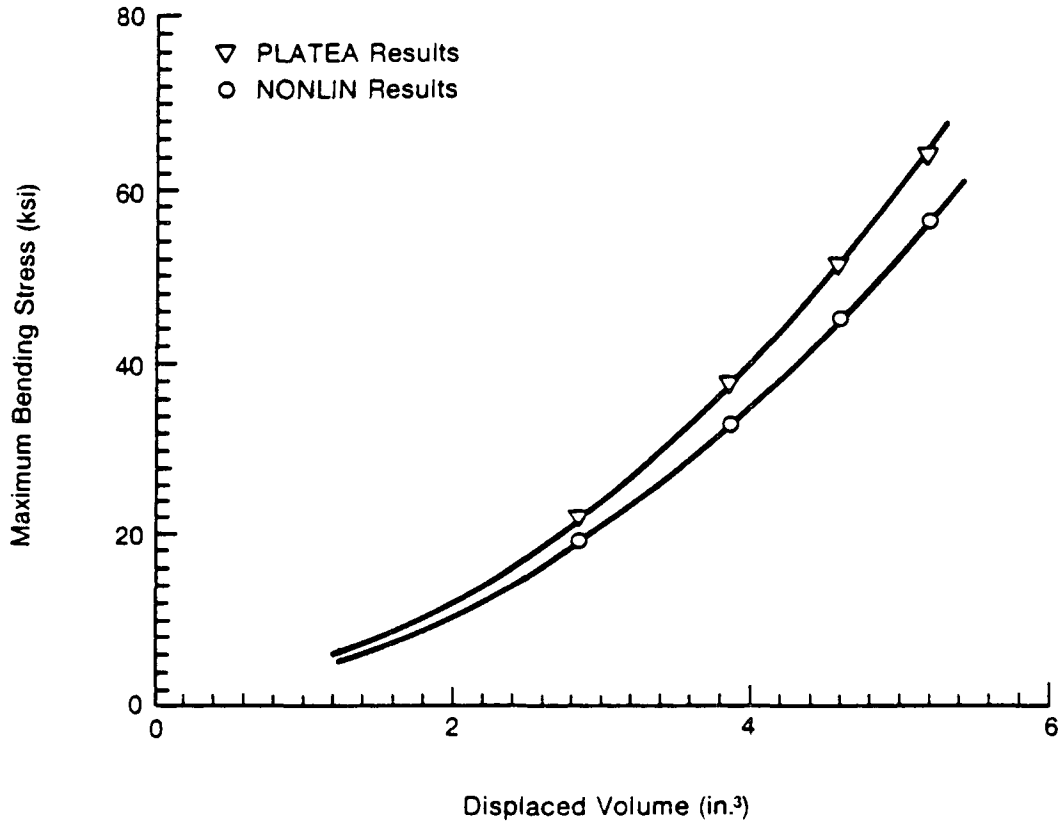

Fig. 2-30 Comparison of PLATEA and NONLIN Code Results for Standard Bendix Diaphragm: Maximum Bending Stress versus Displaced Volume

87831

An improved contour was then developed that reduced the maximum bending stress by about 12%. This contour is pictured in Figure 2-27 and differs from the standard contour in that the outer edge thickness is 0.054 in. and the thinnest region, 0.0125 in., is moved radially outward by 0.42 in. Figures 2-31 and 2-32 show a comparison of results from the NONLIN code for the standard and revised (BEN054) shapes.

The third and fourth shapes analyzed are illustrated in Figure 2-28. These diaphragms include a region of uniform thickness, 0.012-in. thick, that is 1.0-in. long. The first shape (Figure 2-28a) is flat in the 12-mil thick region, while the second incorporates a single convolution in this region with amplitude equal to 0.06-inch. Figures 2-33 and 2-34 compare the results for the flat diaphragm (BENSTR) to those for the standard shape. Maximum bending stress is about 19% lower for this contour. Finally, results for the second diaphragm (Figure 2-28b) showed that maximum bending stress occurred at the peak of the outermost convolution and equaled 88.8 ksi at ΔP equal to 4 psig, with a corresponding volume displacement of 6.5 in.^{3}. This shape offered no improvement, but further analysis could be done on a much shallower convolution or one that spans nearly the full radius of the diaphragm.

One additional possibility exists for the contoured diaphragm and that is to obtain greater volume displacement by substituting titanium for steel. Titanium has a Young's modulus of 16.5×10^6 psi as compared to 30×10^6 psi assumed for steel and therefore deflects 1.8 times more for the same stress assuming linear behavior. Figures 2-35 and 2-36 give the deflection results comparing steel and titanium diaphragms in the revised contour shape of Figure 2-27. Volume displacement is about 40% higher for titanium as compared to steel. Unfortunately, the high cost of titanium may preclude its use in a heat pump designed for mass production.

In summary, it appears that although significant improvements in steel contoured diaphragms can be made through redesign, the volume amplitude at 40 ksi will not reach 5.4 in.^{3}. The contoured diaphragm does have a long history of successful performance, however, and lends itself to hermetic sealing via a welded or brazed connection to the transmission case.

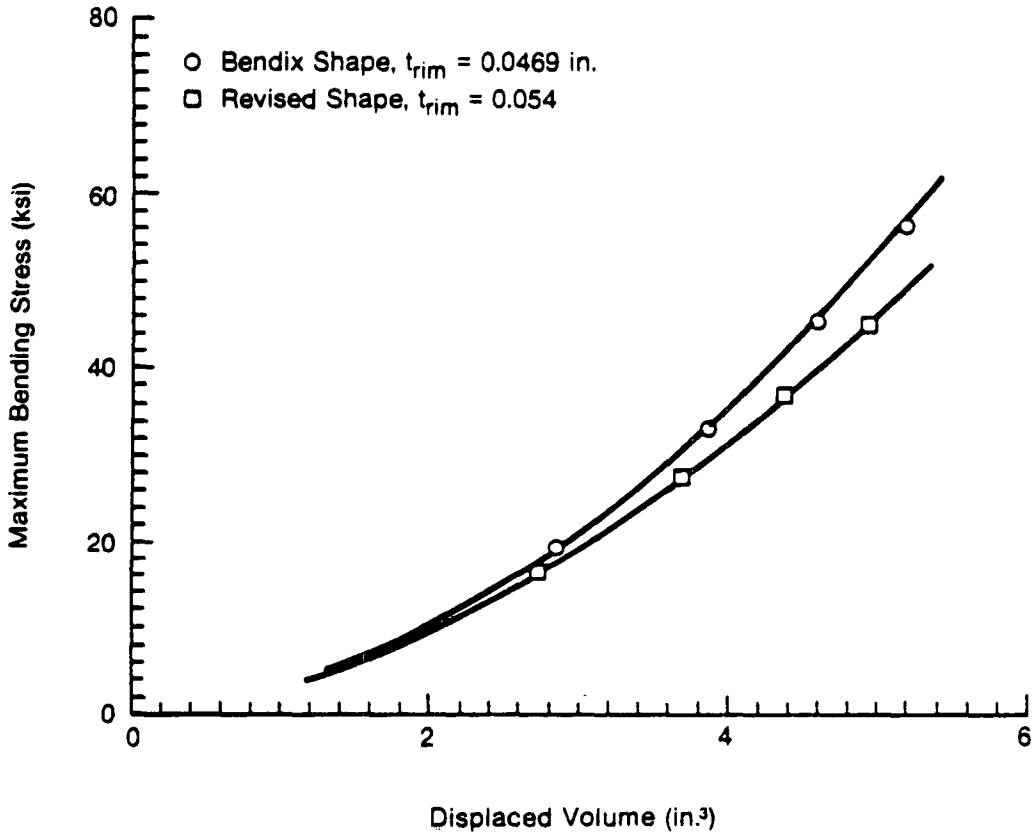

Fig. 2-31 Comparison of NONLIN Code Results for Bendix Standard and Revised Diaphragms: Maximum Bending Stress versus Displaced Volume

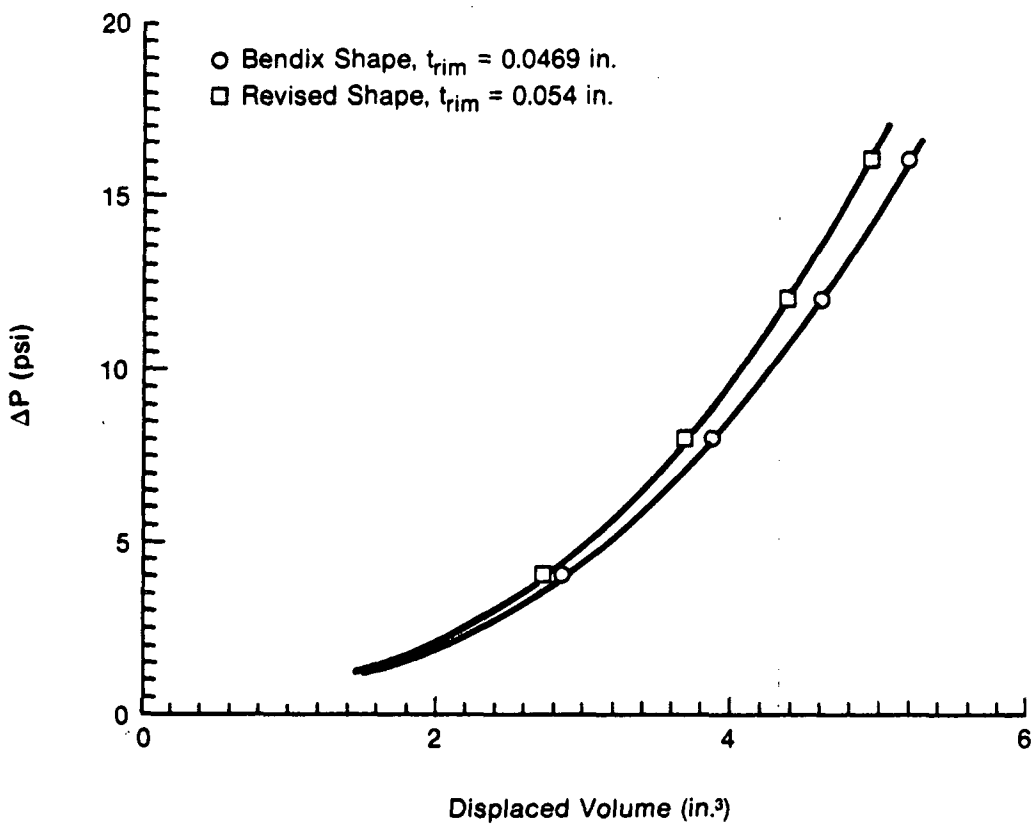

Fig. 2-32 Comparison of NONLIN Code Results for Bendix Standard and Revised Diaphragms: ΔP versus Displaced Volume

87829

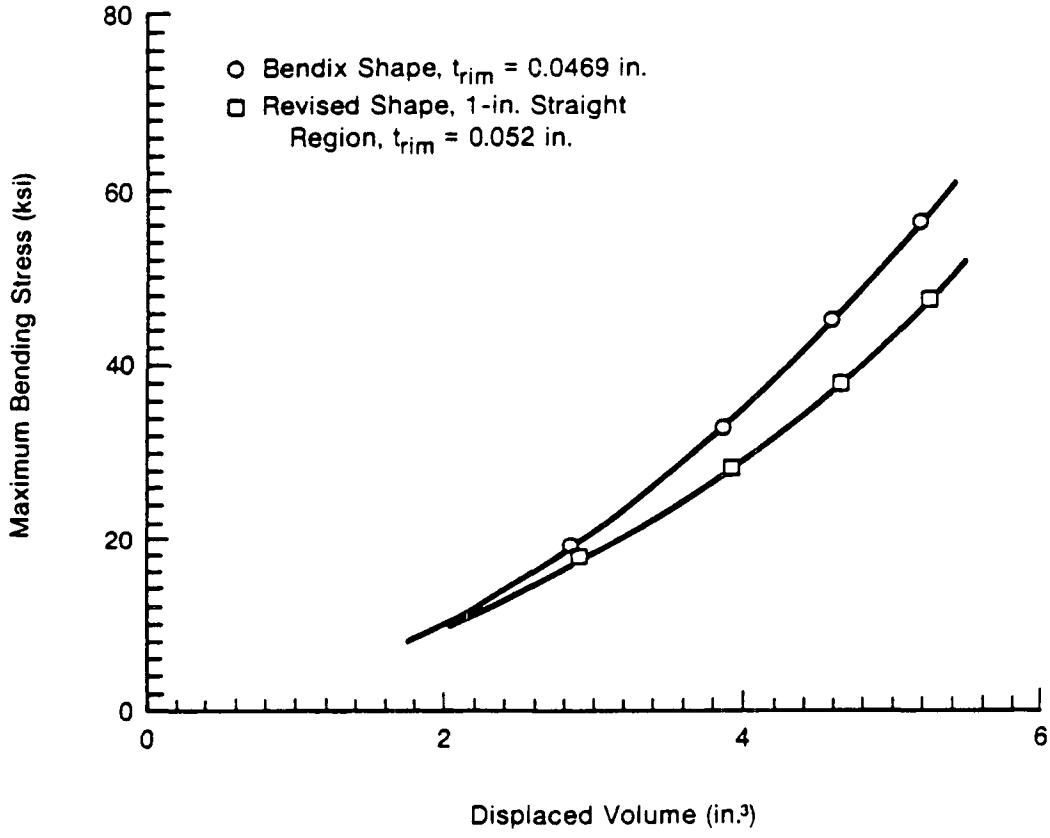

Fig. 2-33 Comparison of NONLIN Code Results for Bendix Standard and Flat Diaphragms: Maximum Bending Stress versus Displaced Volume

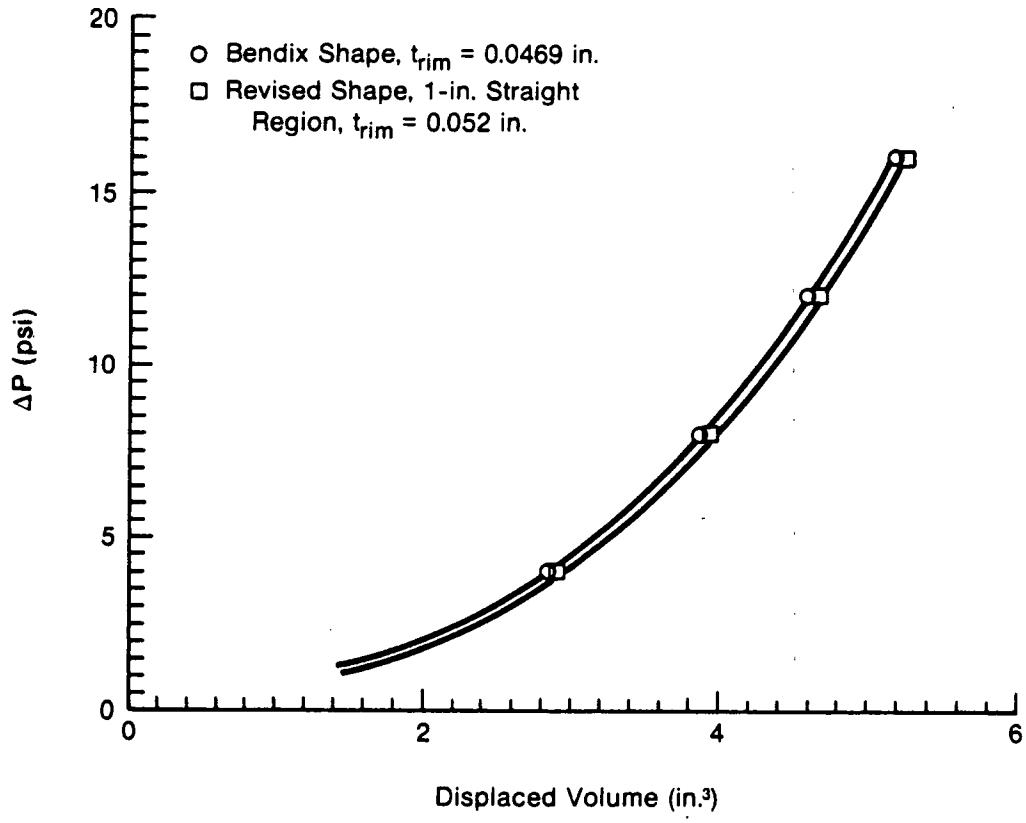

Fig. 2-34 Comparison of NONLIN Code Results for Bendix Standard and Flat Diaphragms: ΔP versus Displaced Volume

87827

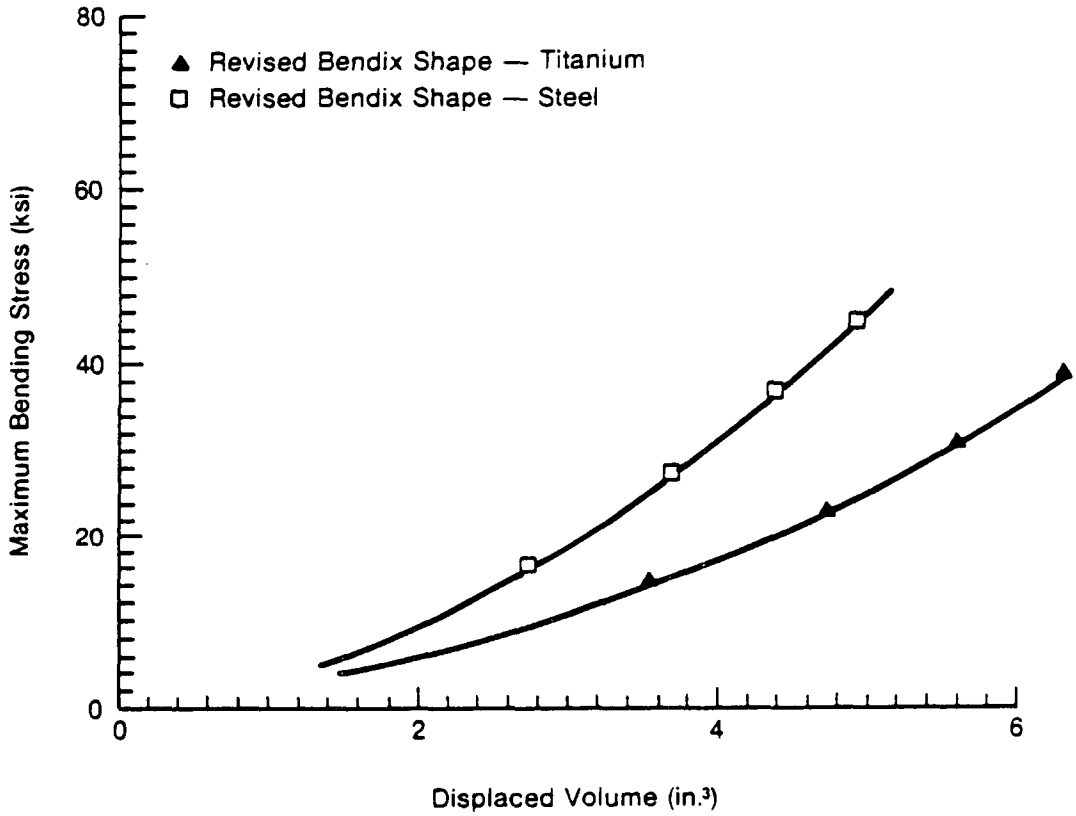

Fig. 2-35 Comparison of NONLIN Code Results for Bendix Revised Steel and Titanium Diaphragms: Maximum Bending Stress versus Displaced Volume

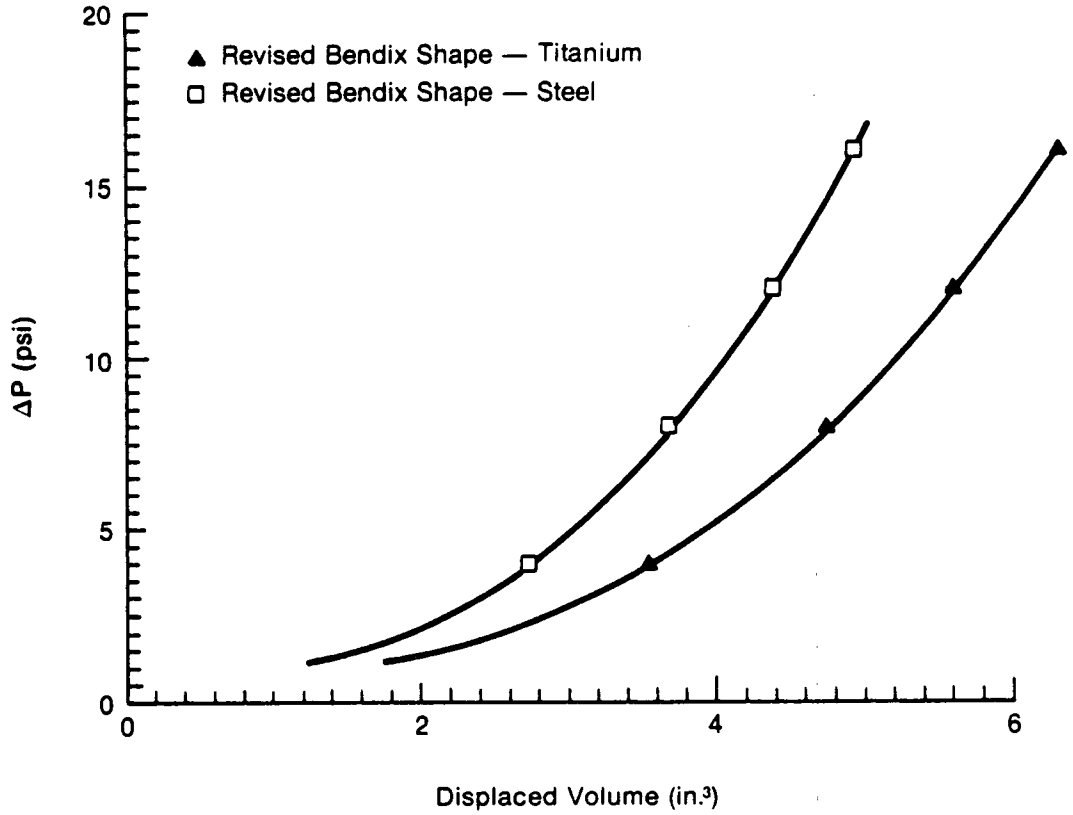

Fig. 2-36 Comparison of NONLIN Code Results for Bendix Revised Steel and Titanium Diaphragms: ΔP versus Displaced Volume

87826

2.4.2 Convoluted Diaphragms

Convoluted diaphragms are typically made from relatively thin sheet steel that is formed to produce axisymmetric waviness. On installation, the diaphragm is tightly clamped between flanges at its OD and at the hub. Two basic configurations of convoluted diaphragms were analyzed in this study: the Zurn shape and the 3-ripple configuration. The Zurn shape has a large hub diameter, and the diaphragm contains only one convolution. The 3-ripple configuration has a smaller diameter hub and three convolutions. Figure 2-37 illustrates the Zurn and 3-ripple configurations and also gives the shell element numbers defined in the NONLIN code.

Results were obtained for these diaphragms in thicknesses of 8, 12, and 16 mil. The 3-ripple design was also analyzed with convolution heights of 0.05, 0.10, and 0.15 in. Figures 2-38 through 2-47 are plots of the results obtained. It is interesting to note that as the amplitude of convolutions increases in the 3-ripple design, the diaphragm becomes more linear but less able to accommodate large volume displacement at 40 ksi maximum bending strength.

Maximum stress typically occurs at the outer clamped edge of the diaphragm. In an effort to reduce the maximum stress, a diaphragm was modeled in which the clamped edge was tilted 30°, as suggested by engineers developing small Stirling engines for artificial hearts.[5] The code predicted that maximum stress is reduced approximately 10% and shifted away from the edge. Volume displacement decreased by more than 10%, however, and no net benefit was obtained. Results presented here are only for the case of a straight clamped edge.

The best performance was obtained at a thickness of 8 mil and with very shallow convolutions in the 3-ripple design. The Zurn shape allows 6.1 in.^{3} at 40 ksi, and the 3-ripple configuration allows 6.9 in.^{3}. However, both these

---

[5]White, M. A. et al. "Hermetic Metal Seals for Stirling Engines." Proceedings of 1984 IECEC. Paper no. 849146, vol. 3: pp 1982-87.

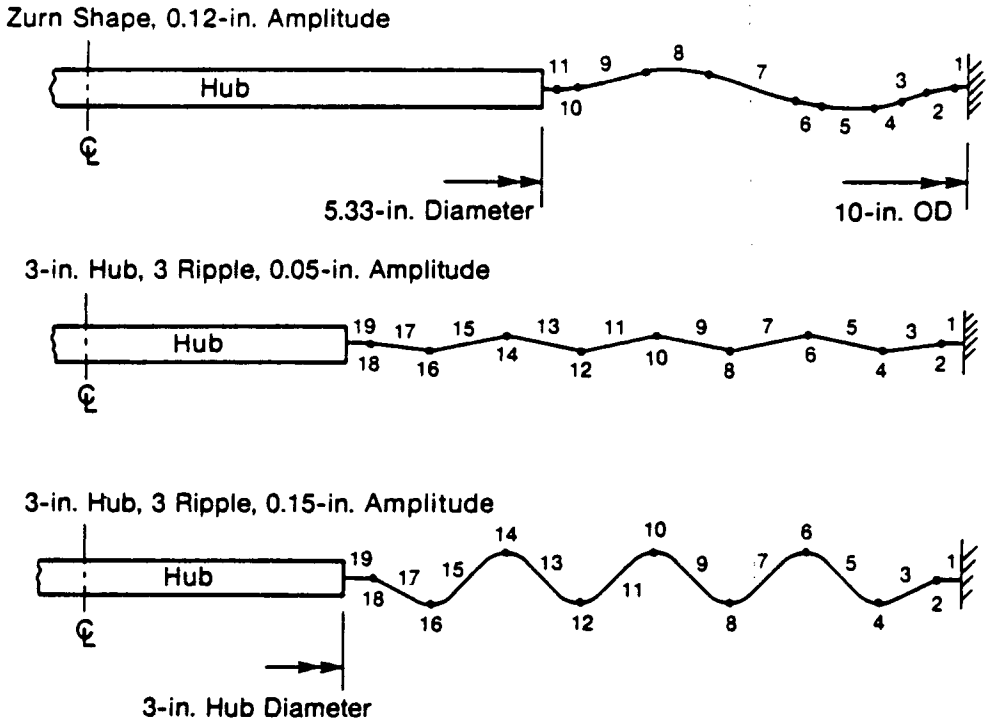

Fig. 2-37 Convoluted Diaphragm Geometries

87838

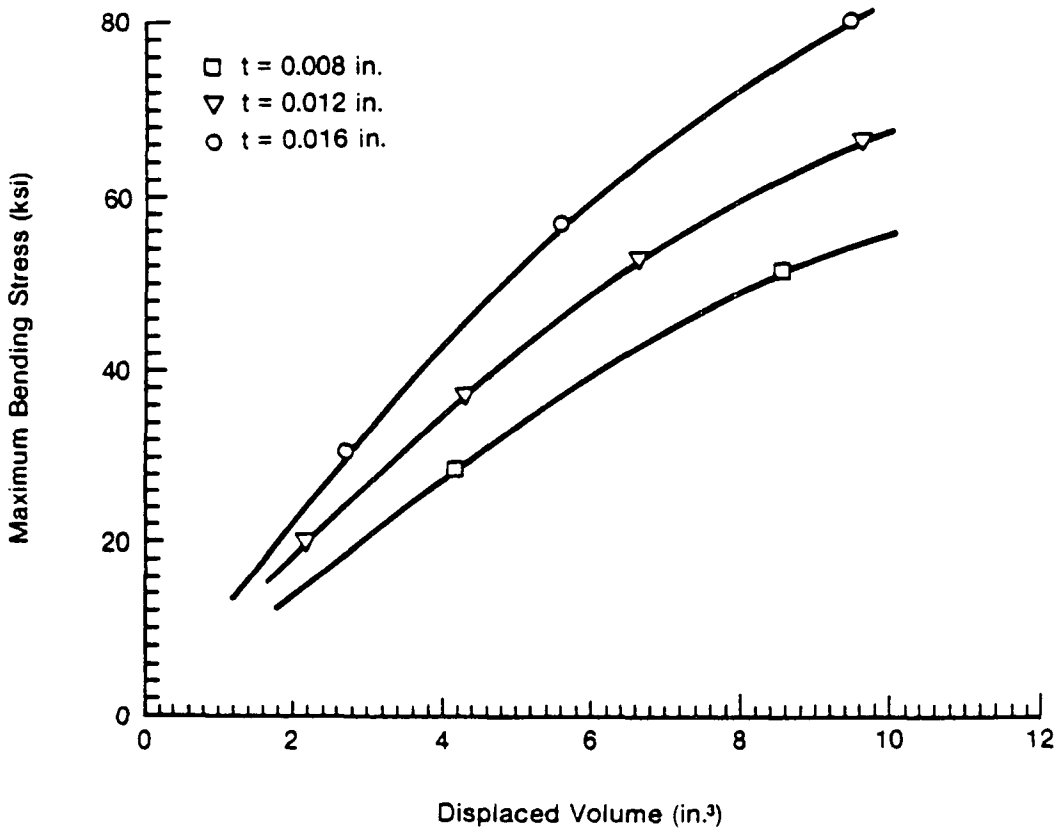

Fig. 2-38 NONLIN Code Results for Zurn Shape Diaphragm (8, 12, 16 mil): Maximum Bending Stress versus Displaced Volume

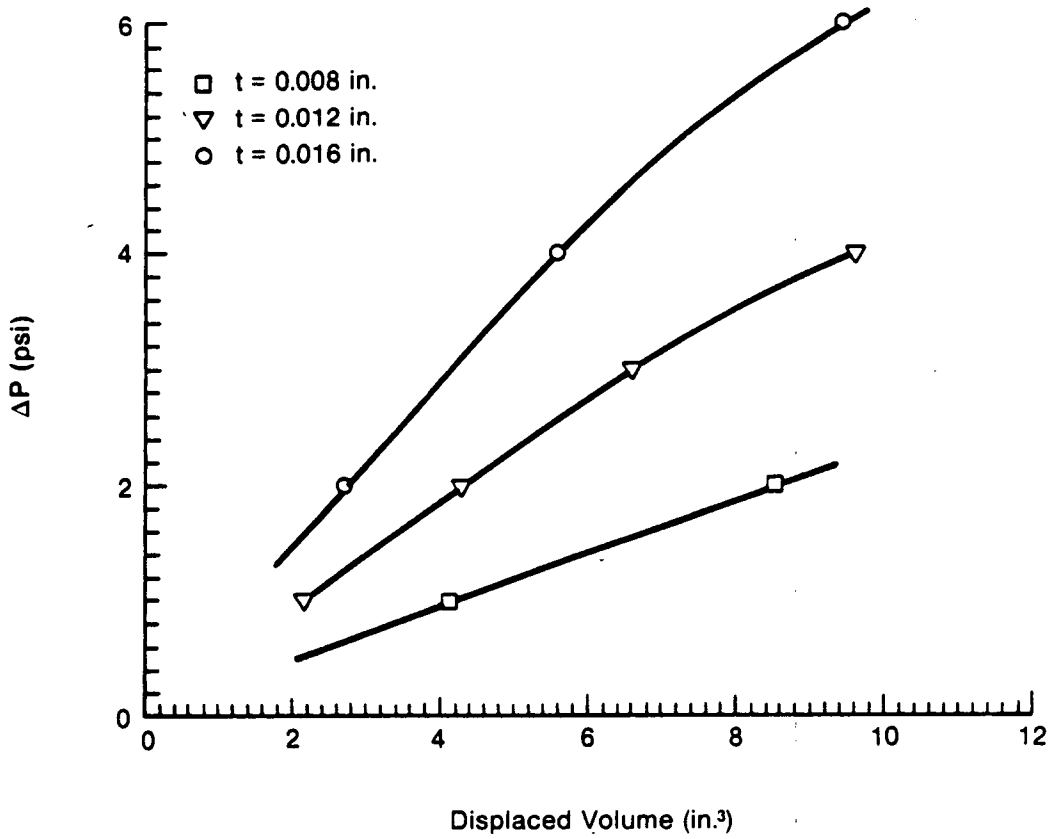

Fig. 2-39 NONLIN Code Results for Zurn Shape Diaphragm (8, 12, 16 mil): ΔP versus Displaced Volume

87824

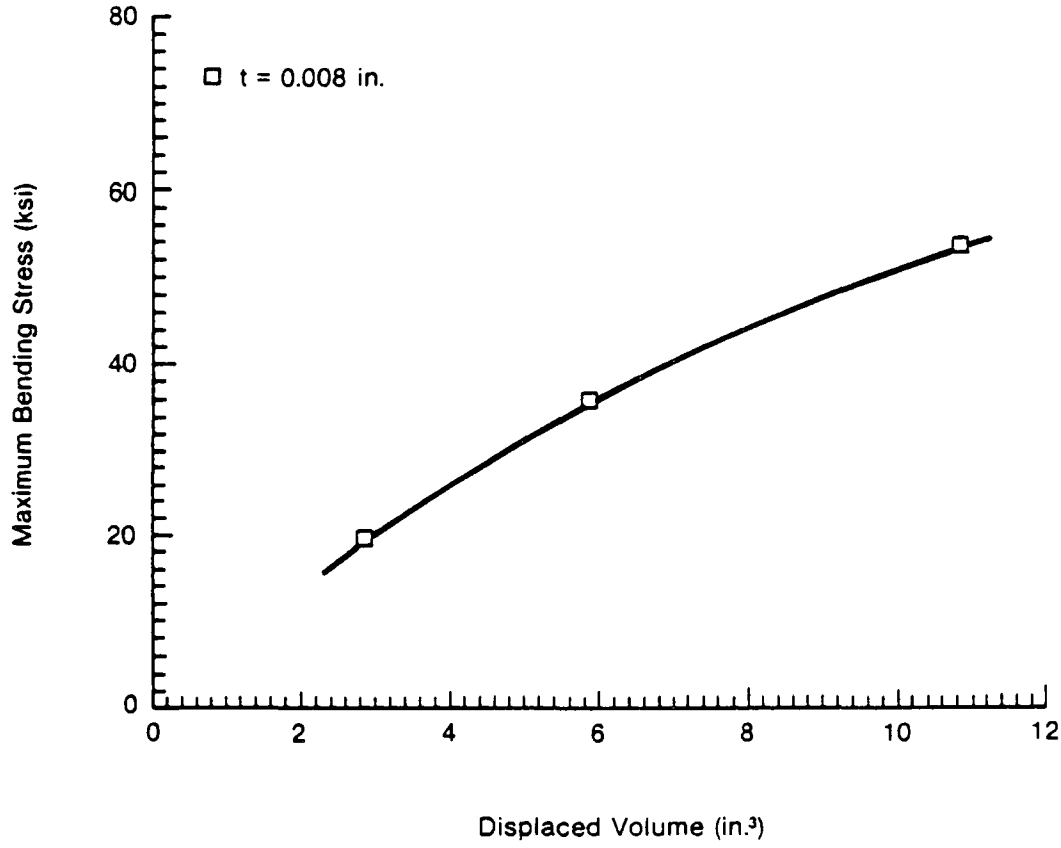

Fig. 2-40 NONLIN Code Results for 3-Ripple Diaphragm (0.05-in. Amplitude, 8 mil): Maximum Bending Stress versus Displaced Volume

878

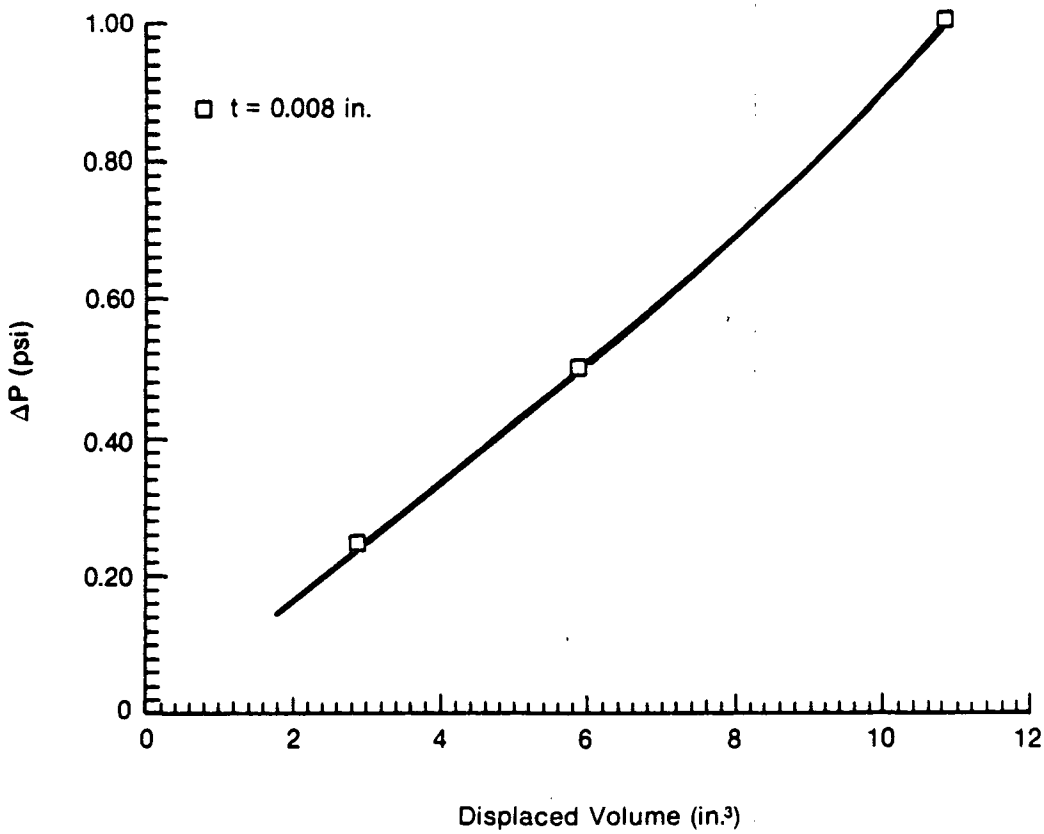

Fig. 2-41 NONLIN Code Results for 3-Ripple Diaphragm (0.05-in. Amplitude, 8 mil): ΔP versus Displaced Volume

87846

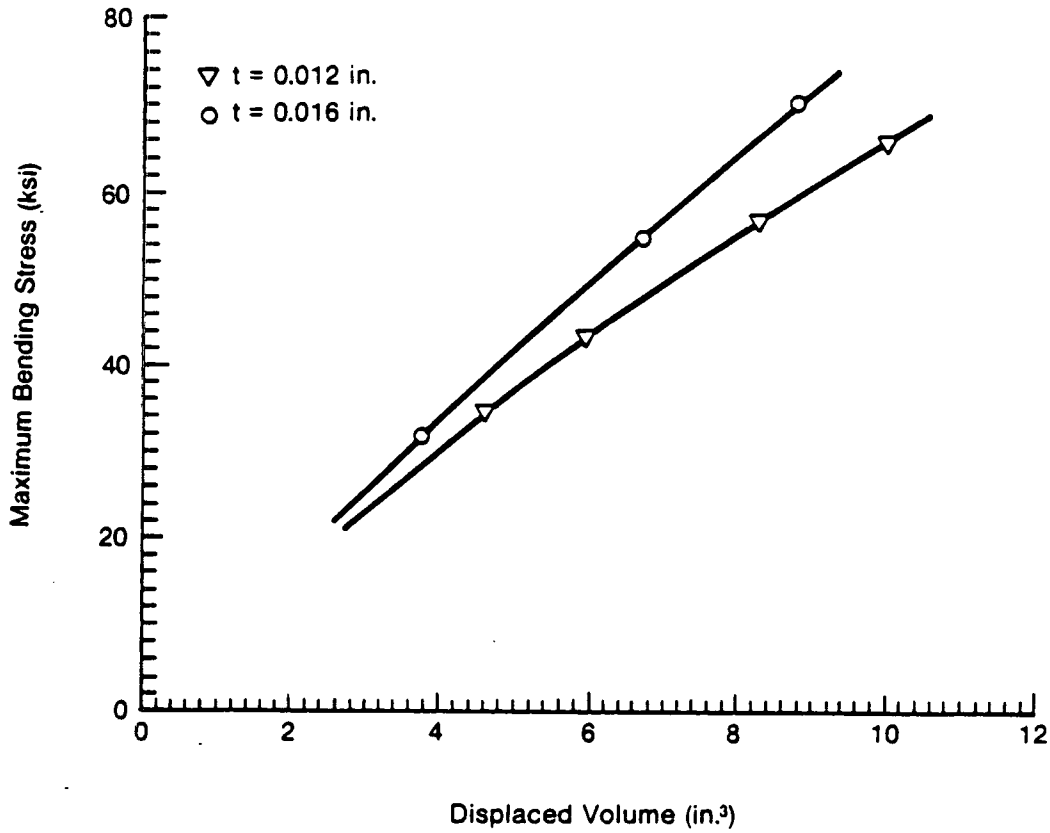

Fig. 2-42 NONLIN Code Results for 3-Ripple Diaphragm (0.05-in. Amplitude, 12 and 16 mil): Maximum Bending Stress versus Displaced Volume

87822

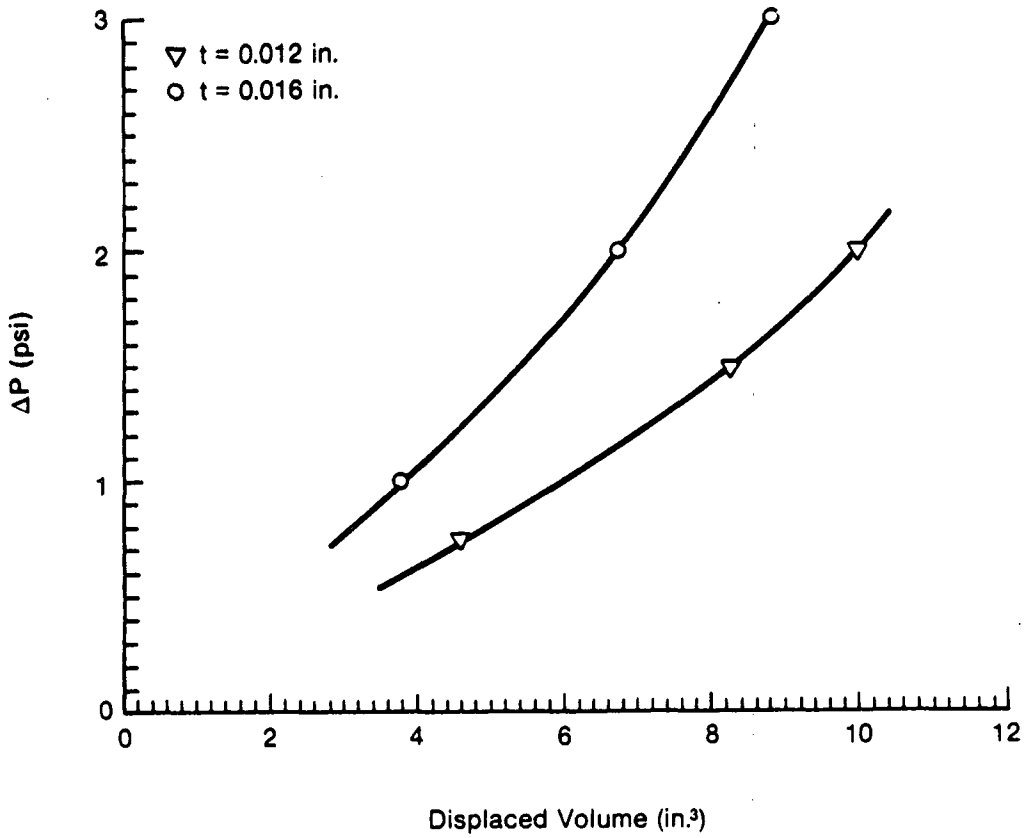

Fig. 2-43 NONLIN Code Results for 3-Ripple Diaphragm (0.05-in. Amplitude, 12 and 16 mil): ΔP versus Displaced Volume

87816

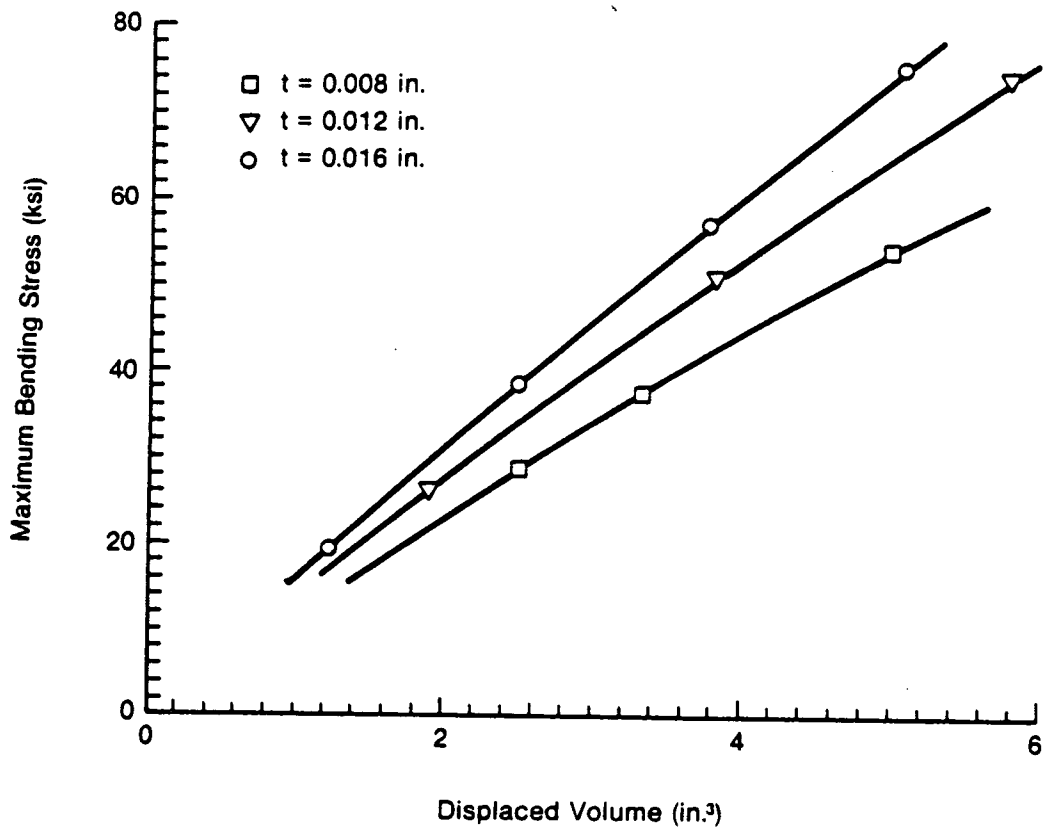

Fig. 2-44 NONLIN Code Results for 3-Ripple Diaphragm (0.10-in. Amplitude, 8, 10, 16 mil): Maximum Bending Stress versus Displaced Volume

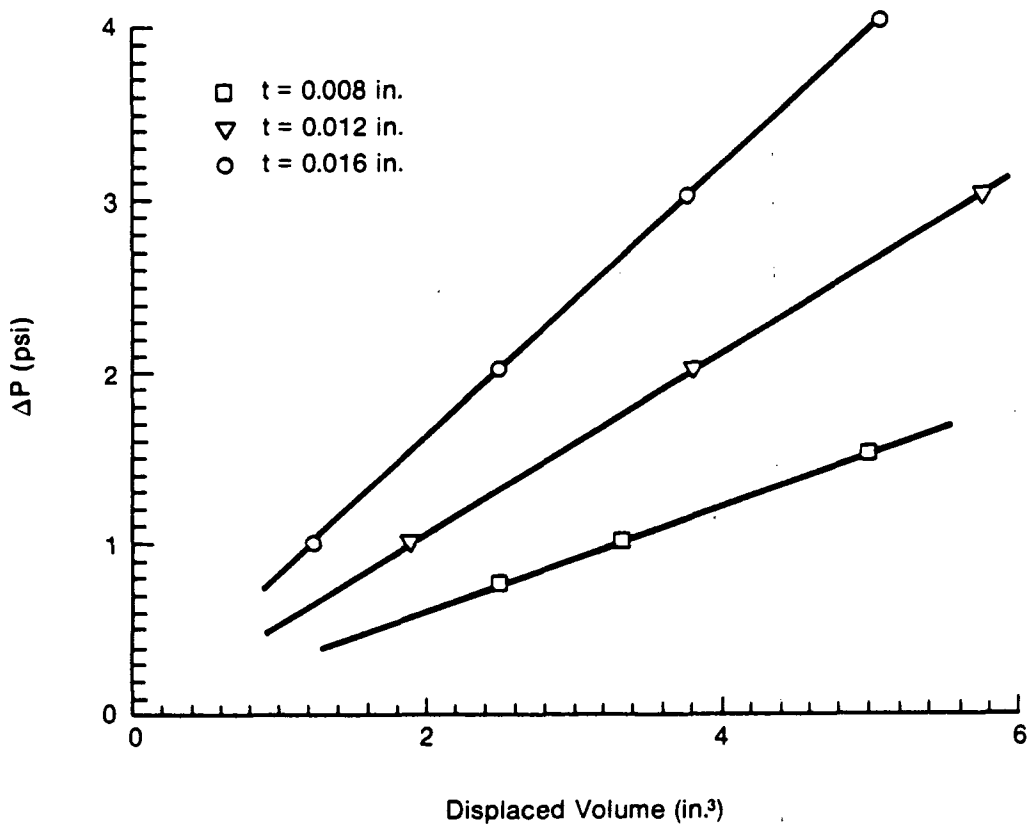

Fig. 2-45 NONLIN Code Results for 3-Ripple Diaphragm (0.10-in. Amplitude, 8, 12, 16 mil): ΔP versus Displaced Volume

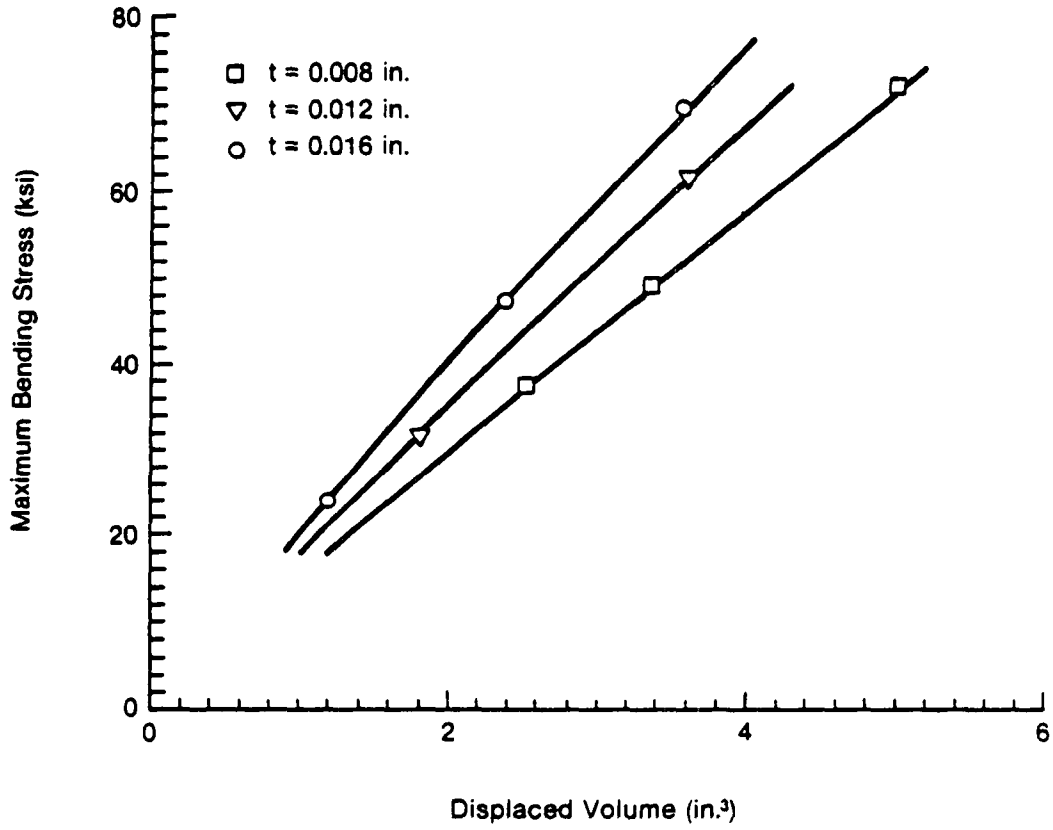

Fig. 2-46 NONLIN Code Results for 3-Ripple Diaphragm (0.15-in. Amplitude, 8, 12, 16 mil): Maximum Bending Stress versus Displaced Volume

87821

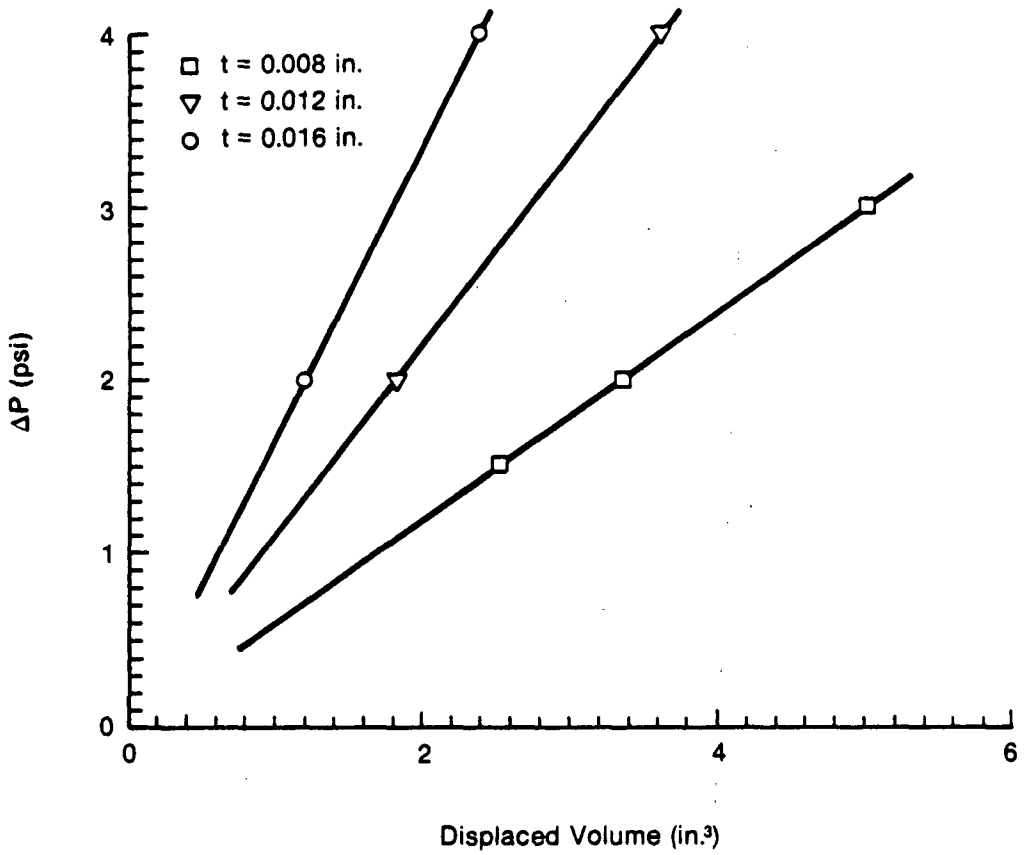

Fig. 2-47 NONLIN Code Results for 3-Ripple Diaphragm (0.15-in. Amplitude, 8, 12, 16 mil): ΔP versus Displaced Volume

87820

diaphragms responded too rapidly to applied ΔP. If stiff centering springs are added to the diaphragm, flexing or potential buckling of the convolutions could occur because of the very low material thickness. Therefore, it is concluded that the convoluted diaphragm would not be useful in this application unless an oil management system is developed that produces very accurate equalization of mean pressures and the diaphragm.

2.4.3 Articulated Diaphragms

Articulated diaphragms utilize elastomeric supports around the outer and inner edges to practically eliminate radial bending stress from the system. Typically, the diaphragm is squeezed between large section O-rings and the hub is free to translate in response to applied pressure loading. The diaphragm itself simply deforms to the shape of a shallow cone as the hub translates. Maximum stress occurs at the inner edge, where circumferential bending stress due to curvature of the cone is additive with tensile hoop stress that arises as the inside diameter of the diaphragm tries to increase. These stresses are generally quite low compared to the bending stress of a similar diaphragm that is clamped at its outer edge.

Articulated diaphragms have been patented in England by E. H. Cooke-Yarborough, who assisted in their analysis for this study (see Appendix B for supporting literature). Testing of this diaphragm type over long duration has been very successful, and no problems have been encountered with either leakage past the O-ring pivot seals or wear of the rubber. The operating conditions for the heat pump, however, are considerably in excess of any tests done previously on articulated diaphragms.

Figure 2-48 illustrates a possible mounting configuration of an articulated diaphragm in the HAHP. In this figure, a static pressure sealing O-ring is shown outboard of the diaphragm pivot seal. This seal may be unnecessary since the two machines currently in use with articulated diaphragms, a thermo-mechanical generator in England and a hydraulic power output Stirling engine owned by NASA-Lewis Research Center, allow the pivot O-rings to also seal internal pressure. Figure 2-48 also illustrates a diaphragm with rather small inside radius. The best configuration analyzed by Cooke-Yarborough has

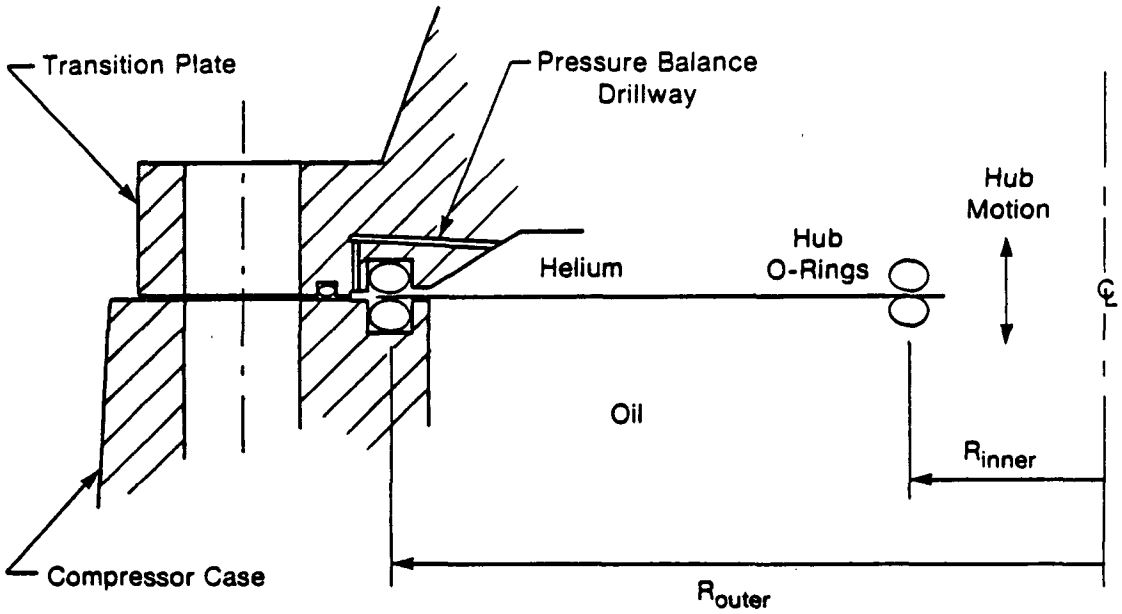

Example Mounting Configuration

Fig. 2-48 Articulated Diaphragm

87836

an inside radius that is 63% of the outside radius. This would yield a hub diameter of 6.25 in. for a diaphragm outer diameter of 10.0 in.

The first diaphragm configuration analyzed by Cooke-Yarborough resulted in 6.305 in.^{3} volume displacement for maximum stress equal to 29.5 ksi (see Table 2-17 and Appendix B). This case was duplicated with the NONLIN code, and somewhat lower stresses were predicted. Table 2-17 summarizes the results obtained, and Figures 2-49 and 2-50 give the NONLIN results for the Case 1a diaphragm in plot form. The discrepancy in results has yet to be resolved, but for further comparisons, the NONLIN code was assumed accurate and was exercised on a model with a working diameter equal to 10.0 in. Material thicknesses of 40 and 60 mil were considered, and Figures 2-51 and 2-52 give the results obtained. The code predicts that a volume amplitude of 7.75 in.^{3} is attainable without exceeding the 40-ksi stress limit. At this volume displacement, ΔP is somewhat low at 2.75 psig, and it is likely that an auxiliary centering spring would have to be added. Material thickness is quite large, however, and no difficulties are anticipated with this aspect of the articulated diaphragm. Also, the use of titanium sheet instead of steel for the articulated diaphragm should be considered, since material costs would not be prohibitive when diaphragm thickness is only 40 to 50 mil.

2.4.4 Results of the Diaphragm Analysis

A summary of deflection results for the contoured, convoluted, and articulated diaphragms is given in Table 2-18. It is seen that the articulated diaphragm offers much greater volume capability than the Bendix-style diaphragm. It also appears that convoluted diaphragms should not be considered unless the oil management system is capable of highly accurate pressure balancing.

Conclusions reached from this study include the following:

- Titanium material cost is very high, $20/lb. Material for a diaphragm with a 0.15-in. thick rim would cost $75.
- A Zurn convoluted diaphragm with centering spring or hub may be superior to the Bendix-style diaphragm. However, the Zurn diaphragm may present a high risk because of thin material.

Table 2-17

Articulated Diaphragm

Cooke-Yarborough's Case 1a:

OD = 10.61 in. ID = 7.764 in. t = 1 mm E = 31.33×10^6 psi

At volume = 6.305 $in.^3$, total stress inner edge = 29.5 ksi

NONLIN Result:

At volume = 6.3 $in.^3$, total stress inner edge = 25.9 ksi

NONLIN Model for Comparison

OD = 10 in. ID = 6.25 in. t = 0.040 to 0.060 in. E = 30×10^6psi

Results plotted in Figures 2-49 and 2-50: At 40 ksi, volume = 7.38 $in.^3$, ΔP = 2.75 psi

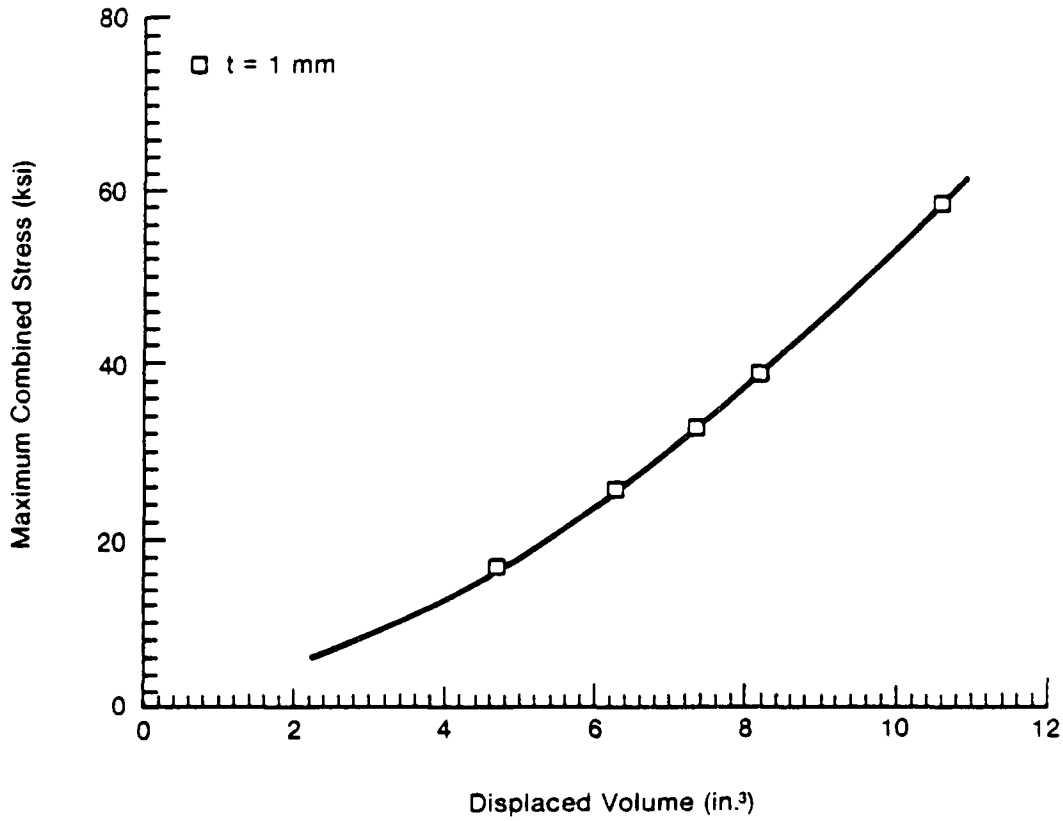

Fig. 2-49 NONLIN Code Results for Case 1A Articulated Diaphragm: Maximum Combined Stress versus Displaced Volume

87839

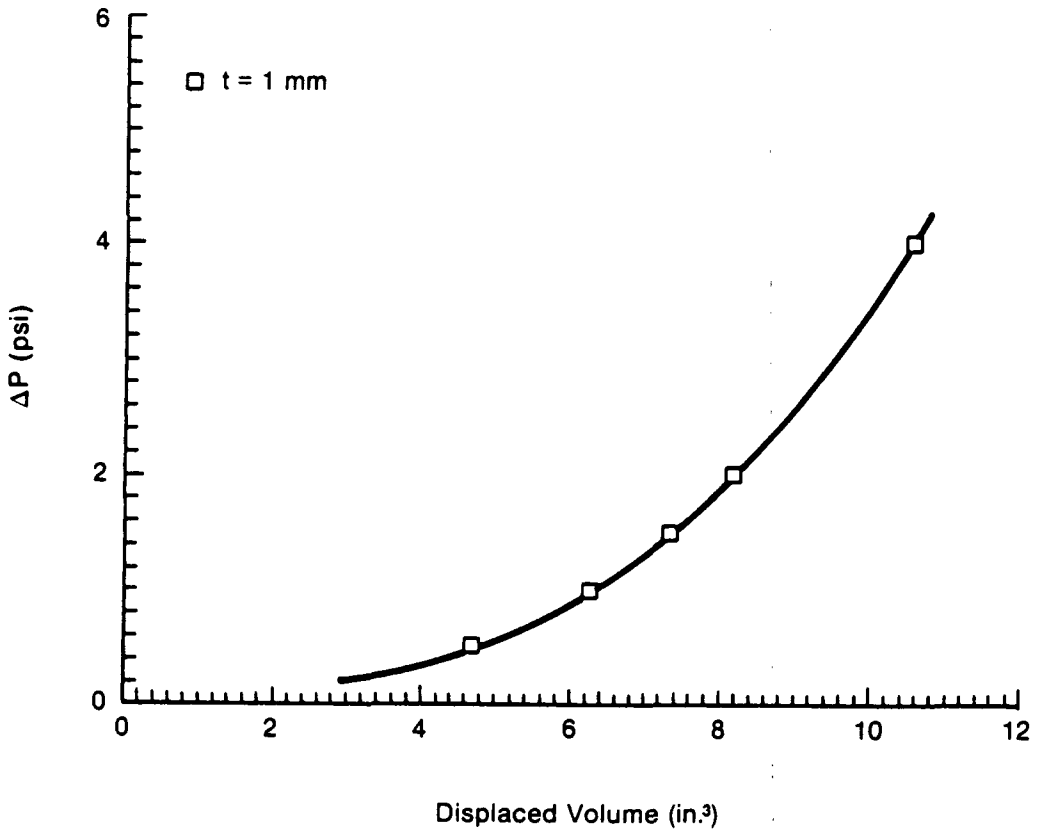

Fig. 2-50 NONLIN Code Results for Case 1A Articulated Diaphragm: ΔP versus Displaced Volume

87812

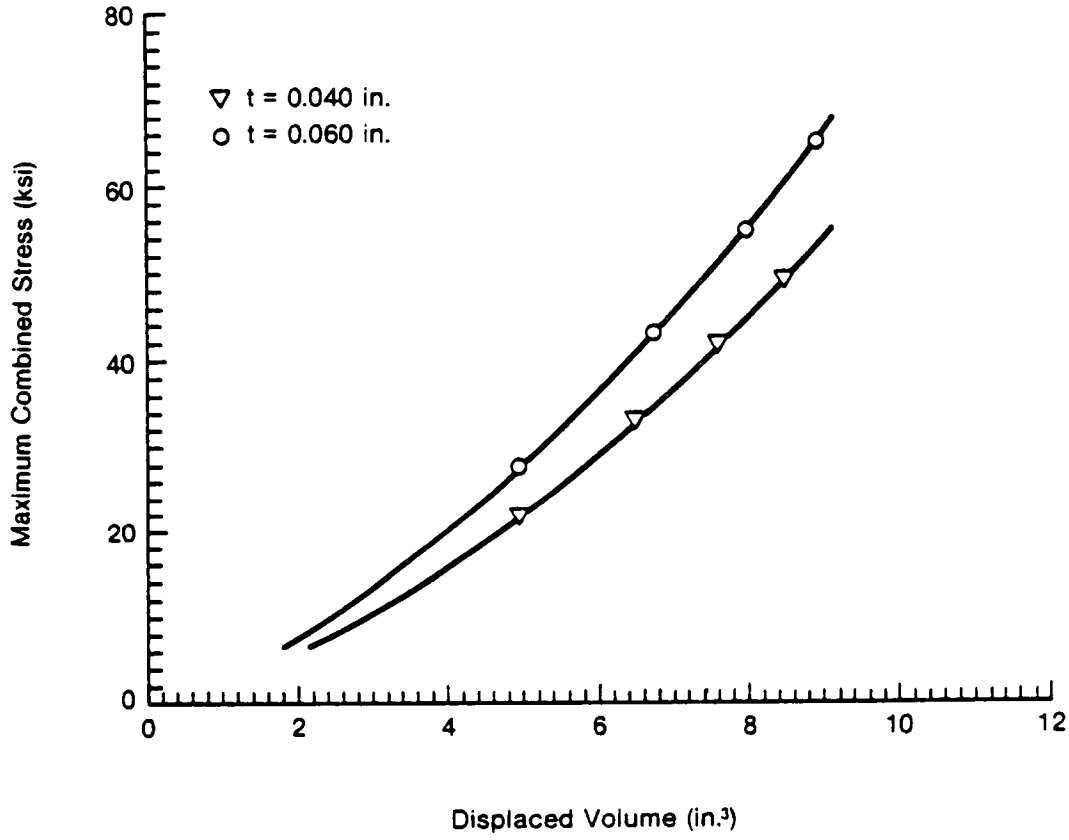

Fig. 2-51 NONLIN Code Results for Articulated Diaphragm (40 and 60 mil): Maximum Combined Stress versus Displaced Volume

87819

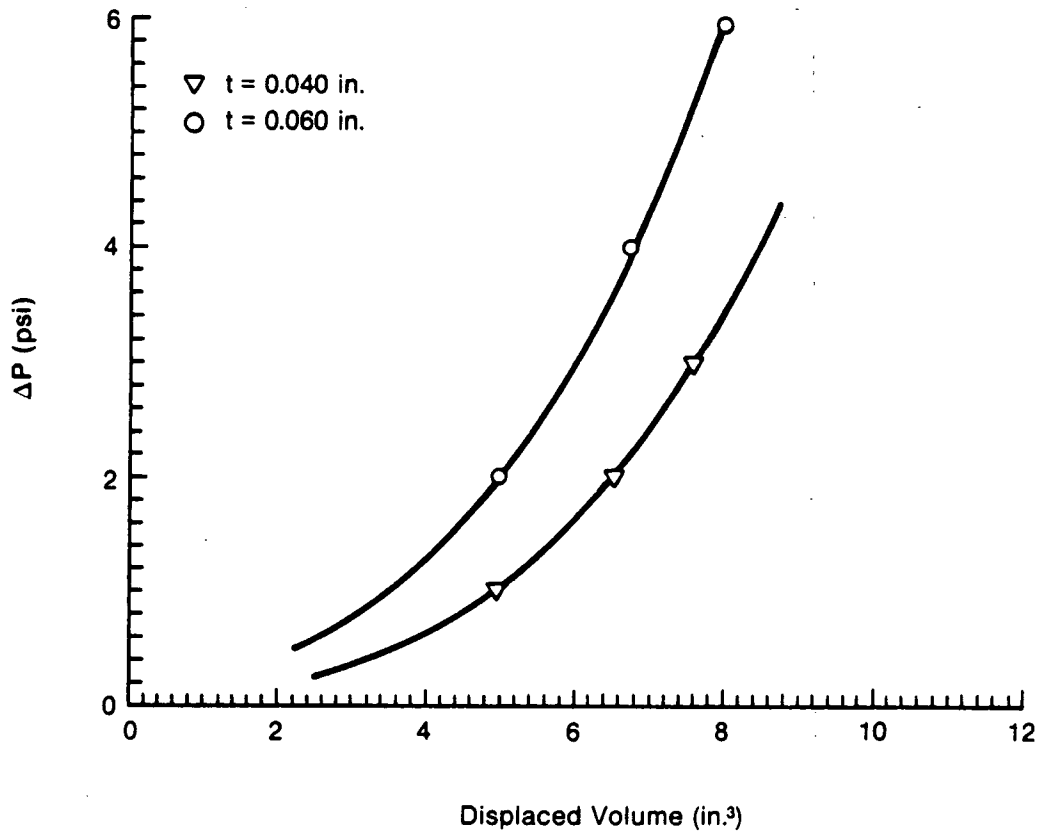

Fig. 2-52 NONLIN Code Results for Articulated Diaphragm (40 and 60 mil): ΔP versus Displaced Volume

87813

Table 2-18

Summary of Results

Improved Bendix Shape, Steel

At 40 ksi --> volume = 4.80 in.^{3}
ΔP at 4.80 in.^{3} = 13 psi

Zurn Convoluted Shape, t = 0.008 in.

At 40 ksi --> volume = 6.10 in.^{3}
ΔP at 6.10 in.^{3} = 1.43 psi

3-Ripple Convoluted, t = 0.008 in.

At 40 ksi --> volume = 6.90 in.^{3}
ΔP at 6.90 in.^{3} = 0.6 psi

3-Ripple Convoluted, amplitudes from 0.5 to 0.15 in.

Volume at 40 ksi decreases as depth of convolution increases

Articulated, OD = 10 in., ID = 6.25 in., t = 0.040 in.

at 40 ksi --> volume = 7.38 in.^{3}
ΔP at 7.38 in.^{3} = 2.75 psi

- An articulated diaphragm with centering spring offers large improvement over the Bendix style. Production cost may be higher due to O-ring grooves and more difficult mounting.

The recommendation is made to actively pursue a final design of the articulated diaphragm as an eventual replacement for the contoured steel diaphragm. This concept offers an attractive combination of high volume capability and good stiffness. If titanium is used instead of steel, the diaphragm working diameter could become 20% smaller than the current 10.0 in. Uncertainties exist concerning the behavior of pivot seals under large deflections and the relative cost of the articulated diaphragm, requiring precision grooves for the O-ring pivots as opposed to the contour machining required for a Bendix-style diaphragm.

If the articulated diaphragm is not pursued at this time, improvements should be made in the contour of the Bendix-style diaphragm.

2.5 Hydraulic Simulator Modifications Review

The hydraulic simulator is a piece of test apparatus (rig) developed at MTI early in the HAHP program to study the characteristics of the hydraulic transmission under simulated operating conditions (see Figure 2-53). This rig consists of a linear motor mounted between two diaphragms, with the space between the motor plunger and diaphragms filled with a hydraulic oil. The hydraulic oil, being incompressible, transmits the motor plunger motion to the diaphragm. Gas springs on the outer side of each diaphragm produce the resonant dynamics for the system. The purpose of the simulator was to determine the feasibility of hydraulically driving a compressor, as well as to evaluate power losses associated with this type of transmission. Test objectives of the rig were to:

- Demonstrate continuous, long-term operation of the system and diaphragms
- Evaluate the hydraulic transmission power losses (oil viscous loss, seal friction, and gas spring thermal hysteresis)

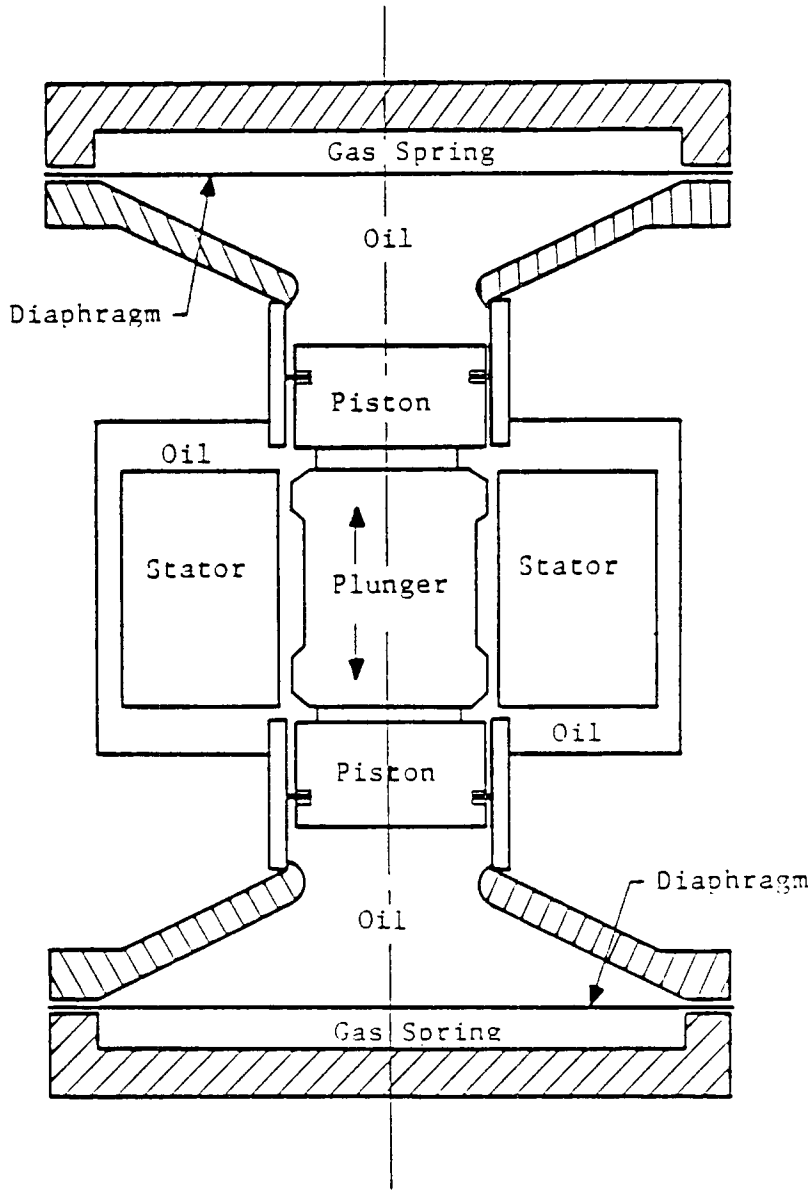

Fig. 2-53 Hydraulic Simulator Test Rig

813002

- Determine the refrigerant in oil solubility effects
- Develop and test an oil management system.

Each of the tests cited above were run successfully, and the results reported in the Phase I/IA Final Report.[6] The objective of this task was to review the hydraulic simulator to see if it could be upgraded to perform compressor testing up to the full 3.0 RT rating point. The limiting factor with the existing design is its limited power capabilities that prevent full capacity compressor tests.

A schematic of the hydraulic simulator driving the breadboard direct-drive compressor is shown in Figure 2-54. The simulator may be used as a driver by dynamically tuning the two masses (motor plunger and compressor piston) through the gas springs, and transmitting power from the motor to the compressor piston through the hydraulic oil. Power delivered to the compressor piston is then used to compress and pump the refrigerant in the compression cylinders. To successfully pump 3.0 RT of refrigerant at the 95°F ambient temperature conditions, however, requires that the hydraulic simulator must be capable of delivering the following total power:

$$P\ (\text{motor}) = PV\ (\text{compressor}) + Q\ (\text{loss, hydraulic transmission}) + Q\ (\text{loss, hydraulic simulator}) \qquad (2\text{-}49)$$

where:

PV (compressor) = measured PV power in compression cylinders, including isentropic PV power and inefficiencies in compression process.

Q (loss, hydraulic transmission) = total hydraulic transmission power loss, including the difference in power delivered to oil by linear motor and compressor PV power

---

[6] "Free-Piston Stirling Engine Diaphragm-Coupled Heat-Actuated Heat Pump Component Technology Program, Phase I/IA Final Report." ORNL/SUB/80-61618/1, Oak Ridge National Laboratory, June 1985.

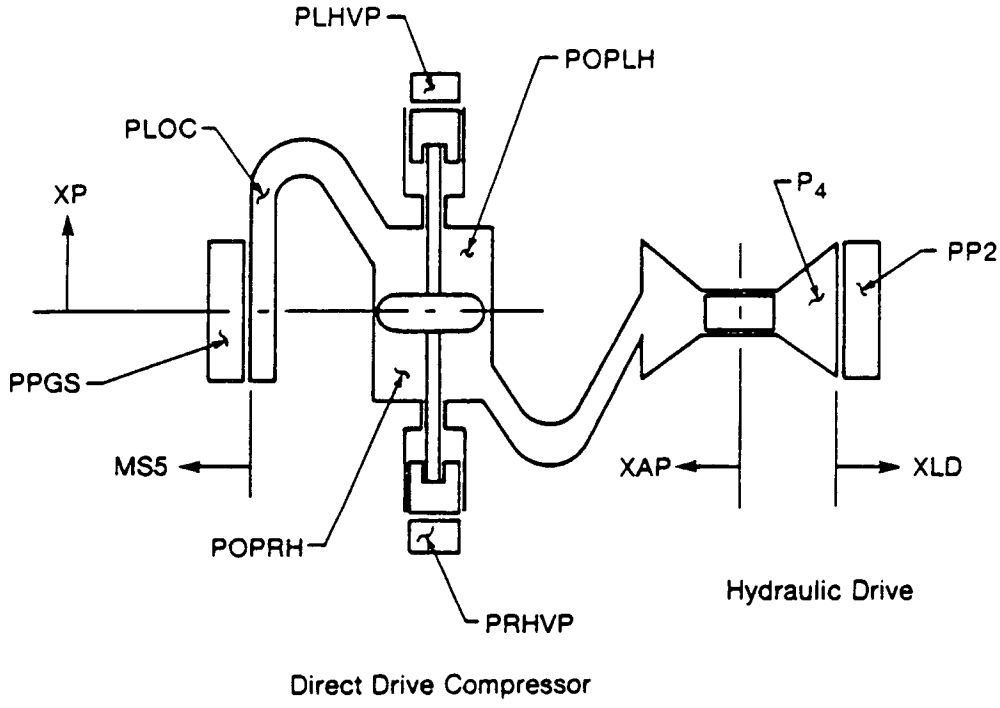

Fig. 2-54 Schematic for Hydraulic Simulator with Direct-Drive Compressor

87837

Q (loss, hydraulic simulator) = losses in hydraulic simulator associated with difference between power delivered to oil and input power to linear motor.

To determine the requirements for P (motor), a compressor was mounted on the hydraulic simulator and a test run with the compression cylinder sealed so that no refrigerant pumping occurred. In this manner, the compressor could be run up to 20-mm strokes without modifying the hydraulic simulator and the total losses of the system measured. Figure 2-55 presents these test results.

2.5.1 Hydraulic Simulator Power Requirements

The data presented in Figure 2-55 shows that for zero refrigerant flow, the compressor achieved its 3.0 RT design stroke of 19 mm with an electrical input power of 2091 W. Computing the compressor PV power for 3.0 RT, as shown in Section 2.3.1.1, for the 95°F ambient temperature conditions:

$$\text{PV (compressor)} = \tag{2-50}$$

$$\frac{580 \text{ lbm/hr } (1.173/0.173) \ (85.7 \text{ psia } (144 \text{ in.}^2/\text{ft}^2) \ (0.662 \text{ lbm/ft}^3)}{(778 \text{ lbf-ft/Btu}) \ (3.41 \text{ Btu/W-hr})}$$

$$\cdot \ (287/85.7)^{0.173/1.173} - 1$$

the compressor PV power is:

$$\text{PV (compressor)} = 2366 \text{ W.} \tag{2-51}$$

Also, considering a typical electrical efficiency of 70% for the linear motor, the equivalent electrical power is:

$$\text{Electric Power} = 2366/0.70 = 3380 \text{ W} \tag{2-52}$$

and the total motor power is:

$$\begin{aligned} \text{P (motor)} &= \text{electric power} + \text{Q (loss)} \\ &= (3380 + 2091) \text{ W} = 5471 \text{ W.} \end{aligned} \tag{2-53}$$

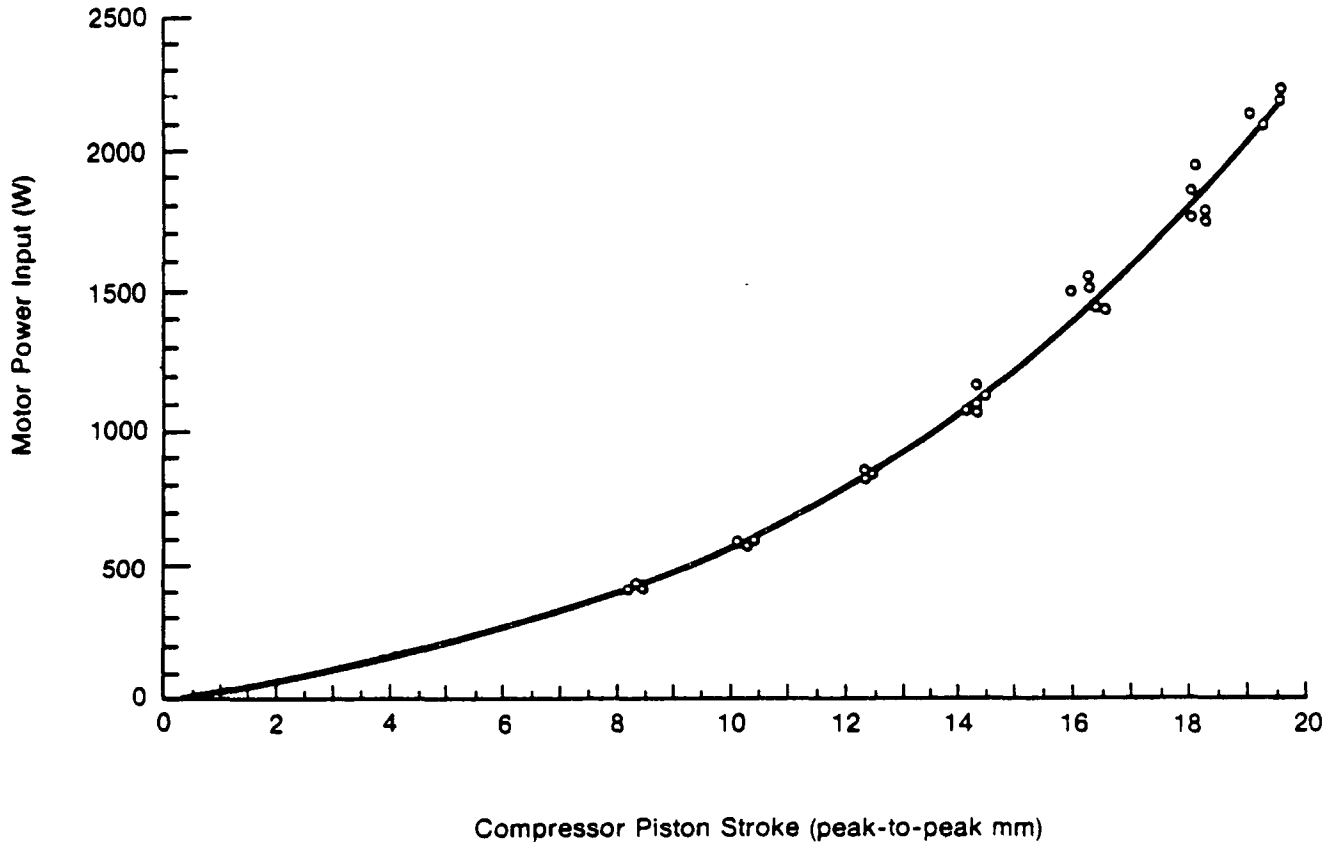

Fig. 2-55 Required Motor Input Power to Overcome Losses in Hydraulic Simulator and Transmission as a Function of Compressor Piston Stroke

87834

This is the required electrical input power to the linear motor to achieve the 3.0-RT capacity with the hydraulic simulator. The present hydraulic simulator limitation is that the linear motor is only capable of delivering 2,500 W continuously and safely. The following sections discuss the alternatives available to upgrade the hydraulic simulator to produce the required 5,471 W.

2.5.2 Hydraulic Simulator Modifications

The options available to upgrade the hydraulic simulator are as follows.

- Option 1 - overpower existing linear motor
  - 40 amp at 230 V (10 kva) variac
  - 40 amp at 440 V power drop to cell No. 4
  - New electrical drive components
  - Motor cooling

  The disadvantage is that it could burn up linear motor.

- Option 2 - Build new, larger linear motor. This requires
  - New linear motor
  - 40 amp at 440 V power drop to cell No. 4
  - Modifications to the hydraulic simulator

  The disadvantage is that it requires building a new motor.

- Option 3 - Add second linear motor. This requires
  - 40 amp at 440 V power drop to cell No. 4
  - Modifications to the hydraulic simulator

  The disadvantage here is that the motor plunger mass doubles.

A cost and technical evaluation was made for each of these options, and a recommendation for upgrading the hydraulic simulator is presented in the following sections.

2.5.2.1 Option 1 - Overpower Existing Linear Motor. The existing hydraulic simulator motor is shown in Figure 2-56. The motor consists of a stationary iron stator that houses two ac coils, one dc coil, and a moving laminated iron

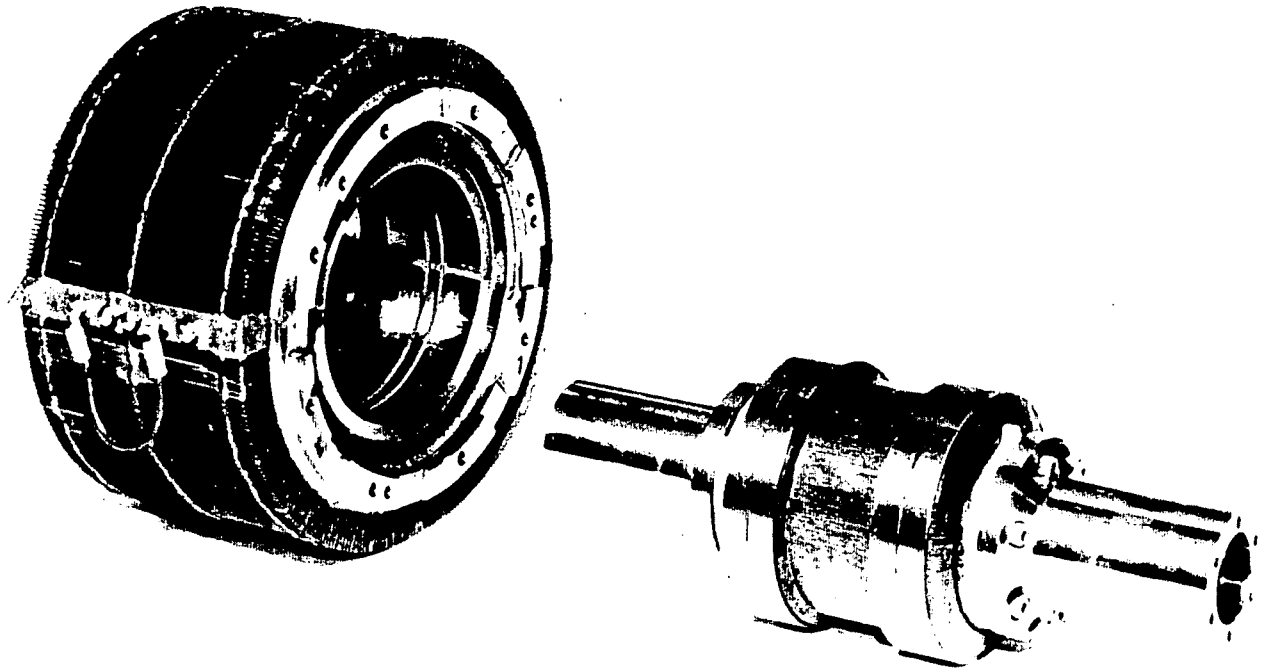

Fig. 2-56 Laminated Stator and Plunger

plunger. The motor may be described as a doubly excited motor in which the dc coil sets up the field in the iron and the ac coils provide the driving force. The mounting of the motor in the hydraulic simulator is shown in Figure 2-57.

The specifications for the motor are:

- Maximum ac input power (facility power): 120 V, 20 amp
- Resistance (all coils in series): 0.44 ohm
- Plunger weight: 16.8 lb.

Option 1 was to raise the motor input voltage by increasing the power drop into the test cell to 440 V and 40 amp, and then, through the use of a 7 kva variac, drive the motor to higher power levels by increasing the current. The advantage to this approach is that no hardware modifications to either the motor or hydraulic simulator would have to be made. The major disadvantage is that at the higher currents, the motor efficiency is reduced, and the increased losses will require some active cooling to prevent the motor from burning up. The effect on motor performance of taking this approach may be seen by considering the force relationship for a linear motor. Linear motor theory states that the electromagnetic driving force produced by the motor is proportional to the current:

$$F_{em} \propto I_m(t) \tag{2-54}$$

Also, noting that the power delivered to the motor plunger is the dot product of the electromagnetic driving force and plunger velocity:

$$PV\ (\text{plunger}) = F_{em} \cdot \dot{X}_p \tag{2-55}$$

where:

$\dot{X}_p$ = motor plunger velocity.

Combining these two equations leads to the expression for the current in an overpowered motor:

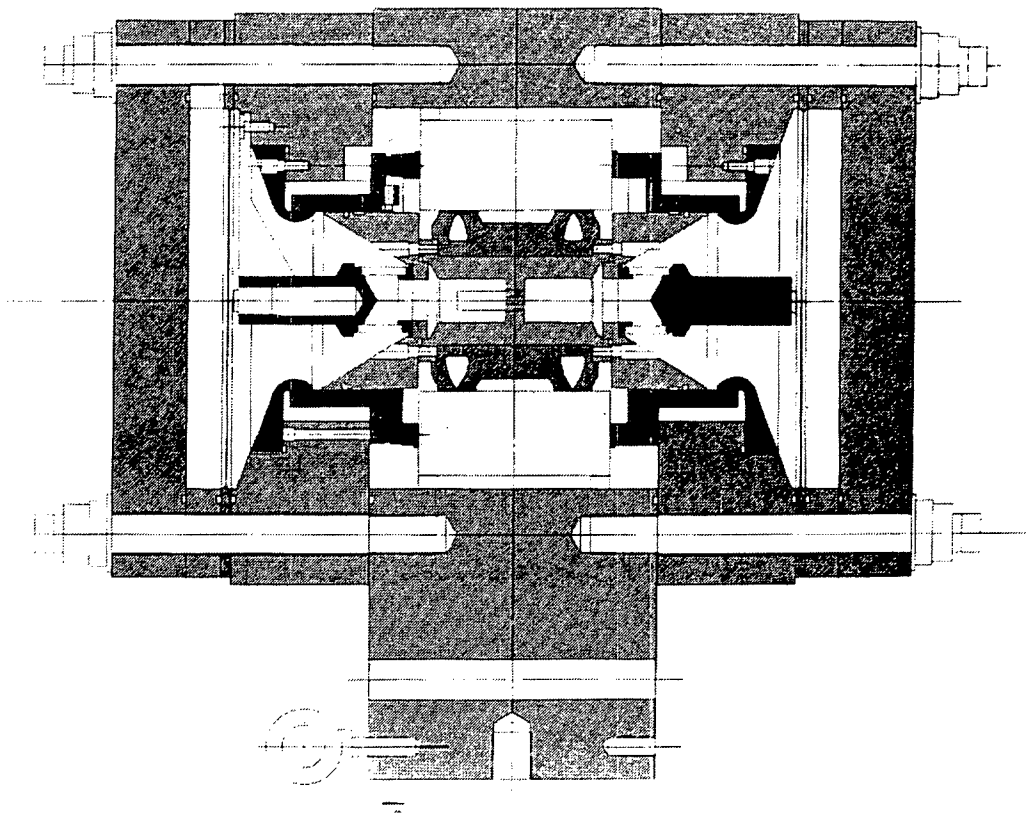

BS-18188

Fig. 2-57 Hydraulic Simulator Layout

$$\frac{[PV\ (plunger)]_{overpowered}}{[PV\ (plunger)]_{normal}} = \frac{[I_m(t) \cdot \dot{X}_p]_{overpowered}}{[I_m(t) \cdot \dot{X}_p]_{normal}} \tag{2-56}$$

Taking an actual data point for the hydraulic simulator plunger power when no refrigerant pumping occurs (as given in Table 2-19) and the compressor PV power as described above, the current for the case when the compressor is pumping 3.0 RT is then:

$$PV\ (compressor) = 2{,}366\ W$$

$$\frac{(2{,}366\ W + 2{,}034\ W)}{2{,}034\ W} \qquad \frac{19.7\ mm}{19.0\ mm} = \frac{[I_m(t)]_{overpowered}}{18.6\ amp} \tag{2-57}$$

$$[I_m(t)]_{overpowered} = 41.4\ amp$$

Thus, the increased power requirement on the motor has raised the current from 18.6 to 41.4 amp. In addition, the rise in coil temperature due to the increased current will raise the coil resistance, further magnifying the I^2R losses in the coil. For copper with a temperature coefficient of resistivity of 0.00393 per °C at 20°C, the increase in coil resistance based on the maximum safe operating temperature limit of 120°C for the MTI linear motor is:

$$R_{120°C} = 0.44\ ohm\ (1 + 0.00393\ 1/°C\ (100°C)) \tag{2-58}$$

$$= 0.61\ ohm$$

and the I^2R loss is:

$$I^2R = (41.4\ amp)^2\ (0.61\ ohm) = 1046\ W. \tag{2-59}$$

Thus, the I^2R loss has increased from 152 to 1046 W. It is this increase in the coil power loss that represents the risk of this approach and establishes the need for some direct motor cooling for this modification to be successful.

Table 2-19

Hydraulic Simulator Test Data
(No Refrigerant Pumping; 8 January 1985; Scan No. 33)

Piston Stroke, mm	19.7
Input Power, W	2,186
Input Current, W	18.6
I^2R Loss, W	152
Simulator Plus Transmission Power Loss, W	2,034

2.5.2.2 Option 2 - Build New, Larger Linear Motor. A second option to increase the power of the hydraulic simulator is to design and fabricate a larger linear motor. The advantages of this approach would be:

- By specifically designing the motor for this application, MTI could select the motor stroke to optimize the hydraulic transmission efficiency and optimize the motor performance for this application.
- The motor could be designed for 220-V operation, which would eliminate the need for costly test cell electrical modifications.
- By employing a permanent magnet motor instead of the Elcon dc coil type motor shown in Figure 2-56, a lightweight plunger could be designed that would reduce the hydraulic transmission's gas spring and hydraulic leakage losses.

Linear motors can be separated into two broad classes: single excited and double excited. The primary example of a single-excited motor is a solenoid. In a solenoid motor, there is only one coil which is excited with a time-varying current. In the double-excited motor, there are two sources of magnetic field excitation. One source sets up a magnetic field in the magnetic circuit of the motor, and the second source is from a coil that is excited with a time-varying current.

The new motor proposed here is a double-excited motor employing permanent magnets on the moving member to provide the magnetic field in the motor circuit and one or more coils in the stationary member to provide the time-varying field. This double-excited design was chosen because of the high power density achieved.

Figure 2-58 is a cross section of the stator and plunger geometry of the selected motor design. The plunger consists of magnet segments that are magnetized radially and mounted in rings on the outside surface of a cylindrical magnetic core. This core acts as a magnetic path of low reluctance between adjacent magnets. The core is actually constructed of axially oriented laminations to minimize eddy-current losses. In this construction, the alternate magnet rings are magnetized with opposite polarities. The first and last magnet rings are half as long in the axial direction as the interior

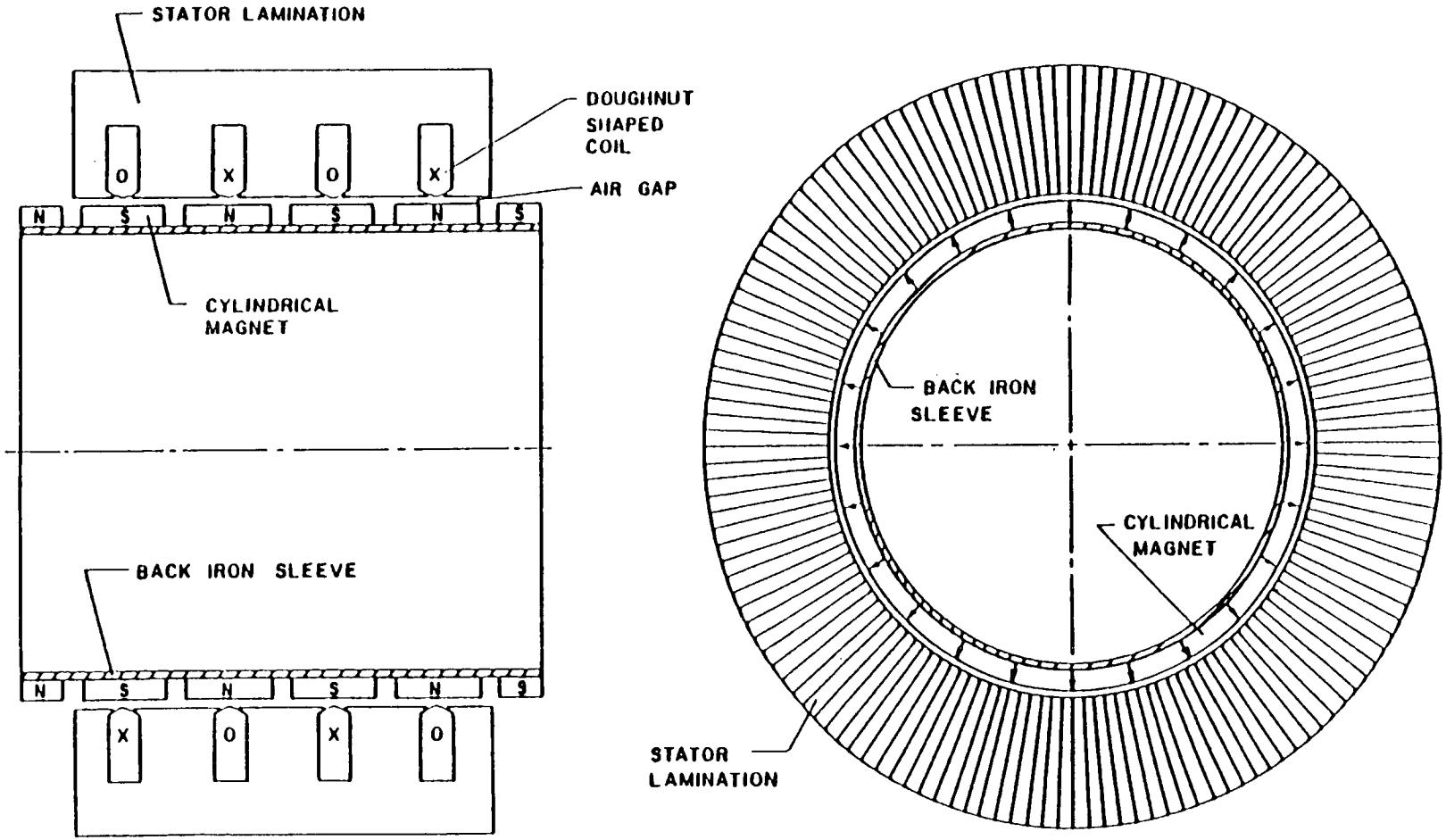

Fig. 2-58 Cross-Section Schematic of Moving-Magnet, Moving-Back-Iron Linear Motor

832858

magnet rings. Adjacent magnet rings are separated by a small distance from each other by nonmagnetic spacers.

The motor stator is made up of laminations which are radially stacked around (concentric with) the plunger. These laminations run lengthwise and contain four slots in which the ac power coils are wound. The coils are also concentric with the plunger. The physical hardware for a permanent magnet motor is shown in Figure 2-59.

2.5.2.3 Option 3: Add Second Linear Motor. The approach of adding a second linear motor to the hydraulic simulator was made after reviewing the simulator drawings to determine if a second motor could be mounted and checking the MTI inventory to see if a second motor was available. Both of these conditions were met, and it was established that adding a second motor was a viable approach provided the system would operate successfully. The technical considerations were:

- Will the added mass of the second plunger alter the resonant dynamics of the system?
- Will the added mass of the second plunger significantly increase the gas spring hysteresis and seal leakage loss?
- Will the increased losses raise the motor temperature and introduce an unacceptable risk?

The total plunger weight (motor plunger plus oil pistons) for the single motor is 22.5 lb. By adding the second plunger, the total plunger weight would be increased to approximately 40 lb.

$$W\ (\text{plunger}) = (22.5 + 16.8)\ \text{lb} = 39.3\ \text{lb}. \qquad (2\text{-}60)$$

The total dynamic weight is:

$$W\ (\text{dynamic}) = W\ (\text{plunger}) + W\ (\text{compressor}) + W\ (\text{oil}) \qquad (2\text{-}61)$$

$$W\ (\text{dynamic}) = (39.3 + 9.0 + 40\ \text{lb}) = 88.3\ \text{lb}.$$

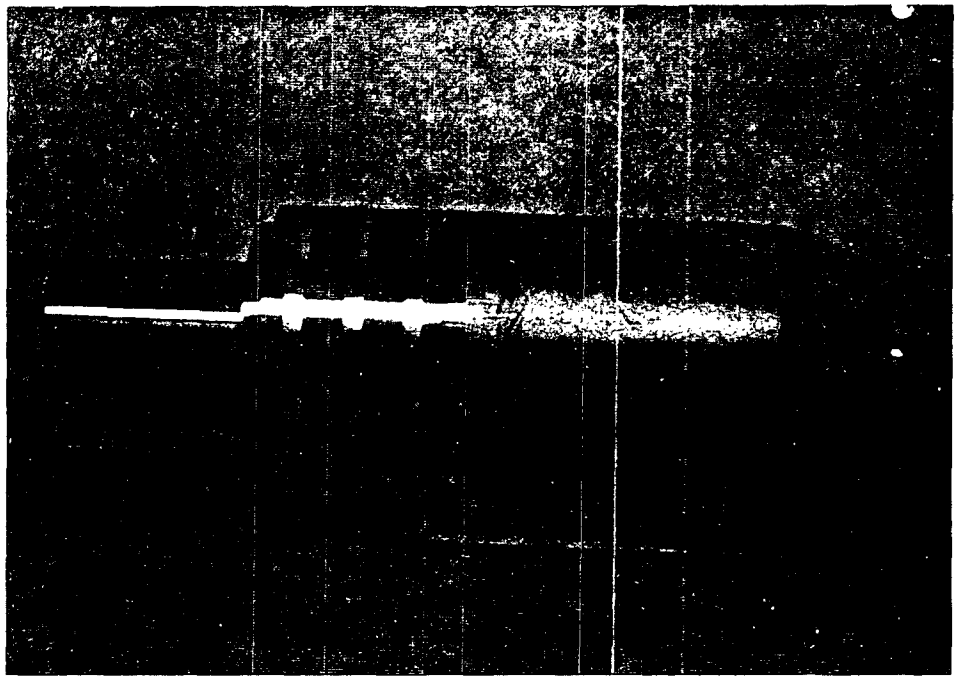

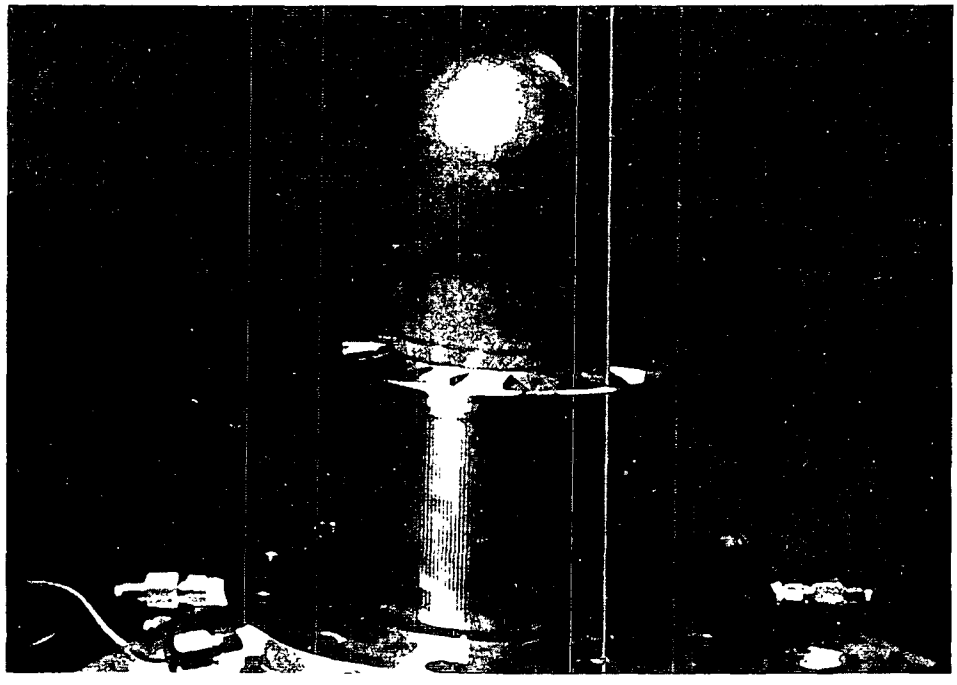

Fig. 2-59 MTI FPSE Engineering Model Linear Motor Displacer Drive System Hardware

In a resonant system, the added mass results in a larger pressure amplitude and, therefore, the associated losses are:

- The gas spring hysteresis loss
- Seal leakage loss.

The pressure amplitude is given by:

$$\Delta P = K/2.0\ (X_p/A_p) \tag{2-62}$$

where:

$K = (2\pi f)^2 (W/g_c)$
W = dynamic weight
X_p = motor plunger stroke amplitude (in.)
A_p = oil piston frontal area (in.^{2})
f = operating frequency (Hz)
g_c = gravitational constant (386 in./sec^2).

Considering the data from Scan 33 recorded on 8 January 1985, where

Compressor Piston Stroke = 19.74 mm
f = 60 Hz
X_p = 5.7 mm = 0.22 in.
A_p = 15.90 in.^{2}

the spring constant is:

$$K = [(2\pi 60(\text{Hz}))^2\ (88.3)\text{lb}]\ /\ 386\ \text{in./sec}^2 = 32{,}511\ \text{lb/in.} \tag{2-63}$$

and the pressure amplitude is:

$$\Delta P = (32{,}511\ \text{lb/in.}\ /\ 2.0)\ (0.22\ \text{in.}\ /\ 15.90\ \text{in.}^2) = 225\ \text{psi} = 15\ \text{bar} \tag{2-64}$$

A comparison of the pressure amplitude and losses caused by the additional weight is shown in Table 2-20. The losses were computed from the following.

Table 2-20

Comparison of Calculated Losses of
Single- and Double-Motor Installations

Parameter	Single-Motor Design	Two-Motor Design
Dynamic Weight, lbm	71.5	88.3
Spring Constant, lbf/in.	26,326	32,511
Pressure Amplitude, bar	12	15
Gas Spring Thermal Loss, W	423	660
Seal Leakage Loss, W	131	205
Hydraulic Transmission Loss, W (less gas spring and seal leakage loss)	1,480	1,480
PV (compressor), W	2,366	2,366
Total Shaft Power, W	4,400	4,711
Current, amp	41.4	22.2
Resistance, ohm	0.61	1.06
I^2R Loss, W	1,046	522.8
Motor Input Power, W	5,446	5,233.8

Gas Spring Power (Thermal) Loss. For the hydraulic simulator, the diaphragm forms a sealed gas spring of fixed surface area. Therefore, the only gas spring loss is the thermal hysteresis loss, which may be found from the MTI-developed equation that is correlated to experimental results through the correlation factor, K,

$$WGS_1 \text{ (hysteresis)} = K/2 \sqrt{\pi k P_m T_m f}\ [(\gamma-1) / \gamma)]^{3/2}\ A_w P_o / P_m^2 \text{ [watts]} \quad (2\text{-}65)$$

where:

k = thermal conductivity of gas
P_m = mean gas pressure
T_m = mean gas temperature
f = frequency
γ = adiabatic gas constant
A_w = gas spring surface area
P_o = pressure amplitude of gas spring
K = experimental correlation factor (1.5).

Gas Spring Power (Seal Leakage) Loss. The seal leakage loss results from the pumping of oil through the clearance gaps on the compressor drive piston and the rings on the hydraulic oil pistons attached to the motor plunger (Figure 2-53) due to the pressure difference across these seals. The root mean square (rms) expression for this loss is:

$$WGS_2 \text{ (seal leakage)} = (\pi g_c / 16\mu)(Dh^3/L)\ \Delta P_o\ (1 + 1.5\varepsilon)^2 \text{ [watts]} \quad (2\text{-}66)$$

where:

g_c = gravitational constant
μ = viscosity of the hydraulic fluid
D = diameter of seal
L = seal length
h = seal clearance gap
ΔP_o = maximum pressure difference across seal
ε = eccentricity ratio of gap.

Motor Electrical Resistance Loss. The electrical circuit for the two-motor drive is shown in Figure 2-60. The circuit differs from the single-motor circuit in that the two motors are series connected, with each motor supplying one-half the driving force.

Therefore:

$$(I^2R)_d = (I^2R)_s/2 \tag{2-67}$$

where the subscripts d and s refer to the double- and single-motor cases. Comparing the power requirements for these two cases as shown in Table 2-20, we see that the motor shaft power has increased slightly for the double-motor case due to the added gas spring and leakage loss, but that the input current is very nearly one-half of the single motor. This would significantly reduce the risk of burning up the motor. However, the losses are within 93% of one another, indicating that both systems would need an oil cooler to prevent excessively high temperatures.

2.5.3 Weighted Assessment of Three Options

Table 2-21 presents a weighted assessment of the three options. Because of the reduced facility requirements and need for motor cooling with the permanent magnet motor, option 2, it becomes the most favorable approach. The rating was performed by assigning a "2" to those items requiring the greatest rework or risk and a "0" for those items requiring no rework. A "1" represents the case where some modification is required -- the amount being minimal. The highest or least preferred score would be a "12".

The single-motor modification represents the least attractive approach to increasing the hydraulic simulator power because of the increased electrical power requirements, the inefficiency of the motor at the high power levels, and the risk associated with burning out the motor. This risk exists even with the addition of motor cooling, which is required to operate the motor at these high power levels.

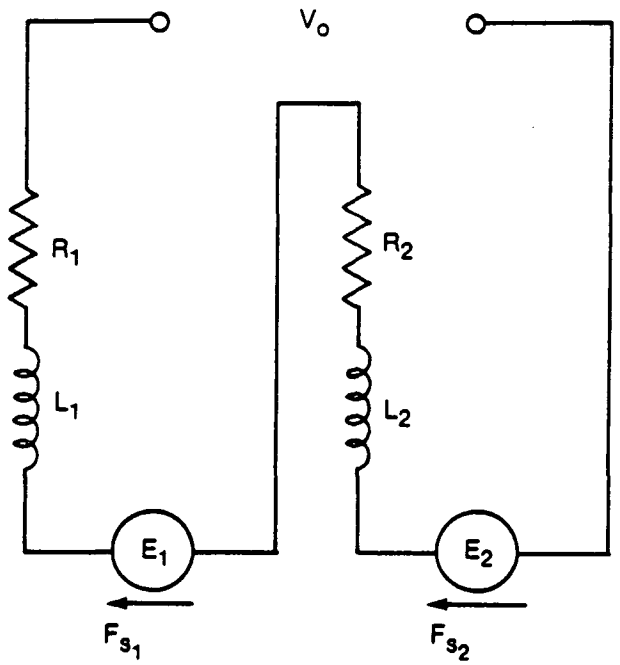

Fig. 2-60 Two-Motor Electrical Circuit

87835

Table 2-21

Weighted Assessment of Hydraulic Simulator Modifications

	Single-Motor Modification	New Motor Modification	Two-Motor Modification
Motor Cost	0	2	0
Hardware Modification Cost	0	1	2
Facilities Cost	2	0	1
Motor Cooling	2	0	0
Hydraulic Oil Cooling	2	1	2
Risk	2	0	1
Total	8	4	6

The two-motor modification requires the greatest change to the hardware in order to mount the second motor. Also, the additional plunger weight of the second motor increases the hydraulic losses, requiring the addition of an oil cooling system.

The major factor influencing the new motor modification is the cost of designing and fabricating a new motor. Some of this cost, however, will be offset by the reduction in facility and hardware modification costs.

SECTION 3.0

PHASE IIB TECHNICAL DISCUSSION

3.0 PHASE IIB TECHNICAL DISCUSSION

3.1 Results of Mark I Heat Pump Module Testing at Lennox

3.1.1 Summary of Test Results

Testing of the Mark I heat pump module was performed at Lennox during the period of 1 April 1987 through 29 May 1987. The testing had two major objectives:

1. To verify the reported performance of the Mark I over a range of ambient conditions from 0 to 95°F

2. To map the performance of the heat pump module over a broad range of evaporator and condenser conditions and compressor piston stroke.

The Mark I heat pump module performed very well at Lennox. The module accumulated over 140 hr of operating time during the test period and provided performance data at 72 test points ranging from evaporator and condenser conditions equivalent to ambient temperature conditions from 0 to 105°F. The heating and cooling performance obtained was:

Capacity	Performance
Heating, 47°F = 60,000 Btu/hr	Heating, 47°F = 1.61
Cooling, 95°F = 3.2 RT	Cooling, 95°F = 0.92

The testing was performed at the Lennox engineering facility in Carrollton, Texas, using their digitally controlled refrigerant calorimeter. Two limitations were imposed on the testing due to the warm ambient temperature conditions in Texas during the test period and the size of the calorimeter (5 RT). First, the warm ambient temperatures limited the condenser saturation temperatures to above 80°F; the two 80°F tests run were achieved by running the tests at 4:00 A.M. to get sufficient condenser cooling. The second limitation encountered was due to the size of the calorimeter and coolant instabilities that occurred due to low refrigerant flows. These two effects limited testing

to saturated evaporator temperatures above -12°F and condenser saturated temperatures to above 80°F.

The following sections summarize the test plan (Section 3.1.2), describe the Lennox test facilities (Section 3.1.3), and discuss the test results (Section 3.1.4). The results of the advanced compressor design task are described in Section 3.2.

3.1.2 Test Plan

The MTI test matrix is divided into six sections -- four sections for performance tests and two sections for other tests. Brief descriptions of each test section are presented below.

Verification Testing. This test section is a data point for which a large volume of data on both Mark I engines exists. This test point is a 2-1/2 RT capacity, 95°F day point (Table 3-1). It was chosen to allow periodic verification that engine and compressor performance was not changing significantly during the test program. This test point was run 12 times during the 8 weeks of testing at Lennox.

Cooling Qualification Testing. This test section consists of an American Refrigeration Institute (ARI) cooling rating point, a 95°F point, an 87°F point, and an 80°F test point. Where the operating limits of the system and facility allowed, multiple compressor piston strokes were evaluated.

Heating Qualification Testing. This test section consists of an ARI heating point, a 32°F point, a 17°F point, and a 0° test point. Where system and facility operating limits allowed, multiple compressor piston strokes were tested.

Parametric Testing. This test section consists of a data matrix established by condenser and evaporator conditions. Data points included condenser temperatures of 80, 90, 100, 120, and 130°F and evaporator temperatures of -20, 0,

10, 20, 25, 35, and 50°F. Again, system and facility limitations determined which test points in the matrix could be accomplished and which test points had to be accomplished at alternate compressor piston strokes.

The test points were all accomplished at steady-state conditions only after the system and calorimeter had stabilized. The data acquisition system for the calorimeter takes 4 data points at 10-min intervals. The MTI data acquisition system takes 12 to 14 data points at 3-min intervals. Both data acquisition systems present the data for all data scans as well as an average for all scans taken.

Three test points (verification, 95°F, and 17°F) were run at three different coolant inlet temperatures of 34, 70, and 104°F.

The matrix of test points covered by the test plan is presented in Table 3-1. For a more detailed description of the test plan, refer to Volume II, Appendix A, "Test Plan: Lennox Industries Evaluation of a Free-Piston Stirling Engine Heat Pump," MTI 87TR20.

Variable Cooler Temperature. The variable cooler temperature tests were run to evaluate the effect of cooler temperature on heat pump performance. Tests were conducted at the verification point ("V," point No. 1), the 95°F ambient point (point No. 3), and the 17°F ambient point (point No. 9). At each point, performance was measured at the three cooler inlet temperatures of 34, 70, and 104°F.

Oil Leakage Evaluation. Oil leakage from the hydraulic transmission was evaluated by running the unit at the verification point over an 8-hr period and measuring the oil lost from the transmission. The hydraulic transmission relies on two chevron seals on the compressor piston shafts to seal the high-pressure oil in the transmission. Oil lost from the transmission must be resupplied from a low-pressure reservoir by the oil management system (the oil management system and chevron seals are discussed in Section 2.3.3). To evaluate the oil leakage, the unit was run at the verification point over a 8-hr period, and the oil that leaked past the chevron seals was collected and recorded over that period.

Table 3-1

Planned Test Matrix

Test Cond No.	Discharge Pressure, psig	Suction Pressure, psig	Liq. Temp. @ Flowrator, °F	Suction Temp., °F	No. of Compressor Strokes	Comments
Verification Testing						
1	261.0	75.6	106.0	51.2	1	See notes 1 through 6
Qualification Testing - Cooling						
2	296.8	76.0	115.0	65.0	2	ARI rating point
3	262.7	76.0	106.0	55.0	2	95° OD point
4	210.8	80.0	90.0	60.0	3	87° OD point
5	181.8	84.0	80.0	65.0	4	80° OD point
Qualification Testing - Heating						
6	226.3	54.9	95.0	50.0	4	ARI rating point
7	195.9	61.5	85.0	45.0	4	47° OD point
8	187.4	43.0	82.0	30.0	3	32° OD point
9	181.8	28.2	80.0	15.0	2	17° OD point
10	168.4	15.1	75.0	-2.0	1	0° OD point
Parametric Testing						
11	143.6	10.1	70.0	0.0	3	80° cond/-20° suct
12	143.6	24.0	70.0	20.0	3	80° cond/0° suct
13	143.6	43.0	70.0	40.0	3	80° cond/20° suct
14	168.4	10.1	80.0	0.0	3	90° cond/-20° suct
15	168.4	24.0	80.0	20.0	3	90° cond/0° suct
16	168.4	43.0	80.0	40.0	3	90° cond/20° suct
17	195.9	24.0	90.0	20.0	3	100° cond/0° suct
18	195.9	61.5	90.0	55.0	3	100° cond/35° suct
19	195.9	84.0	90.0	70.0	3	100° cond/50° suct
20	259.9	43.0	105.0	40.0	3	120° cond/20° suct
21	259.9	61.5	105.0	55.0	3	120° cond/35° suct
22	259.9	84.0	105.0	70.0	3	120° cond/50° suct
23	296.8	43.0	115.0	40.0	3	130° cond/20° suct
24	296.8	61.5	115.0	55.0	3	130° cond/35° suct
25	296.8	84.0	115.0	70.0	3	130° cond/50° suct

Notes

1. Each test condition should be at steady state in which none of the performance parameters differ from scan to scan by more than 3%. There should be atleast 3 scans per test condition at 10-min intervals.
2. The engine coolant loop (water chiller rig) should be maintained at 2.5 gpm for all test conditions.
3. The engine coolant inlet temperature should be 34°F for verification testing and all other test conditions. All qualification and parametric testing should be repeated for 70°F inlet temperature. Qualification test conditions 3 and 9 should be performed at an additional cooling water inlet temperature of 104°F.
4. No oil should be returned to the suction line and provisions to capture and measure oil circulation (as % of refrigerant flow) will be performed at qualification test conditions 3 and 9.
5. The compressor stroke (capacity) and the engine operating parameters should be controlled by personnel at the MTI operator's console. The compressor stroke will vary from 50% to full stroke.
6. There is a total of 144 test points, excluding verification testing, which will be repeated from day to day depending on the repeatability of these data with the data recorded at MTI.

3.1.3 Description of Lennox Test Facility

The Mark I system package was installed in the Lennox test facility as shown in Figure 3-1. This facility consists of an environmentally controlled room called the rain room, a controllable cooling water source referred to as the chiller, and a compressor calorimeter.

The rain room is temperature controlled by two 5-ton refrigeration systems and up to 25 kW of electric heating. For MTI testing, the room was maintained at approximately 70°F.

The chiller is a cooling water loop consisting of a two-speed refrigeration compressor rated at 3- and 5-ton capacity, an electric heating system with triac control, a coolant pump, and instrumentation to measure water flow and temperature. The coolant was water; the test set temperatures were 34, 70, and 104°F. Coolant flow rate was established at approximately 3 gpm.

The calorimeter employs the following main components as shown in Figure 3-2:

- Evaporator - adds heat to the liquid refrigerant to maintain the desired evaporating pressure per the test plan.

- Superheater - adds more heat to bring the vapor to the superheated conditions specified in the test plan.

- Condenser - removes heat from the vaporized refrigerant to maintain the desired compressor discharge pressure per the test plan.

- Mass Flowmeter (micromotion liquid flowmeter) - measures the liquid refrigerant flow as it leaves the condenser.

- Expansion Valve - reduces the refrigerant pressure at the entrance to the evaporator. The expansion valve also controls the liquid refrigerant temperature by varying its residence time in the condenser.

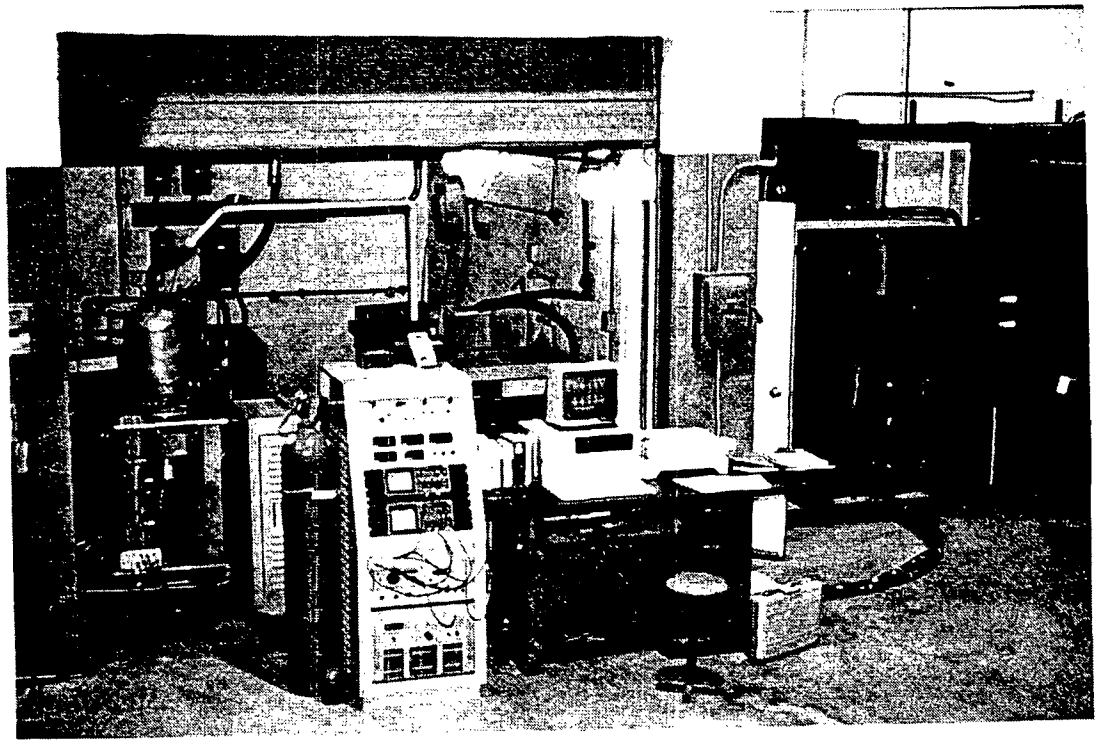

Fig. 3-1 Mark I System Package Installed in Lennox Test Facility

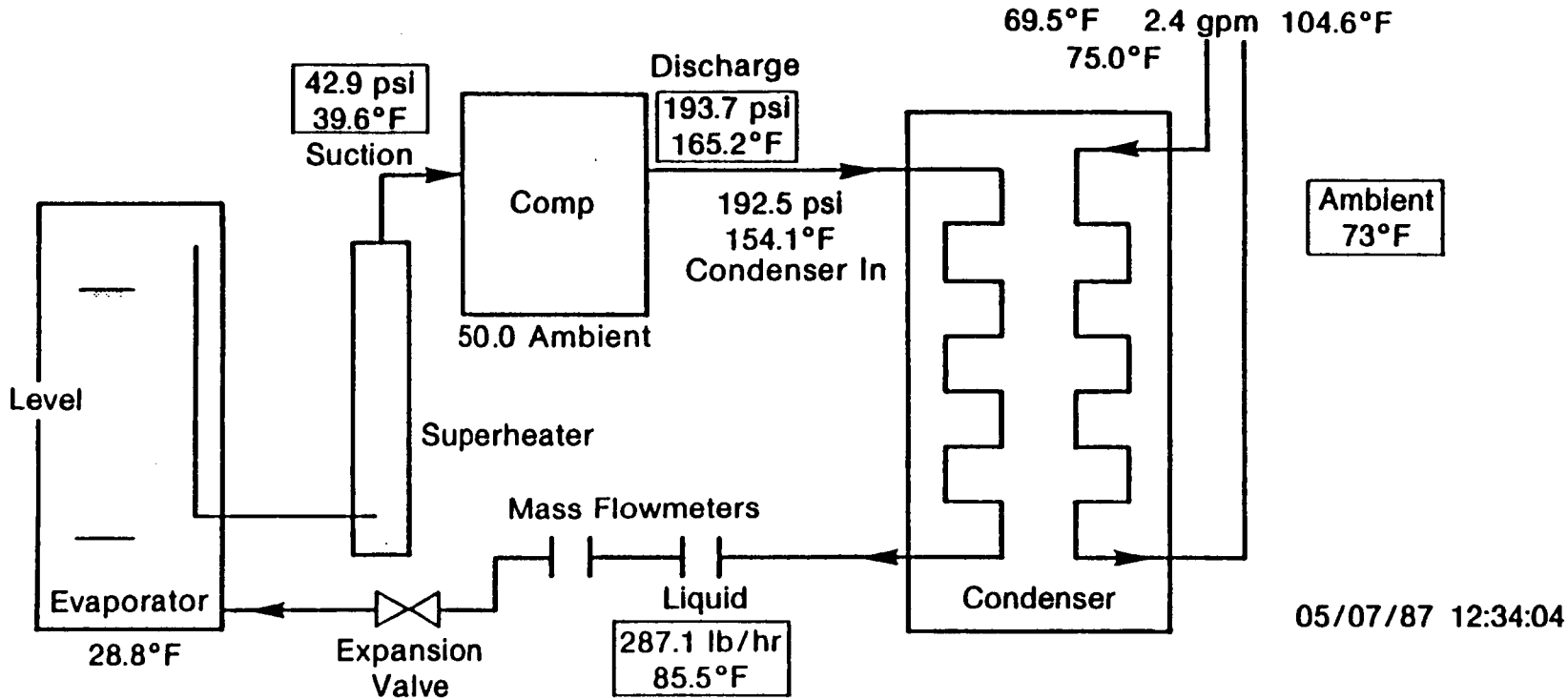

Evap / Cond	19182 / 24343		
ETR / Adj Cal	0 / 19747	95.1%	
FM Cap / Corr FM	20699 / 20757	100.2%	
Vapor Enthalpy =	109.66	AE = 154.24%	

DSCH-P	DSCH-T	LIQ-T	SUC-P	SUC-T	PRESS	TEMP	LIQ
195.9	0.0	85.0	43.0	40.0	43.0	40.0	85.0

Fig. 3-2 Lennox Calorimeter Test Loop

871902-1

Pressures and temperatures are measured at the inlet and outlet of all the major components. Enthalpies are calculated for conditions at the evaporator inlet, superheater outlet, and condenser inlet.

Capacities are calculated by the following methods:

1. Enthalpy change of the refrigerant between the liquid entering the expansion valve and the superheated vapor at the superheater outlet times the mass flow rate.

2. The heat equivalent of the energy supplied to the electric heaters in the evaporator and superheater is the source of heat to the evaporator. This measured amount should balance with No. 1 above.

3. The cooling water flow through the condenser and the ΔT across the condenser yield a balance with No. 1 and No. 2 above.

4. MTI installed an additional liquid Freon flowmeter upstream of the Lennox flowmeter. MTI also monitored conditions at the compressor inlet, compressor outlet, and at the Freon flowmeter. Using these measurements, capacities were calculated from Freon flowmeter to compressor inlet (evaporator) and compressor outlet (condenser).

The consistency and repeatability of these various energy measurements were used to verify the accuracy and quality of the data.

3.1.4 Test Results

At the completion of the testing, 140 hr were accumulated on the Mark I, and the following results were achieved.

3.1.4.1 Verification Testing. The verification test point was run and recorded on numerous occasions over the 64-day test period to check for repeatability and possible degradation in performance. As shown in Figure 3-3, the heat

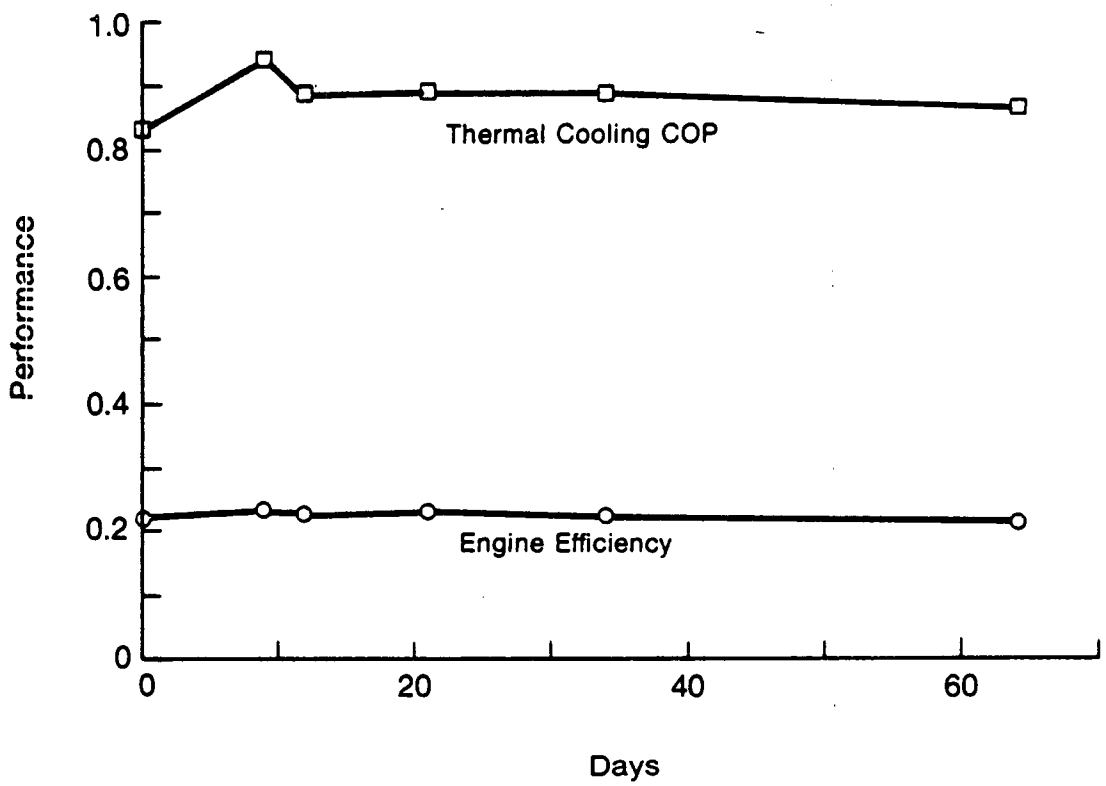

Fig. 3-3 Verification Test Data COP

pump's performance remained relatively constant, and no distinguishable degradation occurred. The repeatability of the verification data over this period has provided a high confidence in its quality and accuracy.

3.1.4.2 Qualification Testing. All of the ambient temperature conditions given in Table 3-1 were completed. The results of these tests are presented in Figures 3-4 and 3-5. Figure 3-4 gives the maximum and minimum capacity range measured, and Figure 3-5 presents both the gross and net COPs for the heat pump module. The electric parasitics used for net COP are also presented in Figure 3-5.

An important aspect of the qualification testing was the validation of the MTI data with the Lennox data. The good agreement between the results obtained at MTI and Lennox, as shown in Figure 3-6, provides this validation.

3.1.4.3 Performance Mapping. The objective of the performance mapping was to develop a family of operating curves for the Mark I over a wide range of evaporator and condenser conditions. From this data, the intent is to develop the computer algorithms needed to perform economic analyses of the heat pump system. The proposed matrix of test points for this testing is given in Table 3-2. Because of several limitations encountered in the testing, not all of the intended points were achieved. These limitations included:

- The warm ambient temperatures in Dallas during April and May prevented most of the 80°F condensing temperatures from being achieved. Two 80°F runs were made by running the tests at 4:00 A.M. to take advantage of the cooler morning ambient temperature.

- The low refrigerant mass flow rate at 0 and -20°F evaporator temperatures prevented stable calorimeter operation. This stability problem also prevented several of the short compressor strokes from being run.

- The high engine PV power at the 130/50 conditions limited the compressor stroke due to high displacer motor current.

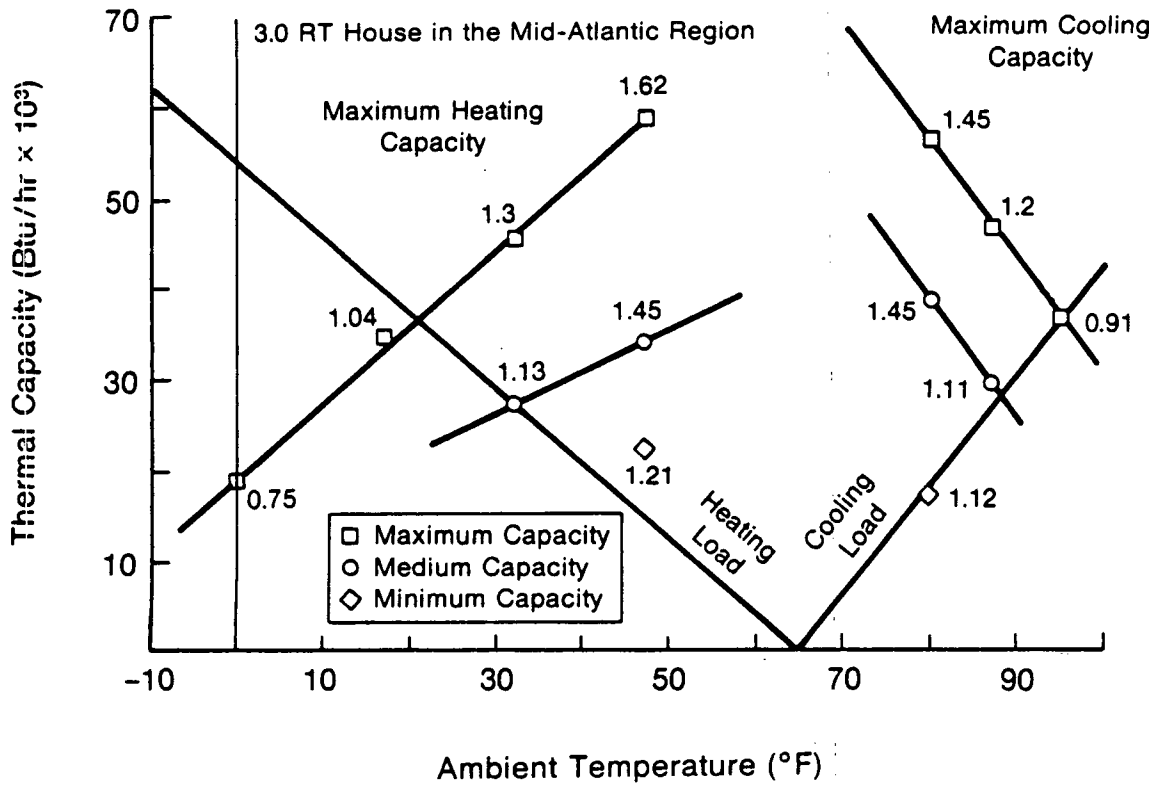

Fig. 3-4 Mark I Performance Thermal Capacity

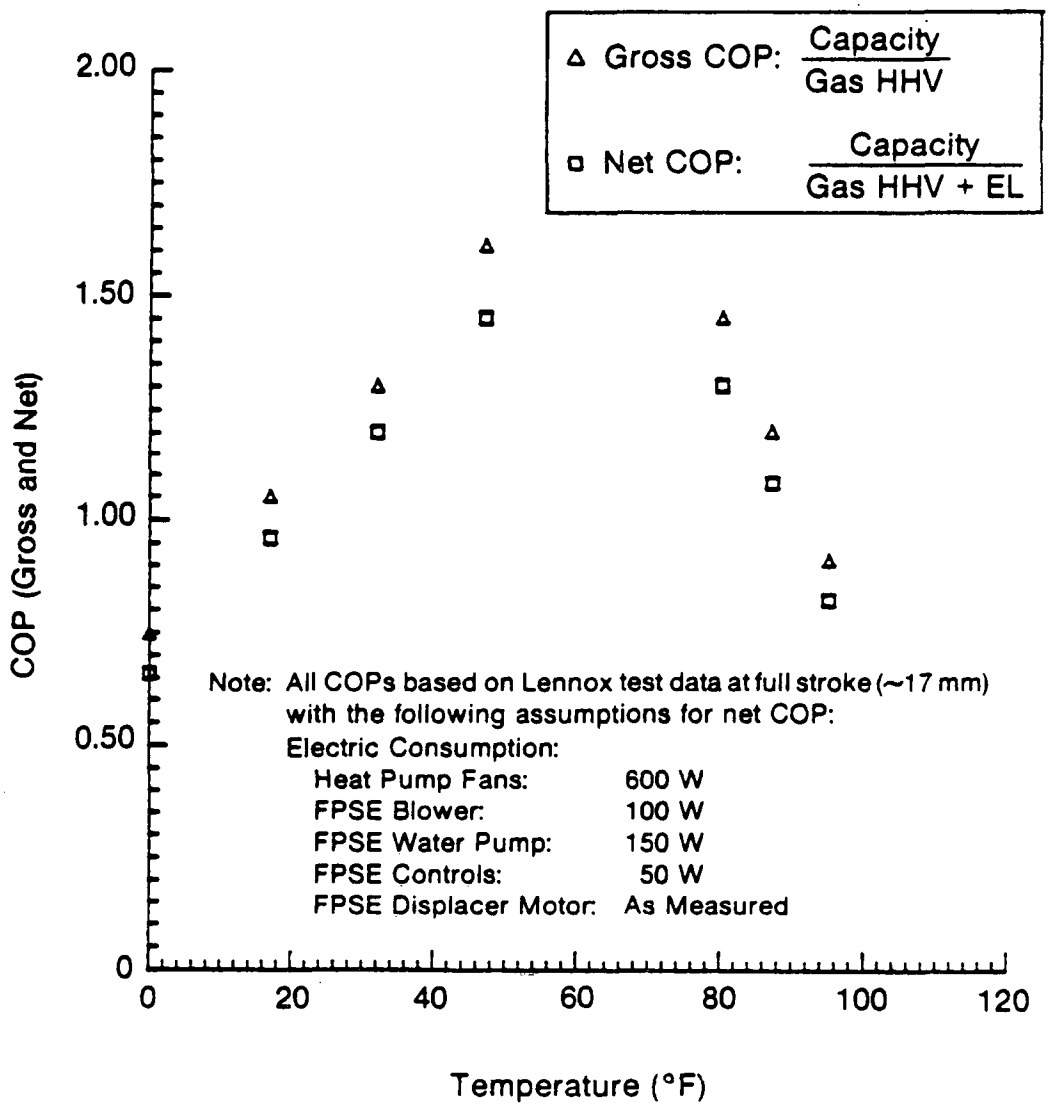

Fig. 3-5 Mark I Heat Pump Module Measured COP

88563

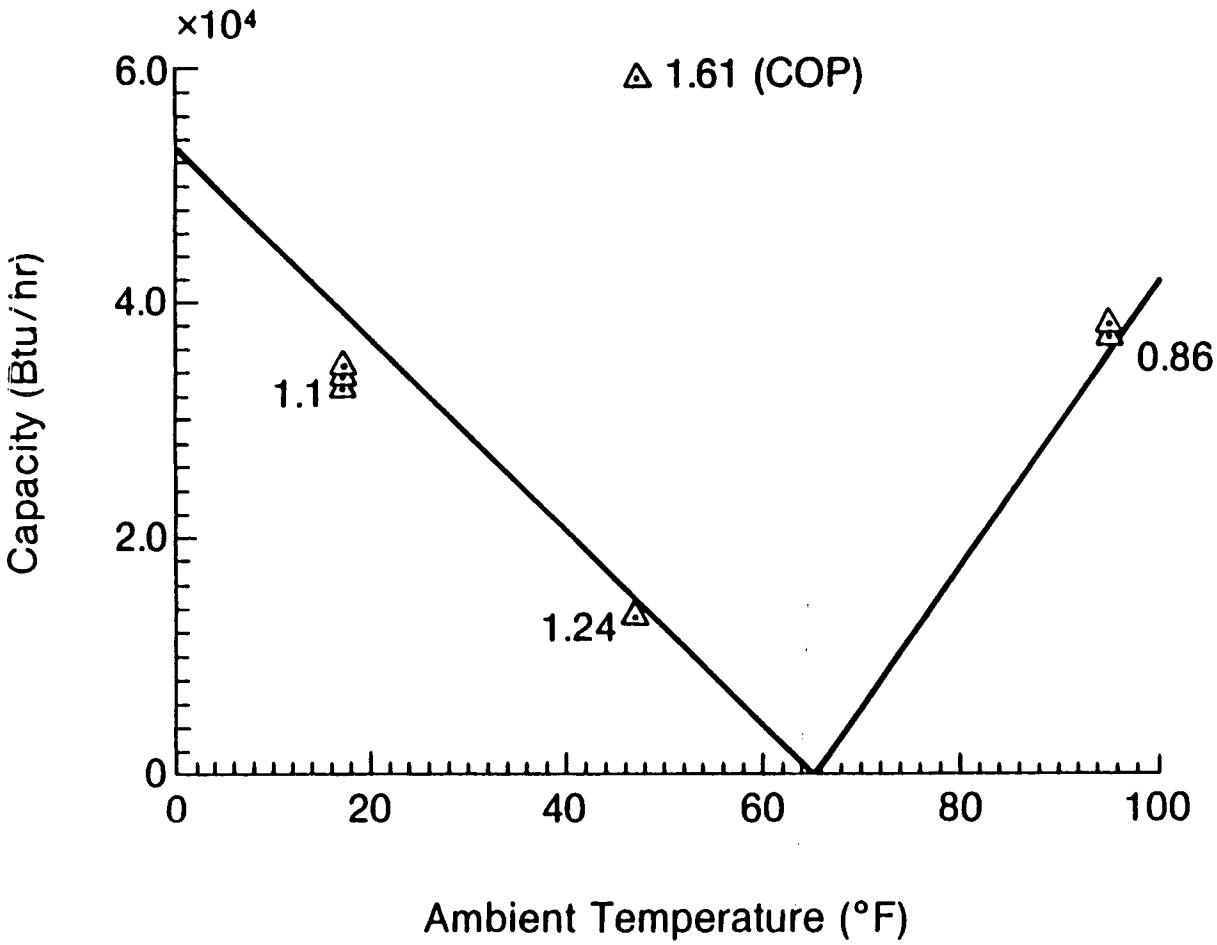

Fig. 3-6 Mark I Heat Pump Module Data Comparison

87163

Table 3-2

Conditions for Compressor Mapping

Condenser Temperature Saturated Discharge, °F	Evaporator Temperature Saturated Suction, °F				
	-20°	0°	20°	35°	50°
80°	X	X	X		
90°	X	X	X		
100°		X		X	X
120°			X	X	X
130°			X	X	X

Notes:

1. Superheat at compressor will be held between 15 and 25°F.

2. Subcooling liquid leaving condenser will not be less than 10°F.

3. Compressor piston stroke setting for the steel diaphragms will be 10, 14, and 18 mm. The stroke will not exceed 18.5 mm.

With these limitations, the mapping points run are given in Table 3-3. The strokes given represent the range of data not restricted by the above limitations. From the above data, it has been possible to draw the parametric curves presented in Volume II, Appendix C.

- Refrigerant Flow versus Evaporator Temperature, Attachment C-1
- Condenser Reject Heat versus Evaporator Temperature, Attachment C-2
- Evaporator Heat Input versus Evaporator Temperature, Attachment C-2
- Engine PV Power versus Evaporator Temperature, Attachment C-3
- Firing Rate versus Evaporator Temperature, Attachment C-4
- Engine Reject Heat versus Evaporator Temperature, Attachment C-4
- Thermal Heating COP versus Evaporator Temperature, Attachment C-5
- Thermal Cooling COP versus Evaporator Temperature, Attachment C-5
- Refrigerant Flow versus Piston Stroke, Attachment C-6
- Firing Rate versus Piston Stroke, Attachment C-7
- Firing Rate versus Evaporator Temperature, Attachment C-7
- Engine Reject Heat versus Piston Stroke, Attachment C-8
- Engine Reject Heat versus Evaporator Temperature, Attachment C-8
- Engine PV Power versus Piston Stroke, Attachment C-9
- Engine Reject Heat versus Evaporator Temperature, Attachment C-9.

These parametric curves are presented for both the high power points, 17-mm piston stroke, and the half-power points, 14-mm piston stroke, in the attachments described above. To complete the curves for the half-power point, several points had to be extrapolated from the higher power by cross plotting the independent parameters against piston stroke and evaporator temperature. The points denoted with the "C" in Table 3-3 represent the calculated values. In performing these extrapolations, it was found that the refrigerant flow ($\dot{m}$) may be expressed as a linear function of piston stroke (Xp):

$$\dot{m} \text{ (fixed evaporator and condenser conditions)} = A_n Xp + B_n \qquad (3\text{-}1)$$

and the engine parameters (EP), engine PV power, firing rate, and engine rejected heat were a quadratic function of piston stroke:

$$EP \text{ (fixed evaporator and condenser conditions)} = aC_n Xp + bD_n Xp^2 \qquad (3\text{-}2)$$

Table 3-3

Completed Performance Mapping Data Points

Test Point No.	Condenser Temp, °F	Evaporator Temp, °F	Piston Stroke, mm High	Medium	Low
1 (VRY)	121	45	0	16.2	0
2 (ARI-C)	130	45	17.3	14C	0
3 (95°F)	121	45	18	17.3	14.2
4 (87°F)	105	47	17.1	14	0
5 (80°F)	95	50	17.2	14	10
6 (ARI-H)	110	30	17	14C	0
7 (47°F)	100	35	17.1	14	12.6
8 (32°F)	97	20	17	15	0
9 (17°F)	95	5	18	17	0
10 (0°F)	90	-12	17.5	0	0
11	80	-20	0	0	0
12	80	0	17.1	15	14C
13	80	20	17.1	14	13
14	90	-20	0	0	0
15	90	0	17.3	14C	0
16	90	20	17	15.1	14
16A[1]	90	35	17	14	12.1
17	100	0	17	14C	0
17A	100	20	17	15.2	14C
18	100	35	17	14	12.6
19	100	50	17.1	14.2	10
20	120	20	17.4	14C	0
21	120	35	17.1	14.7	14C
22	120	50	17	14.1	12.2
23	130	20	0	0	0
23A	130	25	17	14C	0
24	130	35	16.9	15.1	14C
25	130	50	16.2	14.1	13.1
25C[2]	130	50	17	0	0
26	110	50	17.3	14.1	12.1
27	110	35	17	14	0
28	110	20	17	14C	0

[1] A = Added test points.
[2] C = Calculated values.

The accuracy with which these expressions fit the measured data is given in Tables 3-4 and 3-5. These tables present both the measured "average values" and the "computed values" for three arbitrary data points. In each case, the maximum difference between the measured and computed values was 4.5% for the refrigerant flow and 5.7% for the engine PV power. Tables 3-4 and 3-5 also present the spread that was recorded in the data at each point. For the refrigerant flow readings, 4 data scans were taken at 10-min intervals and then averaged. For the engine PV power, a minimum of 10 data scans were taken and then averaged. The spread represents the high and low readings recorded at each data point. These three data points are representative of all of the points and accurately reflect the precision of the curve-fitting equations.

The results of this cross plotting are given in Attachments C-6, C-7, C-8, and C-9 of Volume II, Appendix C. In each case, the extrapolated data are shown in brackets on the plots. The performance maps are presented in Attachments C-1, C-2, C-3, and C-4 of this appendix. The curves for refrigerant flow, engine PV power firing rate (heat input from the natural gas), and engine reject heat provide the basic values for determining performance. The thermal heating and cooling coefficient of performance given in Attachment C-5 are computed from the equations presented in the following two sections.

Cooling Performance. The refrigeration cycle in simplified form is shown in Figure 3-7. Starting at station 1, the liquid refrigerant is evaporated at constant pressure between stations 1 and 2 and slightly superheated (at least 10°F). The superheated refrigerant vapor is compressed between stations 2 and 3 and then cooled and condensed and subcooled (at least 15°F) between stations 3 and 4. Finally, the liquid is passed through an expansion valve, decreased in pressure, and partially vaporized between stations 1 and 4.

The cooling capacity and the cooling COP (assuming perfect thermal isolation from the test cell) are calculated from the following expressions:

$$\text{Cooling capacity}_{\text{system}} = \text{heat absorbed in the evaporator} = (\dot{m}\,(h_2 - h_1) \qquad (3\text{-}3)$$

$$\text{COP (cooling)}_{\text{system}} = \dot{m}\,(h_2 - h_1)/FR \qquad (3\text{-}4)$$

Table 3-4

Variation in Measured Refrigerant Flow

Test Pt No.	Test Conditions Evap Temp, °F	Cond Temp, °F	Piston Stroke, mm	Refrigerant Flow, Btu/hr Average Value	Measured Data High	Low	Calculated Value
19	50	100	17.1	682.1	683.1	679.8	684.8[1]
			14.2	472.1	477.3	466.3	467.5
			10.0	150.8	152.4	148.9	152.7
26	50	110	17.3	643.2	648.7	641.4	644.6
			14.1	400.3	405.5	396.0	396.5
			12.1	239.0	247.5	231.2	241.3
25	50	130	16.2	457.7	463.7	451.4	461.6
			14.1	259.8	269.2	254.0	248.1
			13.1	138.5	141.5	134.9	146.5

[1] Computed from refrigerant mass flow = $A_n X_p + B_n$ (n = scan number), equation 3-1, p 3-15.

Table 3-5

Variation in Measured Engine PV Power

Test Pt No.	Test Conditions Evap Temp, °F	Cond Tem, °F	Piston Stroke, mm	Refrigerant Flow, Btu/hr Average Value	Measured Data High	Low	Calculated[1] Value
19	50	100	17.1	2547.9	2627.6	2473.1	2577.2
			14.2	1691.0	1777.7	1641.6	1632.0
			10.0	596.6	629.9	569.4	631.0
26	50	110	17.3	2780.5	2997.7	2570.9	2803.0
			14.1	1718.4	1848.2	1514.7	1645.1
			12.1	1016.7	1158.6	823.0	1068.9
25	50	130	16.2	2509.2	2604.7	2432.4	2533.1
			14.1	1522.6	1609.6	1435.8	1435.8
			13.1	930.9	1057.6	835.8	993.7

[1]Computed from engine PV power = $C_nX_p + D_nX_p^2$ (n = scan number), equation 3.2, p. 3-15.

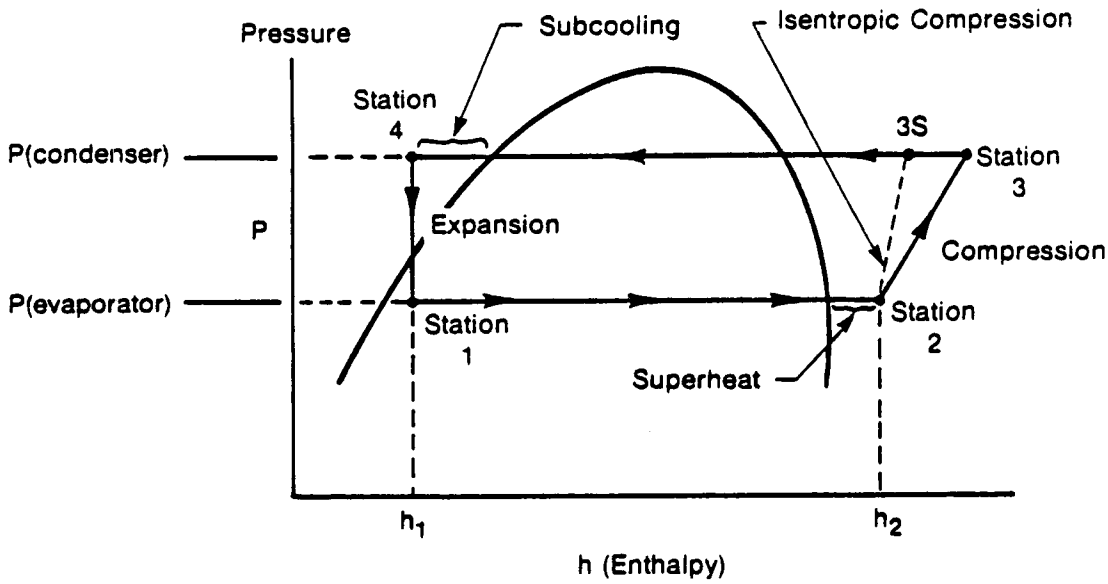

Fig. 3-7 Schematic of Refrigeration Cycle

where:

$\dot{m}$ = refrigerant mass flow rate

h_2 = enthalpy of refrigerant vapor leaving evaporator

h_1 = enthalpy of refrigerant entering evaporator

$h_1 = h_4$ where h_4 is calculated from the actual subcooling at station 4. In plotting this data, h_4 will be corrected to a standard 15°F subcooling.

FR = firing rate of combustor based on value HHV of fuel = $\dot{m}_{gas}$. The HHV of natural gas was measured periodically during the tests with an on-site gas calorimeter.

Heating Performance. The ambient conditions (four points) below 65°F require slightly different calculations for performance evaluation. In the heating mode, performance is based on the energy exchange across the condenser rather than across the evaporator as in the cooling mode. The engine waste heat rejected to the cooling water is also included.

The heating and capacity of the gross thermal heating COP are defined as follows:

$$\text{Heating capacity}_{system} = \text{condenser reject heat} + \text{engine reject heat} \quad (3\text{-}5)$$
$$= \dot{m}\,(h_3 - h_4) + Qrej_{water}\,(0.85)$$

$$\text{Gross Thermal COP (heating)}_{system} = [\dot{m}\,(h_3 - h_4) + Qrej_{water}\,(0.85)] \,/\, FR \quad (3\text{-}6)$$

where:

$\dot{m}$ = refrigerant mass flow rate

h_3 = enthalpy of refrigerant vapor leaving compressor (manifold)

h_4 = enthalpy of refrigerant liquid leaving condenser. h_4 is calculated from the actual subcooling at station 4. Mapping values will be corrected to 15°F of subcooling.

$Qrej_{water}$ = rejected engine heat = $\dot{m}_{water}\,(Cp)(\Delta T)$

FR = firing rate of combustor based on higher HHV of fuel = $\dot{m}_{gas}$ (HHV)

0.85 = standard accepted efficiency of conventional heat

exchangers. As shown earlier in Section 2.0, Figure 2-3, heat recovered from the engine does not include waste heat from the combustor and, therefore, for the cases considered, represents 60% of the overall rejected heat from the heat pump module.

3.1.4.4 Variable Cooler Temperature Evaluation. Three different cooler temperatures (34, 70, and 104°F) were run at the three designated test points: verification, 95°F, and 17°F. The tests consisted of measuring the input gas energy (firing rate, displacer motor power, and heating and cooling COP). The results of the tests are given in Table 3-6 and plotted in Figures 3-8 and 3-9. The data show that raising the cooler temperature increases the displacer motor power but does not affect the thermal COP which remains essentially constant. This result occurs for each of the test points where power is being consumed by the motor, indicating that the thermal efficiency is remaining constant and the net effect is a reduction in PV power that results in a longer displacer stroke required to achieve the same output power. In Figure 3-9, the effect of the increased motor power on the COP is also shown. The gas + EL COP was computed as follows

$$\text{COP (Gas + EL)} = \frac{\text{Cooling Capacity}}{\text{(Firing Rate + Motor Power)}} \tag{3-7}$$

3.1.4.5 Oil Leakage Evaluation. To measure the amount of oil lost from the MARK I hydraulic transmission during normal operation, a test was performed over an 8-hr period to measure this leakage. Referring to Figure 3-10, oil lost from the hydraulic transmission through leakage past the chevron seals will accumulate in two locations. First, the oil can settle behind the compressor piston. Second, it can leak past the compressor piston rings and circulate with the refrigerant into the test loop. The total oil was measured by periodically draining the oil from behind the piston, summing this quantity, and drawing the oil collected in the calorimeter at the end of the 8-hr run.

For the 8-hr period, the heat pump was run at the verification operating point described in Table 3-1. The results obtained were:

Table 3-6

Effect of Cooler Temperature on Performance

Test Pt No.	Inlet Temp, °F	Outlet Temp, °F	Firing Rate, W	Motor Power, W	Gross Thermal COP	Gas + EL COP
1 (V)	32	49.1	10213.7	260.4	0.88	0.81
	32	48.0	9798.9	253.6	0.82	0.75
	32	49.1	10356.2	274.5	0.89	0.82
	32	48.9	10100.8	201.8	0.90	0.84
	70	84.4	10719.3	312.1	0.86	0.78
	32	49.1	10363.2	213.2	0.89	0.83
	32	50.4	10817.9	217.5	0.86	0.81
	70	84.4	11039.0	323.4	0.84	0.77
	104	116.8	10827.1	373.7	0.85	0.76
3 (95°F)	70	84.0	11442.9	493.8	0.93	0.81
	32	55.6	13425.7	494.8	0.83	0.74
	104	118.6	12018.2	567.0	0.88	0.76
9 (17°F)	32	46.4	8139.9	-98.4*	1.10	1.15*
	70	81.7	8077.5	-84.1*	1.03	1.07*
	104	113.0	7540.0	-105.5*	0.95	1.00*

*Power generation results in increased total COP

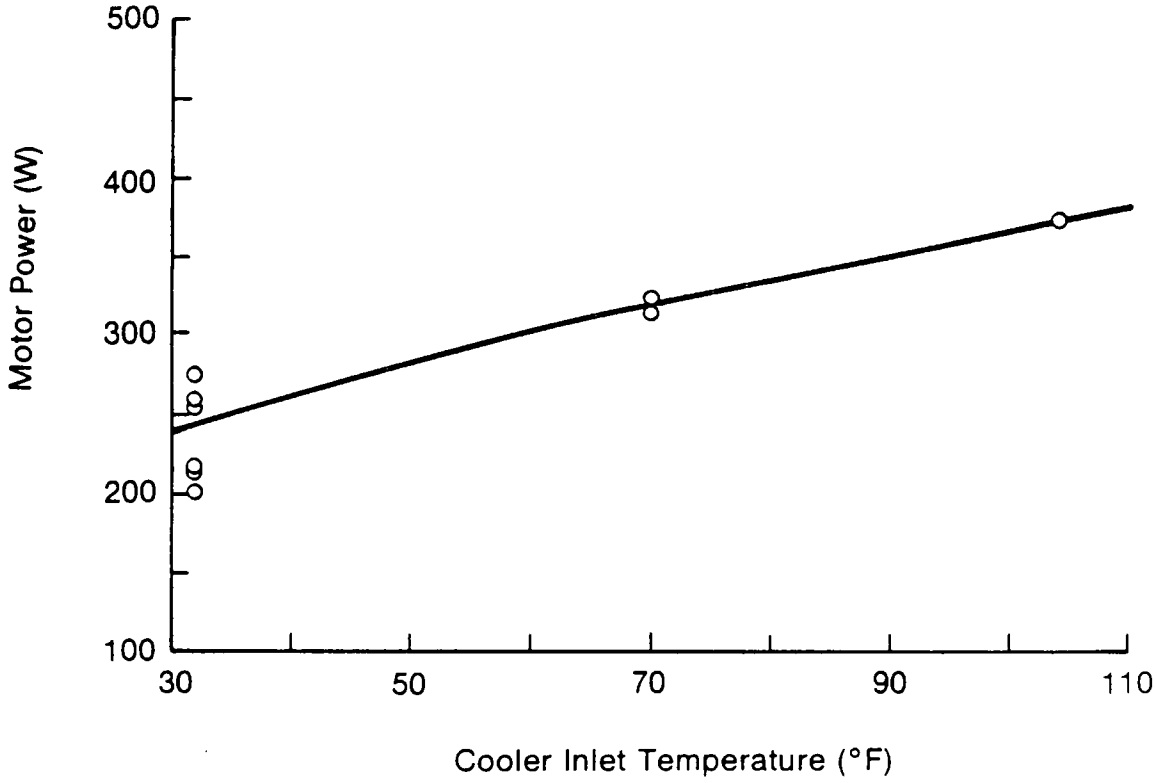

Fig. 3-8 Motor Input Power versus Cooler Inlet Temperature

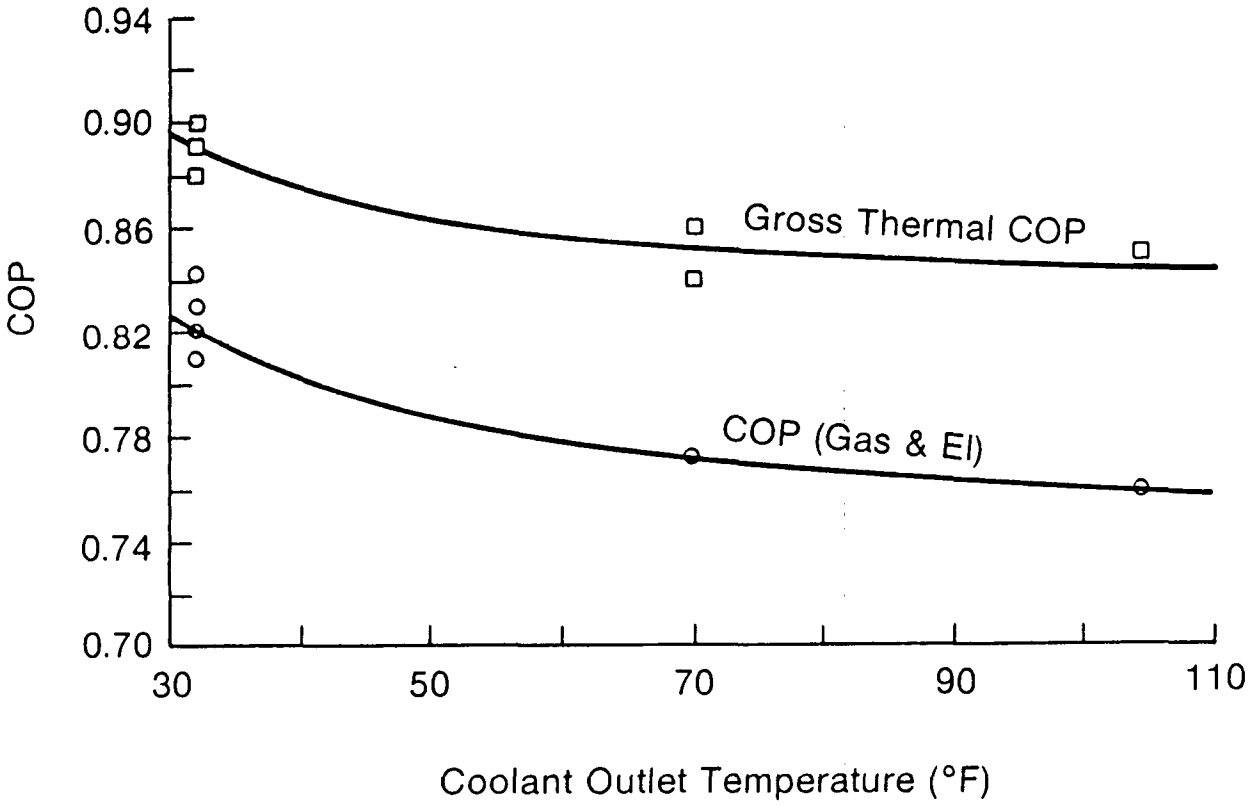

Fig. 3-9 Performance versus Coolant Temperature
(95°F Ambient Temperature Conditions)

881903

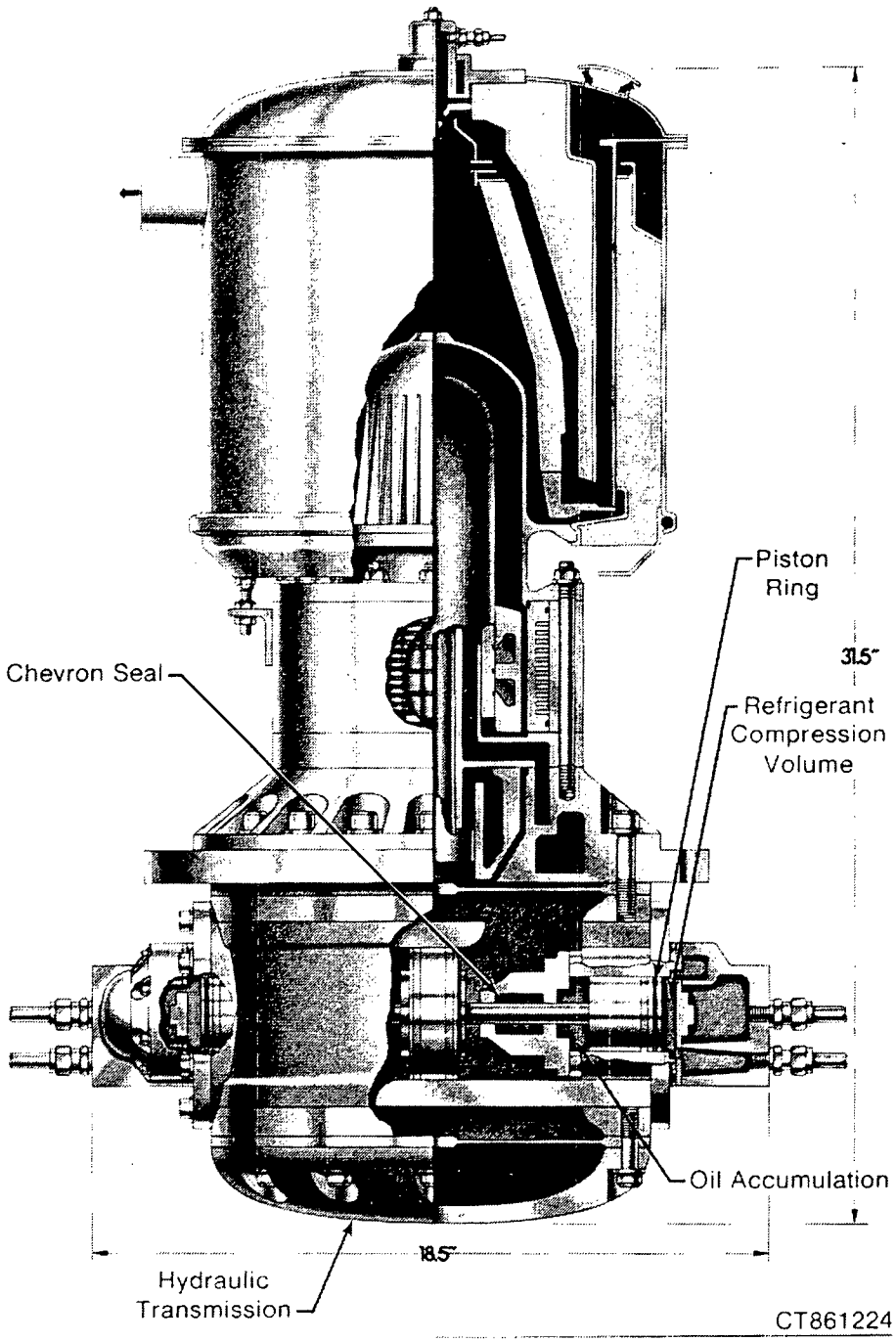

Fig. 3-10 Mark I Hydraulic Transmission

- Oil collected from behind the compressor piston:
  - Net oil collected = 820.2 gm (1.809 lb)
  - % by weight of refrigerant = 0.0067%

- Oil collected from refrigerant loop:
  - Net oil collected = 7.3 gm (0.016 lb)
  - % by weight of refrigerant = 0.00006%

- Total oil leakage 8 hr:
  - Total oil leakage = 827.5 gm (1.825 lb)
  - Total refrigerant = 121.5 kg (267.5 lb).

3.1.5 Conclusions of Lennox Testing

The objectives of the Lennox testing have been achieved. The testing verified the performance of the Mark I FPSE/HP and demonstrated that it achieved the performance goals. In addition, high quality mapping data has been obtained that can be used to formulate algorithms for economic evaluation of the system.

To simplify the economic analyses, the engine performance maps may be represented by linear expressions as shown in Figure 3-11. These data points represent all of the data recorded at the high piston stroke of 17 mm for each of the important engine parameters. The linear regression curve fit for each of these parameters is given in Table 3-7, along with the standard error for the dependent and constant values. From these linear regressions, the heat pump's maximum capacity performance characteristics may be conveniently represented by the family of curves presented in Figures 3-12 through 3-15.

3.2 Advanced Compressor Design

The objective of this task was to assess the breadboard Mark I heat pump lower end, hydraulic transmission, and compressor, for manufacturing cost, performance, and reliability.

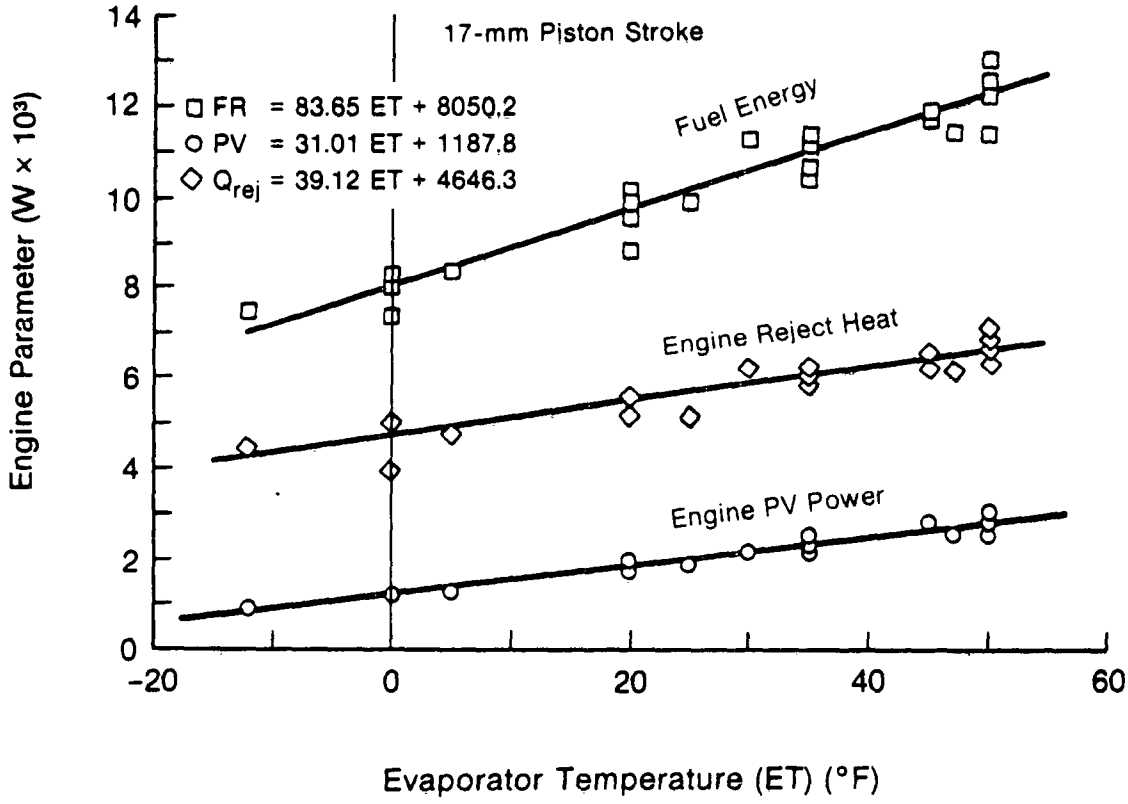

Fig. 3-11 High Stroke Engine Parameters: All Condenser Temperatures

88811

Table 3-7

Linear Regression Curve Fit for Engine Performance Parameters

Engine Parameter	X Coefficient	Constant	Std Error of Y Est	Std Error of Constant
Firing Rate	83.65	8050.21	448.36	83.65
Rejected Heat	39.12	4646.3	290.25	39.12
PV Power	31.01	1187.83	130.86	1.42

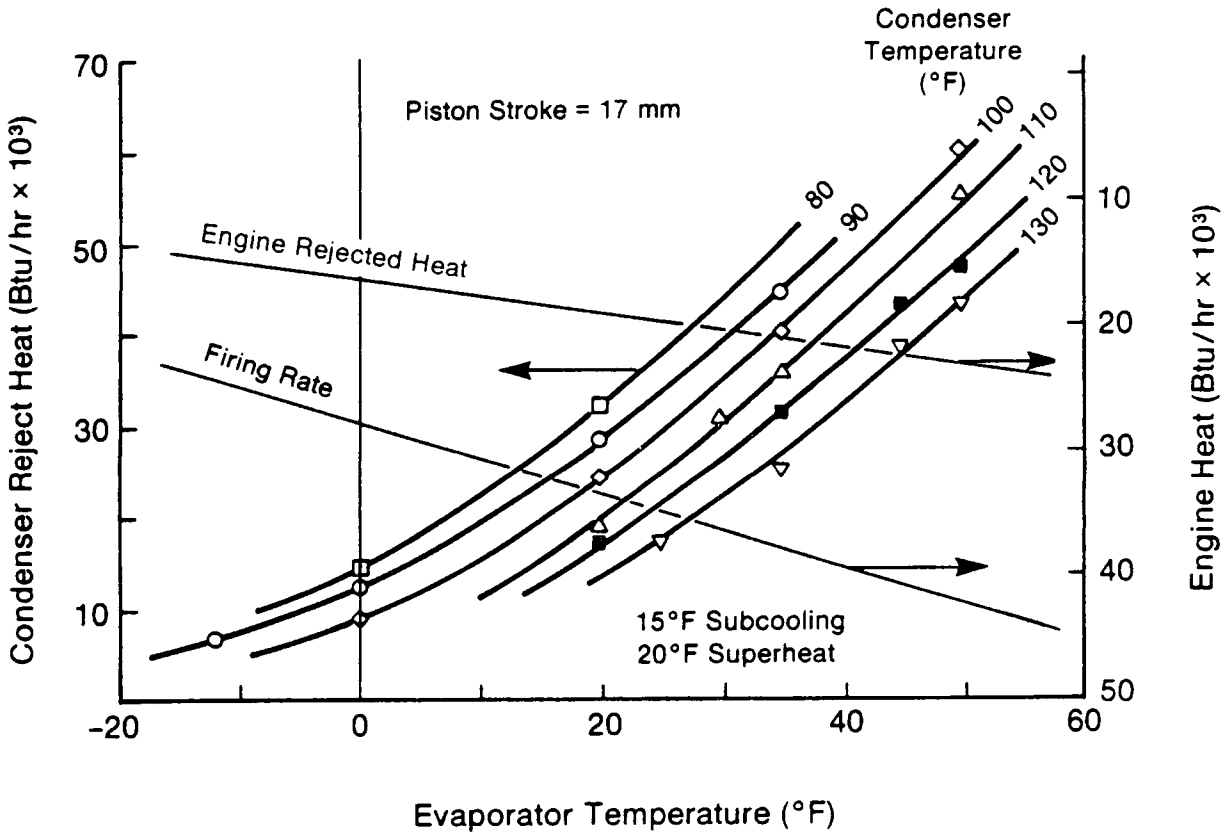

Fig. 3-12 Heat Pump Module Heating Performance

88808

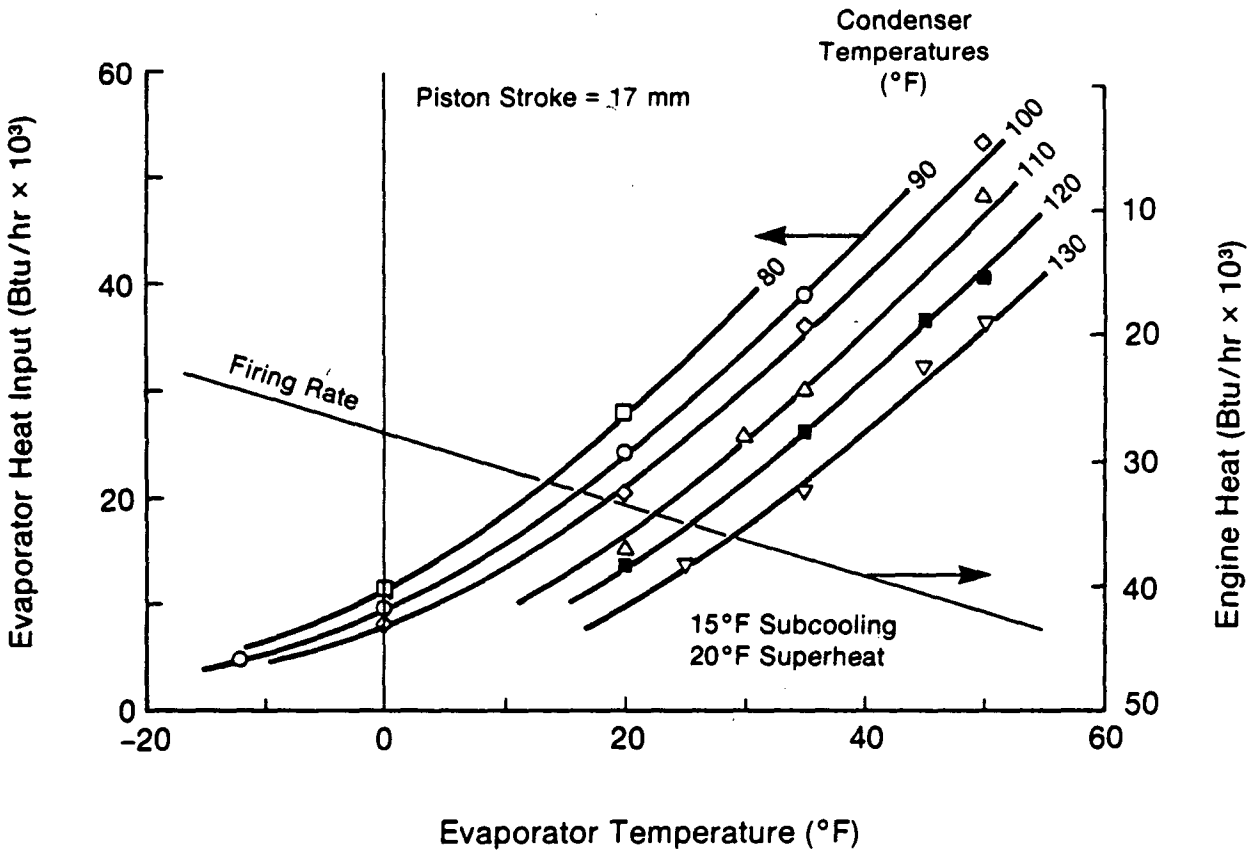

Fig. 3-13 Heat Pump Module Cooling Performance

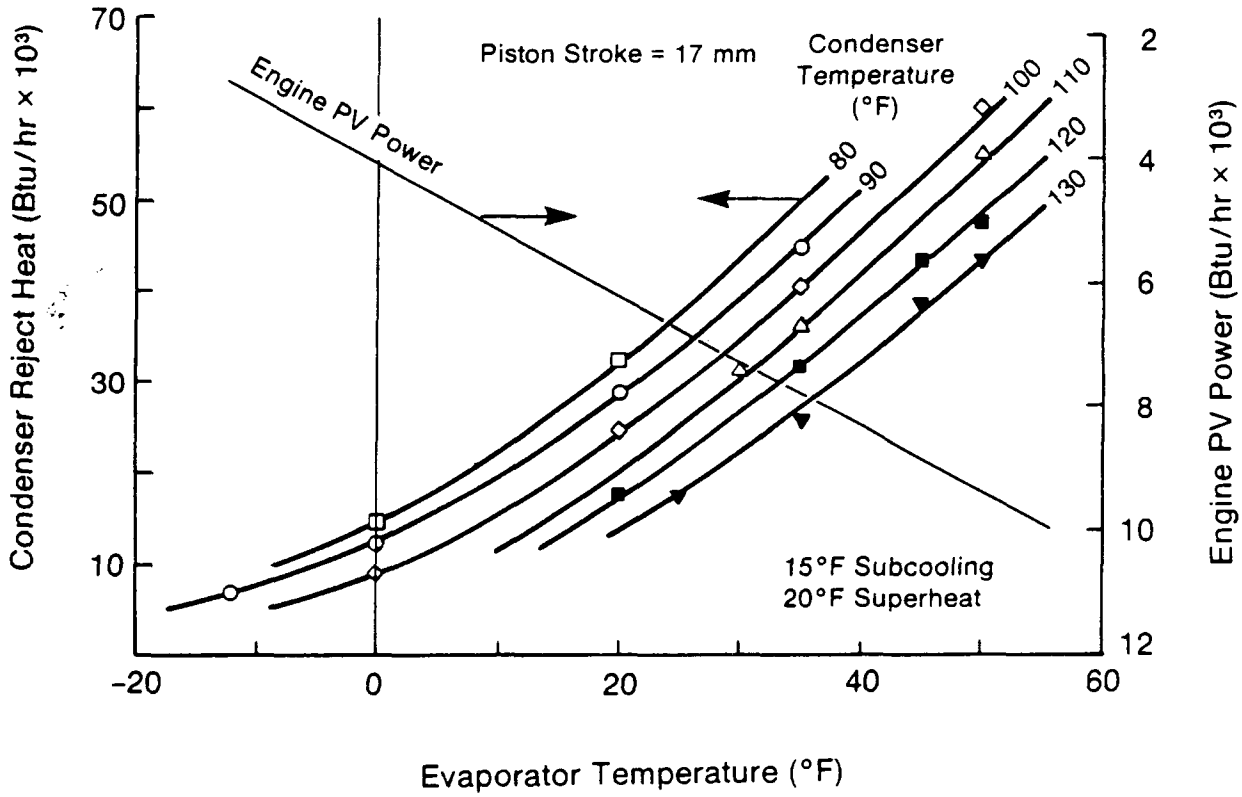

Fig. 3-14 Compressor Heating Performance

88809

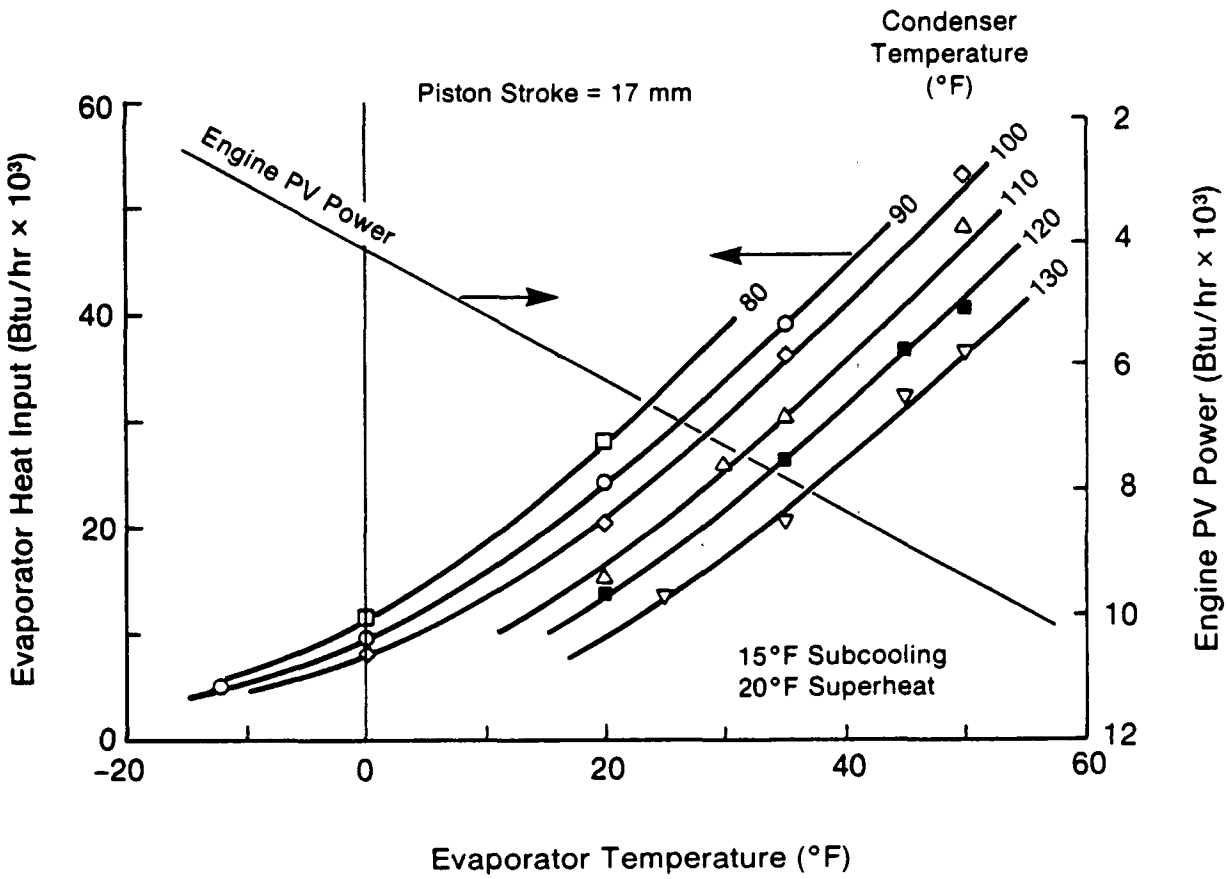

Fig. 3-15 Compressor Cooling Performance

88812

Then, a layout drawing would be developed for a new lower end, designated the Mark II, based on this assessment. As will be shown, because of the stringent requirements imposed by cost, the Mark II lower end design was not finalized during this phase of the program. However, several preliminary designs were evaluated, and their cost evaluations are presented along with several recommendations for achieving the Mark II lower end goals.

The first step in developing a Mark II design was to establish some performance and cost goals. These were established by examining the performance and cost of commercial high efficiency heating and cooling equipment and in consultation with the marketing and engineering staff at Lennox Industries. The result of this investigation was that the Mark II should be designed for a rated cooling capacity of 3.0 RT, with the operating and performance specifications given in Table 3-8. Furthermore, it was established that the manufacturing cost of the lower end, including direct labor, material and purchased parts, and variable burden, should not exceed $250 1986 dollars. The depth and thoroughness of the investigation was enhanced by the support from a John Deere Company value analysis/value engineering (VA/VE) team assigned to the program to evaluate the commercial potential of the FPSE heat pump. Their background and expertise in mass production techniques was indispensable.

The procedure followed for this task was to first assess the performance potential of the Mark I lower end and then, based on the cost and performance evaluation, conceive alternative approaches that might better achieve the goals. This assessment of the Mark I technical potential was made through the testing accomplished at MTI and Lennox, which demonstrated the following key features of the equipment -- technical feasibility, good performance, and laboratory reliability.

Technical feasibility and laboratory reliability were demonstrated by the successful operation, capacity modulation, and control of the Mark I heat pump module in over 300 hr of testing at both MTI and Lennox. During this testing, hydraulic transmission efficiencies between 84 and 87% were consistently measured at the 95°F ambient temperature operating point. Lower end COPs (hydraulic transmission and compressor) in the neighborhood of 4 were measured

Table 3-8

Mark II Design: Operating Points and
Heat Pump Module Performance Parameters

	Cooling			Heating			
Ambient Temp, °F	95	87	80	47	32	17	0
Ts/Td,[1] °F, Sat	45/125	47/105	50/95	35/100	20/100	5/100	-12/90
Capacity, KBtu/hr	36	29	19	18	28	40	55
Gross Thermal COP[2]	1.0					1.5	

[1] Ts = Saturated Evaporator Temperature; Td = Saturated Condenser Condition.
[2] Gross Thermal COP = Capacity (Heating/Cooling)/FR (HHV).

as shown in Figure 3-16. The lower end COP, which does not include engine losses, was defined as:

$$\text{COP (lower end)} = \frac{\text{Refrigerant Heating/Cooling Capacity}}{\text{Engine PV Power}} \qquad (3\text{-}8)$$

Successful demonstration of the operation and performance of the Mark I design leaves cost as the major uncertainty or missing economic parameter. Costs for the Mark I lower end were established by the John Deere VA/VE team. Their costing was done assuming a production base of 50,000 units per year and that modifications would be made to the Mark I to eliminate all laboratory instrumentation. Other than instrumentation modifications, the Mark I lower end was costed as it presently exists without any attempt to value engineer the design. The total cost for the Mark I lower end, including the items shown in Figure 3-17 from the engine diaphragm and below, as well as the vibration absorber and oil management system, was $2,763.39. A summary of the major subassembly costs are presented in Table 3-9. Considering our $250 goal, the requirement for an intensive value analysis and redesign of the Mark I was evident. The procedures followed for the redesign are described in the following sections.

3.2.1 Mark II Design Procedure

The redesign of the Mark I lower end into an advanced, low-cost Mark II design began by examining the major cost elements in the Mark I design. Referring to Table 3-9, we see that the oil management system (described in Section 2.3.3), the vibration absorber (Figure 3-18), and the hydraulic transmission and cylinder sleeves (Figure 3-17) are the major cost elements. The subtotals for these elements are:

• Mechanical Shaft Compressor Components	
- Chevron seal assemblies	$ 78.46
- Stinger rods (piston connecting rod)	31.02
- Oil management system	744.87
Subtotal	854.35
• Vibration Absorber	742.12

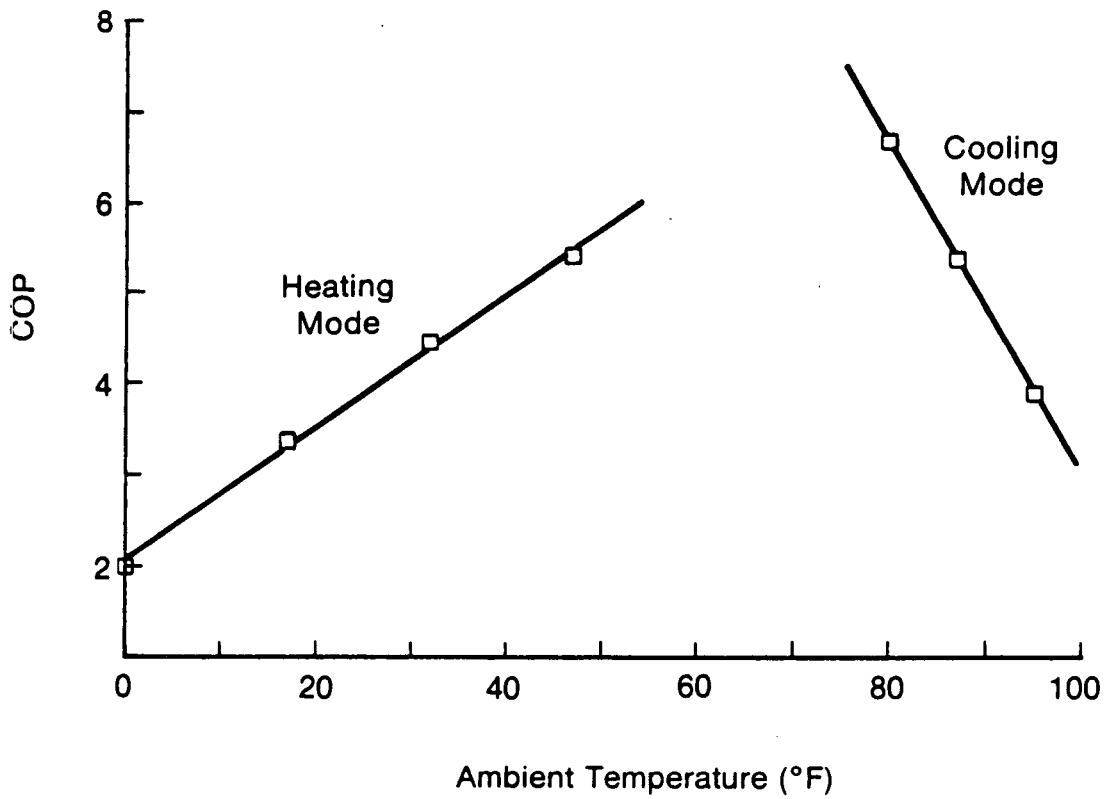

Fig. 3-16 Lower End COP

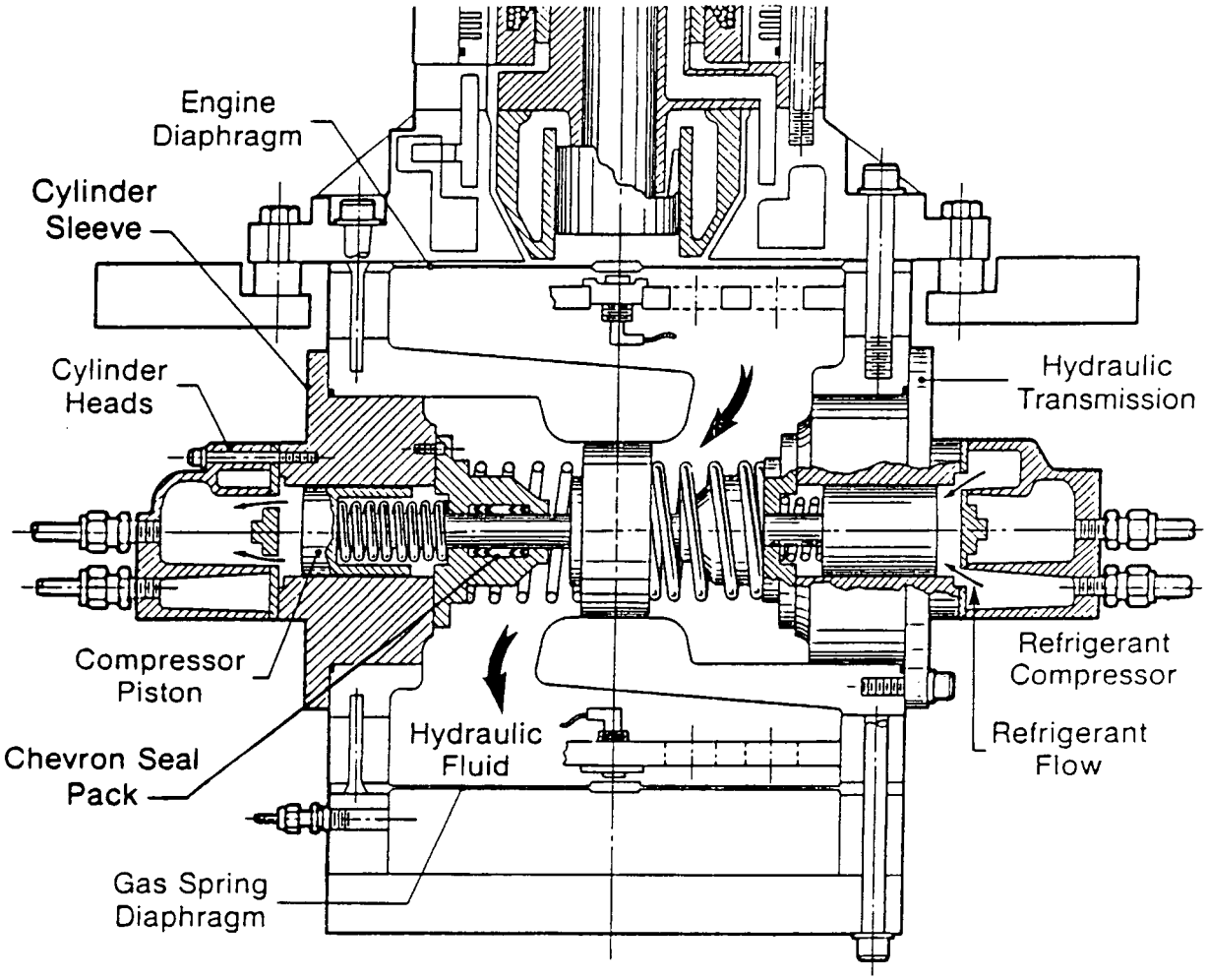

Fig. 3-17 Mark I Lower End Design

Table 3-9

Summary of Major Subassembly Costs

Part Number	Description	No. Per Assembly	Material Cost	Labor Cost	Burden Cost	Total Cost Per Part	Total Cost Per Assembly
1018D06-0181	Diaphragm	2	$ 3.00	$ 2.80	$ 16.92	$ 22.72	$ 45.44
1018E06-0126	Cylinder Sleeve	2	23.50	2.45	15.88	41.83	83.66
1018D06-0130	Cylinder Head	2	8.00	1.74	10.81	20.55	41.10
1018D06-0159	Gas Spring Cover	1	19.00	1.79	11.68	32.47	32.47
1018D06-0160	Gas Spring Housing	1	10.80	1.33	8.54	20.67	20.67
1018E06-0127	Compressor Housing	1	137.50	8.06	55.24	200.80	200.80
1018B06-0131	Discharge Valve	2	2.20	0.00	0.11	2.31	4.62
1018C06-0144	Valve Plate	2	5.50	0.20	1.42	7.12	14.24
1018B06-0177	Piston Journal	2	0.15	0.57	3.38	4.10	8.20
1018C06-0118	Piston Assembly	2	0.00	2.67	15.95	18.62	37.24
1018B06-0117	Piston Ring Assembly	2	0.00	0.62	3.71	4.33	8.66
1018C06-0173	Piston	2	1.28	0.93	5.64	7.85	15.70
1018C06-0142	Chevron Backplate	2	1.50	0.49	3.01	5.00	10.00
1018C06-0120	Chevron Cartridge	2	2.11	1.66	10.05	13.82	27.64
1018C06-0149	Chevron Seal & Assembly	2	0.00	1.30	7.80	9.10	18.20
1018C06-0113	Chevron Cover	2	0.77	1.50	9.04	11.31	22.62
1018C06-0122	Center Bearing	1	403.00	2.51	35.21	440.72	440.72
1018C06-0146	Stinger Rod	2	0.80	2.10	12.61	15.51	31.02
	Subtotal						1,063.00
1018C06-0170	Vib Absorber End Weight	4	2.04	1.15	7.00	10.19	40.76
1018C06-0168	Spacer, Vib Absorber	8	0.08	0.50	2.99	3.57	28.56
1018C06-0168	Spacer, Vib Alm	92	0.08	0.29	1.74	2.11	194.12
1018C06-0167	Spring Leaf	52	0.87	0.51	3.13	4.51	234.52
1018B06-0165	Snubber Supt Ag	4	0.35	0.42	2.56	3.33	13.32
1018B06-0164	Spacer Block	4	0.26	0.45	2.69	3.40	13.60
1018C06-0169	Weights, Top & Bottom	4	4.10	0.88	5.51	10.49	41.96
1018B06-0163	Support Agl	4	0.53	2.53	15.91	18.25	73.00
1018B06-0176	Support Block	4	0.34	0.69	4.17	5.20	20.80
1018C06-0171	Center Block	2	6.14	1.00	6.30	13.44	26.88
1018D06-0175	Vib Assembly	2	0.00	3.90	23.40	27.30	54.60
	Subtotal						742.12
1018xxxxx	Oil Management System	1	699.00	1.56	44.31	744.87	744.87
	Total						2,549.991

1Cost does not include hardware and final assembly and test.

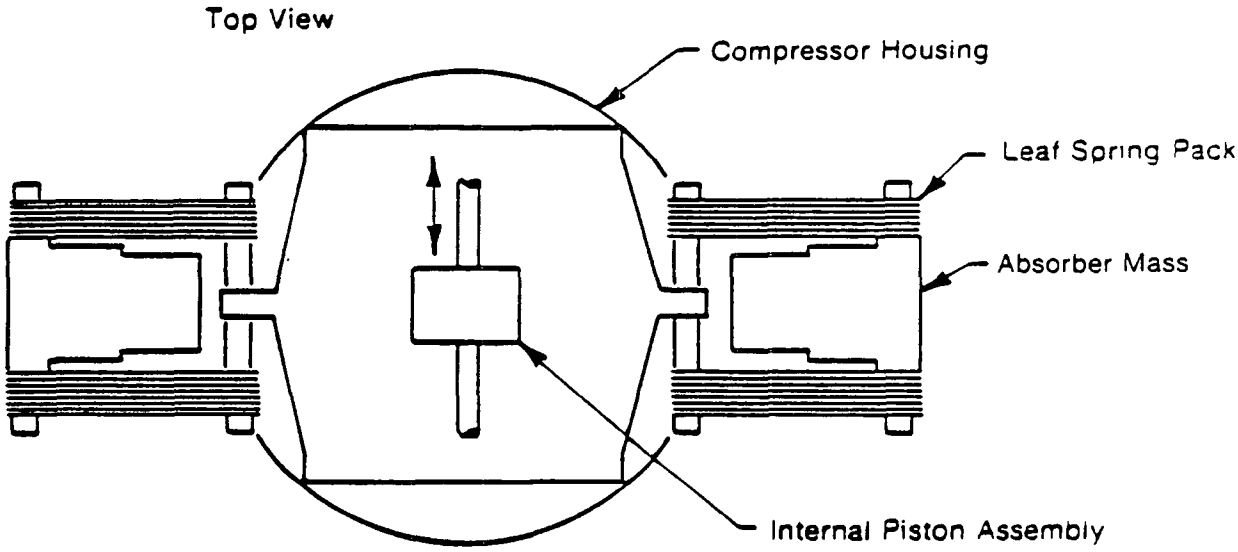

Absorber Specifications

Absorber Dynamic Mass	38 lb_m (each side)
Housing Effective Mass	285 lb_m
Unbalance Force	2442 lb_f – 57.8 Hz. Due to 16.5 lb_m Piston at 22-mm Stroke
Leaf Springs	13 Springs Per Pack; 17-7 PH, 0.071-in Sheet
Maximum Bending Stress	35 ksi at Stroke = 0.204 in.

Fig. 3-18 Vibration Absorbers

- Hydraulic Transmission and Cylinder Sleeves

- Housing	200.80
- Cylinder Sleeves	83.66
Subtotal	284.46

These elements represent 74% of the lower end cost, and any cost reduction here will represent a big step in reducing the overall cost of the lower end.

The procedure followed to achieve an advanced, low-cost Mark II lower end design was to conceive several possible alternative designs that would address the high cost components and then systematically evaluate each of the alternatives for technical feasibility and cost. Figure 3-19 presents the logic followed in evaluating the alternative designs. The diagram starts at the "A" circle and the line to the right depicts the Mark I development. The "D" circles represent the present level of development, with the Lennox testing establishing the technical feasibility, performance, and laboratory reliability of the Mark I. The "E" circles represent evaluation or decision points in the logic tree where, based on the high cost of the Mark I design, the first "E" point represents the point at which alternative design approaches must be developed. The "NG" circle designates a no-go point. The alternatives available are:

- Value engineer the Mark I design by reducing the major cost elements previously described.
- Eliminate the major cost elements by changing the design approach, i.e., eliminate both the oil management system and the leaf-spring-type vibration absorber.

The line extending down from the first "E" represents the first process, and the line extending to the right represents the second process. In developing a design for the second approach, it was concluded (through an internally funded study), that a magnetic coupling between the engine piston and compressor piston would provide a hermetically sealed hydraulic transmission and eliminate the oil management system. By developing a magnetic coupling, it was further concluded that both an oil-filled and gas-filled transmission were feasible. The gas-filled transmission would use either dry lube or gas-

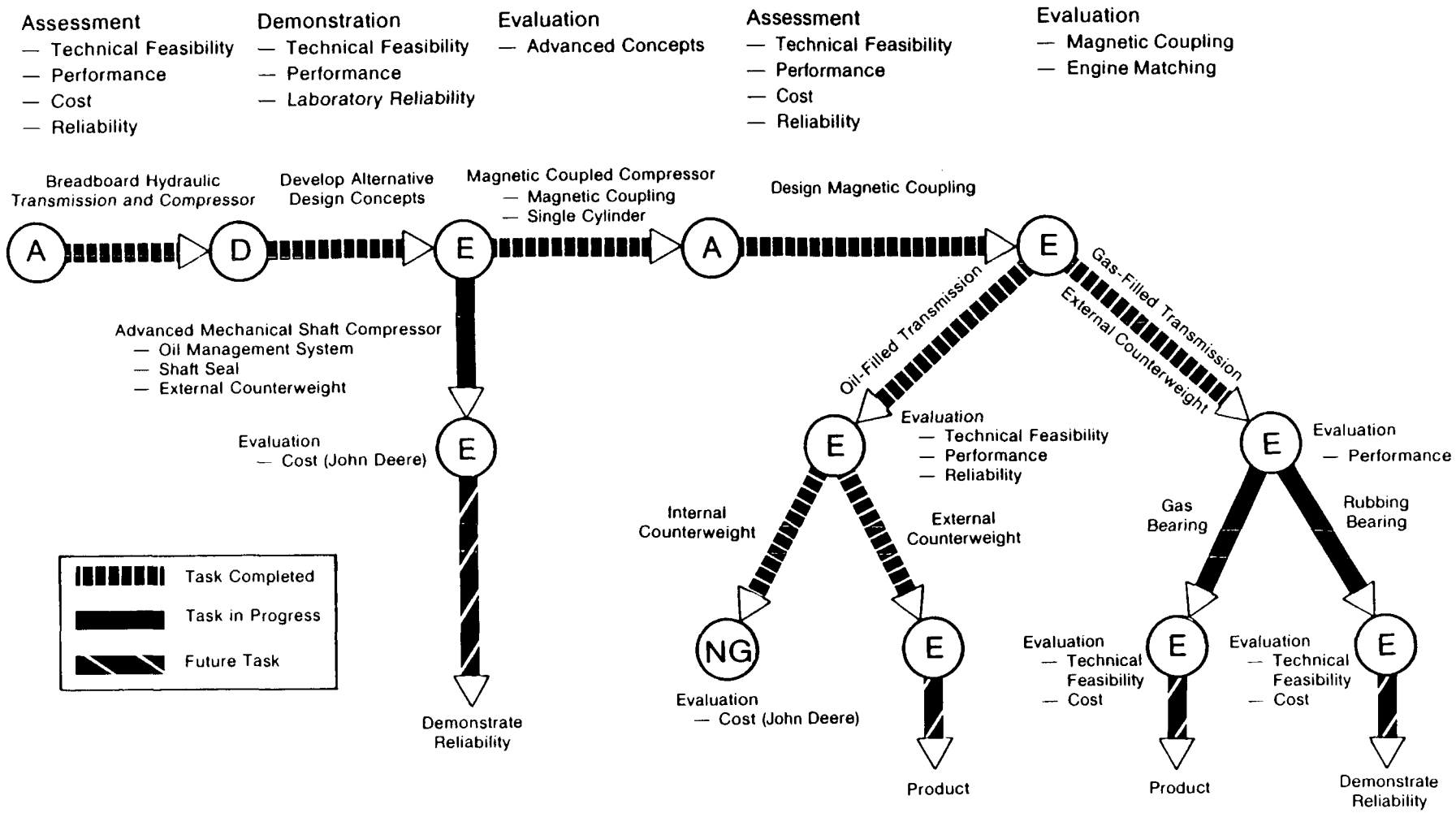

Fig. 3-19 Mark II Compressor Design

88820

lubricated bearings. For the oil-filled lower end, it was further concluded that either an internal or external counterweight could be used, where the internal versus external counterweight decision would be based on cost and performance.

3.2.2 Alternative Design Options

Figure 3-19 specifies the three alternative Mark II lower ends designs that were judged as viable alternatives and defines the decision process considered necessary to arrive at the best alternative. The three design options considered include:

1. A low-cost, advanced mechanical shaft compressor with an oil management system

2. An oil-filled hydraulic transmission with magnetic coupling and single-cylinder compressor

3. A gas-filled lower end with magnetic coupling and single-cylinder compressor.

The design for option No. 1 is shown in Figure 3-20. The lower end in this design consists of components similar to the Mark I but packaged to reduce its size and eliminate overall weight. A hermetic can was placed around the lower end to seal the unit and reduce the pressure loading on the transmission housing to reduce its weight. In comparing this design to the Mark I lower end design and its costs, it was concluded that the cost of an "advanced mechanical shaft" compressor would not reach the $250 goal for the following reasons.

- The cost of the oil management system is too high and cannot be reduced significantly through redesign. This system, with its high pressure pump, valves, and control circuitry, also presents a reliability question for this design.
- The size of the lower end is too big. Because of its size, the transmission housing costs would be excessive.

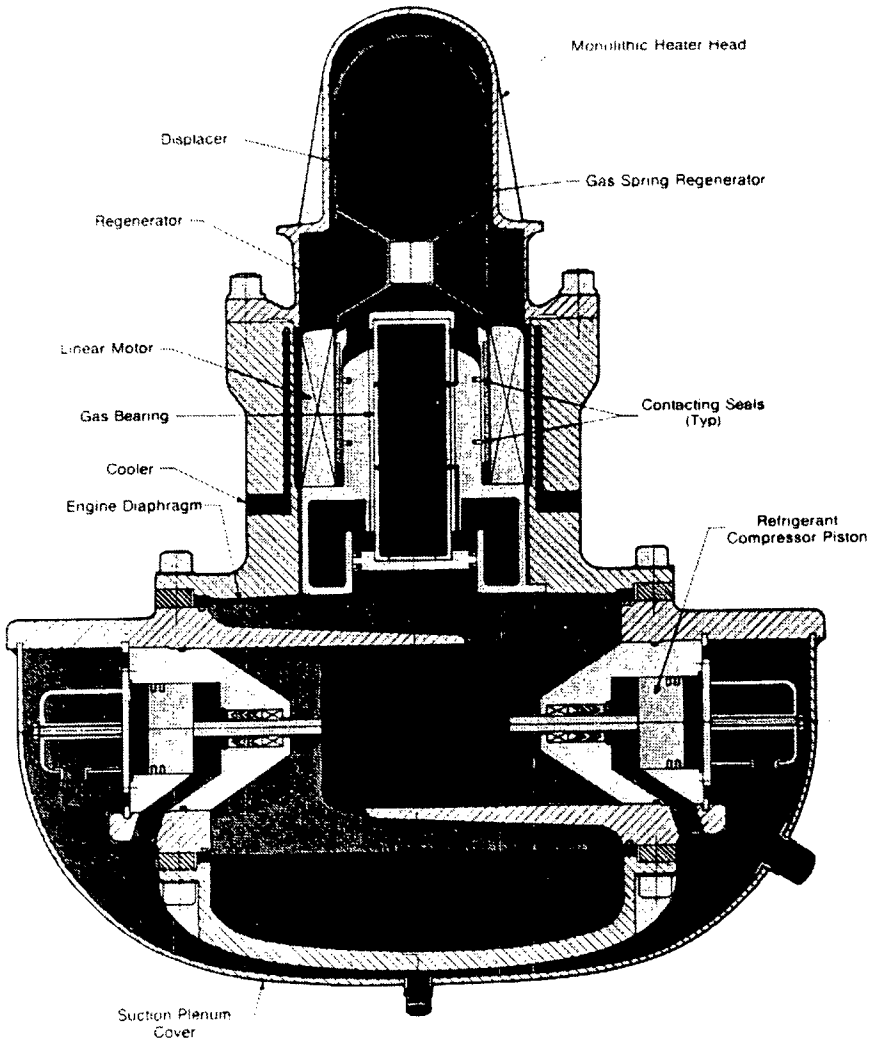

Fig. 3-20 FPSE (Contacting Seals) Coupled to Refrigerant Compressor via Hydraulic Transmission (Chevron Seals)

- The mechanical shaft compressor continues to employ a double-acting compressor which increases cost through the duplication of parts required.

The design for option No. 2, the oil-filled, magnetic-coupled lower end, is shown in Figure 3-21. The use of a magnetic coupling eliminates the need for the oil management system, enables the use of a single-cylinder compressor, and reduces the size of the hydraulic transmission housing. The introduction of this new technology adds some development uncertainty. However, it appears to significantly reduce cost, and this justifies its consideration.

The design for the magnetic coupling is shown in Figure 3-22. The coupling consists of an inner set of magnets mounted on the engine power piston, an outer set of magnets mounted on the compressor piston, and a nonmagnetic hermetic shell (can) mounted between two magnet arrays. The inner portion of the can contains the oil in the hydraulic transmission; the outside of the can contains refrigerant R-22 at the mean suction and discharge pressure. The coupling is designed to transfer the engine PV power to the compressor, as well as to carry the spring and inertia forces exerted on the coupling from the compressor piston dynamics. A force diagram for the coupling is shown in Figure 3-23.

A comprehensive value engineering analysis was performed on this Mark II lower end design that led to two design iterations: the Mark IIVE and IIB. This analysis, discussed in Section 3.2.2.1, has reduced the cost to within $532 of our goal.

In addition to evaluating the effects of the magnetic coupling on cost, the effect of the internal versus external counterweight on performance and overall lower end performance was also evaluated. The design arrived at for the internal counterweight is shown in Figure 3-24. In this design, the hydraulic oil displaced by the engine diaphragm pushes the power piston to the left. The motion of the power piston pushes the vibration balancer to the right, cancelling the power piston inertia imbalance. It also pushes the lower gas spring diaphragm down, compressing the gas in the lower gas spring volume. In evaluating the transmission losses resulting from the counterweight and

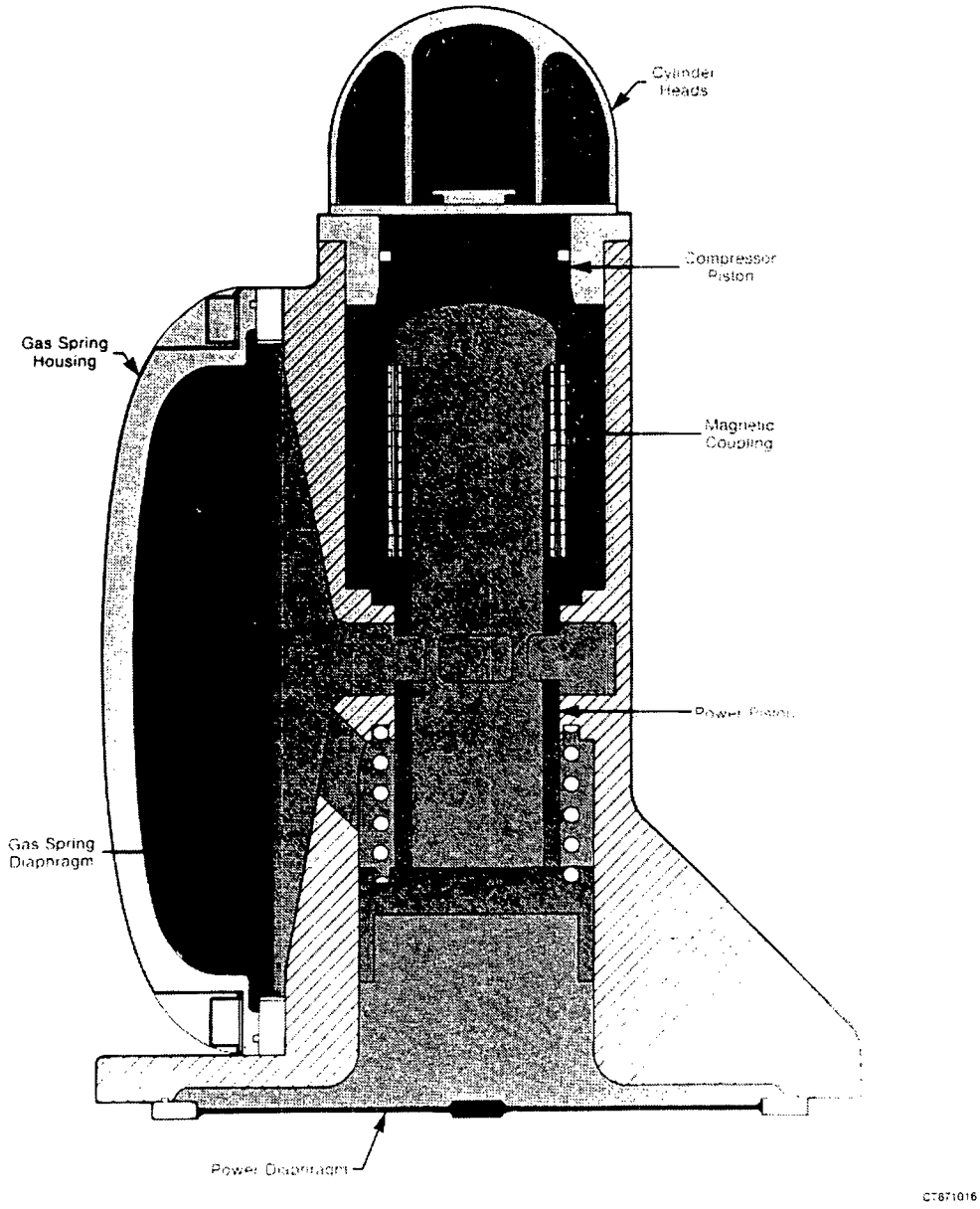

Fig. 3-21 Preliminary Mark II Hydraulic Transmission/Compressor Design

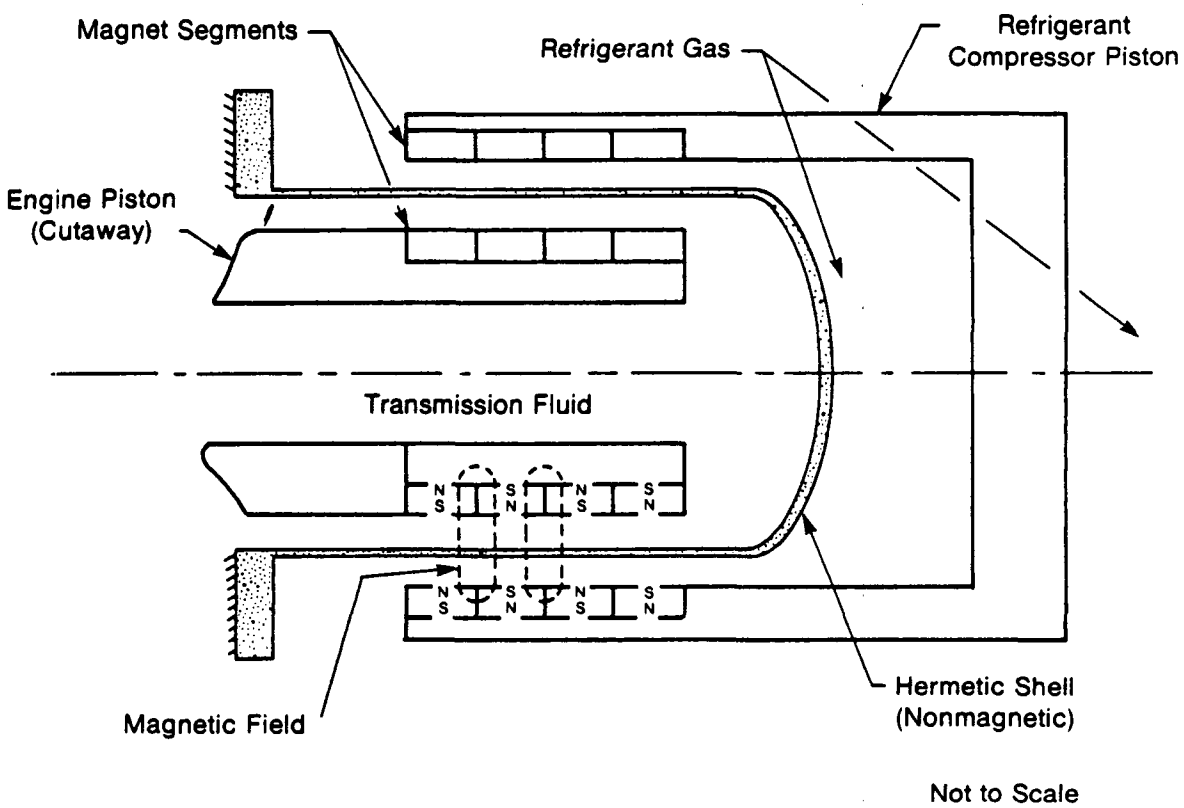

Fig. 3-22 Schematic Representation of Linear Magnetic Coupling

88807

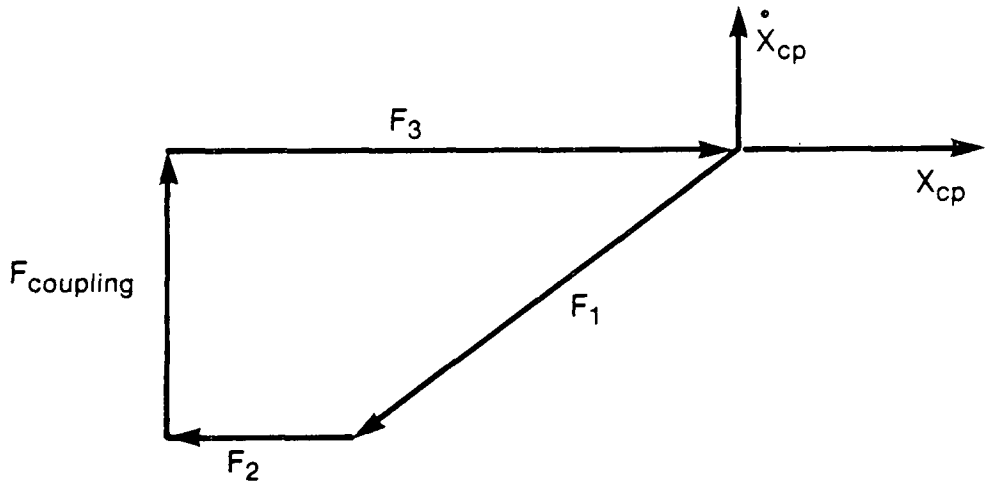

- Force on Compressor Piston from Refrigerant Gas on Compressor (Front) Side of Piston (F_1)
- Force on Compressor Piston from Refrigerant Gas on Back Side of Piston (F_2)
- Inertia Force of Compressor Piston Mass (F_3)
- F_1 and F_2 Are Functions of the Ambient Conditions. These Forces Are Determined from the cylinder computer code
- F_3 Is a Function of Compressor Piston Stroke, Frequency, and Mass
- X_{cp} and $\dot{X}_{cp}$ Are the Compressor Piston Stroke and Velocity, Respectively

Fig. 3-23 Force Diagram for Coupling

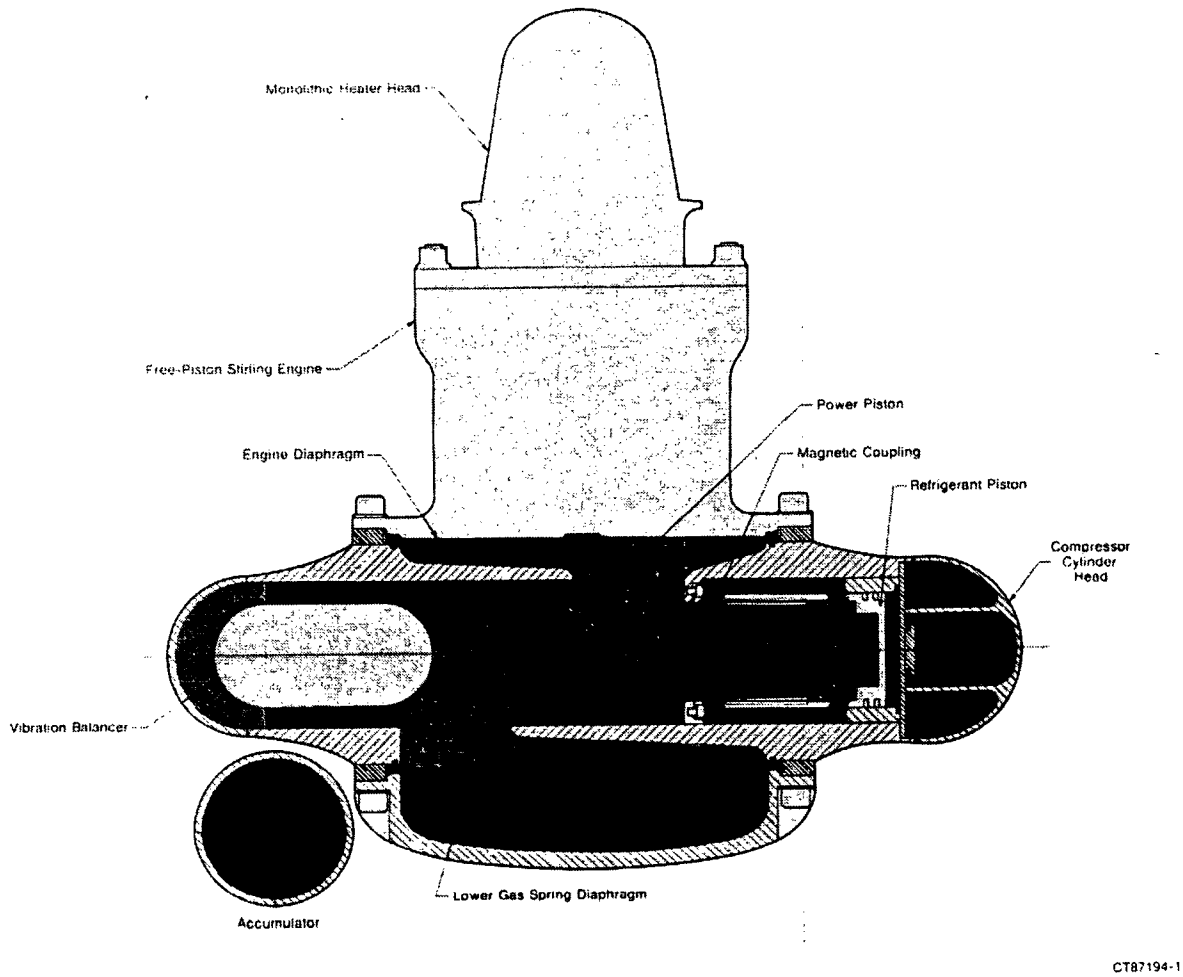

Fig. 3-24 FPSE Coupled to Refrigerant Compressor via Hydraulic Transmission and Magnetic Coupling

comparing them to an external absorber with essentially zero losses, it was judged that the internal counterweight presents too large a performance penalty for the design to proceed. The losses calculated for each of these designs are presented in Tables 3-10, 3-11, and 3-12.

The tables comparing predicted transmission loss show that the in-line configuration with water-based fluid should have a loss of approximately 399 W at 18.4-mm stroke. This is 171 W lower than the total loss for the existing Mark I transmission (10 cs mineral oil) and 133 W lower than the Mark II transmission (water-based fluid) with internal counterweight. Comparing the horizontal configuration (internal counterweight) with the in-line configuration (both water-based fluids), an 85-W excess loss associated with the counterweight and a 48-W excess piston loss can be expected.

The use of a water-based fluid will be beneficial primarily from the standpoint of low thermal expansion coefficient and compatibility with elastomers being considered for the gas spring diaphragm. Commercially available, water-based hydraulic fluids (for example, Union Carbide Hydrolube CC-732) are inexpensive and exhibit pour points lower than -40°F. Viscosity enhancers and stabilizers are typically added to the basic mixture of water/glycol, and special formulations can provide viscosities lower than 10 cs.

Comparison of the overall performance of the Mark I lower end and the Mark II magnetically coupled lower end showed that eliminating the chevron seals with their associated friction and leakage power loss and switching to a single-cylinder compressor increased the lower end COP from 3.22 to 3.55 as defined earlier in this section.

The fluid-filled design has received the major thrust of the work to date, because it most closely represents the technology demonstrated by the Mark I. However, a preliminary design was prepared for option No. 3, the gas-filled lower end, to examine its features. Future plans call for a more in-depth investigation of this approach and a cost evaluation by John Deere. The design for a gas-filled lower end is shown in Figure 3-25. The primary advantage of the gas-filled design is that it eliminates the large flanges required to mount the diaphragms. This could lead to an overall cost reduction by

Table 3-10

Loss Calculations for Existing Direct Acting Transmission

Existing Direct Acting Transmission (Fig. 3-18): XP = 18.41 mm, 57.5 Hz, 10-cs mineral oil

Center Bearing Losses - 2 seal rings, 0.225-in. wide, C = 0.001 in.

Seal Leakage Loss	= 8.8 W	(results from HPORT2 code;
Seal Shear Loss	= 16.2 W	large centerports currently used)
Port Loss	= 65.1 W	
Total	90.1 W	

Hydraulic Loss - $1/2\ pV^2$; assume $A_{flow} = A_p$ and K = 0.0 at top and bottom

Hydraulic Loss = 190 W (hand calculation using $\dot{Q}_{rms} = \frac{2\ \pi\ f\ A_p\ x_p}{\sqrt{2}}$)

Piston Ring Friction - Assume 1-lb preload friction per piston; $\mu = 0.07$

Piston Ring Friction Loss = 58 W

Chevron Seal Friction - 18 lbf from push-pull tests at 50 bar

Chevron Seal Loss = 172 W

Freon Shuttling Loss = 50 W (estimate)

Lower Gas Spring Loss = 10 W (pressure amplitude only 3.2 bar; nitrogen gas)

Total Transmission Loss = 570 W
(Measured loss at 18.41 mm ≈ 494 W)

Table 3-11

Loss Calculations for In-Line Transmission

In-Line Transmission (no counterweight, Fig. 3-22): 18.4 mm, 60 Hz, 2.5-cs water-based fluid

Center Bearing Losses - smaller ports, C = 0.0007 in.

Seal Leakage Loss	≈ 5.0 W	(lower viscosity fluid)
Seal Shear Loss	≈ 18.0 W	
Port Loss	≈ 30.0 W	
Total	53.0 W	

Hydraulic Loss

At Engine Diaphragm	≈ 70 W	(corresponds to K = 0.74)
At Gas Spring Diaphragm	≈ 95 W	(K = 1.0)
	165 W	

Additional 30 to 50 W per spring if centering springs needed.

Piston Ring Friction = 41 W (single piston)

Magnetic Coupling Loss ≈ 50 W (titanium shell)

Freon Gas Spring ≈ 10 W

Freon Centerport Loss ≈ 20 W

Lower Gas Spring ≈ 60 W (helium gas, higher ΔP, includes 10-W capillary loss)

Total Transmission Loss ≈ 399 W without centering springs (reduction of 30% from existing transmission)

Table 3-12

Loss Calculations for Horizontal Transmission

Horizontal Transmission (internal counterweight, Fig. 3-21): 18.4 mm, 60 Hz, 2.5-cs water-based fluid

Piston Seals and Ports = 76 W (additional leak path)

Piston Hydraulic Loss ≈ 190 W (K = 1.0 at both ends)

Counterweight Seal Leakage = 7.4 W (seals are 0.15-in. wide; gap = 0.0005 in.)
Counterweight Seal Shear = 16.4 W
Counterweight Port Loss = 1.0 W

Counterweight Hydraulic Loss ≈ 60 W (24 W at left end; 36 W at right end)

Ring Friction, Magnetic Coupling Freon Gas Spring, Freon Centerports, and Lower Gas Spring ≈ 181 W

Total Transmission Loss = 532 W; 133 W over in-line version (counterweight adds 85 W; horizontal piston adds 48 W)

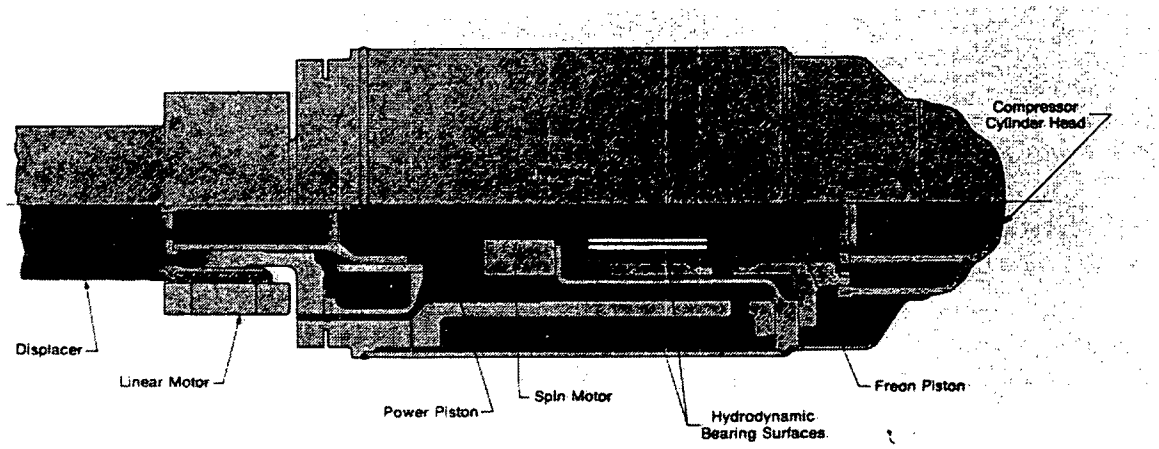

Fig. 3-25 FPSE Coupled to Refrigerant Compressor via Magentic Coupling

making the package smaller. The major unknown at this time, and one that will require further analysis before a conclusion can be drawn regarding its viability, is the requirement for either gas-lubricated or dry-lubricated bearings. The cost and reliability issues of these elements have not been fully evaluated at this time.

3.2.2.1 Results of the VA/VE Study. The benefit of the VA/VE process is presented in Figure 3-26. This figure represents the progress made in reducing the cost of the Mark II lower end. Three design iterations were performed and evaluated by the John Deere team. The Mark IIB design represents a collaborative effort between manufacturing and design engineers, as well as the lowest cost possible for an oil-filled design without major new technological advances in magnet materials. The Mark IIB design is based on using Magnequench III material from Delco Remy, a Division of General Motors.

In reviewing the cost reductions and starting with the original Mark I lower end design (Figure 3-17), the major cost reduction improvements made to the Mark II (Figure 3-21) were:

- Magnetic coupling
- Single-cylinder compressor
- Torque bar vibration absorber
- In-line displacer and power piston motion.

Referring to Section 3.2.1, the use of the magnetic coupling eliminates the components associated with the mechanical shaft compressor ($854.35) and the single-cylinder, in-line compressor reduces the cost for the housing and cylinder sleeves ($279.74). The use of a torque bar vibration absorber, as shown in Figure 3-27, items 10 and 11, replaces the multiple of accurately spaced leaf springs with a single bar. The effect of this design change is to reduce the absorber cost from $949.60 to $99.50. The complete cost breakdown for the Mark II lower end is given in Table 3-13. The major cost elements in this design are the housing, gas spring dome, and the magnetic coupling's hermetic shell. These 3 elements cost $273 or 42% of the overall cost. What this design confirmed was that the large sizes of the housing and gas spring dome were a major factor in the cost. Also, the complexities in making a

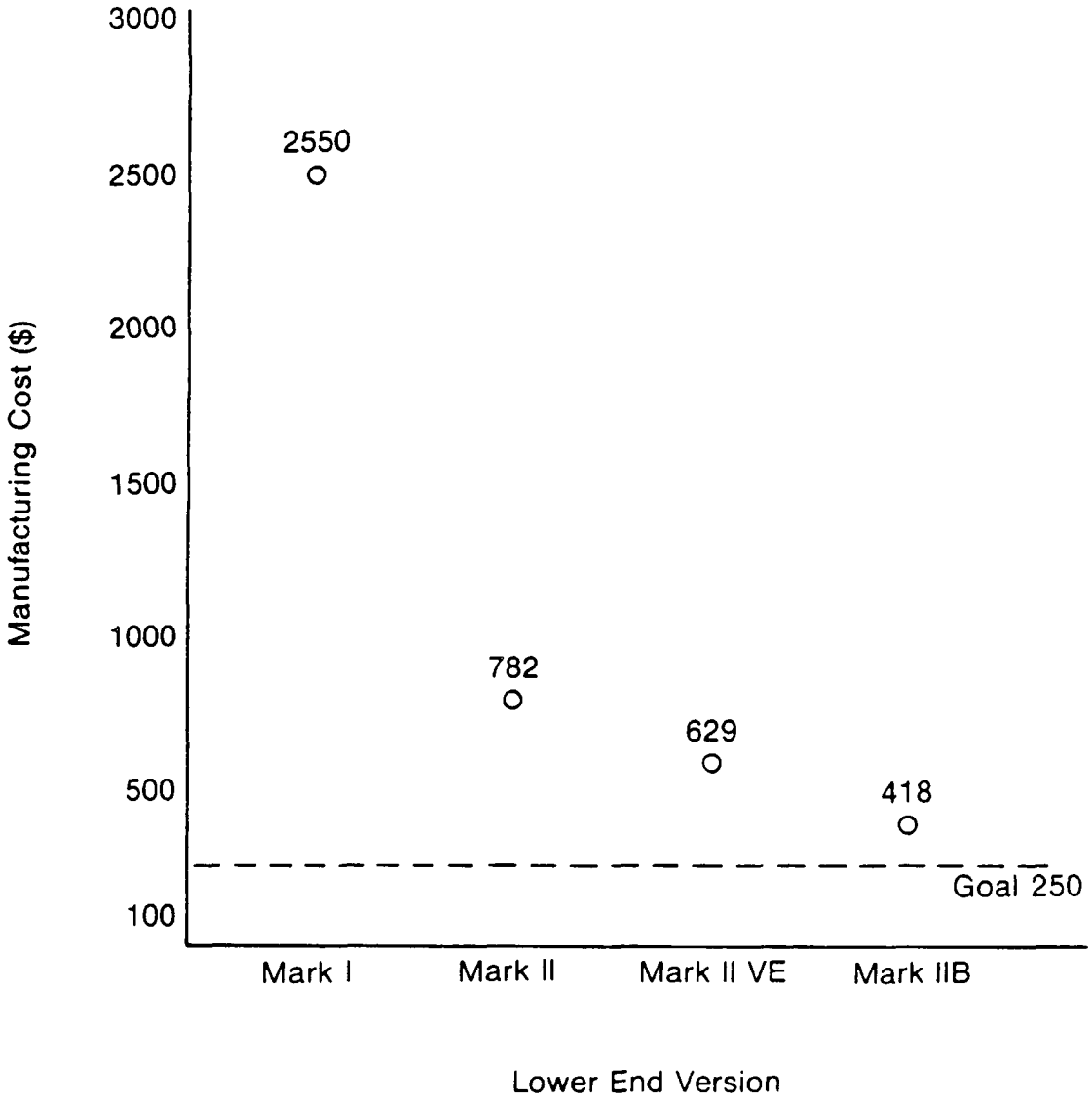

Fig. 3-26 FPSE/HP Lower End Cost Reductions

88814

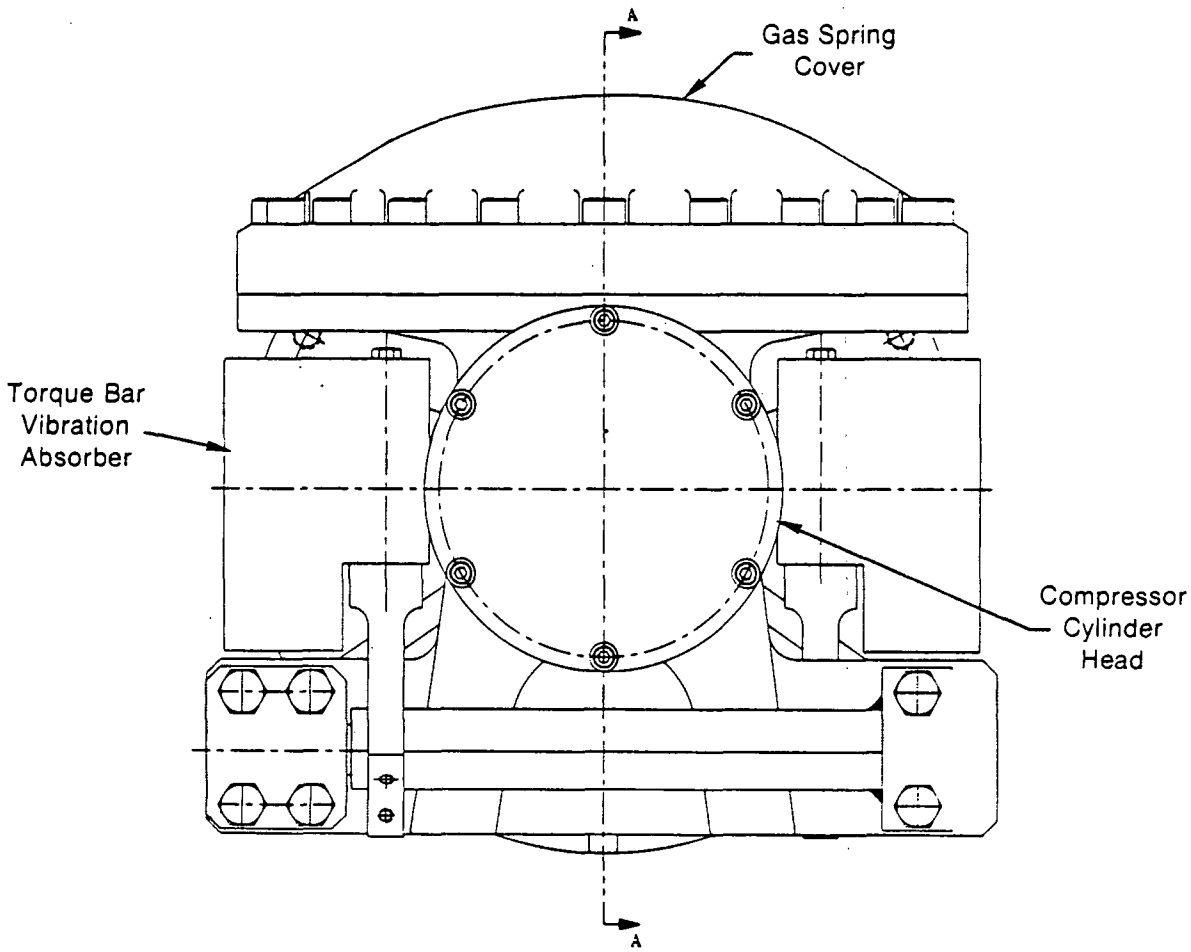

Fig. 3-27 Mark II Torque Bar Vibration Absorber and Compressor Assembly

Table 3-13

Mark II Compressor Cost Summary

Part Number	Description	No. Per Assembly	Material Cost	Labor Cost	Burden Cost	Total Cost Per Part	Total Cost Per Assembly
D060181	Diaphragm	1	$ 3.00	$ 2.80	$ 16.92	$ 22.72	$ 22.72
SKD7935	Gas Spring Dome	1	33.00	3.28	21.32	57.60	57.60
SKD8034	Diaphragm Weldment	1	0.00	1.48	8.89	10.37	10.37
SKC8031	Center Disk	2	0.12	0.53	3.17	3.82	7.64
SKD8032	Diaphragm Braze	1	0.00	0.30	1.80	2.10	2.10
SKD8030	Convoluted Diaphragm	1	1.83	0.07	0.48	2.38	2.38
SKD7938	Housing	1	74.58	4.50	30.72	109.80	109.80
Subtotal							212.61
SKC8002	Compressor Piston	1	1.48	1.41	8.53	11.42	11.42
SKC8003	Cylinder Sleeve	1	3.80	2.57	15.63	22.00	22.00
SKC7994	Compressor Bearing	1	5.90	3.71	22.53	32.14	32.14
SKC7995	Compressor Bearing Assembly	1	31.68	3.29	21.32	56.29	56.29
SKC7986	Power Piston	1	3.80	4.43	26.79	35.02	35.02
SKC7988	Power Piston Assembly	1	31.00	2.74	18.01	51.75	51.75
SKC7884	Hermetic Shell	1	56.24	6.61	42.49	105.34	105.34
Subtotal							
SKB7927	Mounting Plate	2	0.81	0.34	2.08	3.23	6.46
SKB7928	Clamp	2	2.80	1.24	7.55	11.59	23.18
SKC7929	Absorber Mass	2	6.12	1.47	9.12	16.71	33.42
SKC7930	Torsion Bar	2	1.58	0.77	4.68	7.03	14.06
SPILLOW	Pillow Block	2	1.97	0.85	5.18	8.00	16.00
SKD7931	Torsion Bar Assembly	2	0.00	0.46	2.73	3.19	6.38
Subtotal							
SKHEAD	Cylinder Head	1	4.62	1.39	8.58	14.59	14.59
SKDSVLV	Valve Stop	1	2.64	0.00	0.14	2.78	2.78
SKVLVPLT	Valve Plate	1	6.60	0.19	1.49	8.28	8.28
Subtotal							25.65
Total							651.72
20% estimate for hardware, final assembly and test							130.34
Final Total							782.06

Note: The cost studies prepared by Deere and Company include material, labor at $13 per hour, and burden of 600%. The costs presented do not include final assembly, test, paint, packaging, controls, and manufacturing profit.

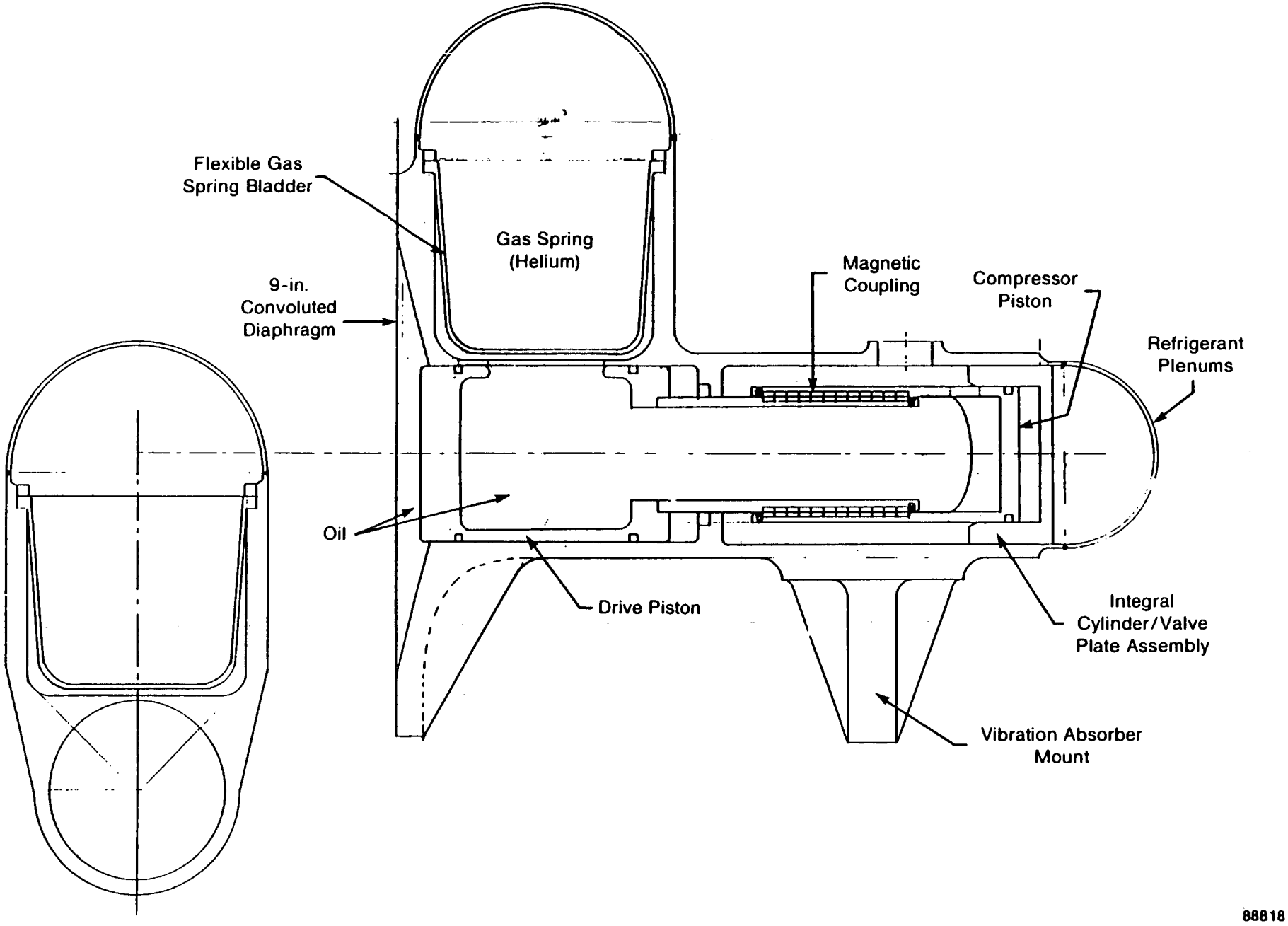

Fig. 3-28 Mark IIVE Compressor Design

precision titanium can to maintain a close clearance gap on either side of the can were expensive. The Mark IIVE design (Figure 3-28) addressed these cost elements by introducing the following features.

- Convoluted and elastomer diaphragms
- Magnetic coupling bearing
- Increased piston stroke.

The housing size was reduced by replacing the 10-in. diameter contoured diaphragm with a more flexible 9-in. convoluted diaphragm, as discussed in Section 2.4, and replacing the gas spring diaphragm with an elastomer. The precision requirements on the titanium can were reduced by eliminating the closely controlled magnetic gap on either side of the can, and between the magnets and can, by designing the can to be a bearing between both moving elements. The piston stroke was increased slightly to reduce the peak force of the magnetic coupling, thus allowing a slightly smaller coupling. The increase in viscous losses associated with the higher piston velocity was considered an acceptable trade-off. The cost breakdown for the Mark IIVE design is given in Table 3-14.

The Mark IIB design is shown in Figure 3-29. This design introduced two additional features: a reduced piston/housing length and a stainless steel coupling can.

Reducing the piston and housing length was achieved by using a thicker, stronger, stainless steel can in the magnetic coupling instead of the titanium can. This provided a stiffer bearing for the power piston to resist the magnetic radial decentering force of the coupling at the point of application of the force, enabling the outboard bearings on the power piston to be reduced. In turn, the shorter piston enables the housing to become shorter. Costs for the Mark IIB design are given in Table 3-15. The overall cost for the Mark IIB is $418, which is very close to the $250 goal and will probably be further reduced as each component is further value engineered. However, before detailed component analyses were performed on the oil-filled lower end design, it was concluded that it would be more productive to perform the VA/VE analyses on the Mark II engine and gas-filled compressor at this time.

Table 3-14

Mark IIVE Improved Compressor Cost Summary

Part Number	Description	No. Per Assembly	Material Cost	Labor Cost	Burden Cost	Total Cost Per Part	Total Cost Per Assembly	Mark IIVE Proposed Cost
D060181	Diaphragm	1	$ 3.00	$ 2.80	$ 16.92	$ 22.72	$ 22.72	$ 2.38
SKD7935	Gas Spring Dome	1	33.00	3.28	21.32	57.60	57.60	41.57
SKD8034	Diaphragm Weldment	1	0.00	1.48	8.89	10.37	10.37	7.00
SKC8031	Center Disk	2	0.12	0.53	3.17	3.82	7.64	0.00
SKD8032	Diaphragm Braze	1	0.00	0.30	1.80	2.10	2.10	0.00
SKD8030	Convoluted Diaphragm	1	1.83	0.07	0.48	2.38	2.38	2.38
SKD7938	Housing	1	74.58	4.50	30.72	109.80	109.80	103.93
Subtotal							212.61	157.26
SKC8002	Compressor Piston	1	1.48	1.41	8.53	11.42	11.42	11.42
SKC8003	Cylinder Sleeve	1	3.80	2.57	15.63	22.00	22.00	9.31
SKC7994	Compressor Bearing	1	5.90	3.71	22.53	32.14	32.14	23.21
SKC7995	Compressor Bearing Assembly	1	31.68	3.29	21.32	56.29	56.29	49.36
SKC7986	Power Piston	1	3.80	4.43	26.79	35.02	35.02	35.02
SKC7988	Power Piston Assembly	1	31.00	2.74	18.01	51.75	51.75	44.54
SKC7884	Hermetic Shell	1	56.24	6.61	42.49	105.34	105.34	105.34
Subtotal							313:96	278.20
SKB7927	Mounting Plate	2	0.81	0.34	2.08	3.23	6.46	0.00
SKB7928	Clamp	2	2.80	1.24	7.55	11.59	23.18	0.00
SKC7929	Absorber Mass	2	6.12	1.47	9.12	16.71	33.42	25.16
SKC7930	Torsion Bar	2	1.58	0.77	4.68	7.03	14.06	0.00
SPILLOW	Pillow Block	2	1.97	0.85	5.18	8.00	16.00	3.66
SKD7931	Torsion Bar Assembly	2	0.00	0.46	2.73	3.19	6.38	34.72
Subtotal							99.50	63.54
SKHEAD	Cylinder Head	1	4.62	1.39	8.58	14.59	14.59	14.59
SKDSVLV	Valve Stop	1	2.64	0.00	0.14	2.78	2.78	2.78
SKVLVPLT	Valve Plate	1	6.60	0.19	1.49	8.28	8.28	8.28
Subtotal							25.65	25.65
Total							651.72	524.65
20% estimate for hardware, final assembly, and test							130.34	104.87
Final Total							782.06	629.52
Mark IIVE Savings								152.54

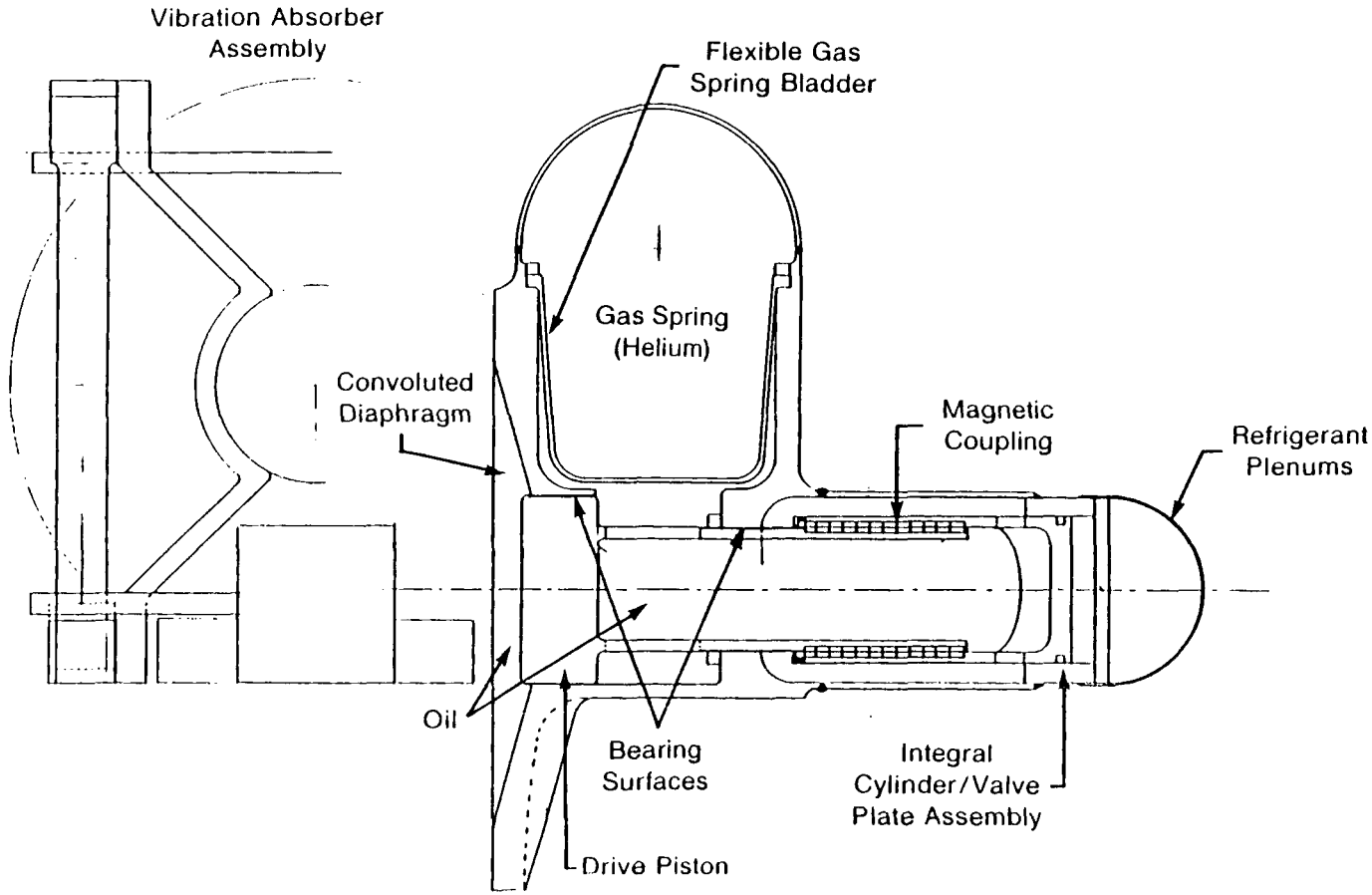

Fig. 3-29 Mark IIB Compressor Design

88819

Table 3-15

Mark IIB Compressor Cost Summary

Part Number	Description	No. Per Assembly	Material Cost	Labor Cost	Total Burden	Cost Per Part	Total Cost Per Assembly
MK2B11	Diaphragm	1	$ 1.83	$0.07	$ 0.51	$ 2.41	$ 2.41
MK2B08	Gas Spring Dome	1	1.14	0.46	2.82	4.42	4.42
MK2B10	Retainer Ring	1	0.68	0.36	2.19	3.23	3.23
MK2B09	Air Bag	1	3.00	0.00	0.15	3.15	3.15
MK2B01	Housing	1	48.08	7.57	47.82	103.47	103.47
	Subtotal						116.69
MK2B04	Compressor Piston	1	4.31	2.77	16.84	23.92	23.92
MK2B06	Valve Plate	1	0.36	0.36	2.18	2.90	2.90
MK2B05	Compressor Piston/ Bearing Assembly	1	25.40	2.48	16.15	44.03	44.03
MK2B02	Power Piston	1	5.21	3.76	22.82	31.79	31.79
MK2B03	Power Piston Assembly	1	27.02	2.00	13.35	42.37	42.37
MK2B15	Hermetic Shell	1	20.48	5.96	36.78	63.22	63.22
	Subtotal						208.23
MK2B13	Absorber Mass	2	5.34	0.87	5.49	11.70	23.39
MK2B14	Mounting Yoke	1	2.80	0.86	5.30	8.96	8.96
MK2B12	Torsion Bar	2	2.28	0.99	6.05	9.32	18.65
	Subtotal						51.00
MK2B07	Cylinder Head	1	0.17	0.60	3.61	4.38	4.38
	Subtotal						4.38
Total							380.30
10% estimate for hardware, final assembly, test, trim, and paint							38.03
	Final Total						418.33

Cost reduction of $6.02 is possible if the housing is changed to a complete casting eliminating the fabrication. Additional savings of $8.96 can be achieved by changing the yoke to a mount on the housing.

3.2.3 Future VA/VE Activities

Future VA/VE tasks will be conducted to determine a minimum cost for the gas-filled lower end. Completing this task will provide the data needed on each of the alternative design approaches to select a preferred design for the Mark II lower end. Similar analyses will also have to be performed for the engine in order to arrive at a minimum Mark II engine cost. It has been estimated that Mark II heat pump module, which includes engine compressor, transmission, combustor, controls, safeties, and packaging, must meet a manufacturing cost goal of $1000 to be commercially viable. Achieving this goal will require several design iterations on the engine as well.

APPENDIX A

DESCRIPTION OF AN FPSE HEAT PUMP

A.0 DESCRIPTION OF AN FPSE HEAT PUMP

A layout drawing of the FPSE/HP compressor assembly is shown in Figure A-1. The power unit, located above the engine diaphragm, is based on the Mark I FPSE being developed at MTI under the GRI-sponsored "Residential FPSE Development Program" for use as a general-purpose Stirling-engine driver for electric generator and heat pump systems. The Mark I engine consists of:

- Natural gas combustor
- Displacer drive subsystem
- Heater head and thermal regenerator
- Cooler.

The lower end of the unit consists of a hydraulic transmission that efficiently transfers engine power to the refrigerant compressor. These subassemblies, along with the gas springs in the power module, form a coupled resonant system that effectively functions with the Stirling engine. In the engine, the displacer shuttles the engine working fluid (helium) between the hot and cold spaces, generating the driving pressure wave for the system. The pistons (refrigerant compressor) extract work from the gas to power the load (refrigerant circuit). Hence, in this system, power is extracted from the engine and delivered to the compressor through the hydraulic fluid, providing a force/displacement transfer path between the engine and compressor. This coupling also applies the proper dynamics to the engine, providing resonant characteristics and volumetric phase relationships.

Hermetic separation between the engine working fluid and refrigerant is achieved by employing a flexible metal diaphragm between the engine and hydraulic system. Engine power is transferred to the compressor through the volumetric displacements of the diaphragm, and corresponding displacement of oil in the hydraulic transmission induced by the pressure wave in the engine. Benefits to be derived from this system as compared to an inertially driven compressor are:

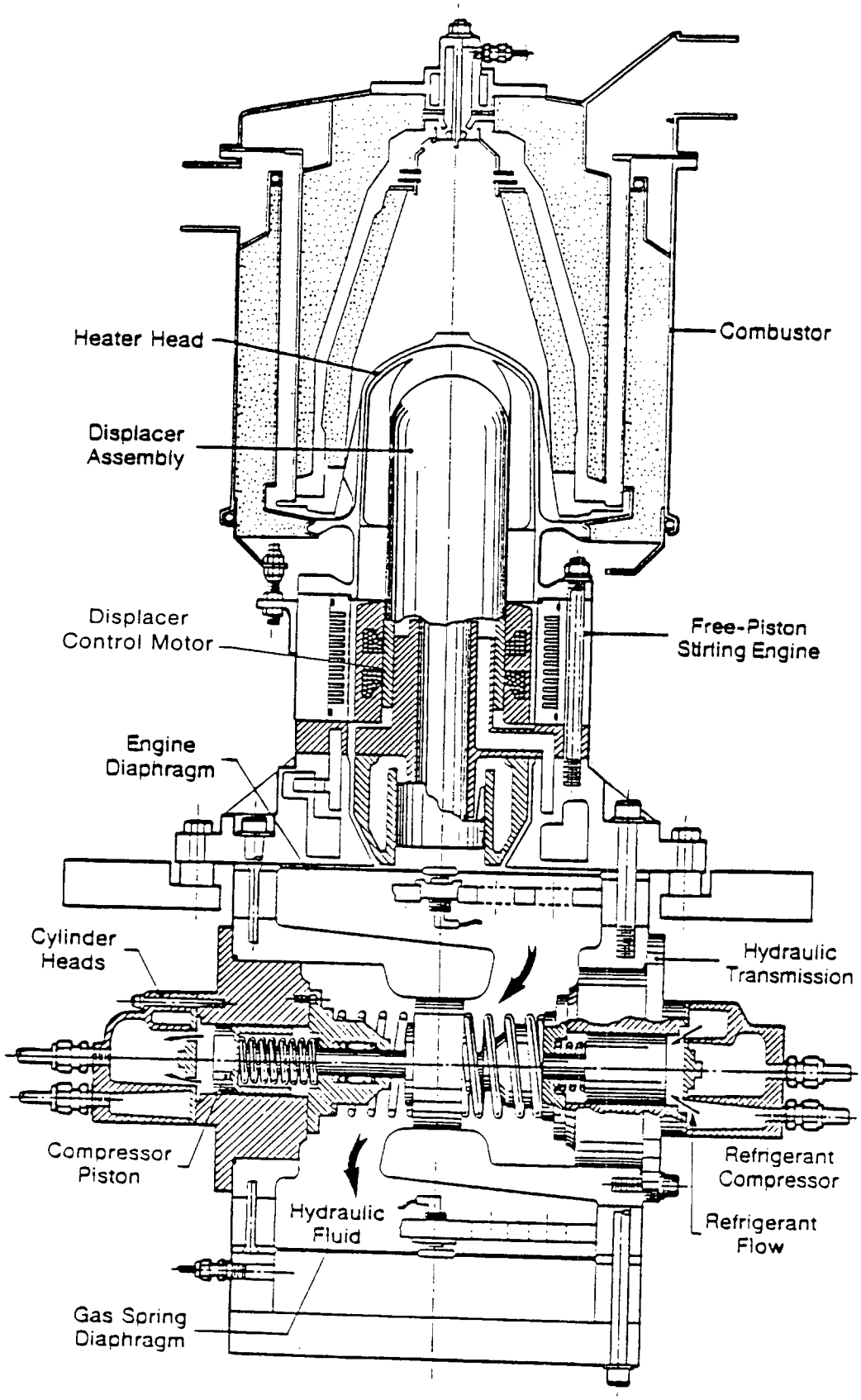

Fig. A-1 Mark I FPSE Heat Pump Compressor Assembly (Configuration is similar to EM No. 4)

- The use of the power transfer diaphragm reduces the system from a three-degree-of-freedom to a two-degree-of-freedom resonant system, improving its operating control and stability.

- Hermetic separation of the working fluids thermally isolates the refrigerant suction flow into the compressor, minimizing the superheating of the suction vapor and the associated penalties in compressor performance

- The compressor closely resembles a conventional heat pump refrigerant compressor, allowing for the design and use of some standard heat pump compressor parts.

A.1 Component Description

This section describes the individual components of the breadboard power module.

A.1.1 Engine Components

Combustor. The combustor consists of a natural-gas turbulent burner and a preheater. Figure A-2 is a schematic diagram of the combustor shown in Figure A-1. During operation at the 95°F ambient operating point, air enters the preheater at 95°F and is warmed to 1467°F by the exhaust gases. The preheated air is mixed with fuel in the burner and ignited, raising its temperature to 3550°F. The hot gas is then passed over the heater head, providing heat input to the engine. The gas from the head enters the preheater at 1550°F and is further cooled by transferring heat to the air intake stream. Combustor efficiency is predicted at 82% for the 95°F operating point, based on the higher heating value for natural gas. Initial rig testing of the combustor has indicated that the combustor will achieve this efficiency.

A drawing of the FPSE external heat system, consisting of the combustor and heater head, is shown in Figure A-3.

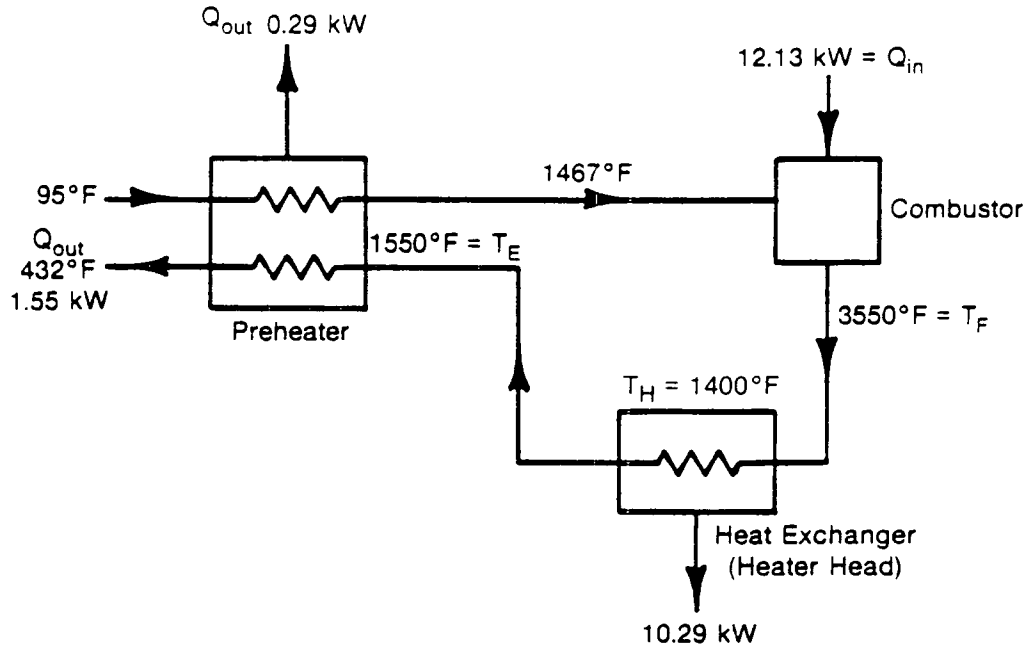

Predicted Efficiency Preheater:	≈0.94
Predicted Efficiency Combustion:	≈1.00
Predicted Efficiency Combustor:	≈0.85 (HHV)
Combustion Temperature:	3550°F
Air Preheater Temperature:	1467°F
A/F:	16.18
QA:	623 $SCFH_{32}$
QF:	38.5 $SCFH_{32}$
Radiation Losses:	2.4%
Heater Head Efficiency:	$0.93 = \frac{T_F - T_E}{T_F - T_H} = \frac{3550 - 1550}{3550 - 1400}$

$$\frac{Q_{in} - Q_{out}}{Q_{in}} = \frac{Q_{heat}}{Q_{in}}$$

Nomenclature:

T_H = Heater Head Temperature
Q_{in} = Heat into the System from Fuel (HHV)
Q_{out} = Heat Lost from the Preheater
A/F = Air/Fuel Ratio
QA = Airflow
QF = Fuel Flow

Fig. A-2 FPSE Combustor Schematic

842133-1

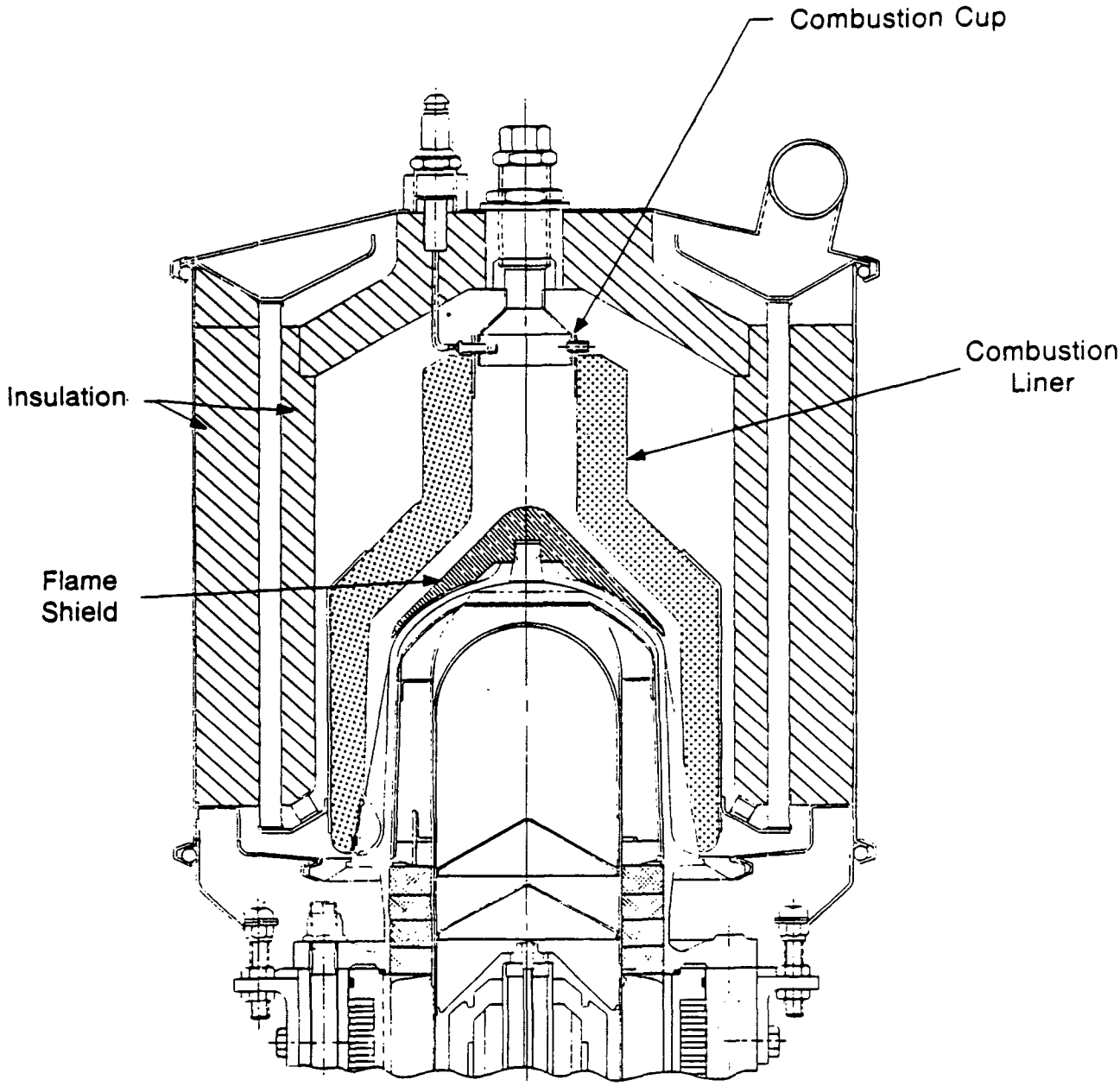

Fig. A-3 FPSE External Heat System

822159

Displacer Drive System. The displacer drive system consists of the displacer, displacer rod, gas bearing support, gas spring pistons and cylinders, and displacer control. The dynamic arrangement for the displacer drive system is shown in Figure A-4. As depicted, the displacer is a free member radially supported by gas bearings on the rod and axially balanced by the dynamic forces. The function of each component in this system is as follows.

Displacer - The displacer is used to shuttle the engine working fluid through the heat exchanger components in the engine to the hot expansion and cool compression volumes.

Displacer Rod - The displacer rod serves two functions: 1) provides radial alignment for the displacer; and, 2) it provides the thermodynamic power required to move the displacer against the losses from the heat exchanger pressure drop, gas spring thermal hysteresis, and gas spring leakage pumping loss.

Gas Bearing Support - Hydrostatic gas bearings are used to provide radial support for the displacer. The gas bearings are located along the displacer rod and are designed to be internally fed by bleeding gas out of the working volumes (compression space) during the high-pressure portion of the cycle.

Gas Spring Piston and Cylinders - Gas springs are employed to provide a restoring force to the displacer, providing its resonant characteristics. As shown in Figure A-5, the displacer gas springs are the heater-side gas spring located in the bottom end (cool end) of the displacer and the load-side gas spring located at the base of the displacer rod.

Displacer Control - The displacer control is a linear electric motor that allows external control of the displacer for start-up and stroke modulation, providing primary engine control to the system for load matching at different ambient operating conditions. Displacer control is achieved by applying a forcing function, F_c (Figure A-4), to the displacer to control stroke.

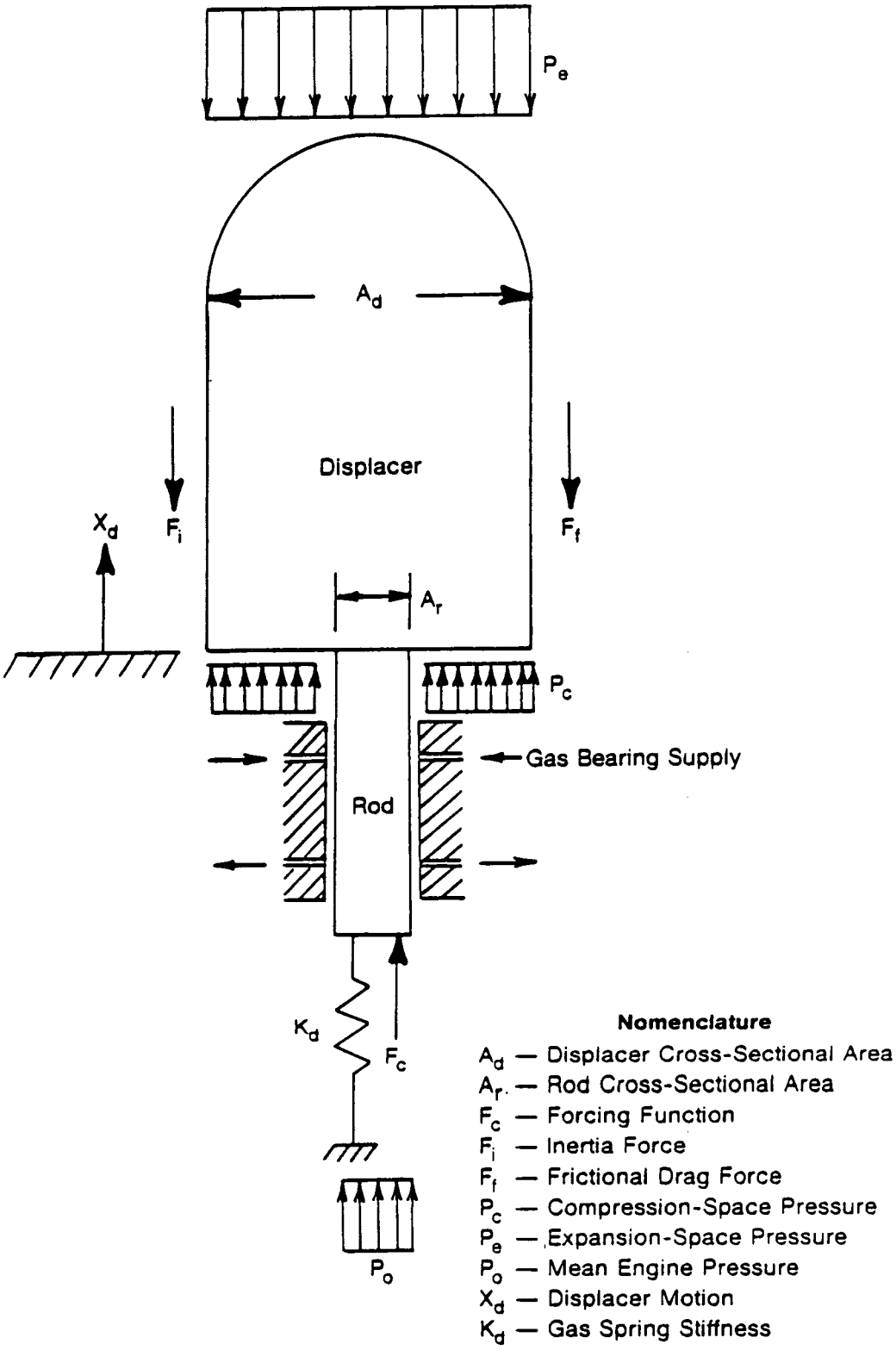

Fig. A-4 Displacer Rod Dynamics

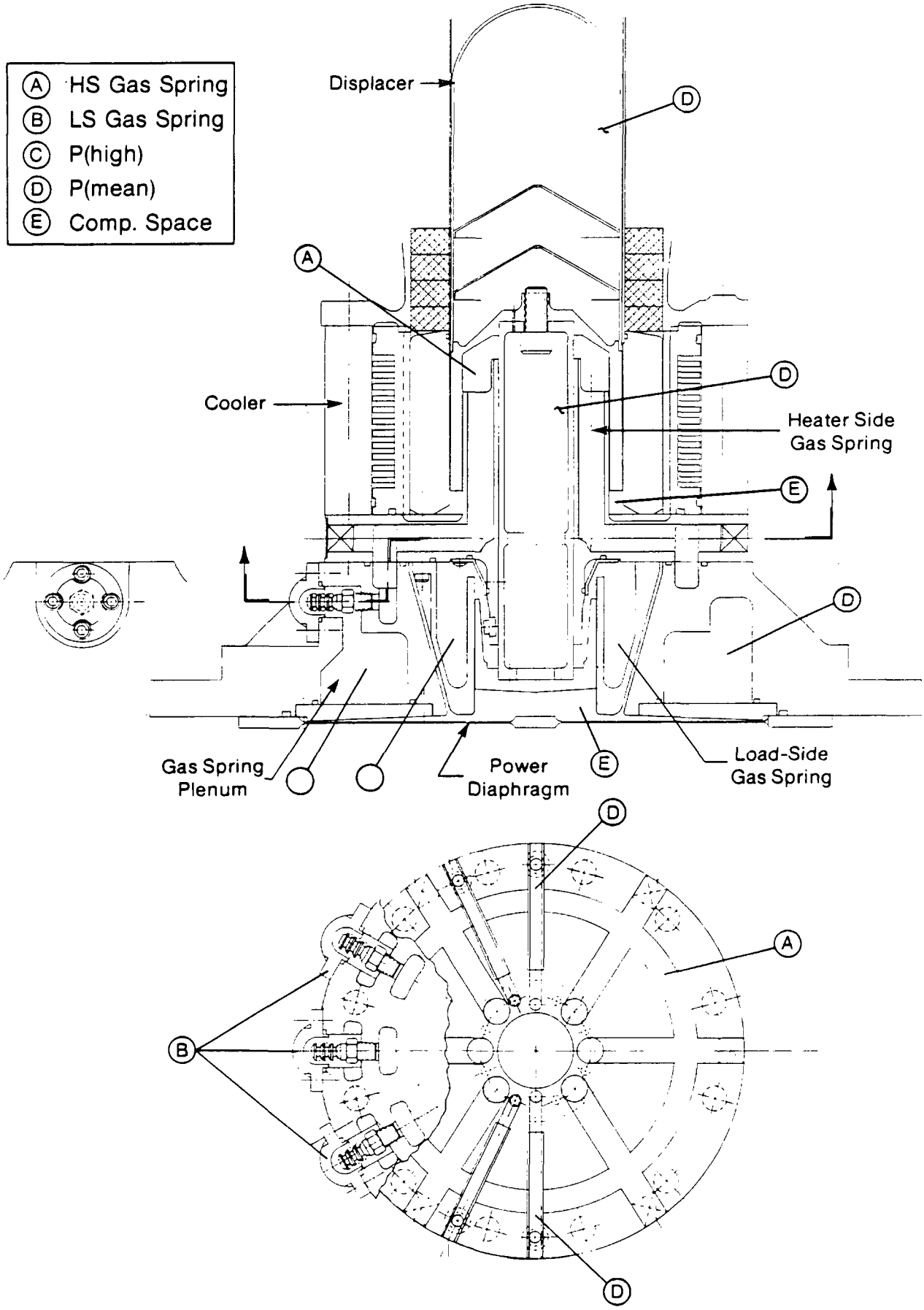

Fig. A-5 FPSE Displacer Gas Spring Design (Mark I engine configuration shown is similar to EM No. 4 FPSE)

85413

Heater Head and Thermal Regenerator. The heater head design for the engine is based on a monolithic heater head concept that has been under development for the past several years. The monolithic heater head design has the potential of being more reliable and less costly because it eliminates the fitting and brazing of the tubes required in a tubular design. The concept of the head is to use a one-piece head construction with fins on the inner and outer sides of the head to transfer the heat from the combusted gases in the combustor to the working fluid of the engine. The monolithic head configuration with external fins is shown in Figure A-6. The lower portion of the head houses an annular thermal regenerator. The regenerator serves to periodically exchange heat in the gas streams being shuttled between the cooler and heater head. This heat exchanger provides the internal storage of heat necessary to approach the ideal potential of Carnot efficiency. Standard, fine wire-mesh materials are used in the regenerator.

Cooler. The cooler is designed for water cooling with internal and external fins to enhance its heat transfer characteristics. The function of the cooler is to reject heat from the working fluid.

A.1.2 Rankine Refrigerant Compressor

The heat pump compressor is a resonant-piston compressor sinusoidally driven by the pressure wave in the engine. In the design for the compressor and hydraulic coupling (shown in Figure A-1), the compressor was positioned horizontally in order to allow the use of pistons, piston cylinders, cylinder heads, and valve assemblies similar to those commonly used in electrically driven, residential-size heat pump compressors. The operation of the compressor, closely linked to the operation of the hydraulic transmission, will be described in the following section.

A.1.3 Hydraulic Coupling (Transmission)

The hydraulic transmission provides the force displacement link between the engine and compressor. It consists of the engine power diaphragm, gas spring diaphragm, hydraulic oil, and compressor gas spring. The transmission transfers power from the engine to the compressor through deflections of the engine

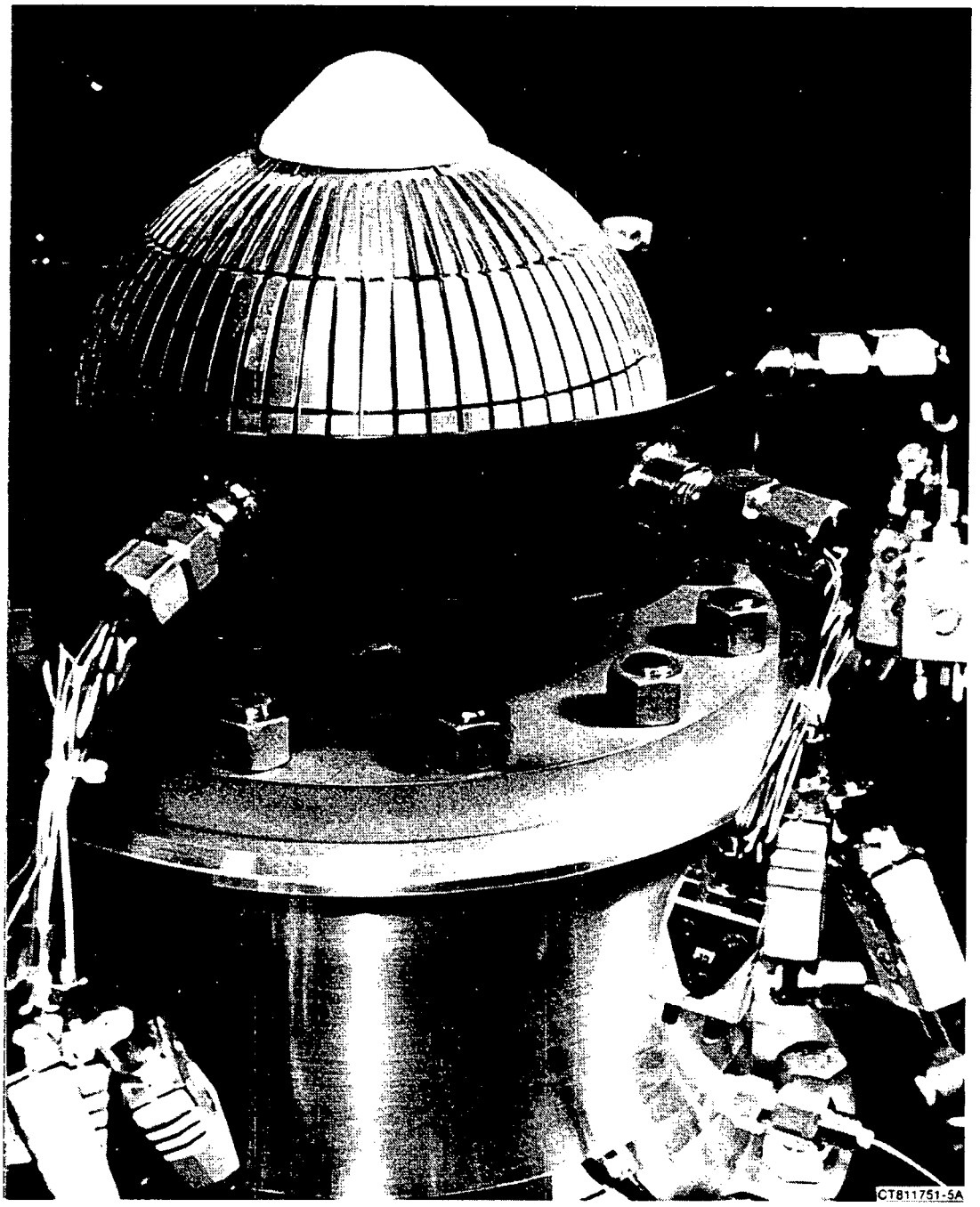

Fig. A-6 Monolithic Heater Head Configuration for EM Engine

power diaphragm, creating a force unbalance across the compressor drive piston (Figure A-1), forcing it to move. Compression spaces on either side of the piston compress the refrigerant. The lower gas spring diaphragm and compressor gas spring provide the restoring force for the compressor piston. Descriptively, the compressor operation can be seen more clearly in Figure A-7, which defines each of the oil volumes and the interaction between the oil and compressor piston. Starting with the downward motion of the engine diaphragm, the pressure increases in volume A, producing movement of the drive piston to the left. This motion produces two effects: 1) the oil in volume B acts on the compressor gas spring diaphragm (located at the bottom) causing it to deflect down, thus creating a restoring force on the drive piston; and, 2) the movement of the compressor piston to the left produces the compression stroke in the left compression volume and the intake stroke in the right compression volume.

The compressor and hydraulic transmission designs were selected for the following important features:

- Engine/compressor fluids are hermetically sealed from one another

- The horizontal design makes the compressor cylinder heads accessible from outside the machine. Thus, repairs can be easily made to the compressor valve assemblies without having to disassemble the entire machine, and the suction manifolds can be insulated to minimize superheating of the suction refrigerant vapor

- The diaphragms allow the Stirling engine power piston and compressor piston to be combined into a single mass, reducing the system from a three-degree to a two-degree-of-freedom system, thus improving the system's operating control.

The hardware for the hydraulic transmission housing and refrigerant compression cylinders is shown in Figure A-8.

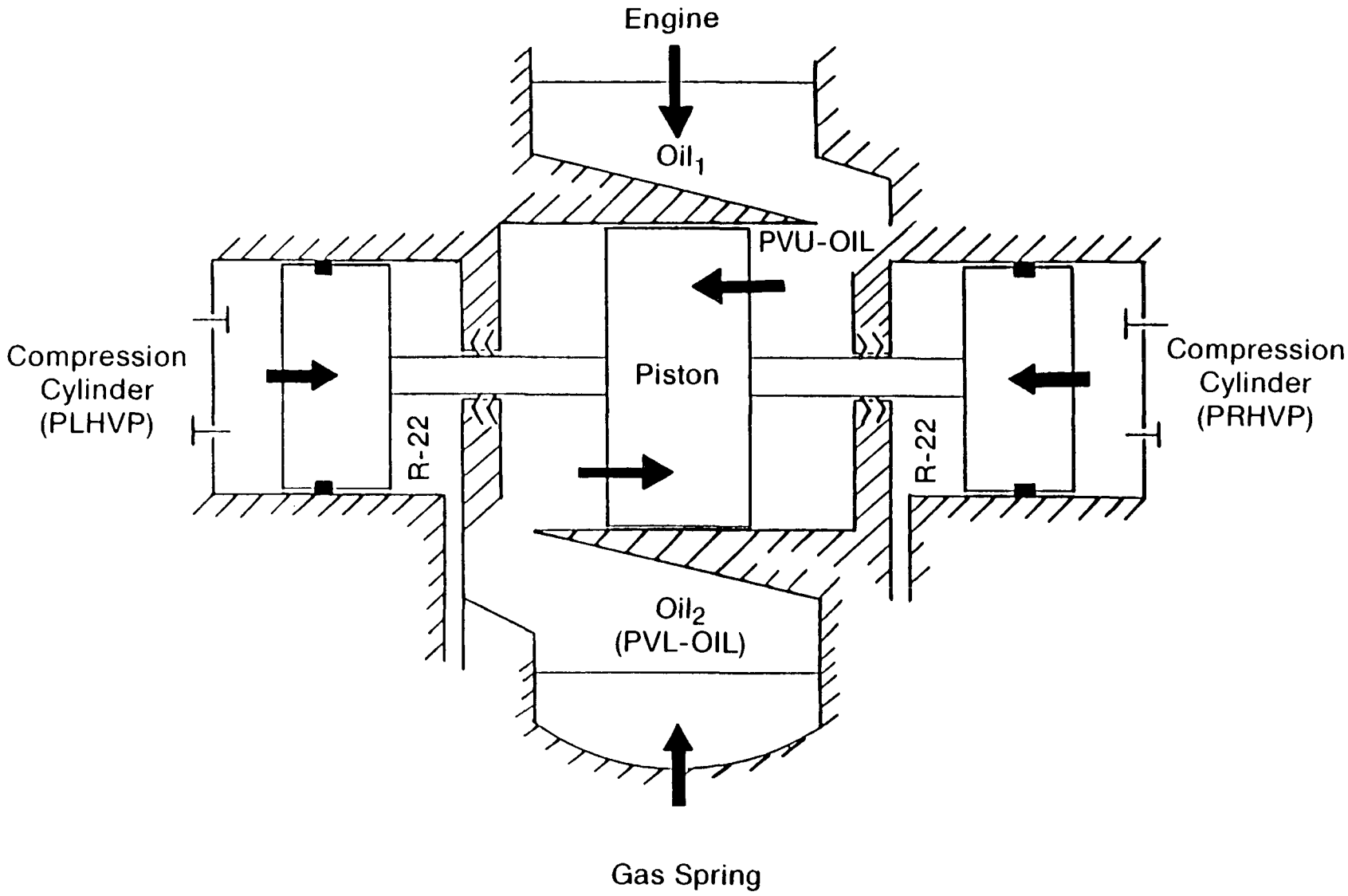

Fig. A-7 Hydraulic Transmission and Compressor Schematic

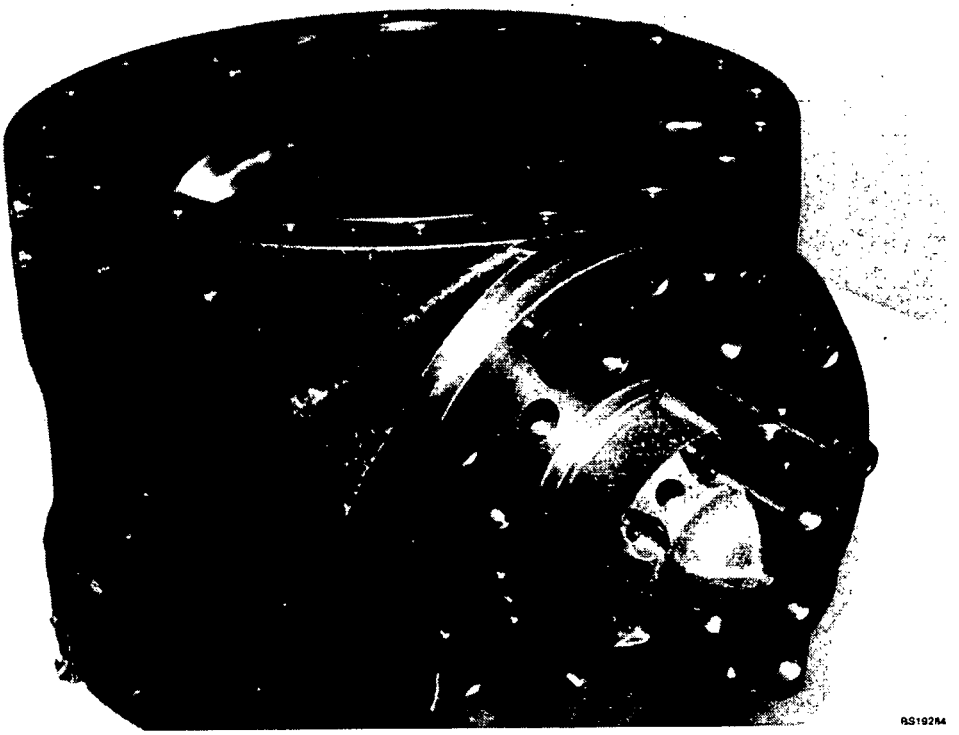

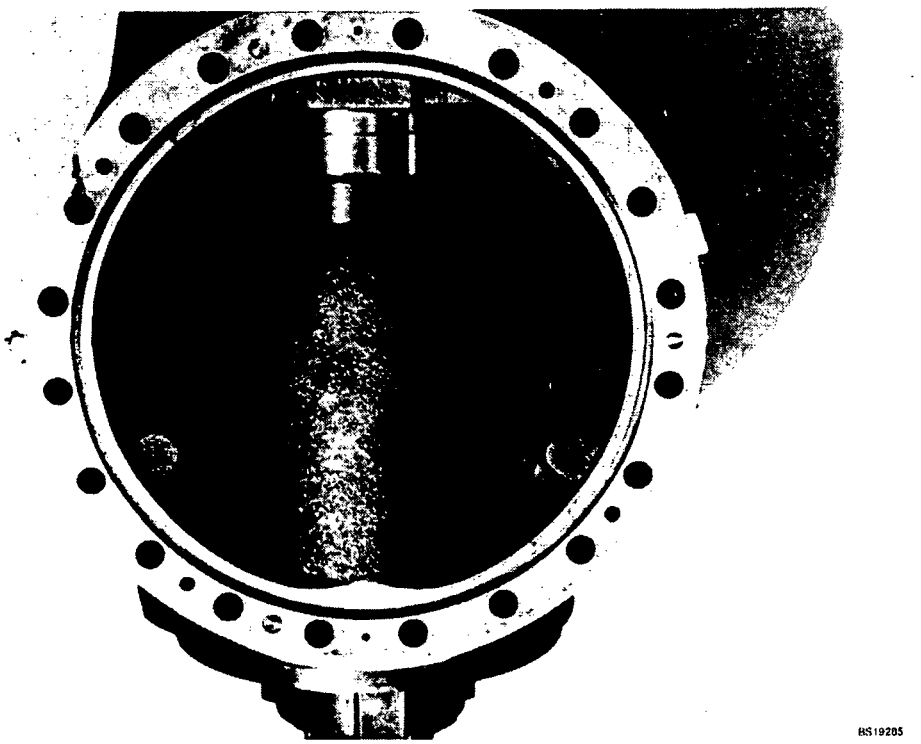

Fig. A-8 Compressor Housing

APPENDIX B

COOKE-YARBOROUGH ARTICULATED DIAPHRAGM ANALYSIS

COOKE-YARBOROUGH TECHNOLOGY (a Limited Company)
Trading address: Lincoln Lodge
Longworth
Nr Abingdon
Oxfordshire OX13 5DU
England

14 March 1986

Dr Ronald Vincent
Mechanical Technology Inc.
968 Albany-Shaker Road
Latham
New York 12110
USA

Dear Ronald

In response to your letter of 25 February, here is the Report giving the results of my calculations on the use of the articulated diaphragm in your Stirling/Rankine heat pump system.

I does appear possible to use such a diaphragm, and to keep the stress down to about 200 MPa with a volume amplitude of 6.3 cu in. The diaphragm material does however have to be somewhat thinner than in the TMG, and this may make fabrication of a suitably flat and stable diaphragm more difficult. There are also some possible additional bending stresses due to finite seal stiffness, which have not been evaluated. Reducing the volume amplitude to 5.4 cu in permits a much stiffer diaphragm, and and will be subject to smaller stresses due to seal stiffness.

As you will see, I have worked out numbers for a variety of combinations of parameters. Cases 1b and 1d appear to be the most favourable.

The Report raises a number of questions. If you think that the results so far are sufficiently hopeful, I would propose preparing a further information package which would address at least some of these questions.

You will see that I have been advised to turn myself into a Limited Company for doing overseas consultancy work. The reasons behind this are somewhat tedious, and relate to the problem of insurance cover.

I have been advised, also, to accompany the Report with a Disclaimer, of which MTI are asked to signify their acceptance. Ideally, my lawyer would have liked to see MTI's signature on this before I submitted the Report, but I persuaded him that this would hold things up too much.

My understanding of the various clauses is as follows.

Clause 1 is in effect the disclaimer mentioned in my letter of 20 September 1985.

Clause 2 is intended to deal with MTI's worry about the possibility of their being sued by a third party if there were a claim against me while I was engaged in work under contract to MTI.

Clause 3 includes in Clause 1 any information passed between us in letters or conversation.

Clause 4 is necessary since the Report deals with a topic for which a third party (Harwell) holds a patent.

Clause 5 asks MTI to signify their acceptance of the other clauses.

There is of course always the possibility of a formal legal interpretation being different from mine.

I must say that the legal and insurance side has proved much more difficult than the technical side (and far less interesting).

I shall naturally be very interested to hear your comments on the Report, and to hear whether MTI will be interested in receiving more information on this topic, as outlined in the Conclusions.

Yours sincerely

PRELIMINARY ASSESSMENT OF AN ARTICULATED DIAPHRAGM FOR USE IN A STIRLING-CYCLE DRIVEN HEAT PUMP

EH Cooke-Yarborough FEng

NOTE:
This information is supplied to Mechanical Technology Inc. by Thurfin Services Limited, trading as COOKE-YARBOROUGH TECHNOLOGY, and is subject to the Disclaimer of which a copy appears at the back of this Report.

13 March 1986

PRELIMINARY ASSESSMENT OF AN ARTICULATED DIAPHRAGM FOR USE IN A STIRLING-CYCLE DRIVEN HEAT PUMP

EH Cooke-Yarborough FEng

SUMMARY

The diaphragm is required to transmit pressure changes between the working gas of a free-displacer Stirling engine and the hydraulic fluid which drives a Rankine heat pump, and between this fluid and the gas in the bounce space.

This Report studies the application of the Articulated Diaphragm (Ref 1) in this application. Calculations are presented of the stresses in the metal and distortions of the seals in various diaphragms designed to give volume amplitudes of 5.4 cu in and 6.3 cu in, within the mechanical constraints of the existing MTI free-displacer engine. It also obtains corresponding figures for a design to a smaller overall diameter, and for a design aimed at minimum seal disortion.

Within the scope of the work covered by this Report, it appears that an articulated diaphragm can be designed to provide a volume amplitude of 6.3 cu in within the mechanical constraints of the existing MTI free-displacer engine, and without exceeding a stress in the diaphragm material of 200 MPa, provided that the seals are not found to introduce excessive radial bending stresses at the edges.

On the basis of the limited information available on the fatigue limit of elastomers, it is concluded that at normal temperatures the alternating component of the stresses in the flexing O-ring seals is well below the fatigue limit.

A number of points are noted, which need clarifying by further work.

BASIS OF CALCULATIONS

An articulated diaphragm consists of a flat metal disc with a large central hole. The outer edge is flexibly sealed to the body of the engine, and the inner edge to a rigid central hub, which moves with the diaphragm. It is assumed that the seals consist of pairs of O-rings, as illustrated in Fig 5 of the attached British Patent Specification 1 539 034.

The flexible seals largely relieve the edges of the diaphragm from radial bending stress. If these stresses can be neglected, the major stresses in the metal are:-

Circumferential bending stresses due to deflection of the diaphragm into a shallow cone.

Hoop stresses due to the inner edge stretching and the outer edge being drawn inwards as the diaphragm deflects.

The first of these varies linearly with deflection, and formulae are available for calculating this stress accurately.

The second varies with the square of deflection. With the deflections currently used in the Thermo-mechanical Generator, it is second-order. Thus only approximate formulae have so far been developed for calculating it. The calculation used ignores the stress relief resulting from radial stretching of the diaphragm, so certainly over-estimates the hoop stresses for this reason. The calculation also assigns equal hoop stresses to the inner and outer edges. This is thought to be a reasonable approximation for radius ratios up to about 1.4, but the calculation may be seriously in error for much larger ratios between the inner and outer radii.

The original design of the diaphragm for the Thermo-Mechanical Generator (TMG) was required to translate a pressure applied to the diaphragm into a force on the central hub. The diaphragm had therefore to have some rigidity. In the heat-pump application the diaphragm has simply to transfer pressure between gas and hydraulic fluid, so in principle no rigidiy is necessary. This can allow the diaphragm to be thinner, reducing the deflection stress, so increased deflection is possible.

The calculations carried out on a diaphragm for the heat-pump show that, because of the increased deflection and reduced bending stresses, the hoop stresses may exceed the bending stresses. Because of the approximations in calculating the hoop stresses, the results obtained must be treated with caution especially for radius ratios greater than 1.4. It is believed, however, that the errors are in the direction of over-estimating stress, so the calculations can be regarded as conservative.

DIMENSIONS

For a given diaphragm stress, the swept volume increases in proportion to the cube of the outer diameter, so this is made as large as possible. The flange of the MTI machine contains 0.562" diameter holes on a 11.5" bolt circle. The inner edges of these holes are therefore at a radius of 139mm.

In the present calculations, the outer seal radius has been made 134.74mm on the centre line of the groove. With a groove width of 7.15 $\pm$0.15mm, this may come within 0.5mm of the holes, so some reduction in diameter may be needed in practice, especially if it is found necessary to back the flexing seals with static seals.

The diaphragm must overlap the centre line of the seal. An overlap of 3.3mm has been chosen, which gives a clearance of 0.28 mm between the diaphragm edges and the groove edges. The overall diaphragm diameter used in the calculations for the present nominal 10" engine structure is therefore actually 276mm (10.87").

The overlap over the seals causes the diaphragm to deflect slightly more than the hub, leading to the Leverage Ratio calculated in the attached tables. This has a significant effect on diaphragm stress and stiffness. (The Diaphragm Stroke given in the attached tables is strictly the hub stroke.)

The O-rings are assumed to be to British Standard 4518, with a minor diameter of 5.7mm nominal. They are compressed to 80% of this.

DISCUSSION OF COMPUTED RESULTS

The results are divided into three groups:-

1) Diaphragms on 10" diameter nominal (Cases 1a to 1f).

2) Diaphragms on 9" diameter nominal (Cases 2a to 2c).

3) One calculation on a 10" nominal diaphragm with the radius ratio increased to minimize seal deflection (Case 3).

10" Diameter Designs

Cases 1a and 1b show that it is possible to design a diaphragm with a volume amplitude of 6.3 cu in without significantly exceeding a stress of 200 Mpa in the diaphragm material. This calls for a diaphragm only 1mm thick, whose stiffness is very low, and highly non-linear. To maintain the mean position of the diaphragm within ±0.5mm will call for the mean pressure differential across it to be held within about 750 or 500 Pascals respectively (0.1 or 0.075 psi). The effective stiffness could be increased as much as may be necessary by using springs to control hub movement.

In practice, the seals are far from being perfectly flexible, and it is probable that in this case they would add a great deal to the stiffness. Consequently the radial bending moments at the edges due to seal stiffness would need to be calculated to ensure that the stress here is not excessive. This is outside the scope of the present study.

Cases 1c and 1d show that if the volume amplitude is limited to 5.4 cu in, then a stiffer diaphragm can be used without significantly exceeding a stress of 200 Mpa. In these cases the stiffness at small deflections is increased by a factor of about 5.

1e and 1f show that if a metal stress of 300 Mpa is acceptable, then a volume amplitude of 6.3 cu in is achievable with a diaphragm 2mm thick, which increases the small-deflection stiffness by a factor of 8. Thus, in Case 1e, to maintain the mean position to within ±0.5mm would now require the pressure differential to be held to within about 2 psi, without the need for added springs.

9" Diameter Designs

Cases 2a to 2c are for a volume amplitude of 5.4 cu in at various radius ratios. It is shown that in each case the volume amplitude can be achieved, provided that a metal stress of about 260 MPa can be accepted. The diaphragm has to be thin, leading to very low stiffnesses near to the mid position, so that springs would need to be added. As in Cases 1a and 1b, radial bending stresses due to seal stiffness would need to be examined.

Design to Minimize Seal Distortion (Case 3)

To achieve this, the inner radius of the diaphragm was reduced to the point where the inner edge stress rose to about 300 MPa. The stiffness of this design, for small deflections, is very low. It has to be repeated that, with such a large radius ratio, the stress calculations are probably in serious error.

Seal distortion is reduced to about two thirds of the value in Cases 1c and 1d. It is thought that this does not justify the shortcomings of this design.

FATIGUE LIMITS

Metal

Report AERE - R7693 is attached. This is a survey carried out 12 years ago of published material on the fatigue of stainless steel. Few of the published tests went beyond 10^7 cycles.

The conclusion is that for EN 58F material the probability of ultimate failure is 50% at a stress just over 300 MPa. Thus 300 MPa appears to be the fatigue limit, that is the stress below which failure is not expected. For the TMG a figure 2/3 of this was chosen, for the following reasons.

The material was being stressed in a manner different from that used in the published tests.

There might be differences in processing between the material used and that on which the published information was based.

A life of 3×10^{10} cycles was a minimum requirement.

This was supported by cycling one diaphragm at 100 Hz continuously for 2 years at a peak stress of 200 MPa.

Limiting the stress to 200 MPa, no diaphragm failures have ever been experienced in well over 120,000 engine hours. In early experiments, some displacer spring failures occurred. In each case these could be traced to poor design, or poor machining, causing the presence of a stress raiser. No failures were experienced once these problems had been

overcome. This suggests that, while 200 MPa is a conservative figure, it is probably not unduly so.

It is suggested that if it is intended to use stresses significantly in excess of 200 MPa, this should be supported by extensive life tests of components identical in material, fabrication and treatment to the components which it is intended to use. The tests should be carried out at a stress of say 10% above the design stress of the component.

Elastomer Seals

There is far less published material available on fatigue of elastomers. The existence of a fatigue limit in a variety of natural and synthetic rubber formulations is supported by Ref 2. This shows that if temperature rise is limited, fatigue failure is caused by the growth of flaws or cuts, considerably enhanced by any oxygen which may be present. In the systems under discussion, stress-raisers due to flaws are unlikely to be present in high-quality O-rings designed for vacuum applications, and the rings are not exposed to oxygen. In the heat-pump application it is of course necessary to ensure that there is compatibility between the hydraulic fluid and the material of the seal, so that flaws are not produced by chemical action.

Ref 3 describes work which leads to the conclusion that, if the heat generated by internal friction is not conducted away fast enough, failure results from temperature rise due to internal energy dissipation. If large temperature rises are prevented by adequate heat conduction, the work suggests that there is a fatigue limit at between 700 to 1000 psi, for a wide range of thermoplastics. The paper does not give the elastic modulus for the materials tested, but if this is 5.3 MPa (the highest of three figures for O-rings given in Ref 4), then 700 psi corresponds to an axial strain of about 90%.

It is not entirely straightforward to relate the tilt and shear strains given in the attached tables to equivalent axial strains, but these can be expected to be of the same order. The tilts given in the attached tables are all less than 10%, and the shear strains are all less than 4%. Comparing these figures with a fatigue limit at a strain of 90%, suggests that there is a larger margin of safety in the seals than there is in the metal of the diaphragm.

It will however be necessary to look at possible temperature rises in the seals. The seal distortions in the attached diaphragm designs are about 4 times greater than in the TMG, so the power dissipation at 115 Hz would be 16 times greater. However, the viscous power dissipation is proportional to the square of frequency, so at 60 Hz the power dissipated per unit length of seal will be about 4 times greater than in the TMG.

In the articulated diaphragm the seals are operated at constant alternating strain (not in the constant-stress condition described in Ref 3), and it is found experimentally

that the rate of heat generation decreases with rising temperature, so the heating process is self-limiting. This is supported by Ref 3, which shows the loss compliance rising with temperature. It should be possible to calculate this temperature rise approximately, but this is beyond the scope of the present Report.

Another aspect which may need examining is slippage between the seal and the metal surfaces between which it is compressed. In the TMG the shear forces are so much smaller than the compression forces that slippage can be excluded as a possibility. However in the heat-pump application the shear forces are considerably greater, so this ought to be re-examined, especially in the context of increased seal stiffness at low temperatures. This is again beyond the scope of the present Report.

Because the power output of the TMG is relatively low, stiffening of the seals at low temperatures causes an added mechanical load, which reduces the oscillation amplitude and so prevents excessive shear force. Most of the TMG power output then goes into mechanical heating of the seal, and this heating soon restores normal flexibility.

In the heat pump application the power generated is much greater, so it may be necessary, when starting under cold conditions, to take precautions to prevent the engine from reaching full amplitude until the seals have achieved normal flexibility.

According to the Du Pont's data, standard Viton begins to stiffen just below 0°C. However special formulations can be provided for dynamic applications down to -40°C.

CENTERING OF HUB

Neither the diaphragm nor the hub are positively located laterally by the seals, so it is possible for the inner and outer edges of the diaphragm to make a metal-to-metal contact with the edges of the recesses which contain the seals. This should cause no problems, provided there is no lateral force tending to feed these metal surfaces towards one another as they wear. If the diaphragm were not quite horizontal, the weight of the hub might provide such a lateral force. To counter this possibility, it is desirable to provide independent means of locating the hub laterally. In the TMG, a flexing metal strip across the diameter provides this location, but with the larger hub stroke in the heat pump application, something more elaborate may be needed.

The possible need to provide added hub stiffness has already been mentioned. A stack of double-acting springs of the type described by in Ref 5 would perform both functions. This could be located in the hydraulic fluid.

PRESSURE DIFFERENTIAL ACROSS DIAPHRAGM

This depends both on diaphragm stiffness and on hub mass, so cannot be calculated until a figure for hub mass has been obtained. Hub design is beyond the scope of the present Report.

This pressure differential is expected to be small, and not to add significantly to the stresses calculated in the attached tables.

CONCLUSIONS

Within the scope of the work covered by this Report, it appears that an articulated diaphragm can be designed to provide a volume amplitude of 6.3 cu in within the mechanical constraints of the existing MTI free-displacer engine, and without exceeding a stress in the diaphragm material of 200 MPa (Cases 1a and 1b), provided that the seals are not found to introduce excessive radial bending stresses at the edges. This design does however, require a material thickness of only 1mm, which may lead to practical problems in making a sufficiently flat and stable diaphragm. If the smaller volume amplitude of 5.4 cu in is acceptable, then a 1.7mm diaphragm can be used (Cases 1c and 1d). This is 5 times stiffer, and should make acceptable flatness easier to achieve.

In both cases the most favourable radius ratio appears to be in the region of 1.6 (Cases 1b and 1d).

On the basis of the limited information available on the fatigue limit of elastomers, it is concluded that at normal temperatures the alternating component of the stresses in the flexing O-ring seals is well below the fatigue limit.

A number of points have been noted, which need clarifying by further work.

These include:-

Calculation of radial bending stresses due to finite seal stiffness.

Approximate calculation of temperature rise in seals.

Calculation of shear forces between seals and contacting metal surfaces, and of the coefficient of friction necessary to ensure that slippage does not occur.

Design of springs to locate hub laterally, and to provide increased stiffness.

Approximate calculation of hub mass.

Calculation of alternating pressure difference across diaphragm, and resultant pressure stresses.

REFERENCES

1) Cooke-Yarborough "Articulated Diaphragms for Thermo-mechanical Generators". Proceedings of 20th Intersociety Energy Conversion Conference" ISBN 0-89883-728-6, August 1985, pp 3.338-3.343.

2) Lake and Lindley "The Mechanical Fatigue Limit for Rubber". Journal of Applied Polymer Science, Vol 9, 1965, pp 1233-1251.

3) Riddell, Koo and O'Toole "Fatigue Machanisms of Thermoplastics". Polymer Engineering and Science, October 1966, p363.

4) Curro and Salazar "Mechanical Behaviour of O-Rings". Rubber Chemistry and Technology. Vol 46, No 2, June 1973, p 530

5) Cooke-Yarborough "Metal Spring for Tuning and Positioning the Displacer of a Short-stroke Stirling Engine" Proceedings of 20th Intersociety Energy Conversion Conference" ISBN 0-89883-728-6, August 1985, pp 3.212-3.217

13 March 1986

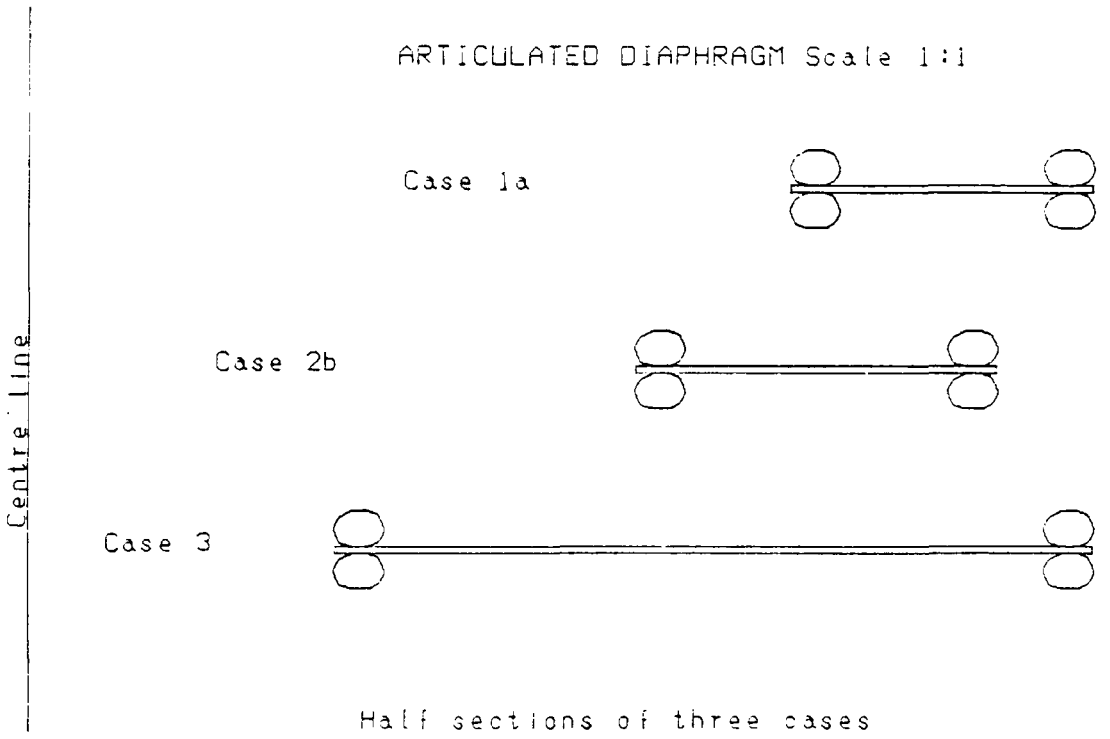

Half sections of three cases

ARTICULATED DIAPHRAGM Program 13 Mar 86 Run on 13 Mar 86 Case 1a
6.3 cu in volume amplitude Thickness 1mm Diam. 10" nominal

GIVEN DATA

Diaph rad ratio	1.4
Outer Seal Radius	.13474
Inner Seal Radius	.1019
Seal depth (80%)	.00456
Diaphragm Overlap	.0033
" Thickness	.001
" Stroke	.00467
Pressure Diff.	0
Elastic Modulus	2.16E11
Poisson's Ratio	.283

DERIVED DATA

Seal Radius Ratio	1.322277
Diaphragm " "	1.4
Diaphragm area	.0442635
Seal Leverage "	1.200974

RESULTS

Swept Volume (cc)	206.7103
Vol Amp. (cu in)	6.304665

STRESSES AT INNER EDGE (MPa)

Bending	84.66127
Hoop	118.7067
Total	203.3680

STRESSES AT MID-CIRCLE (MPa)

	Circumferential	Radial
Bending	70.55106	19.96595
Stretching	12.44173	43.96372
Pressure		
Total	82.99279	63.92967

STIFFNESS	N/mm	Pa/mm
Small deflections	66.66542	1506.105
Full deflection	165.5996	3741.227

SEALS

Tilt	7.110231 %
Radial shear	2.600068 %

ARTICULATED DIAPHRAGM Program 13 Mar 86 Run on 13 Mar 86 Case 1b
6.3 cu in volume amplitude Thickness 1mm Diam. 10" nominal

GIVEN DATA

Diaph rad ratio	1.6
Outer Seal Radius	.13474
Inner Seal Radius	.089575
Seal depth (80%)	.00456
Diaphragm Overlap	.0033
" Thickness	.001
" Stroke	.00517
Pressure Diff.	0
Elastic Modulus	2.16E11
Poisson's Ratio	.283

DERIVED DATA

Seal Radius Ratio	1.504214
Diaphragm " "	1.6
Diaphragm area	.0400531
Seal Leverage "	1.146131

RESULTS

Swept Volume (cc)	207.0745
Vol Amp. (cu in)	6.315772

STRESSES AT INNER EDGE (MPa)

Bending	77.88458
Hoop	115.3762
Total	193.2608

STRESSES AT MID-CIRCLE (MPa)

	Circumferential	Radial
Bending	59.91122	16.95487
Stretching	13.91628	49.17413
Pressure		
Total	73.82750	66.12900

STIFFNESS	N/mm	Pa/mm
Small deflections	39.78343	993.2674
Full deflection	112.2647	2802.897

SEALS

Tilt	5.723458 %
Radial shear	2.249846 %

ARTICULATED DIAPHRAGM Program 13 Mar 86 Run on 13 Mar 86 Case 1c
5.4 cu in volume amplitude Thickness 1.7mm Diam. 10" nominal

GIVEN DATA

Diaph rad ratio	1.4
Outer Seal Radius	.13474
Inner Seal Radius	.1019
Seal depth (80%)	.00456
Diaphragm Overlap	.0033
" Thickness	.0017
" Stroke	.004
Pressure Diff.	0
Elastic Modulus	2.16E11
Poisson's Ratio	.283

DERIVED DATA

Seal Radius Ratio	1.322277
Diaphragm " "	1.4
Diaphragm area	.0442635
Seal Leverage "	1.200974

RESULTS

Swept Volume (cc)	177.0538
Vol Amp. (cu in)	5.400141

STRESSES AT INNER EDGE (MPa)

Bending	123.2755
Hoop	87.08867
Total	210.3642

STRESSES AT MID-CIRCLE (MPa)

	Circumferential	Radial
Bending	102.7296	29.07247
Stretching	9.127820	32.25378
Pressure		
Total	111.8574	61.32626

STIFFNESS	N/mm	Pa/mm
Small deflections	327.5272	7399.495
Full deflection	450.9176	10187.13

SEALS

Tilt	6.090134 %
Radial shear	2.470778 %

ARTICULATED DIAPHRAGM Program 13 Mar 86 Run on 13 Mar 86 Case 1d
5.4 cu in volume amplitude Thickness 1.7mm Diam. 10" nominal

GIVEN DATA

Diaph rad ratio	1.6
Outer Seal Radius	.13474
Inner Seal Radius	.089575
Seal depth (80%)	.00456
Diaphragm Overlap	.0033
" Thickness	.0017
" Stroke	.00445
Pressure Diff.	0
Elastic Modulus	2.16E11
Poisson's Ratio	.283

DERIVED DATA

Seal Radius Ratio	1.504214
Diaphragm " "	1.6
Diaphragm area	.0400531
Seal Leverage "	1.146131

RESULTS

Swept Volume (cc)	178.2363
Vol Amp. (cu in)	5.436206

STRESSES AT INNER EDGE (MPa)

Bending	113.9646
Hoop	85.47817
Total	199.4427

STRESSES AT MID-CIRCLE (MPa)

	Circumferential	Radial
Bending	87.66506	24.80921
Stretching	10.31008	36.43138
Pressure		
Total	97.97514	61.24059

STIFFNESS	N/mm	Pa/mm
Small deflections	195.4560	4879.923
Full deflection	286.7440	7159.098

SEALS

Tilt	4.926381 %
Radial shear	2.120180 %

ARTICULATED DIAPHRAGM Program 13 Mar 86 Run on 13 Mar 86 Case 1e
6.3 cu in volume amplitude Thickness 2mm Diam. 10" nominal

GIVEN DATA

Diaph rad ratio	1.4
Outer Seal Radius	.13474
Inner Seal Radius	.1019
Seal depth (80%)	.00456
Diaphragm Overlap	.0033
" Thickness	.002
" Stroke	.00467
Pressure Diff.	0
Elastic Modulus	2.16E11
Poisson's Ratio	.283

DERIVED DATA

Seal Radius Ratio	1.322277
Diaphragm " "	1.4
Diaphragm area	.0442635
Seal Leverage "	1.200974

RESULTS

Swept Volume (cc)	206.7103
Vol Amp. (cu in)	6.304665

STRESSES AT INNER EDGE (MPa)

Bending	169.3225
Hoop	118.7067
Total	288.0293

STRESSES AT MID-CIRCLE (MPa)

	Circumferential	Radial
Bending	141.1021	39.93190
Stretching	12.44173	43.96372
Pressure		
Total	153.5438	83.89562

STIFFNESS	N/mm	Pa/mm
Small deflections	533.3234	12048.84
Full deflection	731.1917	16519.08

SEALS

Tilt	7.110231 %
Radial shear	3.379699 %

ARTICULATED DIAPHRAGM Program 13 Mar 86 Run on 13 Mar 86 Case 1f
6.3 cu in volume amplitude Thickness 2mm Diam. 10" nominal

GIVEN DATA

Diaph rad ratio	1.6
Outer Seal Radius	.13474
Inner Seal Radius	.089575
Seal depth (80%)	.00456
Diaphragm Overlap	.0033
" Thickness	.002
" Stroke	.00516
Pressure Diff.	0
Elastic Modulus	2.16E11
Poisson's Ratio	.283

DERIVED DATA

Seal Radius Ratio	1.504214
Diaphragm " "	1.6
Diaphragm area	.0400531
Seal Leverage "	1.146131

RESULTS

Swept Volume (cc)	206.6739
Vol Amp. (cu in)	6.303555

STRESSES AT INNER EDGE (MPa)

Bending	155.4679
Hoop	114.9303
Total	270.3982

STRESSES AT MID-CIRCLE (MPa)

	Circumferential	Radial
Bending	119.5907	33.84416
Stretching	13.86250	48.98409
Pressure		
Total	133.4532	82.82825

STIFFNESS	N/mm	Pa/mm
Small deflections	318.2674	7946.139
Full deflection	462.6697	11551.41

SEALS

Tilt	5.712388 %
Radial shear	2.868721 %

Lincoln Lodge, Longworth, Nr Abingdon, Oxfordshire, OX13 5DU, England

Tel: Longworth (0865) 820224

21 May 1986

Dr Ronald Vincent
Mechanical Technology Inc
968 Albany-Shaker Road
Latham
New York 12110
USA

Dear Ron

As agreed in our telephone conversation yesterday, I enclose a copy of Colin West's 1971 Harwell Memorandum (2431) on "Corrugated Diaphragms for Thermo-mechanical Generators".

The articulated diaphragm had not then been thought of, and the flat diaphragm with which he compares the corrugated diaphragm was of course the original design. This was rigidly brazed to a central hub, and was rigidly clamped at its outer edge. The main stresses were therefore cantilever bending stresses.

The main purpose in using corrugations was to avoid the large variations in diaphragm stiffness which resulted from stresses due to radial temperature gradients in the flat diaphragm.

In the case of the articulated diaphragm, the resilient mounting relieves these stresses, so corrugations are not needed for this purpose (though they would improve linearity).

You say that you are concerned about the low stiffness of the articulated diaphragm. As I said on the telephone, the effectiveness of a diaphragm as a spring depends on the volume of diaphragm material and on the uniformity with which it is stressed.

Material under simple tension is uniformly stressed. Stainless steel uniformly stressed to 200 MPa will store just under 100 kilojoules per m^3.

A beam deflected to constant radius stores energy less efficiently because the stress varies from the maximum at the surfaces to zero at the centre. The articulated diaphragm approximates to this case. Calculations for a particular case show an energy storage about 15% of that of uniformly-stressed material.

A beam deflected as a cantilever stores energy still less uniformly, because the stress varies not only through the material but also along its length. The rigidly-mounted diaphragm approximates to this case. A calculation done in 1969 by Colin West (AERE Memo 2177) indicated an energy

EH Cooke-Yarborough Limited (trading as COOKE-YARBOROUGH TECHNOLOGY)
Registered Office: 25 Thurloe Street, London SW7 2LH

storage about 7.5% of that of the uniformly-stressed material.

Not only does the articulated diaphragm store more energy per unit volume of material, but it can also be thicker, and so contains a larger volume of material, than a rigidly-mounted diaphragm.

This suggests that, within given constraints of swept volume, diameter and stress, other types of diaphragm will not give you better energy storage and greater stiffness than the articulated diaphragm.

If necessary, the stiffness of the articulated diaphragm can be increased greatly by increasing the thickness. There is a reduction in swept volume, but the loss is not great, as Fig 2 of my Miami paper shows.

As mentioned in the 13 March Report I sent you, stiffness can also be increased by supporting the hub with a spring, such as described in my other Miami paper (859072). Two such springs cascaded would accomodate a stroke of 4mm and would have an overall stiffness of about 1000 N/mm. Used to support the hub in Case 1c, they would increase the stiffness at small deflections to 30000 Pa/mm. Thus to maintain the mean hub position to within ±0.5mm would require the pressure differential to be held to within ±2.5 psi, which is quite close to your target.

The springs would also perform the function of centering the hub (see Page 6 of my 13 March Report).

I shall be interested to hear the results of your investigation of the corrugated diaphragm, and how these compare with those for the articulated diaphragm.

Yours sincerely

ARTICULATED DIAPHRAGM Program 13 Mar 86 Run on 13 Mar 86 Case 2a
5.4 cu in volume amplitude Thickness 1mm Diam. 9" nominal

GIVEN DATA

Diaph rad ratio	1.4
Outer Seal Radius	.12204
Inner Seal Radius	.0928286
Seal depth (80%)	.00456
Diaphragm Overlap	.0033
" Thickness	.001
" Stroke	.00486
Pressure Diff.	0
Elastic Modulus	2.16E11
Poisson's Ratio	.283

DERIVED DATA

Seal Radius Ratio	1.314681
Diaphragm " "	1.4
Diaphragm area	.0364841
Seal Leverage "	1.225939

RESULTS

Swept Volume (cc)	177.3125
Vol Amp. (cu in)	5.408031

STRESSES AT INNER EDGE (MPa)

Bending	109.0862
Hoop	162.4856
Total	271.5718

STRESSES AT MID-CIRCLE (MPa)

	Circumferential	Radial
Bending	90.90516	25.72616
Stretching	17.03022	60.17747
Pressure		
Total	107.9354	85.90363

STIFFNESS	N/mm	Pa/mm
Small deflections	84.25609	2309.395
Full deflection	219.6770	6021.180

SEALS

Tilt	8.318662 %
Radial shear	3.128620 %

ARTICULATED DIAPHRAGM Program 13 Mar 86 Run on 13 Mar 86 Case 2b
5.4 cu in volume amplitude Thickness 1mm Diam. 9" nominal

GIVEN DATA

Diaph rad ratio	1.6
Outer Seal Radius	.12204
Inner Seal Radius	.0816375
Seal depth (80%)	.00456
Diaphragm Overlap	.0033
" Thickness	.001
" Stroke	.00536
Pressure Diff.	0
Elastic Modulus	2.16E11
Poisson's Ratio	.283

DERIVED DATA

Seal Radius Ratio	1.494901
Diaphragm " "	1.6
Diaphragm area	.0330092
Seal Leverage "	1.163356

RESULTS

Swept Volume (cc)	176.9294
Vol Amp. (cu in)	5.396347

STRESSES AT INNER EDGE (MPa)

Bending	99.41108
Hoop	154.9717
Total	254.3827

STRESSES AT MID-CIRCLE (MPa)

	Circumferential	Radial
Bending	76.47006	21.64103
Stretching	18.69215	66.04999
Pressure		
Total	95.16221	87.69101

STIFFNESS	N/mm	Pa/mm
Small deflections	49.71527	1506.102
Full deflection	147.0711	4455.454

SEALS

Tilt	6.633253 %
Radial shear	2.676576 %

ARTICULATED DIAPHRAGM Program 13 Mar 86 Run on 13 Mar 86 Case 2c
5.4 cu in volume amplitude Thickness 1mm Diam. 9" nominal

GIVEN DATA

Diaph rad ratio	1.8
Outer Seal Radius	.12204
Inner Seal Radius	.0729333
Seal depth (80%)	.00456
Diaphragm Overlap	.0033
" Thickness	.001
" Stroke	.00581
Pressure Diff.	0
Elastic Modulus	2.16E11
Poisson's Ratio	.283

DERIVED DATA

Seal Radius Ratio	1.673309
Diaphragm " "	1.8
Diaphragm area	.0304879
Seal Leverage "	1.134401

RESULTS

Swept Volume (cc)	177.1348
Vol Amp. (cu in)	5.402611

STRESSES AT INNER EDGE (MPa)

Bending	99.73933
Hoop	164.3423
Total	264.0816

STRESSES AT MID-CIRCLE (MPa)

	Circumferential	Radial
Bending	71.24238	20.16159
Stretching	22.27309	78.70349
Pressure		
Total	93.51547	98.86509

STIFFNESS	N/mm	Pa/mm
Small deflections	37.31210	1223.832
Full deflection	123.3502	4045.871

SEALS

Tilt	5.915694 %
Radial shear	2.532981 %

ARTICULATED DIAPHRAGM Program 13 Mar 86 Run on 13 Mar 86 Case 3
5.4 cu in volume amplitude Thickness 1mm Diam. 10" nominal

GIVEN DATA

Diaph rad ratio	3.5
Outer Seal Radius	.13474
Inner Seal Radius	.04274
Seal depth (80%)	.00456
Diaphragm Overlap	.0033
" Thickness	.001
" Stroke	.00657
Pressure Diff.	0
Elastic Modulus	2.16E11
Poisson's Ratio	.283

DERIVED DATA

Seal Radius Ratio	3.152550
Diaphragm " "	3.5
Diaphragm area	.0269552
Seal Leverage "	1.071739

RESULTS

Swept Volume (cc)	177.0960
Vol Amp. (cu in)	5.401427

STRESSES AT INNER EDGE (MPa)

Bending	106.2891
Hoop	187.1040
Total	293.3931

STRESSES AT MID-CIRCLE (MPa)

	Circumferential	Radial
Bending	47.23958	13.36880
Stretching	43.28308	152.9437
Pressure		
Total	90.52266	166.3125

STIFFNESS	N/mm	Pa/mm
Small deflections	17.73567	657.9672
Full deflection	71.78117	2662.976

SEALS

Tilt	3.570652 %
Radial shear	1.677658 %

859426

ARTICULATED DIAPHRAGMS FOR THERMO-MECHANICAL GENERATORS

E. H. Cooke-Yarborough
Consultant
Longworth, Oxfordshire, England

ABSTRACT

The Thermo-mechanical generator is a Stirling engine which uses the deflection of a metal diaphragm, not the movement of a piston, to deliver its power output. In this way almost indefinite operating life can be achieved.

A metal diaphragm of given overall size has its swept volume and permissible pressure differential both limited by stresses in the metal. Flexible mounting of the diaphragm at its edges permits an increase in swept volume by a factor better than 3, with a substantial increase in the permissible pressure differential, without increase in stress. Used in a Thermo-mechanical Generator, the new diaphragm is already providing twice the power output of the original design, with very conservative stress rating.

The paper provides a basis for diaphragm stress calculation, and shows that such diaphragms are capable of much larger increases in power-handling capacity.

THE THERMO-MECHANICAL GENERATOR (TMG)(1) uses a metal diaphragm (2,3) to convert an alternating pressure change in the working gas into an alternating force on a rigid central hub, so that this force can be applied to a linear alternator or other mechanical load. In this respect it differs from diaphragms required simply to transmit pressure from one fluid to another. Not only must it be fixed to a rigid central hub, but also it must itself have adequate rigidity.

The design of the diaphragm used in the Harwell Thermo-mechanical Generators (4) is constrained by the need to minimise the sum of the bending stresses due to the deflection of the diaphragm centre hub and the bending stresses due to gas pressure difference between the two sides of the diaphragm. These factors lead to compromises which have been described in detail (2,3), and lead in turn to a diaphragm design whose stroke is limited to about ½% of the diaphragm diameter. Consequently, for a given swept volume, the diaphragm diameter may be inconveniently large.

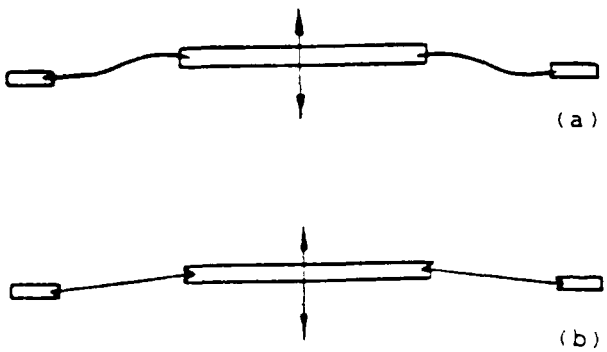

Fig 1 (a) Rigidly-mounted diaphragm
(b) Articulated diaphragm

Deflection of the diaphragm results in radial bending stresses which are at a maximum at the inner edge. The shape to which such a diaphragm is deflected is indicated in Fig 1a.

The Articulated Diaphragm (5) is not rigidly fixed at its edges, but is mounted flexibly. Thus when the diaphragm deflects, there are negligible bending stresses at the edges, and the diaphragm deflects to the shape of a shallow cone, as illustrated in Fig 1b. Deflection introduces tangential bending stresses and hoop stresses whose counterparts in a conventional diaphragm are regarded as small compared with the radial bending stresses. Consequently it is possible to deflect an articulated diaphragm considerably further, while keeping the maximum stress within acceptable limits.

SAE/P-85/16A/$02.50
Copyright 1985 Society of Automotive Engineers, Inc.

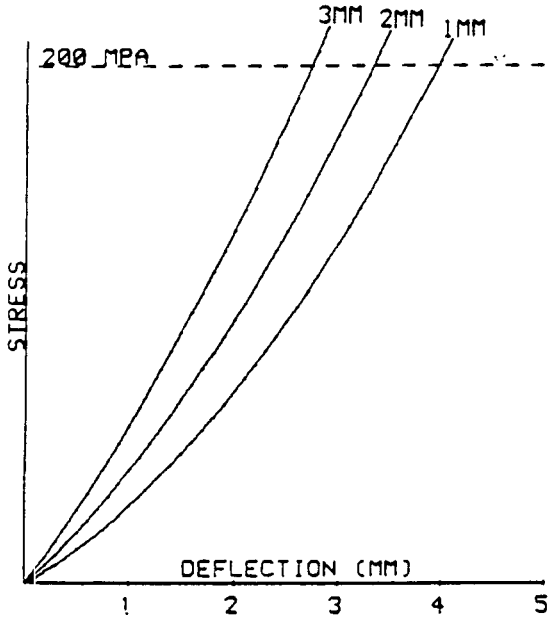

Fig 2 Stress at inner edge of Articulated Diaphragm, for three diaphragm thicknesses

The main stresses in such a diaphragm arise as follows:

First, because the diaphragm is deflected into a shallow cone, it becomes curved, and there is a tangential bending strain. The radius of curvature is at a minimum at the inner edge. The resultant stress varies linearly with deflection.

Second, as the diaphragm deflects, its outer edge is subject to a compressive hoop stress, while its inner edge comes under tensile hoop stress. These stresses vary with the square of deflection.

DEFLECTION STRESSES

Both of these stresses at the inner edge are calculated in Appendix A. Fig 2 shows these stresses calculated for three articulated diaphragms of the same lateral dimensions but of three thicknesses.

It has been shown (6) that for the stainless steel used, the maximum stress should be limited to 200 MPa. It will be seen in Fig 2 that, with the 1mm diaphragm, this stress is reached at a deflection of 4.25mm, decreasing slowly to 2.75mm for the 3mm diaphragm. The overall diameter is 352mm in each case, so the stroke is 2.4% of the overall diameter in the first case, and 1.5% of the overall diameter in the second. There is thus an increase in swept volume by a factor of between 3 and nearly 5 over a rigidly-fixed diaphragm of the same overall diameter.

Diaphragm deflection causes movements at the edges, which must be accomodated by slight flexing of the edge seals. Appendix C calculates the amount of flexing involved.

The present production TMG has (a-b) = 50mm, x = 0.7mm and h = 2mm, so from Exp (C1), the maximum radial movement is only 24 micrometres. If full advantage were taken of the increased stroke, the deflection x would increase to say 3mm, and the radial movement would then be 0.24mm.

With a seal thickness of say 5mm, the shear is 0.5% in the first case, and 5% in the second.

The seal must also accomodate the tilting movement. The maximum slope is 1.4% in the first case and 6% in the second.

Thus the articulated diaphragm does not make exacting demands on the flexing of the seals. No seal failures or leakages have taken place in any TMG using an articulated diaphragm. It is hoped to make seal design and performance the subject of a future publication.

PRESSURE STRESSES

With a conventional diaphragm, a careful compromise is necessary between pressure stress and deflection stress. With the articulated diaphragm, this compromise is less pressing, for the following reasons:-

First, with the edges of the articulated diaphragm relieved of radial bending stress, the maximum stress due to pressure occurs near the mid-circle, where the tangential deflection stress is below its maximum, and the tangential hoop stress is nearly zero.

Second, the diaphragm can be made thicker, as already shown. This reduces the pressure stress, which is inversely proportional to the square of the thickness.

In the early TMGs using a conventional diaphram, the diaphragm stress limited the helium pressure which could be used. With this limitation relaxed by use of the articulated diaphragm, there are other factors (mainly associated with heat transfer) which make it difficult to operate TMGs of the existing design above about 2 atmospheres mean helium pressure.

For this reason the stresses due to pressure are at present relatively small. They have therefore been dealt with only by the very approximate treatment given in Appendix B. This shows that the pressure stress in an articulted diaphragm is 1.5 times that of a conventional diaphragm of the same dimensions.

This increased pressure stress can be more than offset by the increased thickness which the use of an articulated diaphragm permits. Thus, if the diaphragm thickness is doubled, the pressure stress will be 38% of that of an otherwise similar conventional diaphragm.

In TMGs of more advanced design, operating at higher pressures, more careful analysis of pressure stresses will be required, as part of an overall programme of optimising diaphragm dimensions and deflection.

COMBINATION OF STRESSES AT MID-CIRCLE

In addition to the radial bending stress due to pressure calculated in Appendix B, we have to consider:-

An induced tangential stress μ times this stress.

Tangential bending stress due to deflection at the inner edge. The stress at the inner edge is calculated in Appendix A. Since the deflection is nearly conical, this stress decreases approximately inversely with radius.

An induced radial stress μ times this stress.

Radial stress resulting from hoop stress. This is calculated in Appendix D.

An induced tangential stress μ times this stress.

COMPUTATION OF DIAPHRAGM STRESSES

A computer program has been written which makes use of the formulae developed in the Appendices. It calculates the stresses due to deflection, and also calculates approximately the alternating pressure changes in a lossless TMG of given internal dimensions, on the basis described in (7). The stresses resulting from these pressures are evaluated. Some of the stresses tend to oppose one another, or to be at right angles, so the program provides separate figures for the various stresses at mid-circle. The computed diaphragm stresses of a lossless Stirling engine having the dimensions of the HoMach TMG, which delivers about 155w ac (8), are given in the Table.

TABLE
DIAPHRAGM STRESSES IN HOMACH TMG

Inner edge stresses (MPa)

Tangential bending	26.2
Tangential hoop stress	4.6

Mid-circle stresses (Mpa)

	Tangential	Radial
Bending	21.9	6.3
Stretching	1.4	5.0
Pressure	-2.8	-1.0

It will be seen that the combined stresses are well below the acceptable limit of 200 MPa. This design is currently very conservative, and does not yet make full use of the potential of the articulated diaphragm. There is clearly considerable scope for further development of the TMG using this diaphragm.

CONCLUSIONS

A diaphragm has been described which enables a Thermo-mechanical Generator to operate with a larger stroke and at higher pressure than could be permitted with the original Harwell design. This has already made possible the introduction of a TMG delivering more than twice the power of the original design, within approximately the same overall dimensions.

The stresses in the diaphragm have been calculated, and it is shown that, in the present design of TMG, these stresses are much smaller than the acceptable maximum stress in the diaphragm material.

There is scope for considerable improvement in the methods of calculating stresses, and such improvement will be necessary as increases in the power produced by the TMG cause the diaphragm stress limits to be approached.

REFERENCES

1 EH Cooke-Yarborough, E Franklin, J Geisow, R Howlett and CD West. "Thermomechanical Generator: an efficient means of converting heat to electricity at low power levels." Proc. IEE, Vol 12, No 7, July 1974.

2 EH Cooke-Yarborough. "Diaphragm Design for a Thermomechanical Generator." Harwell Memo. AERE - M 2021, February 1968.

3 CD West. "Diaphragm calculations and design for the Thermomechanical Generator." Harwell Memo. AERE - M 2177, March 1969.

4 EH Cooke-Yarborough, and FW Yeates. "Efficient Thermo-mechanical Generation of Electricity from the Heat of Radioisotopes." Record of 10th IECEC (IEEE Cat. No. 75CHO 983-7 TAB), August 1975.

5 EH Cooke-Yarborough. "Improvements in or Relating to Resilient Coupling Devices". British Patent Specification 1 539 034 filed 5 April 1976.

6 EH Cooke-Yarborough. "Fatigue characteristics of the Flexing Members of the Harwell Thermo-mechanical Generator". Harwell Report AERE - R 7693, November 1973.

7 EH Cooke-Yarborough. "Simplified Expressions for the Power Output of a Lossless Stirling Engine". Harwell Memo. AERE - M 2437, March 1974.

8 JR McBride and EH Cooke-Yarborough. "The HoMach TMG: A New Stirling Power Source for Unattended Operation" Proc. 19th IECEC. ISBN 0-89448-115-0, August 1984.

9 LE Andreeva. "Elastic Elements of Instruments" (Moscow 1962). Israel Program for Scientific Translations, Jerusalem. 1966.

10 JC Heap. "Formulas for Circular Plates subjected to Symmetrical Loads and Temperatures". USAEC TID-23984, December 1966.

LIST OF SYMBOLS

a — Outer radius of diaphragm.
A_p Function of a/b tabulated in (9).
b Inner radius of diaphragm.
$B_{q_{in}}$ Function of a/b tabulated in (9).
$B_{q_{out}}$ Function of a/b tabulated in (9).
E Elastic modulus of diaphragm material. (Taken as 2.16×10^{11} for stainless steel.)
h Thickness of diaphragm.
M_{tb} Tangential bending moment at radius b.
P Maximum pressure difference appearing across diaphragm.
W Load applied to inner edge of diaphragm.
x Deflection of diaphragm from mid position.
μ Poisson's ratio for the diaphragm material. (Taken as 0.283 for stainless steel.)

APPENDIX A - STRESSES AT INNER EDGE OF DIAPHRAGM

In calculating these, use is made of formulae derived by Heap (10). Case 12 of (10) deals with an articulated diaphragm loaded at the inner edge by a force W, while Case 60 deals with distributed loading of a similar diaphragm by a pressure P per unit area.

The formulae make use of functions of a/b and μ, which will be designated as follows:-

$$f_1 = (1+\mu)\left[\tfrac{1}{2}\left(\frac{1-\mu}{1+\mu}\right) + \frac{a^2}{a^2-b^2}\ln\frac{a}{b}\right]$$

$$f_2 = \tfrac{1}{2}\left(\frac{3+\mu}{1+\mu}\right)\left(1-\frac{b^2}{a^2}\right) + 2\left(\frac{1+\mu}{1-\mu}\right)\left(\frac{b^2}{a^2-b^2}\right)\left(\ln\frac{a}{b}\right)^2$$

$$f_3 = \frac{(1+\mu)a^2}{a^2-b^2}\left[\tfrac{1}{2}\left(\frac{3+\mu}{1+\mu}\right) - \left(\frac{1}{1+\mu}+\ln\frac{a}{b}\right)\frac{b^2}{a^2} + \tfrac{1}{2}\left(\frac{1-\mu}{1+\mu}\right)\frac{b^4}{a^4}\right]$$

$$f_4 = \frac{1}{8}\left(\frac{5+\mu}{1+\mu}\right) - \tfrac{1}{2}\left(\frac{3+\mu}{1+\mu}\right)\frac{b^2}{a^2} + \frac{1}{8}\left(\frac{7+3\mu}{1+\mu}\right)\frac{b^4}{a^4}$$

$$+ \tfrac{1}{2}\left(\frac{3+\mu}{1-\mu}\right)\frac{b^2}{a^2}\ln\frac{a}{b} - 2\left(\frac{1+\mu}{1-\mu}\right)\left(\frac{b^2}{a^2-b^2}\right)\frac{b^2}{a^2}\left(\ln\frac{a}{b}\right)^2$$

We will first consider the case where the deflection produced by pressure is just balanced by a force W_p applied at the inner edge, so that the inner edge is not deflected.

Equating the expressions for deflection in Cases 12 and 60, we obtain:-

$$W_p = \pi P a^2 f_4/f_2$$

From Case 12, the tangential bending moment due to W_p is:-

$$\frac{W_p f_1}{2\pi} = \frac{Pa^2 f_1 f_4}{2f_2}$$

From Case 60, the tangential bending moment due to the pressure P is:-

$$Pa^2 f_3/2$$

These two bending moments act in opposition, so the net tangential bending moment at the inner edge, when there is pressure but no deflection is:-

$$\frac{Pa^2}{2}\left(\frac{f_1 f_4}{f_2} - f_3\right) \qquad \text{(A1}$$

We now consider the extra bending moment due to deflection of the diaphragm from its rest position by a distance x.

From Case 12:-

$$x = \frac{3Wa^2(1-\mu^2)}{2\pi Eh^3} f_2$$

Where W is the force to deflect the diaphragm by an amount x.

Thus:-

$$W = \frac{2\pi Eh^3 x}{3a^2(1-\mu^2)f_2}$$

Also from Case 12, the bending moment at the inner edge is:-

$$Wf_1/2\pi$$

Thus the bending moment due to deflection x is:-

$$\frac{Eh^3 x}{3a^2(1-\mu^2)}\ \frac{f_1}{f_2} \qquad \text{(A2}$$

Combining Expressions (1) and (2), the total bending moment is therefore:-

$$\frac{Eh^3x}{3a^2(1-\mu^2)}\frac{f_1}{f_2} + \frac{Pa^2}{2}\left(\frac{f_1 f_4}{f_2} - f_3\right) \qquad \text{(A3}$$

To obtain the bending stress, we multiply the above expression by $6/h^2$.

The tangential bending stress at the inner edge is therefore:-

$$\frac{2Ehx}{a^2(1-\mu^2)}\frac{f_1}{f_2} + \frac{3Pa^2}{h^2}\left(\frac{f_1 f_4}{f_2} - f_3\right) \qquad \text{(A4}$$

The calculations in (10) are for small deflections. When the deflection approaches the thickness of the diaphragm material, the hoop stress begins to be significant . The following calculation of the effect of hoop stress approximates by considering only first-order strains. In practice the stresses due to such strains lead to second-order strains which tend to relieve the first-order strains. These second-order strains are neglected, so the approach will over-estimate the first-order strains and the resultant stress. The approach is therefore a conservative one.

One consequence of this approach is that, if a strip of the diaphragm material is stretched, the Poisson effect is permitted to make it thinner, but not narrower. To maintain its width, a lateral stress is set up perpendicular to the initial stress and smaller by a factor μ (Poisson's Ratio, taken as 0.283 for stainless steel). The effect of this is to make the effective coefficient of elasticity of the material greater than the true value by a factor $1/(1-\mu^2)$, an increase of about 9% for stainless steel.

If the diaphragm is deflected by x, and the distance a-b measured along the deflected diaphragm remains constant, this now becomes a slant distance, so the inner radius b is forced to increase, and the outer radius a to decrease, as shown in Fig 3.

If we assume that both change by the same amount, then the increase of b is:-

$$\frac{x^2}{4(a-b)}$$

Therefore the hoop tensile strain at the inner edge is:-

$$\frac{x^2}{4b(a-b)} \qquad \text{(A5}$$

and the hoop stress is:-

$$\frac{Ex^2}{4b(a-b)(1-\mu^2)} \qquad \text{(A6}$$

Likewise the hoop compression stress at the outer edge is:-

$$\frac{Ex^2}{4a(a-b)(1-\mu^2)} \qquad \text{(A7}$$

For deflections comparable with, or larger than, the diaphragm thickness, these hoop stresses should be added to the stress given by Exp (A4).

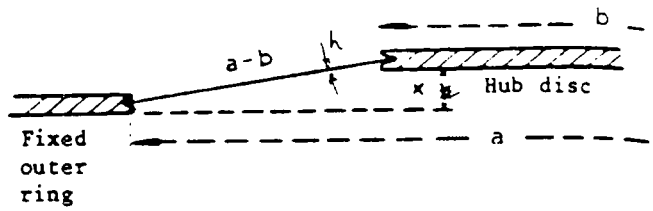

Fig 3 Generation of hoop stresses

APPENDIX B - PRESSURE STRESS AT MID-CIRCLE

The formulae presented in (10) give stresses at the inner and outer edges of the diaphragm, but not at intermediate radii. Formulae for the slope of the diaphragm at any radius are given. The tangential bending stress can be calculated from this. Differentiation of this slope would give the curvature, from which the radial bending stress at this radius could be deduced.

Because the pressure stress is relatively small at the pressure differences at present used in the TMG, a more approximate method has been used, which draws on earlier work on conventional diaphragms (2,3). It is assumed that the pressure stress is at a maximum at approximately mid-way between the inner and outer edges.

If the ratio between the outer and inner radii is not large, we can approximate by treating any narrow radial sector of the diaphragm as a beam with an evenly distributed load.

In the case of a conventional diaphragm, the equivalent beam is encastré. The bending stresses at the two ends can be taken as the average between the bending stresses at the inner and outer edges of the diaphragm.

The corresponding equivalent to an articulated diaphragm is a beam simply supported

at both ends. Use of standard formulae to compare the deflections and stresses in the two types of beam show that, other things being equal, in the simply-supported beam the maximum bending stress is at the centre and is 1.5 times the bending stress at the ends of the encastré beam.

Thus, in the articulated diaphragm, the pressure stress is increased by a factor 1.5 over the mean of the pressure stresses at the inner and outer edges of the encastré diaphragm having the same dimensions.

Expressions for the latter have been derived in Appendix 1 of (2).

Thus the pressure stress at the mid-circle of an articulated diaphragm is:-

$$1.5p\frac{a^2}{h^2} A_p\left(B_p - \frac{(B_{q_{in}} + B_{q_{out}})}{2}\right) \qquad \text{(B1}$$

APPENDIX C

MOVEMENT AT THE DIAPHRAGM EDGES

The edges of the diaphragm tilt, as the diaphragm deflects. They also move inwards and outwards radially. These movements have to be accomodated by the edge seals.

The strain at the edges has been calculated in Appendix A. This corresponds to the movement mid-way between the two faces. The largest movement from the mid-position will be of the face which is concave at maximum deflection. This movement will correspond to the effects of the strain combined with the effect of tilting.

The tilt angle is $x/(a-b)$, so the movement due to tilting alone is $hx/2(a-b)$.

The radial movement due to strain at either edge is $x^2/4(a-b)$, so the total movement is:-

$$\frac{x}{(a-b)}\left(x+\frac{h}{2}\right) \qquad \text{(C1}$$

APPENDIX D

RADIAL STRESSES AT MID-CIRCLE

Since we assume that stresses are not relieved by secondary strains, there will be a radial stretching stress which opposes radial strains between the inner and outer edges when the diaphragm is deflected. These are calculated below:-

Suppose that the hoop stress varies linearly with radius r from the positive value given by Exp (A6) at radius b to the corresponding negative value given by Exp (A7) at radius a.

Hoop stress at radius r due to deflection of diaphragm hub:-

$$\frac{Ex^2}{2(1-\mu^2)(a-b)^2}\left(\frac{a+b}{2r} - 1\right)$$

Radial stress due to stress in a ring of material of width dr:-

$$\frac{Ex^2}{2(1-\mu^2)(a-b)^2}\left(\frac{a+b}{2r} - 1\right)dr$$

To obtain the total stress at $(a+b)/2$, the mid-circle of the diaphragm, this expression is integrated from b to $(a+b)/2$.

The resultant stress is:-

$$\frac{Ex^2}{2(1-\mu^2)(a-b)^2}\left(\frac{a}{b} - 1 - \ln\left(\frac{a}{2b} + \frac{1}{2}\right)\right) \qquad \text{(D1}$$

859072

METAL SPRING FOR TUNING AND POSITIONING THE DISPLACER OF A SHORT-STROKE STIRLING ENGINE

E. H. Cooke-Yarborough
Consultant
Longworth, Oxfordshire, England

ABSTRACT

The Thermo-mechanical Generator is a Stirling engine which achieves an almost indefinite operating life by completely avoiding any relative motion between surfaces in contact. Sliding seals, or bearing surfaces to guide the movement of the displacer, cannot therefore be used. An alternative therefore has to be found to the rod and cylinder, forming a gas spring, which is used in almost all free-piston Stirling engine.

A mechanical spring was used in earlier TMGs to provide the restoring force necessary to tune the mass of the displacer to the operating frequency, and to locate the displacer laterally and axially. Because of conflicting requirements, this spring proved very difficult to make.

The paper describes the design of an improved spring for an enlarged TMG. This spring is easier to manufacture, and can relieve the mounting points of bending stress. It is therefore easy to cascade several such springs.

A FREE-DISPLACER STIRLING ENGINE usually requires to have its displacer mechanically tuned, so that the mass of the displacer resonates with the stiffness of a restoring spring at a frequency near to the design operating frequency of the engine. Means must also be provided for feeding mechanical power into the displacer, so as to maintain it in oscillation.

In many designs of free-piston Stirling engine, this tuning is effected with a gas spring, which may, for example, consist of a rod attached to the cold end of the displacer, sliding in a stationary small-diameter cylinder which contains the gas providing the spring force. As well as functioning as a spring, this arrangement allows the alternating component of gas pressure in the main working volume, acting on the area of the rod, to provide the cyclic force necessary to maintain the displacer in oscillation.

In other arrangements the small-diameter cylinder in which the rod slides is located within the power piston, and moves with it.

In still other arrangements the relative positions of rod and cylinder are interchanged.

All these depend on a sliding seal (or on a very close clearance) between rod and cylinder, and have the following disadvantages:-

- Mechanical friction and/or leakage in this seal will cause losses.
- Any static friction will inhibit self-starting.
- Any wear in the seal will change the excitation of the displacer, and may limit the life of the engine.
- The cycling of the gas pressure inside the cylinder is neither fully isothermal nor fully adiabatic, so irreversible losses result.
- The mean position of the displacer can drift axially, and means have to be provided to offset this.

MECHANICAL SPRINGS

The Thermo-mechanical Generator is intended to have an operating life at least as good as that of a generator using thermo-electric semiconductors, so from the outset the use of sliding seals was avoided. Instead, the TMG delivers its mechanical power by deflection of a metal diaphragm, so it operates with a very short stroke. The displacer can therefore be mounted on a flat metal spring, which provides the restoring force required to tune the displacer mass mechanically, and also to locate the displacer axially and laterally in the cylinder. In this way all the above disadvantages are avoided. The general arrangement of the TMG (Ref 2) is illustrated in Fig 1.

There is no sliding seal between the displacer and the cylinder wall. The clearance

SAE/P-85/164/$02.50
Copyright 1985 Society of Automotive Engineers, Inc.

between these two surfaces acts as the regenerator, or as part of it. To minimize heat loss through the regenerator, this clearance should be as small as mechanical tolerances permit, so accurate lateral location is required.

The displacer spring has therefore to meet some exacting requirements:-

It must be capable of positive attachment both to the displacer and to the body of the TMG.

It must be mechanically stable.

It must not significantly impede the flow of gas in the working volume.

The clearances necessary to permit spring deflection should add as little as possible to the dead volume.

The mechanical stresses in the spring should be kept safely below the fatigue limit.

Before considering the design of the new spring, it is useful first to note the lessons learned from the spring used in the earlier TMGs.

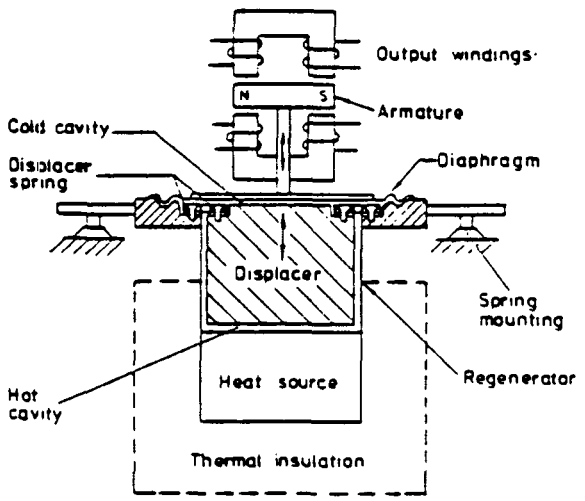

Fig 1 General arrangement of TMG

25- AND 60-WATT HARWELL TMGs

Figure 2 shows this spring. It is formed from a single disc of stainless steel, and consists of two coaxial rings. The outer ring is bolted at two points to the TMG body, while the inner ring is bolted at two points to the displacer. The inner and outer rings are joined by bridges on axes at right angles to the axes passing through the four fixing points. The central disc is linked to the inner ring by two further bridges, so that it moves at a fraction of the displacer amplitude. This disc is intended to act as an isothermalizer in the compression space.

The outer diameter of the inner ring is equal to that of the displacer, so the slots between the two rings provide a path for the gas flowing along the clearance between displacer and cylinder.

The outer ring is the longer, and partly to offset the resultant reduction in stiffness, it is also made wider than the inner ring. It remains nevertheless less stiff than the inner ring, so deflects by about 60% of the total deflection, while the inner ring deflects by about 40%. This approximately equalizes the stresses in the two rings.

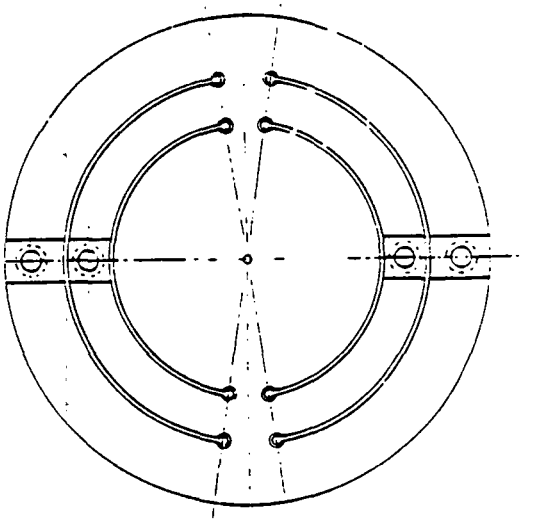

Fig 2 Double-ring displacer spring used in the Harwell TMGs

For calculation of stresses, each ring can be regarded as consisting of four curved double cantilevers, so deflection of the spring flexes 16 cantilevers. The bases of these cantilevers are close to the mounting points or to the bridges. Consequently the mounting points and the bridges are subject to bending moments when the spring deflects.

The early experimental springs were found to fret at the mounting points. This was attributed to the bending moments at these points causing curvature of the interface between spring and mounting surface, and thus slight relative movement between these surfaces.

The radius of curvature at the base of a cantilever subject to a bending moment is inversely proportional to the cube of the thickness of the material in this region. It was found experimentally that this fretting could be eliminated by doubling the thickness of the spring material near to the mounting points, and thus reducing eight-fold the curvature produced by a given bending moment.

At the bridges there are no interfaces, and therefore there is no fretting. The bending moments in these regions are shared between the bridges joining the two rings and those joining the inner ring to the isothermalizer. Without the central isothermalizer disc, the stresses in the bridges between the inner and outer rings would have been unacceptably high.

The spring was designed to the same stress

limit as the diaphragm: 200 Megapascals (Ref 1). This involved a certain amount of uncertainty, because local stresses in this relatively complex structure could not readily be calculated. A few failures in experimental springs could be attributed to stress raisers, but these were eliminated by minor design changes, and by careful attention to the machining techniques used. No failures have occurred in the field in TMGs operating for a total of more than 120,000 machine-hours (Ref 2), so it can be concluded that this design is adequately conservative.

The spring is, however, difficult to make. Stainless steel is not an easy material to machine, and to provide the thickness at the mounting points, the spring has to be machined from stock of more than twice the final spring thickness. Machining the four narrow slots is also difficult, and there are frequent tool breakages. Moreover the removal of large amounts of material destroys the stress balance, so that frequent stress relieving is necessary to prevent distortion.

Other lessons learned were:-

The spring imposes considerable bending moment on the displacer end cap, which has to be designed to resist this moment, while keeping mass to a minimum.

The clearance between the outer ring and the stationary TMG body forms part of the compression volume. This clearance is at a maximum at the point in the cycle where the expansion volume is also at a maximum. In effect therefore this clearance increases the effective dead volume substantially.

While the central isothermalizer disc gave some improvement in power output in the 25-watt TMGs operating at 1 atmosphere, it is much less effective in the higher-powered TMGs operating at about 2 atmospheres (Ref 3).

THE HOMACH TMGs

Compared with the Harwell TMGs, these new TMGs (Ref 4) have twice the displacer diameter. However, like the earlier designs, they have no separate heat exchangers, heat transfer taking place over the large surface areas of the shallow expansion and compression cavities. In order to avoid the need for greater transfer of heat per unit cavity area, the helium pressure and displacer stroke remain almost unchanged.

The doubling of the displacer diameter without increase of deflection makes it possible to use a displacer spring consisting of a single ring equivalent to one of the two concentric rings of the earlier design.

It was decided to make the new spring equivalent to the inner ring of the earlier design in order to avoid the added dead volume mentioned above. Keeping the ring diameter within the displacer diameter also has practical advantages in construction of the TMG as a whole.

Calculation of the mechanical losses due to non-isothermal heat transfer (Ref 5) had shown that subdividing the compression space with an isothermalizer was unhelpful, so this was eliminated. The spring thus consists of a single ring, with four attachment points, and the machining of narrow slots is entirely avoided.

SCALING OF SPRING DIMENSIONS

At this stage we still consider the spring to be thickened in the region of the four attachment points, and will avoid the practical problem arising from the stationary and moving attachment points being at the same radius.

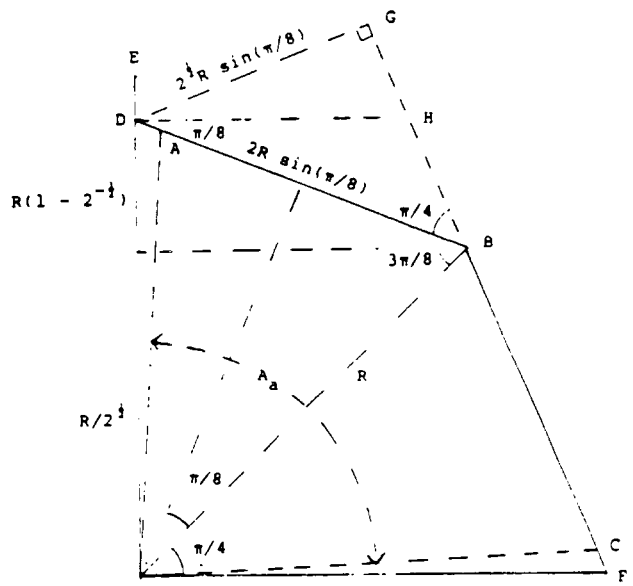

Fig 3 Geometrical construction used in Appendix to calculate neutral radius

To simplify calculation, we approximate by making the ring into a regular octagon, so that each 90° arc between adjacent mounting points contains two straight cantilevers AB and BC, joined at B, as shown in Fig 3. These cantilevers cover an arc Aa, which is a little less than 90°. The mounting points are at D and F, and the regions DA and CF are assumed to be thickened, so that they do not flex significantly.

The resultant stiffness consists of a major component due to the flexing of the cantilevers and a smaller component due to torsion. To a first order, this stiffness is proportional to the radial width of the ring and to the cube of the ratio between the thickness and the radius.

The maximum spring stress occurs at the base of each cantilever. To a first order this stress is proportional to the deflection and to the thickness, and is inversely proportional to the square of the radius.

We can now see the effect on the properties

of the spring of doubling the lateral dimensions on the TMG, while reducing the spring from two rings to one.

Consider first the stiffness of the spring. If all the dimensions of the spring are doubled, its stiffness is doubled. Use of a spring consisting of a single ring rather than two in series, doubles the stiffness again, resulting in a four-fold increase in stiffness.

If the diameter of the displacer is doubled, while its length and density are kept constant, its mass is increased four-fold. Thus the ratio of mass to stiffness is unchanged, and so therefore is the mechanical resonant frequency.

Consider now the stresses in the spring. Although the overall spring deflection is unchanged, there is now only one ring, so the deflection of this is doubled. Its thickness is also doubled (see above), and so is its radius, so the stress is unchanged.

It was noted earlier that the inner ring of the original spring design contributed rather less than 50% to the total deflection. Consequently when this ring is scaled up 2:1 to form the new spring, the deflection available for a given stress is about 20% less than the deflection provided by the original spring. There is of course a corresponding reduction in displacer swept volume.

This disadvantage could be avoided by using a larger ring, scaled-up from the outer ring of the original spring, but this is inconvenient in the present design of TMG, as already indicated.

SPRING MOUNTING

In general, it is not convenient to have the fixed and moving mounting points at the same radius, so it may be necessary either to provide the spring with lugs outside the ring for the fixed mounting points or lugs inside the ring for the displacer mounting points, or, as we shall see, both.

The Appendix calculates the bending moments in external and internal lugs. Expression (5) shows that for the internal lugs there is a radius R_0 at which there is no bending moment. A mounting point at this radius has zero bending stress.

This is an important result. It means that the displacer end cap, to which the spring is mounted, need not be designed to resist bending stresses. It also means that there is no bending moment in the lug at this point, so there will be no fretting if the thickness of the internal lug is made no greater than that of the rest of the spring.

In an external lug (Fig 4) the bending moment increases with increasing distance from the centre of the spring, so the mounting point will be subject to fretting unless the lug is made at least twice as thick as the spring.

It has to be concluded that, if spring performance is not to be reduced, the external lugs must be made thicker than the spring, so the potential advantage of reduced machining are not realised in this case.

In cases where both the moving and the stationary attachments can be made to internal lugs (Fig 5), bending moments can be eliminated at all these points. The fretting problem then does not arise, so the spring can be made from stock almost as thin as the final spring, and is flat on both sides.

EXPERIMENTAL RESULTS

Several experimental springs have been made, in order to check the neutral radius. The results are as follows (dimensions in mm):-

Spring	A	B	C	D
Outer radius	134	134	126.5	126.5
Thickness	6.3	7.35	6.3	6.3
Breadth	34.5	34.5	31	31
Mean radius	116.7	116.7	111	111
Lugs	thin	thick	thin	thick
Neutral radius				
Measured	78	74	77	67
Calculated	67.5	67.5	66	66
Ratio	1.16	1.1	1.17	1.02

A thin lug is one which has the same thickness as the spring, while a thick lug is of about twice the spring thickness.

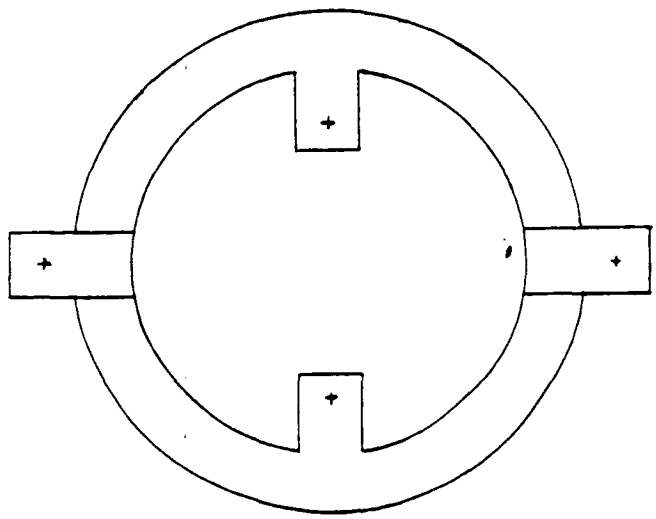

Fig 4 Spring with two thick external lugs and two thin internal lugs

Spring A is the only one to have four internal lugs (Fig 5). All the others have two internal lugs. Spring B (used in the present design of TMG) has two external lugs (Fig 4).

In the calculations in the Appendix it is assumed that the lugs are rigid. It will be seen that cases B and D, which use thick lugs, come closest to the calculated neutral radii. The neutral radius is not easy to measure accurately, so the agreement with theory is

reasonably good.

If the lugs are of the same thickness as the spring, they will flex, and, in effect form part of the spring. This has not been treated theoretically, but it seems from the results obtained with springs A and C that the use of thin lugs increases the neutral radius significantly.

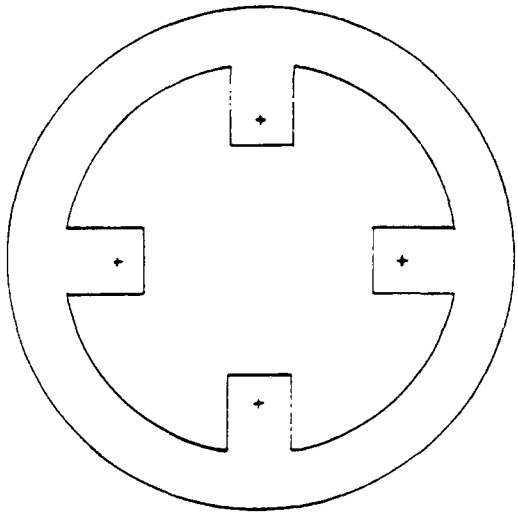

Fig 5 Spring with four thin internal lugs

CONCLUSIONS

A flat spring has been described which can be made from flat stock little if any thicker than the final spring.

It can be positively attached to two components in relative motion, and will act both in tension and in compression.

There is nearly zero bending moment at the points of attachment, so fretting is eliminated.

Springs making partial use of this principle are used to support and to tune the displacers of TMGs currently being manufactured by HoMach Systems.

Springs with four internal lugs can be stacked, each spring being attached to each of its two neighbours by one pair of its lugs. A stacked spring of this sort can be positively fixed at its two ends, so can be used in both tension and compression, a capability not otherwise readily obtainable with axially symmetrical springs.

Thus, although the spring was originally designed for short-stroke applications, it should be possible to use it in Stirling engines, and elsewhere, where a longer stroke is required.

REFERENCES

1) EH Cooke-Yarborough: "Fatigue Characteristics of the Flexing Members of the Harwell Thermo-mechanical Generator". Harwell Report AERE-R7693. Her Majesty's Stationary Office. March 1974.

2) EH Cooke-Yarborough: "Diaphragm Stirling Engines: Achievements and Future Potential". Proc I Mech E Conference on Stirling Engines ISBN 0 85298 489 8. March 1982.

3) EH Cooke-Yarborough and NL Spotteswood: "A 60-Watt Thermo-mechanical Generator as the Main Power Source for a Major Lighthouse". Proc Xth Conference of the International Association of Lighthouse Authorities, Tokyo 1980.

4) JR McBride and EH Cooke-Yarborough: "The HoMach TMG: A New Stirling Power Source for Unattended Operation". Proc. 19th IECEC ISBN 0-89448-115-0. August 1984.

5) EH Cooke-Yarborough and DJ Ryden: "Mechanical Power Loss Caused by Imperfect Heat Transfer in a Nearly-Isothermal Stirling Engine". Proc. 20th IECEC. August 1985.

6) EH Cooke-Yarborough: "Annular Spring". UK Patent Application GB 2136087A. Sept. 1984.

7) LE Andreeva: "Elastic Elements of Instruments". Translated from the Russian. Israel Program for Scientific Translations. IPST Cat. No. 2152. 1966.

8) A Morley:"Strength of Materials". Longmans, Green & Co.

9) OW Esbach and M Souders: "Handbook of Engineering Fundamentals" J Wiley & Sons.

10) FH Newman and VHL Searle: "The General Properties of Matter". Ernest Benn Ltd.

LIST OF SYMBOLS

A_a Angle subtended at centre of spring by one spring arc.

b breadth of spring section.

d thickness of spring section.

E Elastic modulus of spring material.

h Deflection of spring from mid position.

M_r Bending moment in lug at radius R + r.

N Shear modulus of spring material.

R Mean radius of ring which forms the spring.

r Distance measured radially outwards from R.

R_0 Radius at which bending moment is zero.

S_a Slope angle at tip of loaded cantilever.

T_t Torsional couple applied to free end of cantilever.

V_c Force applied to free end of cantilever.

APPENDIX: BENDING MOMENTS IN LUGS

The following calculations make use, where appropriate, of formulae given in standard texts (Refs 6 to 10).

Each of the four arcs forming the spring is regarded as consisting of two equal cantilevers, each of length $A_aR/2$, fixed at A and at C, and joined at B. This is shown in Figure 3.

If the spring is deflected vertically by h, the deflection between A and B is h/2, and the vertical cantilever force at B is:-

$$V_c = \frac{Ehbd^3}{A_a^3R^3} \qquad (1$$

Slope angle S_a of tip of single cantilever loaded by a force V_c:

$$V_c \times \frac{12A_a^2R^2}{8Ebd^3}$$

Substitute V_c from Expression (1). Slope angle is:-

$$\frac{3h}{2A_aR}$$

Angle through which cantilever must be twisted to make tip parallel with radius at B:-

$$\tan^{-1}\left(\tan\left(\frac{3h}{2A_aR}\right) \times \tan\left(\frac{A_a}{4}\right)\right)$$

Both angles are small, so this twist angle approximates to 3h/8R. The torque produced by this twist in a beam of length $A_aR/2$ is:-

$$\frac{24b^3d^3N}{20A_aR(d^2 + b^2)} \times \frac{3h}{16R}$$

Since N = 0.4E, the couple is:-

$$T_t = \frac{9Ehb^3d^3}{100\ A_aR^2(d^2 + b^2)} \qquad (2$$

The couple produced by twisting of the cantilever BC exerts a force at D through the arm DG, whose length is:-

$$2^{\frac{1}{2}}\ R \sin\frac{\pi}{8}$$

The vertical force exerted at D due to the twisting of this cantilever is therefore:-

$$\frac{T_t}{2^{\frac{1}{2}}\ R \sin\frac{\pi}{8}}$$

The position of a point on an external lug is represented by E in Fig 3. If DE = r, the bending moment at E is the sum of two components:-

that due to twice the vertical cantilever force at B (V_c) acting on an arm of length $r + R(1 - 2^{-\frac{1}{2}})$.

twice the component of the the twisting moment T_t which acts tangentially about DH. This component is equal to $T_t\cos(\pi/8)$.

The total bending moment in a lug at radius R + r is therefore:-

$$M_r = 2V_c(r + R(1 - 2^{-\frac{1}{2}})) + 2T_t\cos\frac{\pi}{8} \qquad (3$$

The bending moment in an external lug increases rapidly with distance outwards from the ring.

If a lug is extended radially inwards, the bending moment in the lug is at a maximum where it joins the ring. The bending moment here can be calculated by making r in Expression (3) equal to -b/2.

The bending moment decreases with distance from the centre of the ring, and there is a radius R_0 at which the bending moments in the lug cancel. To find this radius, we make r in Expression (3) equal to $R_0 - R$, and equate to zero.

This yields:-

$$R_0 = 2^{-\frac{1}{2}}\ R - \frac{T_t}{V_c}\cos\frac{\pi}{8} \qquad (4$$

Substituting for T_t from Expression (2) and V_c from Expression (1) gives the neutral radius:-

$$R_0 = R\left(2^{-\frac{1}{2}} - \frac{9\cos(\pi/8)}{100} \cdot \frac{A_a^2\ b^2}{(b^2 + d^2)}\right)$$

Thus:-

$$R_0 = R\left(0.707 - 0.083\ \frac{A_a^2b^2}{(d^2 + b^2)}\right) \qquad (5$$

ORNL/Sub/86-47985/2&V1,V2
Dist. Category UC-95d

INTERNAL DISTRIBUTION

1. F. C. Chen
2. F. A. Creswick
3. R. C. DeVault
4. P. D. Fairchild
5. S. K. Fischer
6-11. A. F. Frederick
12. W. Fulkerson
13. M. A. Kuliasha
14. F. C. Maienschein
15. R. W. Murphy
16-20. G. T. Privon
21. D. E. Reichle
22. E. Rogers
23-27. M. O. Saunders
28. R. B. Shelton
29. T. J. Wilbanks
30-31. Central Research Library
32. Document Reference Section
33. Laboratory Records-RC
34-35. Laboratory Records
36. ORNL Patent Office

EXTERNAL DISTRIBUTION

37-48. R. A. Ackermann, Mechanical Technology, Inc., 968 Albany-Shaker Road, Latham, NY 12110
49. William Beale, Sunpower, Inc., 6 Byard Street, Athens, OH 45701
50. Glendon M. Benson, Energy Research and Generation, Inc., Lowell and 57th Streets, Oakland, CA 94608
51. Don Beremand, NASA-Lewis Research Center, 21000 Brookpark Road, Cleveland, OH 44135
52. Dick Bloomquist, Code 2752, David W. Taylor Naval Ship R&D Center, Annapolis, MD 21402
53. T. A. Braun, Tectonics Research, Inc., 9556 West Bloomington Freeway, Minneapolis, MN 55431
54. J. P. Budliger, Battelle-Geneva, 7 route de Drize, 1227 Carouge (Geneva), SWITZERLAND
55. J. G. Carbonell, Associate Professor of Computer Science, Carnegie-Mellon University, Pittsburg, PA 15213
56. Stig C. Carlqvist, Societe ECA, Boite Postale 16, 92194 Meudon Cedex, FRANCE
57. Dick Cawley, Lennox Industries, Inc., 1600 Metrocrest Drive, Carrollton, TX 75006
58. W. S. Chiu, General Electric Company, P.O. Box 527, King of Prussia, PA 19406
59. M. Clinch, Gas Research Institute, 8600 West Bryn Mawr Avenue, Chicago, IL 60631
60. E. H. Cooke-Yarborough, Lincoln Lodge, Longworth Nr Abingdon, Oxfordshire, OX13, 5DU, ENGLAND
61. J. J. Cuttica, Vice President of Research and Development, Gas Research Institute, 8600 W. Bryn Mawr Avenue, Chicago, IL 60631
62. J. G. Daley, Argonne National Laboratory, 9700 South Cass Avenue, Argonne, IL 60439
63. D. K. Darooka, General Electric Company, P.O. Box 527, King of Prussia, PA 19406
64. R. L. Demler, Foster-Miller Associates, Inc., 350 2nd Avenue, Waltham, MA 02254

65. G. R. Dochat, Mechanical Technology, Inc., 968 Albany-Shaker Road, Latham, NY 12110
66. J. E. Dudenhoefer, NASA-Lewis Research Center, 21000 Brookpark Road, Cleveland, OH 44135
67. T. Finkelstein, Stirling Associates International, P.O. Box 643 Beverly Hills, CA 90213
68. R. J. Fiskum, Energy Conversion Equipment Branch, CE-112, GF-217/FORS, U.S. Department of Energy, 1000 Independence Avenue SW, Washington, DC 20585
69. M. Foster, Homach Systems, Ltd., Hargraves Road, Groundwell Industrial Estate, Swindon Wilts, SN2, 5AZ, ENGLAND
70. A. A. Frank, Mechanical Engineering Dept., California Davis, Davis, California 95616
71. S. Freedman, Gas Research Institute, 8600 West Bryn Mawr Avenue, Chicago, IL 60631
72. D. R. Gedeon, Gedeon Associates, Box 141 A, South Canaan Road, Athens, OH 45701
73. Ted Gilles, Lennox Industries, Inc., Promenade Towers, P.O. Box 400450, Dallas, TX 75240
74. S. M. Gillis, Dean of the Graduate School, Duke University, 4875 Duke Station, Durham, NC 27706
75. L. Goldberg, University of Minnesota, Department of Civil and Mineral Engineering, 500 Pillsbury Drive SE, Minneapolis, MN 55455
76. B. S. Goldwater, Mechanical Technology, Inc., 968 Albany-Shaker Road, Latham, NY 12110
77. A. C. Harvey, Foster-Miller Associates, Inc., 350 2nd Avenue, Waltham, MA 02254
78. Bob Holtz, Argonne National Laboratory, 9700 South Cass Avenue, Argonne, IL 60439
79. R. C. Hundt, Lennox Industries, Inc., 1600 Metrocrest Drive, Carrollton, TX 75006
80. P. Huntley, Borg-Warner Research, 1200 South Wolf Road, Des Plaines, IL 60018
81. B. C. Hwang, Code 2722, David Taylor Naval Ship R&D Center, Annapolis, MD 21402
82. H. S. Izawa, Washington Gas Light Company, Research Department, 6801 Industrial Road, Springfield, VA 22151
83. L. N. Johansson, Stirling Power Systems, 7101 Jackson Road, Ann Arbor, MI 48103
84. F. R. Kalhammer, Vice President, Electric Power Research Institute, P.O. Box 10412, Palo Alto, CA 94303
85. J. P. Kalt, Professor of Economics, Kennedy School of Government, Harvard University, 79 John F. Kennedy Street, Cambridge, MA 02138
86. T. Kapus, CE-113, Building Equipment Division, U.S. Department of Energy, 1000 Independence Avenue SW, Washington, DC 20585
87. K. P. Lee, Aspen Systems, Inc., 275 Boston Post Road, Marlborough, MA 01752
88. Bengt Lindquist, Swedish Council for Building Research, Sankt Goransgatan, S-11233 Stockholm, SWEDEN
89. A. R. Maret, Gas Research Institute, 8600 West Bryn Mawr Avenue, Chicago, IL 60631
90. J. C. Mayor, Swiss Federal Institute for Reactor Research, CH-5303 Wurenlingen, SWITZERLAND

91. R. C. Meier, General Electric Company, P.O. Box 527, King of Prussia, PA 19406
92. R. J. Meijer, Stirling Thermal Motors, Inc., 2841 Boardwalk, Ann Arbor, MI 48104
93. D. E. Morrison, Professor of Sociology, Michigan State University, 201 Berkey Hall, East Lansing, MI 48824-1111
94. N. P. Nightingale, Mechanical Technology, Inc., 968 Albany-Shaker Road, Latham, NY 12110
95. Herbert Nilsson, United Stirling AB, P.O. Box 856, S-201 80 Malmo, SWEDEN
96. W. H. Percival, United Stirling, Inc., 1800 Diagonal Road, Alexandria, VA 22314
97. R. L. Perrine, Professor, Engineering and Applied Sciences, Civil Engineering Department, Engineering I, Room 2066, University of California, Los Angeles, CA 90024
98. B. Qvale, Laboratory for Energetics, The Technical University of Denmark, DTH Building 403, DK-2800 Lyngby, DENMARK
99. E. A. Reid, Jr., Columbia Gas System Service Corporation, 1600 Dublin Road, Columbus, OH 43215
100. P. Riggle, Joint Center for Graduate Study, University of Washington, 100 Sprout Road, Richland, WA 99352
101. J. D. Ryan, Energy Conversion Equipment Branch, CE-112,GF-217/FORS, U.S. Department of Energy, 1000 Independence Avenue SW, Washington, DC 20585
102. J. G. Schreiber, NASA-Lewis Research Center, 21000 Brookpark Road, Cleveland, OH 44135
103. J. R. Senft, Department of Mathematics/Computer Science, University of Wisconsin, River Falls, WI 54022
104. J. G. Slaby, NASA-Lewis Research Center, 21000 Brookpark Road, Cleveland, OH 44135
105. J. L. Smith, Jr., Mechanical Engineering Department, Massachusetts Institute of Technology, Cambridge, MA 02139
106. P. F. Swenson, The East Ohio Gas Company, East 9th Avenue at Superior, P.O. Box 5759, Cleveland, OH 44101
107. W. P. Teagan, Arthur D. Little, Inc., 20 Acorn Park, Cambridge, MA 02140
108. R. C. Tew, NASA-Lewis Research Center, 21000 Brookpark Road, Cleveland, OH 44135
109. W. M. Toscano, Aspen Systems, Inc., 275 Boston Post Road, Marlborough, MA 01752
110. V. J. Van Griethuysen, Air Force Wright Aeronautical Laboratories, Wright-Paterson Air Force Base, OH 45433
111. D. A. Vaughn, ATTN: STRBE-EMP, Belvoir R&D Center, Ft. Belvoir, VA 22060
112. G. Walker, University of Calgary, Department of Mechanical Engineering, 2500 University Drive NW, Calgary, CANADA T2N1N4
113. B. P. Wang, Mechanical Engineering Department, University of Texas at Arlington, P.O. Box 19023, Arlington, TX 76019
114. M. A. White, University of Washington, Joint Center for Graduate Study, 100 Sprout Road, Richland, WA 99352
115. L. Williams, Logan Lewis Library, Research Division, Carrier Corporation, Carrier Parkway, Syracuse, NY 13221
113. J. Wurm, Institute of Gas Technology, 3424 South State Street, Chicago, IL 60616

114. Y. Yamashita, New Energy Development Organization, Sunshine 60 29F, 101 3-Chome Higashi-Ikebukuro, Toshima-Ku, Tokyo 170 JAPAN
115. Institute for Energy Analysis, ORAU Library, Oak Ridge, TN 37831
116. Office of the Assistant Manager for Energy R&D, U.S. Department of Energy, Oak Ridge Operations, P. O. Box 2001, Oak Ridge, TN 37831-8600
117-341. Given distribution for Category UC-95d

☆U.S. GOVERNMENT PRINTING OFFICE: 1985- 548-119/50129